Linear and Nonlinear Stratified Spindown over Sloping Topography

by

Jessica A. Benthuysen

B.S., University of Washington, 2004

Submitted in partial fulfillment of the requirements for the degree of

Doctor of Philosophy

at the

MASSACHUSETTS INSTITUTE OF TECHNOLOGY

and the

WOODS HOLE OCEANOGRAPHIC INSTITUTION

June 2010

Author .....

Joint Program in Oceanography/ Applied Ocean Science and Engineering
Massachusetts Institute of Technology
and Woods Hole Oceanographic Institution
March 31, 2010

Certified by .....

Steven J. Lentz
Senior Scientist
Thesis Supervisor

Certified by .....

Leif N. Thomas
Assistant Professor
Thesis Supervisor

Accepted by .....

Karl Helfrich
Chair, Joint Committee for Physical Oceanography
Woods Hole Oceanographic Institution

Linear and Nonlinear Stratified Spindown over Sloping Topography

by

Jessica A. Benthuysen

Submitted to the Joint Program in Oceanography/Applied Ocean Science and Engineering
on March 31, 2010, in partial fulfillment of the
requirements for the degree of
Doctor of Philosophy in Physical Oceanography

Abstract

In a stratified rotating fluid, frictionally driven circulations couple with the buoyancy field over sloping topography. Analytical and numerical methods are used to quantify the impact of this coupling on the vertical circulation, spindown of geostrophic flows, and the formation of a shelfbreak jet.

Over a stratified slope, linear spindown of a geostrophic along-isobath flow induces cross-isobath Ekman flows. Ekman advection of buoyancy weakens the vertical circulation and slows spindown. Upslope (downslope) Ekman flows tend to inject (remove) potential vorticity into (from) the ocean. Momentum advection and nonlinear buoyancy advection are examined in setting asymmetries in the vertical circulation and the vertical relative vorticity field. During nonlinear homogeneous spindown over a flat bottom, momentum advection weakens Ekman pumping and strengthens Ekman suction, while cyclonic vorticity decays faster than anticyclonic vorticity. During nonlinear stratified spindown over a slope, nonlinear advection of buoyancy enhances the asymmetry in Ekman pumping and suction, whereas anticyclonic vorticity can decay faster than cyclonic vorticity outside of the boundary layers.

During the adjustment of a spatially uniform geostrophic current over a shelfbreak, coupling between the Ekman flow and the buoyancy field generates Ekman pumping near the shelfbreak, which leads to the formation of a jet. Scalings are presented for the upwelling strength, the length scale over which it occurs, and the timescale for jet formation. The results are applied to the Middle Atlantic Bight shelfbreak.

Thesis Supervisor: Steven J. Lentz
Title: Senior Scientist

Thesis Supervisor: Leif N. Thomas
Title: Assistant Professor

Acknowledgments

I thank my advisors, Leif Thomas and Steve Lentz, for their scientific guidance and support. I greatly appreciate the respect that they have shown me throughout the past several years. They have allowed me the freedom to explore new ideas and have helped focus and shape these ideas into feasible projects. With patience, open doors, and constructive criticism, they have set true examples of how to do science as well as how to be a scientist.

I thank Raffaele Ferrari who always encouraged me to think about the big picture. I thank Glen Gawarkiewicz for giving me the opportunity to participate in a cruise to the Middle Atlantic Bight shelfbreak front and the opportunity to learn about autonomous underwater vehicles. Finally, I thank Ken Brink for chairing my defense and helpful discussions ranging from writing to numerical modelling.

Thanks to the students who have helped me along this journey. To my officemates at MIT and WHOI: Shin Kida, Max Nikurashin, Claude Abiven, Christie Wood, Kjetil Våge, and Rebecca Dell. To my PO classmates for their support: Beatriz Peña-Molino and Katie Silverthorne as well as Stephanie Waterman, Hristina Hristova, and Rachel Horwitz. Finally, thanks to Melanie Fewings, Greg Gerbi, and Carlos Moffatt for being good mentors who I can always count on for advice.

I thank my parents, Jim and Mei, and my sister, Jackie, for being supportive of all my endeavors. I also thank my undergraduate advisor, Bill Criminale, for introducing me to fluid dynamics and boundary layer theory.

Funding for my research and education was provided by MIT EAPS, the WHOI Academic Programs Office and the MIT Presidential Fellowship. Financial assistance from the Houghton Fund is also acknowledged.

Contents

Chapter 1

Introduction

Ocean bottom boundary layers are regions adjacent to topography where turbulence mixes heat, momentum and biogeochemical tracers. These regions serve as a dynamical control on the circulation by dissipating energy and shape the local characteristics of the marine environment by redistributing tracers. Tracers, such as sediment and nutrients, are transported by the lateral circulation near the bottom as well as the vertical circulation into and out of these layers. In order to quantify these momentum and tracer fluxes, an understanding of the strength and structure of this circulation is needed.

Friction plays an important role in driving this lateral and vertical circulation. The boundary exerts a frictional stress on the flow that reduces the near bottom velocity within a frictional boundary layer, the Ekman layer. This frictional force induces an ageostrophic Ekman flow down the pressure gradient through a subinertial balance between the frictional force, the Coriolis acceleration, and the horizontal pressure gradient. The vertically-integrated Ekman flow, the Ekman transport, is directed to the right (left) of the frictional force in the Northern (Southern) Hemisphere. Convergences and divergences in the Ekman transport eject fluid out of, Ekman pumping, or inject fluid into, Ekman suction, the boundary layer. This process drives an ageostrophic secondary circulation that can accelerate or decelerate the geostrophic flow in the interior.

Observational and theoretical studies have examined the role of cross-isobath Ekman advection of buoyancy in setting the structure of the ocean bottom boundary layer as well as the frictionally driven circulation. Over an insulated stratified sloping boundary, downslope (upslope) Ekman advection of buoyancy induces a positive (negative) buoyancy anomaly and tilts the isopycnals near the bottom. This isopycnal tilting leads to vertical shear in the geostrophic flow, reducing the bottom stress and hence weakening the Ekman transport (MacCready and Rhines 1991, Trowbridge and Lentz 1991). An arrested Ekman layer occurs when this buoyancy anomaly is sufficiently large to reduce the bottom stress to zero. This process, known as *buoyancy shutdown* of the Ekman transport, has important consequences for the interior flow field (MacCready and Rhines 1991). By weakening the Ekman transport, buoyancy shutdown also weakens Ekman pumping and suction. When the Ekman flow is arrested, the interior geostrophic flow can evolve unimpeded by frictional forces.

The purpose of this thesis is to examine how coupling between the frictionally driven flow and the buoyancy field over sloping topography modifies the vertical circulation and the interior geostrophic flow through feedback by secondary circulations. Analytical and numerical techniques are used to address how this coupling impacts the temporal evolution and spatial characteristics of the flow. The results of this analysis are applied to observations to determine the extent that cross-isobath Ekman advection of buoyancy can explain the structure of flows over stratified sloping topography.

In the following sections, an overview of previous research is presented regarding the significance of cross-isobath Ekman advection of buoyancy on the structure and dynamics of flows along stratified boundaries. This overview addresses notable studies, with a primary focus on observations, that have shaped our current understanding of frictionally driven flows over stratified sloping topography. Then, the goals of this dissertation are presented, with relation to open questions unanswered by previous research, followed by an outline of the thesis chapters.

1.1 Background and Motivation

Previous research has identified cross-isobath Ekman advection of buoyancy as a potentially important mechanism influencing currents over stratified shelves and slopes. Observational and theoretical studies have ranged from examining the one-dimensional bottom boundary layer dynamics to accounting for lateral variations in its structure. These studies have considered different aspects of this mechanism, which can be categorized into the following four questions.

How does cross-isobath Ekman advection of buoyancy:

- influence the height of the bottom boundary layer?
- impact mixing processes by shear or convective instability?
- couple with the lateral Ekman flow and on what timescales?
- modify the vertical circulation and feedback into the geostrophic flow by secondary circulations?

These questions have been examined in different flow regimes along stratified sloping topography. These regimes include coastal currents along continental shelves and the upper continental slopes off of the west and east coast of the United States as well as the more weakly stratified deep western boundary currents along the lower continental slope in the North and South Atlantic ocean. A particular region of interest is the frontal system along the Middle Atlantic Bight shelfbreak, where the gradually sloping continental shelf intersects the steeply sloping continental slope off of the east coast of the United States. Studies of these regions reveal where cross-isobath Ekman advection of buoyany may or may not be important to the subinertial dynamics over sloping topography.

The overview of past research is presented in three parts. The impact of cross-isobath Ekman advection of buoyancy on the structure of bottom boundary layers over the continental shelves and slopes is presented in section 1.1.1. In section 1.1.2, observations of flows near the Middle Atlantic Bight shelfbreak are presented as motivation for studying how these stratified bottom boundary layer processes over slopes

feedback into the coastal currents. Finally, observations supporting or refuting the importance of cross-isobath Ekman advection of buoyancy on bottom boundary layers in deep western boundary currents is presented in section 1.1.3.

1.1.1 Bottom boundary layers over continental shelves and upper continental slopes

Over continental shelves and upper continental slopes, characteristics in the near bottom flow and tracer fields distinguish bottom boundary layers from the overlying flow. First, currents tend to veer counterclockwise downward, which is consistent with the direction of Ekman veering predicted by a balance between frictional forces and the Coriolis acceleration (e.g. Weatherly 1972, Wimbush and Munk 1970, Kundu 1976, Mercado and Van Leer 1976). Second, small scale measurements of temperature as well as velocity gradients can be used to distinguish the bottom boundary layer as a region with high levels of turbulent kinetic energy dissipation (e.g. Perlin et al. 2005, Moum et al. 2004). Third, temperature, salinity, and density tend to appear vertically well-mixed within a bottom mixed layer (e.g. Weatherly and Niiler 1974, Weatherly and Van Leer 1977, Pak and Zaneveld 1977). Observations indicate that the Ekman layer thickness, determined from Ekman veering, may (e.g. Mercado and Van Leer 1976) or may not (e.g. Perlin et al. 2005) equal the bottom mixed layer thickness.

Observational and numerical studies have shown that coupling between frictionally driven flows and the density field can impact the thickness of the frictional bottom boundary layer and the bottom mixed layer. Over a flat bottom, Weatherly and Martin (1978) argued on dimensional grounds that stratification reduces the bottom boundary layer height from the unstratified case. By including stratification in the scaling for the frictional boundary layer height, they showed that the revised stratified scale height was qualitatively consistent with previous estimates of bottom boundary layer thickness over the West Florida continental shelf (Weatherly and Van Leer

1977). From examination of near bottom temperature profiles in the Florida current, Weatherly and Niiler (1974) suggested that horizontal advection of buoyancy over sloping topography was key in explaining the formation of bottom mixed layers. Weatherly and Van Leer (1977) also suggested that patterns of warming (cooling) within the bottom boundary layer may be explained by frictionally driven downslope (upslope) flows due to downwelling (upwelling) favorable along-shelf flows.

Weatherly and Martin (1978) used a numerical model, with the Mellor-Yamada level 2 turbulence closure scheme, to examine how the frictional bottom boundary layer is modified by upslope or downslope Ekman advection of buoyancy. The thickness of the bottom boundary layer is specified by the height at which the turbulence vanishes away from the bottom. For upslope Ekman flows, they showed that the bottom boundary layer height tended to remain constant and approximately equal to their stratified bottom boundary layer height scale. In contrast, for downslope Ekman flows, their model showed a thickening of the bottom boundary layer beyond this scale estimate. Model results compared with Weatherly and Van Leer's (1977) observations showed qualitative agreement in bottom boundary layer heights.

Over the northern California shelf, estimates of the bottom mixed layer height reveal a dependence on the stratification, the along-shelf current magnitude and the along-shelf current direction (Lentz and Trowbridge 1991). From the Coastal Ocean Dynamics Experiment (CODE) during the summer of 1981 and 1982, Lentz and Trowbridge (1991) showed that thicker bottom mixed layers tended to occur with weaker stratification and stronger along-shelf flow. Furthermore, as shown in figure 1-1, the direction of the along-shelf flow correlates with an asymmetry in the bottom mixed layer heights, with thicker (thinner) heights for poleward, downwelling (equatorward, upwelling) favorable along-shelf flow.

Cross-isobath Ekman advection of buoyancy can explain this asymmetrical bottom mixed layer structure (Lentz and Trowbridge 1991). A downwelling favorable flow drives lighter fluid under denser fluid, reducing the stratification and supporting the growth of the bottom mixed layer, while an upwelling favorable flow drives

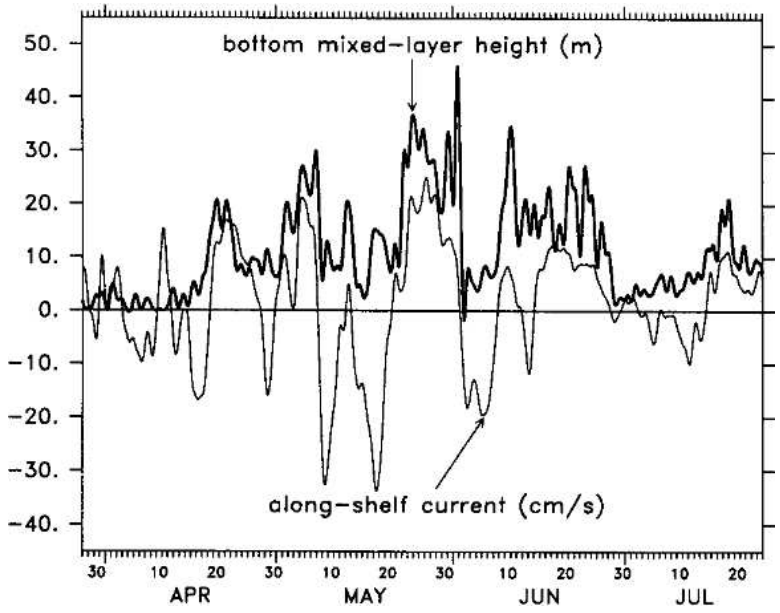

Figure 1-1: During CODE (1982), bottom mixed layer heights correlate with direction of the along-shelf currents. Bottom mixed layer heights are thicker when the along-shelf current is poleward (positive) and downwelling favorable while thinner when the along-shelf current is equatorward (negative) and upwelling favorable (from Lentz and Trowbridge (1991)).

denser fluid upslope, increasing the stratification and inhibiting the growth of the bottom mixed layer (Lentz and Trowbridge 1991). Trowbridge and Lentz (1991) used a one-dimensional mixed layer model, with a bulk Richardson number based mixing criterion, to examine this asymmetric response in the bottom mixed layer to upwelling or downwelling flows. Bottom mixed layer height estimates from the CODE observations showed good agreement with these model results.

Recent observations have also found evidence in support of this correlation between the asymmetrical bottom structure with the direction of the along-shelf current. Analysis of measurements over the Oregon continental shelf in the spring of 2001 showed that the greatest bottom mixed layer heights occured upon relaxation of upwelling favorable winds (Perlin et al. 2005). Furthermore, the highest measured turbulence within the bottom boundary layer occurred during this period (Perlin et al. 2005). From these measurements, as shown in figure 1-2, Moum et al. (2004) determined that these two features are due to convective mixing driven by an offshore

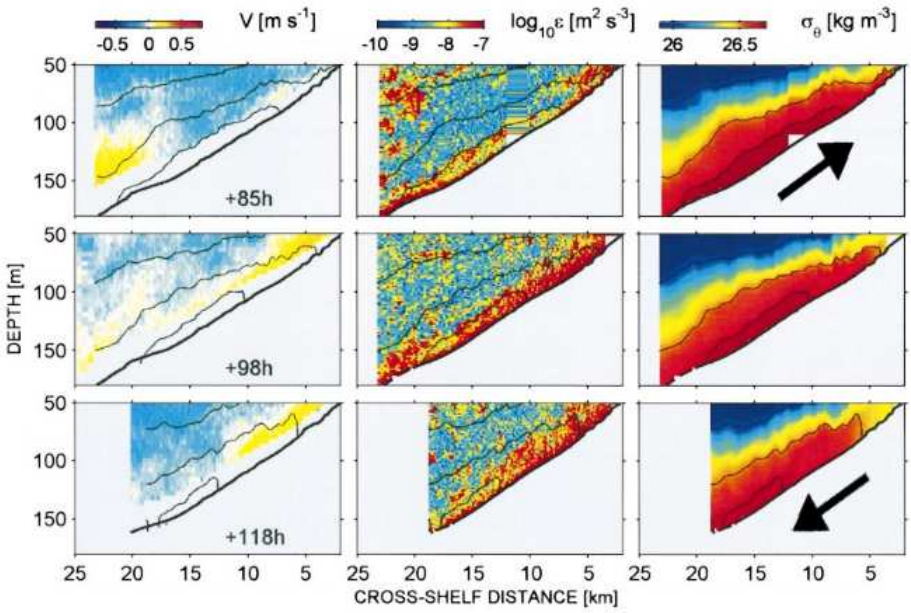

Figure 1-2: The cross-shelf sections for along-shelf flow (positive poleward), V, turbulent kinetic energy dissipation rate, ϵ, and potential density, σ_θ, is shown in time, where time is with respect to May 19, 2001. The arrows are included for clarity to indicate the direction of Ekman transport associated with upwelling favorable winds (+85 hours), weak winds (+98 hours), and downwelling favorable winds (+118 hours) (modified from Moum et al. (2004)). Winds were upwelling favorable for six days prior to the reversal in wind direction. During the relaxation of upwelling winds, the bottom boundary layer thickens and shows high levels of dissipation.

transport of lighter fluid under denser fluid within the bottom boundary layer during the relaxation of upwelling favorable winds.

The preceding studies demonstrate how cross-isobath Ekman advection of buoyancy controls the height of the bottom mixed layer. The following works have explored how these changes to the bottom mixed layer height feed back into the frictionally driven flow within the bottom boundary layer. Trowbridge and Lentz (1991) used a one-dimensional numerical model to show that upslope or downslope Ekman advection of buoyancy produced thermal wind shear within the bottom mixed layer and a reduction in the bottom stress.

This reduction in bottom stress and corresponding weakening of frictionally driven flows was further examined in laboratory experiments (MacCready and Rhines 1991),

one-dimensional models with no-slip boundary conditions and constant mixing coefficients (MacCready and Rhines 1991), no-slip and a gradient Richardson number mixing criterion (MacCready and Rhines 1993), a quadratic bottom drag with a gradient Richardson number mixing criterion (Ramsden 1994), a quadratic bottom drag with the Mellor-Yamada Level 2 turbulence closure scheme (Middleton and Ramsden 1996), and a quadratic bottom drag with a series of turbulent closure schemes (Brink and Lentz 2009). Buoyancy shutdown timescales indicate faster Ekman arrest for increasing slope angle and cross-isobath buoyancy gradients, and these timescales and associated bottom boundary layer heights are found in the above references (see also Garrett et al. 1993 for a comprehensive review).

Despite numerous numerical studies, observational evidence of arrested Ekman flow over shelves and slopes is limited. This lack of observations may be due to instrument limitations since near bottom flows tend to align along-shelf and cross-shelf flows are weak with respect to current meter accuracy (Lentz and Trowbridge 1991). From the Sediment Transport Events on Shelves and Slopes (STRESS) program during the winters of 1988-1989 and 1990-1991, Trowbridge and Lentz (1998) used time series of temperature, salinity, and velocity to test the subinertial Ekman balance over the northern California shelf. They test the hypothesis that the along-isobath bottom stress is proportional to the cross-isobath transport, the cross-isobath transport is modified by a buoyancy force, and temporal variability in the buoyancy field is due to cross-isobath advection of buoyancy. In contrast to previous studies with no along-isobath variations, along-isobath advection of buoyancy gives rise to a significant contribution in the vertically-integrated along-isobath momentum balance and heat balance within the bottom mixed layer (Trowbridge and Lentz 1998). In agreement with these previous studies, cross-isobath advection of buoyancy is a significant term in the vertically-integrated cross-isobath momentum balance and tends to dominate over the bottom stress term during downwelling events when the bottom mixed layer is thick (Trowbridge and Lentz 1998). Further analysis of STRESS observations shows that the poleward along-isobath flow is reduced near the bottom

and its vertical shear is consistent with thermal wind balance on timescales of the order of a week or longer (Lentz and Trowbridge 2001). Thus, the downward tilting isopycnals, consistent with offshore flow, lead to weakening bottom stress, which provides observational support for buoyancy shutdown of the cross-isobath Ekman flow (Lentz and Trowbridge 2001).

This section has addressed previous research on the role of cross-isobath Ekman advection of buoyancy in setting the height of the bottom boundary layer and the strength of the frictionally driven flow through coupling between the cross-isobath Ekman flow and the buoyancy field. In the next section, observations of coastal current systems are presented in which modelling studies have addressed the importance of a cross-isobath Ekman buoyancy flux in setting the current structure.

1.1.2 Bottom boundary layer feedback on coastal currents, with application to the Middle Atlantic Bight

Modelling studies have examined how a cross-isobath Ekman buoyancy flux modifies the bottom boundary layer, which feeds back into the temporal and spatial evolution of the overlying currents (Chapman and Lentz 1997, Chapman 2000a, Chapman 2002a), with application to coastal currents along the eastern North American shelf. A series of studies have examined the frictional offshore spreading of a buoyant current on the shelf (Chapman 1986, Wright 1989, Chapman and Lentz 1994, Yankovsky and Chapman 1997, Chapman 2000b, Chapman 2002b) with interest in the position of the greatest lateral density gradient bounding the buoyant shelf waters from the denser waters offshore. These and other works (e.g. Gawarkiewicz and Chapman 1992) address the possible dynamical significance of the shelfbreak to the existence of the observed shelfbreak front, a density front that is located where the gently sloping continental shelf intersects the more steeply sloping continental slope (Fratantoni and Pickart 2007).

Results of these modelling studies suggest that an offshore Ekman buoyancy flux

can potentially play an important role in both the structure of the bottom boundary layer and the overlying flow in coastal currents. In this section, a general description of the coastal circulation in the western North Atlantic Ocean is given, with particular attention given to flows near the Middle Atlantic Bight shelfbreak. This description includes open questions that will be explored in this thesis.

In the western North Atlantic Ocean, the coastal circulation is dominated by an equatorward flow over a shelf width of approximately 100-200 km over a depth 100-200 m (see the comprehensive review by Loder et al. 1998). Freshwater sources to the continental shelf include the transport of fresh subpolar water onto the Labrador shelf, continental runoff, and sea ice melting (Loder et al. 1998). At the shelfbreak, this equatorward flowing cool, fresh water comes into contact with the relatively warm, salty water over the slope (Fratantoni and Pickart 2007). These two water masses form a thermohaline front that is partially density compensating and supports a surface-intensified jet (shown in figure 1-3 and figure 1-4).

Observations of this shelfbreak current system are focused on the Middle Atlantic Bight, which extends from Georges Bank to Cape Hatteras. From oxygen isotope measurements, Chapman and Beardsley (1989) suggested that the equatorward flow along the Middle Atlantic Bight was part of a buoyancy-driven coastal current originating south of Greenland. Since the mean flow opposes the direction of the mean eastward along-shelf wind stress, previous studies (e.g. Stommel and Leetmaa 1972, Csanady 1976) have suggested that this flow is associated with an along-shelf pressure gradient. This along-shelf pressure gradient may arise from an along-shelf forcing mechanism (Chapman et al. 1986) or from the large-scale circulation in the western North Atlantic (see the review by Beardsley and Boicourt 1981).

In a recent study, Lentz (2008) analyzed current meter records longer than 200 days to quantify the mean circulation. With observations and a model for the mean circulation, Lentz (2008) determined that the mean near-bottom flow was directed offshore seaward of the 55 m isobath. This offshore near-bottom flow tends to reduce the bottom stress by buoyancy shutdown. However, the model shows that the

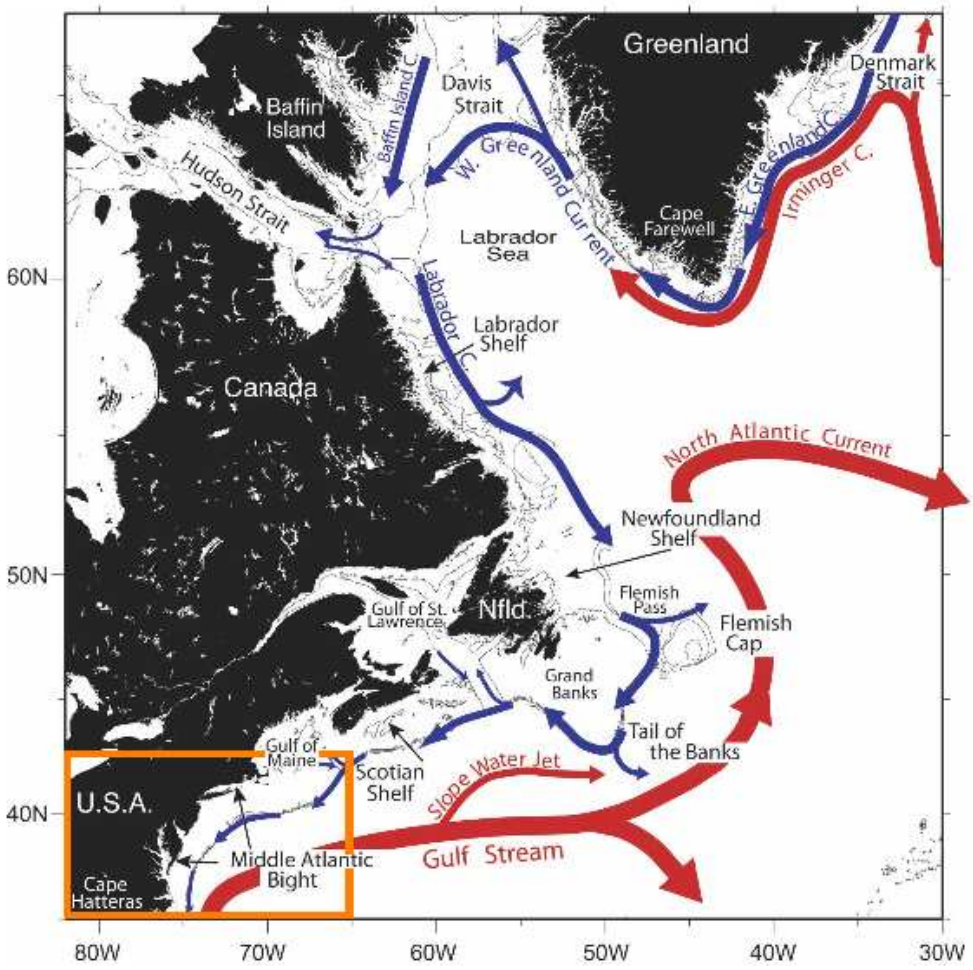

Figure 1-3: This schematic illustrates the surface circulation of the western North Atlantic Ocean, where the warm currents of Gulf Stream origin (red arrows) flow adjacent to the shelfbreak jet (blue arrows) along the shelfbreak. The Middle Atlantic Bight is indicated within the orange box (modified from Fratantoni and Pickart (2007)).

contribution of buoyancy shutdown to the mean depth-averaged along-shelf flow is subdominant with respect to (in order of largest to smallest contributions) an along-shelf pressure gradient, wind stress, and interior buoyancy gradients, owing to a weak slope angle of approximately 6×10^{-4} along the mid and outer shelf (Lentz 2008).

Although this result suggests that other mechanisms may play a more important role in the dynamics of the mean along-shelf flow over the Middle Atlantic Bight shelf, the question remains how this flow regime transitions offshore of the shelfbreak onto the more steeply sloping upper continental slope. Near the shelfbreak, observations suggest that the mechanisms controlling the bottom boundary layer are important for understanding the overlying flow dynamics and tracer fields.

Observations near the Middle Atlantic Bight shelfbreak

Observations near the Middle Atlantic Bight shelfbreak have focused on describing the properties of the thermohaline front, jet, the structure of the bottom boundary layer, and upwelling near the shelfbreak. These features are important for understanding the transport of tracers along-shelf (in which the jet can act as a downstream conduit), cross-shelfbreak exchange (between the shelf and the deep ocean), as well as vertical exchange (e.g. upwelling of nutrients from depth). Linder and Gawarkiewicz (1998) used hydrographic data ranging from the early 1900s to April 1990 to quantify climatological mean cross-shelf sections for temperature, salinity, density, and along-shelf geostrophic flow fields over the shelfbreak (see figure 1-4). On Nantucket Shoals (39° - 41°N, 69°- 72°W), the temperature field is strongly modified by seasonal variability, with the formation of a thermocline in the summer and its subsequent destruction by vertical mixing from storms in the fall and winter (Linder and Gawarkiewicz 1998). In contrast, the salinity fields remain approximately constant throughout the seasons, so that temperature variability controls the density variability (see Linder and Gawarkiewicz 1998 for further discussion on seasonal variability in the water properties). The frontal boundary has been historically characterized as the 10°C isotherm (Wright 1976), the 34.5 isohaline (Beardsley and Flagg 1976), and the 26.5 kg m^{-3}

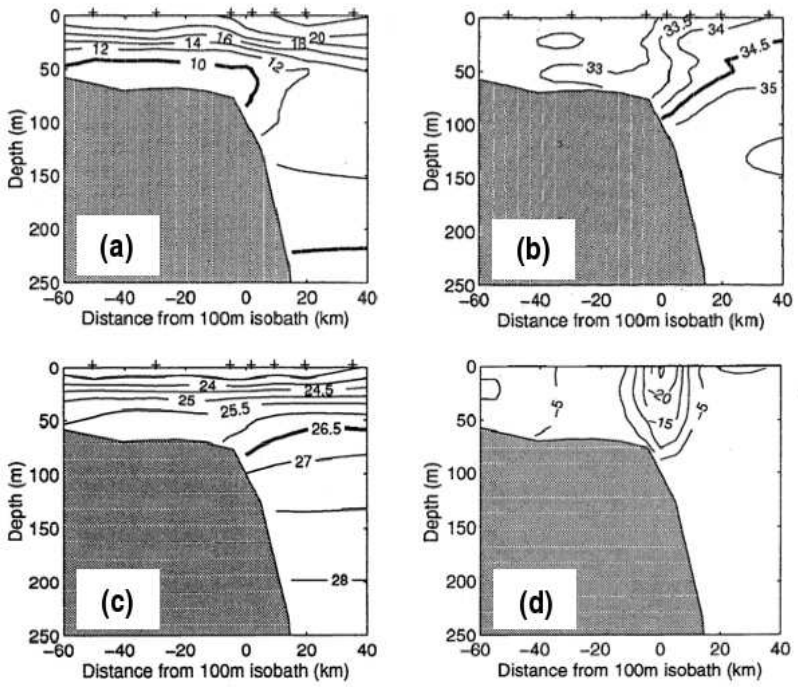

Figure 1-4: From the Nantucket Shoals region, August and September averaged sections are shown for (a) temperature (°C), (b) salinity, (c) density (kg m^{-3}), and (d) the geostrophic flow (cm s^{-1}) with bottom reference flow speeds from the Nantucket Shoals Flux Experiment. The contour intervals are (a) 2°C, (b) 0.5, (c) 0.5 kg m^{-3}, and (d) 5 cm s^{-1} (from Linder and Gawarkiewicz (1998)).

isopycnal. From computations of bimonthly fields, Linder and Gawarkiewicz (1998) determine that the temperature difference across the front ranges from 2-6°C, while the salinity difference is 1.5-2 psu. With a climatology of synoptic sections along the Middle Atlantic Bight, Fratantoni and Pickart (2007) estimate that the salinity difference across the front is 1.3 psu over 30 km. Across the foot of the front, the absolute cross-shelf buoyancy gradient, estimated as 1.9×10^{-7} s^{-2} from a 0.2 kg m^{-3} density difference over 10 km, is strong relative to the buoyancy gradient at the surface and remains relatively constant despite seasonal shifts in the foot of the front (Linder and Gawarkiewicz 1998).

Observations of the thermohaline and density front also reveal a baroclinic jet at the shelfbreak, and effort has been made to quantify its flow speed, width, and lateral shear. From the Linder and Gawarkiewicz (1998) climatology along the Nan-

tucket Shoals, the mean geostrophic speeds of the shelfbreak jet range from 0.2-0.3 m s^{-1} and estimates of transport range from 0.2-0.3 Sv (1 Sv $\equiv 10^{-6}$ m^2 s^{-1}). The width of the jet is determined from the contour representing half of the maximum surface velocity, given the sum of the geostrophically balanced along-shelf flow with an estimate of near bottom speeds. From this definition, the width of the jet is 15-20 km, except for December and January when the jet is 40 km wide. The cross-shelf position of the jet core tends to vary seasonally with a 15 km seasonal drift, with onshore movement in spring and summer and offshore movement in the late fall and winter, although its mean annual position is 5 km seaward of the 100 m isobath. From the laterally sheared jet structure, the Rossby number, defined as the ratio of the vertical relative vorticity to the local Coriolis parameter, is a maximum of 0.4 on the offshore (cyclonic) side of the jet and ranges from -0.1 to -0.2 on the onshore (anticyclonic) side of the jet.

In more recent observations, Fratantoni et al. (2001) presented a high resolution mean description of the Middle Atlantic Bight shelfbreak jet from synoptic sections near 70°W during fall and winter 1995-1997. They analyzed shipboard ADCP (Acoustic Doppler Current Profiler) velocity measurements to determine the geostrophic and ageostrophic secondary circulation along a cross-section over the shelfbreak. Their analysis revealed that the jet core was located between the 100 m isobath and the shelfbreak at the 180 m isobath. The jet was geostrophic at leading order and surface intensified with alongstream speeds exceeding 0.1 m s^{-1}. They estimated that the mean jet width was 25 km using the Linder and Gawarkiewicz (1998) definition of the jet width. Lateral shears in the shelfbreak jet correspond to Rossby numbers of approximately $\pm$ 0.2. In the streamwise coordinate system, the cross-stream flow shows an enhanced convergence at the surface and bottom, which they attribute to local convergences in the along-shelf bathymetry feeding the downstream acceleration of the mean jet.

Downstream of this location at approximately 74°W, Rasmussen et al. (2005) used shipboard ADCP measurements to examine the shelfbreak front structure from

four cross-shelf sections taken during November 2000. From two of the sections, they showed that the foot of the front intersected the bottom at the 120 m and 140 m isobath, which are significantly deeper than the 75 m isobath presented in the Linder and Gawarkiewicz (1998) climatology. Furthermore, the predominantly along-isobath jet had strong speeds of 0.6 m s^{-1}, three times the climatological value, with a cross-shelf width of 20-30 km, leading to maximum Rossby numbers of about $\pm$ 0.6. The largest cross-shelf buoyancy gradients were located at the foot of the front and the overlying buoyancy gradients were in geostrophic balance with the jet core. They conclude that discrepencies between these synoptic sections and the climatology may arise from smoothing of data in the climatology.

In order to examine the structure of the bottom boundary layer near the Middle Atlantic Bight shelfbreak, two approaches have been used. First, Houghton (1995) examined data from the Shelf Edge Exchange Processes (SEEP-II) experiment to calculate bottom mixed layer heights near the front. Then, these heights were compared to both Weatherly and Martin's (1978) scaling for the height of the bottom boundary layer from a one-dimensional model of flow over a stratified flat bottom and Trowbridge and Lentz's (1991) scaling for the height of the bottom mixed layer subject to a downslope Ekman buoyancy flux. From ADCP velocity data onshore of the shelfbreak, calculations of veering angles above the bottom are predominantly positive, consistent with an Ekman flow. By using the veering angle, the bottom boundary layer thickness ranges from 10 - 40 m. From CTD (conductivity-temperature-depth) data, Houghton (1995) determined the bottom mixed layer thickness from the height at which there was a vertical change in temperature of 0.02°C with respect to the temperature at 1 m above the bottom. With this definition, a cross-shelf spatial pattern emerged with bottom mixed layer heights ranging from 4-18 m on the shelf, a minimum at the foot of the front, and increasing to 40 m on the upper slope. Houghton (1995) found reasonable comparison between bottom mixed layer estimates with Weatherly and Martin's (1978) scaling. However, he found smaller bottom mixed layer heights than predicted from Trowbridge and Lentz's (1991) scaling. Houghton

(1995) concluded that temporal variability at the shelfbreak might preclude the bottom mixed layer growth to a height predicted for an arrested, initially downwelling Ekman flow, and the existence of the density front (a two-dimensional structure with curvature in the cross-shelf buoyancy field) at the shelfbreak might also limit the bottom boundary layer growth.

The second approach used to examine the structure of the bottom boundary layer near the shelfbreak has been to focus on the layer's detachment, in which fluid is predicted to upwell from the bottom boundary layer along the shelfbreak front. From the Shelfbreak PRIMER experiment at approximately 70°W during 1995-1997, Pickart (2000) used temperature measurements from CTDs to determine the thickness of the bottom boundary layer, defined as a weakly stratified layer above the bottom. Pickart (2000) found that the bottom boundary layer was thick (15-20 m) shoreward of the shelfbreak front, thin (5-7 m) near the shelfbreak front, and then thicker seaward of the front. This spatial pattern agrees with Houghton's (1995) measurements. Since along-isopycnal upwelling is assumed to reduce the lateral tracer gradients along that layer, the detachment of the bottom boundary layer is quantified by calculating the accumulated temperature change, in which the along-isopycnal temperature gradient is integrated along an isopycnal (Pickart 2000). Pickart (2000) used this method to show that along-isopycnal upwelling occurred on the onshore side of the front. This upwelling appeared to coincide with a convergence in the cross-shelf flow in the bottom boundary layer as well as in the interior from flow sections constructed from ADCP measurements. Pickart (2000) estimated an along-isopycnal upwelling speed of 3.7 cm s^{-1} (equal to a vertical upwelling rate of 8 m day^{-1} for an isopycnal slope of 0.0025) by using the along-isopycnal distribution of the accumulated temperature change in an advective-diffusive model. Pickart (2000) also estimated a vertical upwelling of 23 m day^{-1} from ADCP measurements. In a seasonal depiction of the detached bottom boundary layer during the Shelfbreak PRIMER experiment, detachment occured along the 26.0 kg m^{-3} isopycnal throughout the year (Linder et al. 2004). Following Pickart (2000), the detached bottom boundary layer was estimated

to reach 80 m above the bottom in the winter, whereas it was only able to reach 25 m above the bottom in the summer owing to strong stratification near the surface.

Other studies near the shelfbreak front have examined the secondary circulation structure as well as the vertical or along-isopycnal upwelling along the front. In a series of tracer experiments, Houghton (1997), Houghton and Visbeck (1998), Houghton et al. (2006) released dye in order to examine the secondary circulation near the shelfbreak front. In May 1996 along one of the Shelfbreak PRIMER transects, Houghton (1997) revealed a convergent flow near the shelfbreak front, where the injected dye remained in the bottom mixed layer of depth 3-6 m. The dye flowed upslope rather than upwell into the interior because the dye was released offshore of the shelfbreak front. In a subsequent study in May 1997, the dye was released into a bottom mixed layer of depth 10-20 m and upwelled along the front at a rate of 4-7 m day^{-1} (Houghton and Visbeck 1998). During the New England Shelfbreak Productivity Experiment (NESPEX) in August 2002, dye was released in the bottom boundary layer inshore and offshore of the frontal boundary, identified as the 34.5 isohaline or the 26.1 kg m^{-3} isopycnal, as well as in the interior along the frontal boundary (Houghton et al. 2006). They estimated upwelling rates of 6-10 m day^{-1} (Houghton et al. 2006).

From measurements of phytoplankton and suspended sediment levels, Barth et al. (1998) inferred the secondary circulation about the shelfbreak front. They showed that a band of suspended particulate matter extended upwards from the foot of the front and inshore of the frontal boundary at the 25.8 kg m^{-3} isopycnal. By using ADCP velocity measurements, Barth et al. (1998) assumed a balance between the convergence in the cross-shelf flow and upwelling to estimate an upwelling rate of 9 $\pm$ 2 m day^{-1} on the inshore side of the front. From June to July 1999 at approximately 67° W, Barth et al. (2004) used a subsurface isopycnal float to measure a mean along-isopycnal vertical velocity of 17.5 m day^{-1} at the shelfbreak front, which translated to a 5 day transit time from the bottom boundary to the surface.

The observed along-isopycnal upwelling at the shelfbreak can impact the local marine ecosystem by transporting nutrient-rich water from depth to the surface.

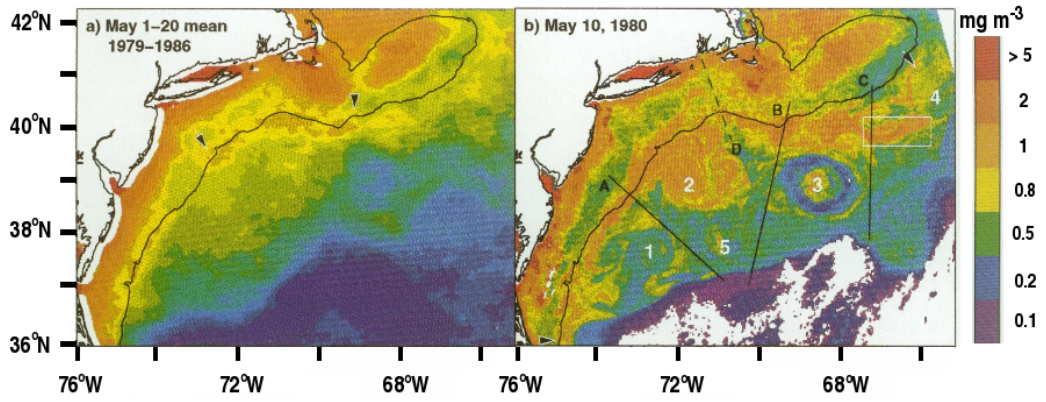

Figure 1-5: The Coastal Zone Color Scanner-derived pigment concentration is shown for (a) a mean from May 1-20 from the years 1979-1986 and (b) a synoptic section on May 10, 1980. The 100 m isobath is shown in black and the arrows indicate the along-shelf endpoints of the shelfbreak chlorophyll enhancement. This region corresponds to a portion of the orange boxed region for the Middle Atlantic Bight shown in the previous figure (modified from Ryan et al. (1999)).

Linder et al. (2004) note that the vertical extent of along-isopycnal upwelling is important for sustaining enhanced levels of phytoplankton at the shelfbreak (Malone et al. 1983, Marra et al. 1990). During the summer, the development of the thermocline tends to suppress the vertical extent of the upwelling and the supply of nutrients to the euphotic zone (Linder et al. 2004). For the spring transition from well-mixed to stratified conditions (mid-April to June), Ryan et al. (1999) used the pigment concentrations from the Coastal Zone Color Scanner to show that a band of enhanced levels of chlorophyll occurred along the Middle Atlantic Bight shelfbreak, which could be explained by upwelling of nutrients. Ryan et al. (1999) suggested that the along-shelf advection of chlorophyll and nutrients along the shelfbreak front could also contribute to the along-shelf band of enhanced chlorophyll levels. Thus, an understanding of the processes that control the structure of the shelfbreak front, the corresponding jet, and the strength of the upwelling along the front has important consequences for explaining the temporal and spatial patterns of biological productivity in this region.

These compelling observations motivate further theoretical investigation to de-

termine the underlying mechanisms that control the circulation near the shelfbreak. A key question arises as to the dynamical significance of the shelfbreak given the persistence of the shelfbreak front, jet, and upwelling near the shelfbreak in the observations. Since the shelfbreak represents a location of transition from weak to strong slope angles, to what extent can these features be explained by differential cross-isobath Ekman advection of buoyancy leading to spatial variations in bottom mixed layer heights and buoyancy shutdown timescales? These questions will be addressed in Chapter 4.

1.1.3 Bottom boundary layers in deep currents along continental slopes

The impact of a cross-isobath Ekman buoyancy flux on the structure of bottom boundary layers in the deep ocean is important for our understanding of what processes set the abyssal structure of the stratification or potential vorticity. Climatological distributions of potential vorticity within the deep ocean show different regimes with potential vorticity contours following or deviating from latitudinal circles or closing to form uniform regions (O'Dwyer and Williams 1997). The outcropping of isopycnal layers along boundaries can provide pathways for feeding boundary modified fluid into the interior. Armi (1978) suggested that topography serves as locations where tracers are modified by vertical mixing in bottom mixed layers of 50 m to 150 m thickness, which then detach and are advected into the interior. The question remains as to what processes drive this boundary mixing and redistribution of tracers.

Several mechanisms, including internal wave reflection and breaking, can serve as the source of this boundary enhanced vertical mixing (see references within Garrett et al. 1993, McPhee-Shaw and Kunze 2002). Cross-isobath Ekman advection of buoyancy can also impact the characteristics of mixing and the height of these bottom mixed layers. Although evidence presented in the previous sections suggests that buoyancy shutdown of the Ekman transport can occur in coastal flows, buoy-

ancy shutdown processes in the deep ocean remain inconclusive. Time scale estimates of buoyancy shutdown range from days to weeks on continental slopes to years on abyssal plains (MacCready and Rhines 1991, MacCready and Rhines 1993). In this section, observational and theoretical studies are presented which either suggest the importance or unimportance of buoyancy shutdown on the dynamics of deep western boundary currents.

If buoyancy shutdown were to impact the dynamics of the deep western boundary currents, these currents could presumably flow frictionlessly along the continental slope (MacCready and Rhines 1993). Analysis of observations along the western continental slope of the Brazil Basin consider the importance of cross-isobath Ekman advection of buoyancy on the dynamics of deep western boundary currents. The North Atlantic Deep Water Deep Western Boundary Current (NADW DWBC) flows poleward over a slope inclined at an angle of approximately 0.01 from the horizontal, and the Antarctic Bottom Water Deep Western Boundary Current (AABW DWBC) flows equatorward over a slope inclined at an angle of approximately 0.002 from the horizontal (Durrieu De Madron and Weatherly 1994). In the Southern Hemisphere, the frictionally driven flow associated with the NADW DWBC is oriented upslope, leading to a thinning bottom mixed layer, and the frictionally driven flow associated with the AABW DWBC is oriented downslope, with a thickening bottom mixed layer. Durrieu De Madron and Weatherly (1994) used hydrographic data to determine that the bottom mixed layer thickness was consistent with the expected orientation of the Ekman buoyancy flux for both currents. From estimates of the buoyancy shutdown timescale and the bottom mixed layer thickness, they concluded that the cross-isobath Ekman buoyancy flux was sufficient to set-up a frictionless bottom boundary layer for the NADW DWBC but was insufficient to set-up a frictionless bottom boundary layer for the AABW DWBC.

In contrast to the conclusion that cross-isobath Ekman advection of buoyancy leads to a frictionless bottom boundary layer in the NADW DWBC flow (Durrieu De Madron and Weatherly 1994), observational studies of the NADW DWBC in the

Northern Hemisphere support other mechansims responsible for the structure of the bottom mixed layer. During the summer of 1992, Stahr and Sanford (1999) used absolute velocity profilers to make high resolution measurements of flows near the bottom along the Blake Outer Ridge. The Blake Outer Ridge extends out of the continental shelf south of Cape Hatteras. Past observations at this site revealed thick bottom mixed layers, on the order of 100 m, in both concentration of suspended particulates and in temperature (Amos et al. 1971, Eittreim et al. 1975). Eittreim et al. (1975) noted that the DWBC was oriented in the downwelling favorable direction, thus leading to a downslope Ekman buoyancy flux and convective mixing, which they termed the Ekman thermal pump. However, Amos et al. (1971) suggested that these well-mixed layers could arise by turbulent mixing dependent on the roughness of the bottom topography and the magnitude of the current. These two possible explanations motivated Stahr and Sanford's measurements (1999) to determine which mechanism was responsible for these well-mixed layers in the DWBC at the Blake Outer Ridge.

From the density and current profiles as well as measurements of turbulent kinetic energy dissipation rate, Stahr and Sanford (1999) identified a frictional bottom boundary layer (BBL), where currents veered in the Ekman sense over 20-50 m above the bottom, embedded within a thicker bottom mixed layer (BML), where density was vertically well-mixed on the order of 200-300 m above the bottom. In contrast to previous one-dimensional models for buoyancy shutdown, the measurements taken along a cross-isobath section revealed a laterally varying structure in the bottom boundary layers, as shown in figure 1-6. In contrast to the hypothesis that the well-mixed layer arose by a downslope Ekman buoyancy flux (Eittreim et al. 1975), the density measurements revealed weak cross-isobath buoyancy gradients, in which isopycnals in the center of the current tended to align parallel to the sloping topography (Stahr and Sanford 1999). Furthermore, the along-slope flow had most of its vertical shear within the frictional bottom boundary layer and had little vertical shear within the bottom mixed layer (Stahr and Sanford 1999). Thus, these observations serve as

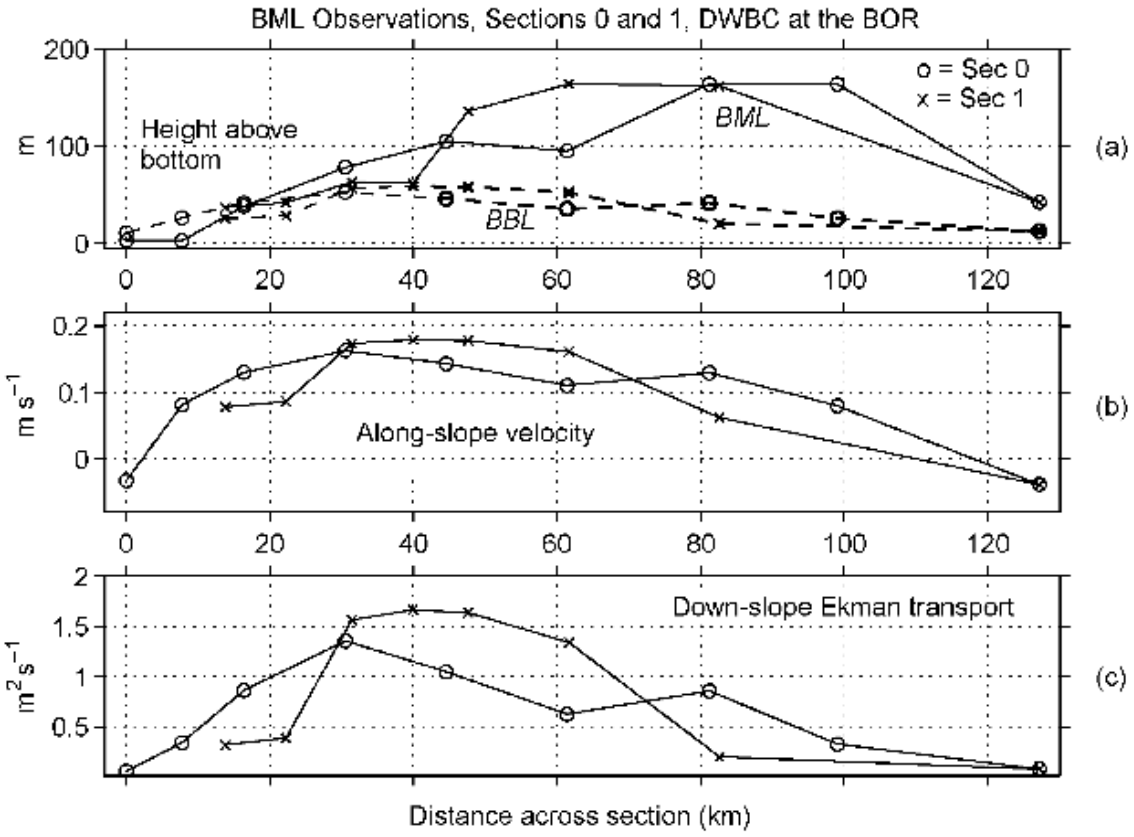

Figure 1-6: Observations from two cross-sections of the DWBC at the Blake Outer Ridge (BOR) are shown where increasing distance across each section is downslope and the slope angle is approximately 0.02. (a) The bottom mixed layer (BML) height is calculated from the density field, and the frictional bottom boundary layer (BBL) height is calculated from the friction velocity. (b) The mean along-slope speed in the DWBC is shown within the BML but above the BBL. (c) The strength of the downslope Ekman volume transport per unit width in the BBL correlates with the BBL thickness (from Stahr and Sanford 1999).

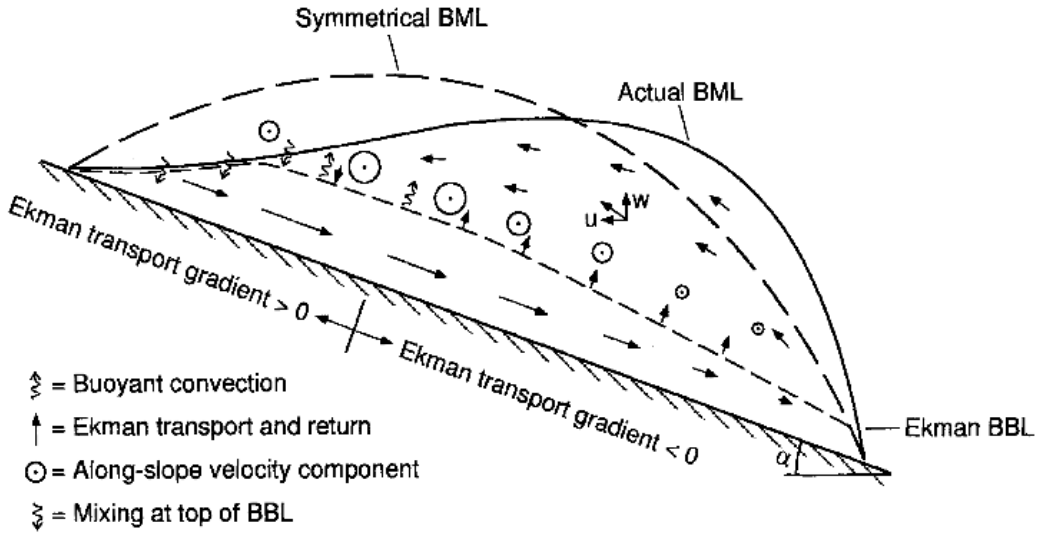

Figure 1-7: A schematic of the asymmetrical bottom mixed layer (BML) height corresponding to observations shown in figure 1-6 is compared with a symmetrical BML structure. The observations indicate a frictional bottom boundary layer (BBL) embedded within the BML. The BML height is due to (i) fluid entrainment on the upslope side of the current where the BBL height coincides with the BML height, (ii) flow into the BBL on the upslope side of the current, (iii) flow out of the BBL on the downslope side of the current, and (iv) weak convection out of the bottom boundary layer at the center of the current (from Stahr and Sanford (1999)).

evidence that buoyancy shutdown is not the leading order process at play in these bottom boundary layers at this location.

The observations, illustrated in figure 1-7, reveal a thicker bottom mixed layer on the downslope side of the current, where there is a region of convergence in the downslope Ekman transport, and a thinner bottom mixed layer on the shallower side of the current, where there is a region of divergence in the downslope Ekman transport (Stahr and Sanford 1999). These observations suggest that laterally varying processes are necessary to explain the structure of the current and the bottom mixed layer.

Although Stahr and Sanford's (1999) observations demonstrate an example in which buoyancy shutdown of the Ekman transport is a subdominant process, one can pose the question of how lateral variations in the cross-isobath Ekman buoyancy flux

modify the lateral structure of the bottom mixed layer, in which vertical shear in the geostrophic flow tends to reduce the bottom stress. Then, how would nonnegligible cross-isobath buoyancy gradients modify the structure of the circulation shown in figure 1-7? What are the relative contributions of vertical advection by Ekman pumping and suction or convective mixing by a downslope Ekman buoyancy flux to the thickness of the bottom mixed layer and what are the consequent effects on the resulting bottom stress? Furthermore, given a laterally sheared along-isobath flow, can one categorize the importance of momentum advection versus buoyancy advection to the bottom boundary layer flow? Chapters 2 and 3 address the modification of the bottom boundary layer structure and frictional flow in laterally sheared along-isobath currents in which buoyancy shutdown plays a leading order role.

1.2 Dissertation goals and methodology

The preceding sections have indicated observational and modelling evidence for the significance of cross-isobath Ekman advection of buoyancy on the dynamics of bottom boundary layers over sloping topography in different flow regimes. A fundamental question unanswered by these studies is how cross-isobath Ekman advection of buoyancy modifies the vertical circulation. This vertical circulation can redistribute tracers and modify the dynamical properties of the flow outside of the bottom boundary layer. The goal of this thesis is *to address the impact of coupling between cross-isobath Ekman flows and the buoyancy field on (i) the distribution of tracers, (ii) the vertical circulation, and (iii) the subsequent feedback of this circulation on the interior geostrophic flow.*

This thesis addresses the temporal and spatial evolution of geostrophic along-isobath flows at midlatitudes with emphasis on laterally sheared coastal flows over constant slopes as well as the formation of a jet and upwelling near a shelfbreak. In order to isolate the effect of cross-isobath Ekman advection of buoyancy on the adjustment of these flows, the spindown of an initially barotropic along-isobath flow over

a stratified sloping bottom is considered. Thus, surface forcings from wind stress or diabatic sources or sinks are not considered. Analytical methods are used to identify the key parameters characterizing the strength of the vertical circulation into or out of the bottom boundary layer, the structure of the interior secondary circulation, and the timescales over which the geostrophic along-isobath flow evolves. Process-oriented numerical modelling is used to test the extent to which these analytical scalings hold and determine where the theory breaks down.

Thesis outline

The adjustment of an initially barotropic along-isobath flow over an insulated, linearly stratified sloping boundary is examined in three parts. The next two chapters examine the adjustment problem in which the boundary is inclined at a constant angle to the horizontal, and the subsequent chapter examines the adjustment problem over a shelfbreak. In Chapter 2, the linear evolution of a laterally sheared along-isobath flow is examined subject to constant mixing coefficients. An analytical framework for viscous, diffusive flows is constructed to show how coupling between the frictionally driven flow and the buoyancy field can both generate and suppress Ekman flows. This framework is used to formulate and solve a coupled set of equations describing the evolution of the frictionally driven dynamics, the buoyancy field, and the geostrophic flow as both spindown and buoyancy shutdown proceed. This framework is also used to quantify the sources or sinks of potential vorticity by diabatic and frictional processes at the stratified sloping boundary.

In Chapter 3, the linear analysis of Chapter 2 is extended into the nonlinear regime. The nonlinear evolution of a laterally sheared flow over a stratified sloping bottom is considered and compared to the nonlinear evolution of a geostrophic flow in a homogeneous fluid over a flat bottom. This problem contrasts the roles of momentum and buoyancy advection in producing an asymmetry in Ekman pumping and Ekman suction as well as in the spindown of cyclonic and anticyclonic vorticity.

In Chapter 4, the adjustment of a laterally uniform along-isobath flow is examined

over a stratified shelfbreak. In this configuration, a flat shelf intersects an idealized continental slope at the shelfbreak, which is modelled with a discontinuity in the slope angle. The implications of lateral variations in the offshore Ekman buoyancy flux on convergences or divergences in the Ekman transport are examined. Analytical and numerical techniques are used to show how buoyancy shutdown over the slope gives rise to Ekman pumping offshore of the shelfbreak and the formation of a shelfbreak jet.

Finally, in Chapter 5, the key results of this thesis are summarized and directions for future research are suggested.

Chapter 2

Linear stratified spindown over a sloping bottom

Abstract

The linear adjustment of a laterally sheared along-isobath flow over an insulated sloping boundary in a stratified, rotating fluid is investigated analytically and numerically for constant viscosity and diffusivity. The time-dependent evolution of the flow and its secondary circulation is examined subject to buoyancy forces that both generate and suppress Ekman flows. First, diffusion of the stratification generates an upslope Ekman transport that is laterally uniform for constant stratification. This upslope Ekman transport arises on a buoyancy generation timescale and asymptotes to a steady-state. Second, stratified spindown is suppressed by coupling between the Ekman flow and the buoyancy field on a buoyancy shutdown timscale. The ratio of the spindown timescale to the buoyancy shutdown timescale measures the extent to which buoyancy shutdown modifies spindown through Ekman pumping. During spindown, the potential vorticity of the fluid is modified by Ekman advection of buoyancy and diffusion of the stratification. Ekman advection of buoyancy tends to increase (decrease) the potential vorticity when the transport is upslope (downslope), while diffusion of the stratification tends to reduce the potential vorticity. The ratio of the initial Ekman transport to the steady-state upslope Ekman transport measures the relative importance of the two processes to the net potential vorticity flux. An increase in the slope angle, stratification, or viscosity for fixed Prandtl number amplifies the net change in potential vorticity during spindown. The results of this study are discussed for flows over the continental shelf and slope.

2.1 Introduction

In a rotating fluid, frictional processes drive Ekman flows that have important consequences for the dynamics of the circulation as well as the modification and redistribution of tracers. Lateral variations in the Ekman transport induce Ekman pumping and suction that drive interior secondary circulations, which can accelerate or decelerate the interior of the fluid. On a flat bottom, classical stratified spindown occurs when the secondary circulation decelerates the flow. For constant stratification, the buoyancy field adjacent to the boundary evolves uniformly by diffusion and remains decoupled from the Ekman dynamics in the small Rossby number regime. On an insulated sloping bottom, buoyancy forces at the boundary become coupled to the Ekman dynamics and not only generate Ekman flows (e.g. Thorpe 1987) but suppress the deceleration of geostrophic flows owing to the buoyancy shutdown of the Ekman transport (e.g. Siegmann 1971, MacCready and Rhines 1991). Buoyancy shutdown is the process by which Ekman advection of buoyancy generates cross-isobath density gradients and vertical shear in the geostrophic flow, thereby reducing the bottom stress and weakening the Ekman flow. The purpose of this work is to examine the linear adjustment of a laterally sheared along-isobath flow over a stratified sloping bottom in a semi-infinite domain when both stratified spindown and buoyancy shutdown take place. This work investigates how buoyancy forces couple with the time-dependent Ekman dynamics to modify the buoyancy field, the vertical circulation and the potential vorticity at the sloping boundary.

Over a flat bottom in a semi-infinite domain, the stratified geostrophic flow adjusts in three stages. First, within an inertial period, $\mathcal{T}_{inertial} = 2\pi f^{-1}$, an Ekman layer forms in a depth $\delta_e = \sqrt{2\nu/f}$, where ν is the viscosity and f is the planetary vorticity. Then, the geostrophic flow decelerates on a spindown timescale, $\mathcal{T}_{spindown} = E^{-1/2} f^{-1}$, by the interior secondary circulation set up by Ekman pumping and suction. The Ekman number, $E = (\delta_e/H_P)^2$, is assumed small and H_P is the depth of the secondary circulation which is assumed less than the height of the domain (Holton 1965). Holton

(1965) demonstrated that spindown results in a geostrophic flow with vertical shear over a height $H_P = fL/N$, where L is the horizontal length scale of the geostrophic flow, N is the buoyancy frequency and the aspect ratio, $\Gamma = H_P/L$, is assumed small and equal to the Prandtl ratio, f/N. Holton (1965) also showed that density variations occur over a diffusive boundary layer of depth $\delta_T = E^{1/4}H_P$, which is thicker than the Ekman layer and decoupled from the Ekman dynamics. Viscous effects arise in the interior flow on a diffusive timescale, $\mathcal{T}_{diffusive} = E^{-1}f^{-1}$, and remove the geostrophic shear left by spindown.

Over a sloping bottom, buoyancy forces become coupled to the Ekman dynamics and can either generate or suppress Ekman flows. In order to satisfy an insulating boundary condition, diffusion of the stratification tilts the isopycnals adjacent to the boundary and induces a cross-isobath pressure gradient that drives a cross-isobath flow. For a nonrotating fluid, Phillips (1970) and Wunsch (1970) examined the steady-state balance in which upslope advection of density by a secondary circulation balanced a vertical diffusive density flux. From Phillips's (1970) nonrotating solution, Thorpe (1987) presented the steady-state solution for the Ekman transport in a rotating fluid with constant stratification over a boundary inclined at an angle θ. In steady-state, the tilted isopycnals geostrophically balance an along-isobath flow and an upslope Ekman transport, $M_{Thorpe} = \kappa \cot\theta$, for constant diffusivity, κ (Thorpe 1987). This steady-state is achieved by a balance between Ekman advection of buoyancy and diffusion of the stratification. The structure of this solution raises the question of the appropriate timescale for the upslope Ekman transport to arise in time-dependent flows, since the solution predicts an infinitely large upslope Ekman transport in the limit of vanishingly small slope angle.

For an along-isobath flow over a sloping bottom, the induced Ekman transport is suppressed by buoyancy forces. MacCready and Rhines (1991) showed that for a uniform flow, cross-isobath Ekman advection of density tilted the isopycnals and, by thermal wind shear, reduced the bottom stress. For long times, the Ekman transport decays as $(t/\mathcal{T}_{shutdown,\ MR})^{-1/2}$ and approaches Thorpe's steady-state solution in a

time $\mathcal{T}_{shutdown,\ MR} = (\sigma^{-1} + S)(\cos\theta S^2(1+S))^{-1} f^{-1}$, where $\sigma = \nu/\kappa$ is the Prandtl number and $S = (N \tan\theta/f)^2$ is the slope Burger number (MacCready and Rhines 1991). When the initial flow has vertical relative vorticity, stratified spindown by Ekman pumping and suction also leads to a decaying Ekman transport in time. Then, both spindown and buoyancy shutdown couple in their influence on the Ekman transport. Chapman (2002a) examined the suppression of stratified spindown by buoyancy shutdown in a finite-width current with horizontal piece-wise structure over a sloping bottom, with a sufficiently small Rossby number, $\epsilon = U/fL$, to neglect advection of momentum. In his model, the dynamics of buoyancy shutdown are specified by a set of equations for the magnitude of the interior flow, which is assumed uniform within the current away from the boundary, and the bottom mixed layer depth, which grows until the vertical shear within the layer is large enough for shutdown of the Ekman transport. Ekman pumping and suction is constrained to the edges of the current over an infinitesimal width and implicitly assumed to decay as the bottom mixed layer thickens. However, the solution for the Ekman transport is crucial for understanding how the vertical circulation and tracers, such as potential vorticity, are modified by buoyancy shutdown.

The potential vorticity (PV) field is modified at boundaries by diabatic and frictional forces (Marshall and Nurser 1992). At the air-sea interface, heating and cooling as well as wind forcing (Thomas 2005) transfer PV into and out of the ocean. At stratified sloping boundaries, Rhines (1998) suggested that the intersection of isopycnal layers at the boundary acts as a source of PV for the ocean interior. Hallberg and Rhines (2000) as well as Williams and Roussenov (2003) numerically examined the transfer of PV from the sloping sidewalls in density layered models. These analyses that use layered models do not address the coupled interactions between diabatic and frictional forcings on the PV dynamics. The bottom enhanced diapycnal mixing that thickens the density layer and lowers the PV also drives a frictionally driven secondary circulation that thins the density layer by upslope Ekman advection of buoyancy. Similarly, upslope or downslope Ekman advection of buoyancy thins or

thickens, respectively, the density layer, which then reduces the frictionally driven circulation by buoyancy shutdown. This work aims to clarify the feedback and relative roles of diabatic and frictional forces in determining the total PV flux into and out of the sloping boundary.

The problem is formulated in section 2.2 for the linear adjustment of a stratified along-isobath flow over a sloping bottom with constant viscosity and diffusivity, and the buoyancy generation and buoyancy shutdown timescales are presented. In section 2.3, the generation of the upslope Ekman transport by the adjustment of the stratification is examined and shown to asymptote to Thorpe's steady-state solution (1987). In section 2.4, the adjustment of a uniform, along-isobath flow is solved for the full-time behavior of the Ekman transport, in contrast with only the long-time behavior presented in MacCready and Rhines (1991) and Duck *et al.* (1997). In section 2.5, the adjustment of an initially barotropic along-isobath flow with a sinusoidal lateral structure is examined subject to spindown and buoyancy shutdown. Solutions are presented for the vertical and lateral structure of the flow, the density field, and the Ekman pumping and suction, which was not determined in Chapman's work (2002a). The analytical solutions are then compared to numerical solutions with parameters that are applicable to flows on continental slopes. In section 2.6, a scaling for the PV flux is determined for the adjustment of the stratification as well as the adjustment of uniform and laterally sheared flows. The analytical model is used to explicitly show that frictional and diabatic forcings couple on the slope in modifying the PV flux, which was not demonstrated in previous numerical studies. Numerical calculations for the net change in the PV field are then interpreted in light of the analytical analysis. Finally, in section 2.7, the role of mixing in the suppression of spindown by buoyancy forces as well as the potential importance of buoyancy shutdown to flows on continental shelves and slopes is discussed.

2.2 Theoretical formulation

The linear adjustment of an along-isobath flow is examined for a hydrostatic, incompressible, Boussinesq fluid in a coordinate system that is rotated at an angle θ with respect to the horizontal, as shown in figures 2-1 and 2-2. The slope angle is assumed sufficiently small such that $\cos\theta \approx 1$ and $\sin\theta \approx \theta$. The density field is assumed only temperature-dependent and is defined in the unrotated coordinate system as $\rho = \rho_o + \hat{\rho}(z) - \frac{\rho_o}{g} b$, where the background stratification is constant and $N^2 = -\frac{g}{\rho_o}\frac{d\hat{\rho}}{dz}$. Buoyancy, b, is defined as the buoyancy anomaly with respect to the background density field, $\rho_o + \hat{\rho}$. The total pressure field is decomposed into a component due to the background stratification and a dynamical component, p. In the rotated coordinate frame, the flow is composed of an along-isobath flow, u, in the x-direction, a cross-isobath flow, v, in the y-direction, and a flow normal to the sloping boundary, w, in the z-direction. The viscosity and the diffusivity are assumed constant. The equations that describe the linear dynamics for a flow with no along-isobath variations are

$$\frac{\partial u}{\partial t} - f(v + \theta w) = \nu\left(\frac{\partial^2 u}{\partial y^2} + \frac{\partial^2 u}{\partial z^2}\right), \tag{2.1}$$

$$\frac{\partial v}{\partial t} + fu = -\frac{1}{\rho_o}\frac{\partial p}{\partial y} - \theta b + \nu\left(\frac{\partial^2 v}{\partial y^2} + \frac{\partial^2 v}{\partial z^2}\right), \tag{2.2}$$

$$0 = -\frac{1}{\rho_o}\frac{\partial p}{\partial z} + b, \tag{2.3}$$

$$\frac{\partial b}{\partial t} - N^2\theta v + w\left(N^2 + \frac{\partial b}{\partial z}\right) = \kappa\left(\frac{\partial^2 b}{\partial y^2} + \frac{\partial^2 b}{\partial z^2}\right), \tag{2.4}$$

$$\frac{\partial v}{\partial y} + \frac{\partial w}{\partial z} = 0. \tag{2.5}$$

The nonlinear advection of buoyancy term is necessary to include in (2.4) because the vertical gradient in the buoyancy anomaly at the boundary is as large as the background stratification from (2.8). This set of equations is solved subject to the

following no-slip, no normal flow, and no normal buoyancy flux boundary condition:

$$u = v = 0 \text{ at } z = 0, \tag{2.6}$$

$$w = 0 \text{ at } z = 0, \tag{2.7}$$

$$\frac{\partial b}{\partial z} + N^2 = 0 \text{ at } z = 0, \tag{2.8}$$

$$u \to u(t = 0, y) \text{ as } z \to \infty, \tag{2.9}$$

$$v, w, b \to 0 \text{ as } z \to \infty. \tag{2.10}$$

Following Thomas and Rhines (2002), the solution to this set of equations is determined by decomposing the flow into interior, Ekman layer and thermal boundary layer components, where the variables u, v, w, p, and b are designated with the corresponding i, e, and T subscripts. In the interior domain, a laterally sheared along-isobath flow evolves geostrophically from vortex stretching and squashing by an ageostrophic secondary circulation over a depth $H_P = fL/N$, where L is the length scale that characterizes the lateral variations of an initially barotropic flow. In the Ekman layer, the momentum balance is between the Coriolis and frictional terms over a height $\delta_e = \sqrt{2\nu/f}$, where the small angle approximation is applied. In the thermal boundary layer, buoyancy variations occur over a height $\delta_T = \sqrt{2\kappa t}$, which grows diffusively in time. The Prandtl number is assumed order one, which means that the thermal boundary layer depth is thicker than the Ekman layer depth for times longer than an inertial period. Furthermore, a scale separation exists between flows in the thermal boundary layer and the interior domain when $t < \sigma E^{-1} f^{-1}$, *i.e.* times that are less than a diffusive timescale for $\sigma = 1$.

The coupling between the frictionally driven flows and the stratification is examined with this flow decomposition. The timescales over which the Ekman transport is either generated by diffusion of the stratification or suppressed by Ekman advection of the buoyancy field are determined. First, consider the case with no initial along-isobath flow. In figure 2-1a, diffusion of the stratification causes the isopycnals to tilt adjacent to the bottom in order to satisfy the insulating boundary condition.

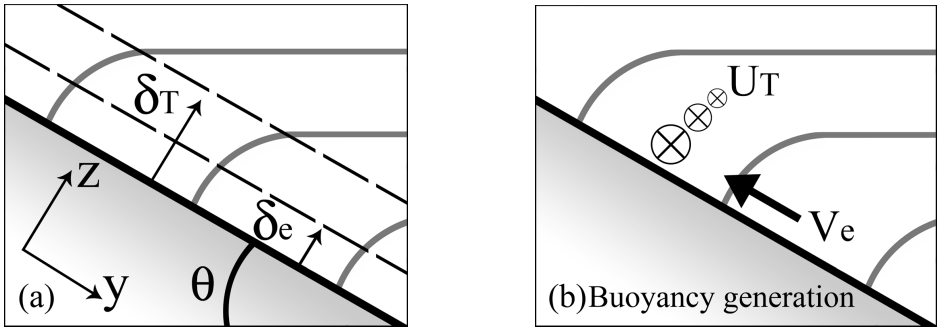

Figure 2-1: Buoyancy generation of the Ekman transport. (a) Diffusion of buoyancy tilts the isopycnals (grey contours) normal to the boundary and forms a thermal boundary layer of depth δ_T that is assumed thicker than an Ekman layer of depth δ_e. (b) The tilted isopycnals generate a vertically sheared geostrophic along-isobath flow, U_T, and a cross-isobath Ekman flow, V_e, with an upslope Ekman transport.

This tilting of the isopycnals is equivalent to a positive buoyancy anomaly, which scales as $\Delta b_T \sim N^2 \delta_T$. A geostrophically balanced along-isobath flow develops in the thermal boundary layer with magnitude $\Delta u_T \sim \theta \Delta b_T / f$. By the no-slip boundary condition, an Ekman flow arises with an upslope Ekman transport, as shown in figure 2-1b. Upslope Ekman advection of buoyancy cools the thermal boundary layer by an Ekman buoyancy flux, which scales as $\kappa \Delta b_e / \delta_e \sim \kappa S N^2 \delta_T \sigma / \delta_e$. This Ekman buoyancy flux impedes the heating of the thermal boundary layer that grows by diffusion of the stratification when the Ekman buoyancy flux, $\kappa \Delta b_e / \delta_e$, is the same order of magnitude as the diffusive flux of the background stratification, κN^2. From these scalings, these fluxes balance on buoyancy generation timescale

$$\mathcal{T}_{generation} = \sigma^{-1} S^{-2} f^{-1}. \tag{2.11}$$

For constant stratification, this process occurs independently of the initial along-isobath flow and the upslope Ekman transport has no cross-isobath variations, which means that this solution does not contribute to the vertical circulation emanating from the bottom boundary layer.

In contrast, an initial along-isobath flow drives an upslope or downslope Ekman flow, as shown in figure 2-2a. Lateral shear in the along-isobath flow induces Ek-

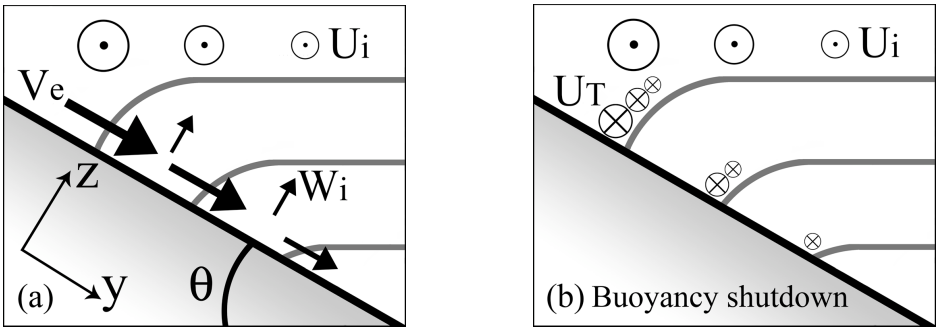

Figure 2-2: Buoyancy shutdown of the Ekman transport. (a) The along-isobath flow, U_i, drives a cross-isobath Ekman flow, V_e, with Ekman pumping, W_i, arising from convergences in the Ekman transport. The cross-isobath Ekman flow advects the buoyancy field and fluxes heat into the thermal boundary layer, which tilts the isopycnals. (b) The tilted isopycnals generate a vertically sheared geostrophic along-isobath flow, U_T, that reduces the Ekman transport as well as the Ekman pumping.

man pumping and suction by convergences and divergences in the Ekman transport. In this case, cross-isobath Ekman advection of the background stratification gives rise to an Ekman buoyancy flux, which scales as $\kappa \Delta b_e / \delta_e \sim \kappa S^{1/2} N U \sigma / \delta_e$. This Ekman buoyancy flux heats (cools) the thermal boundary layer for downslope (upslope) Ekman flows, resulting in a thermal boundary layer buoyancy anomaly that scales as $\Delta b_T \sim \Delta b_e \delta_T / \delta_e$. Physically, this buoyancy anomaly reduces the cross-isobath pressure gradient that drives the Ekman flow. As shown in figure 2-2b, the buoyancy anomaly geostrophically balances an along-isobath flow, with magnitude $\Delta u_T \sim \theta \Delta b_T / f$, that opposes the initial along-isobath flow. Then, buoyancy shutdown of the Ekman flow occurs when the along-isobath flow in the thermal boundary layer is the same order of magnitude as the initial along-isobath flow, U. From these scalings, this process occurs on the buoyancy shutdown timescale

$$\mathcal{T}_{shutdown} = \sigma^{-1} S^{-2} f^{-1}. \tag{2.12}$$

The buoyancy shutdown timescale derived here is equal to the leading order buoyancy shutdown timescale derived by MacCready and Rhines (1991) for slope Burger numbers less than one and order one Prandtl numbers. The buoyancy shutdown

timescale is invariant to the coefficient of mixing. Thus, if the diffusivity is reduced, where σ is fixed, the Ekman buoyancy flux to the thermal boundary layer is reduced. However, the thermal boundary layer depth is also reduced to the extent that the buoyancy anomaly within this layer is independent of the diffusivity on the buoyancy shutdown timescale. The steps to buoyancy shutdown for viscous and diffusive flows contrasts with buoyancy shutdown that occurs by only advection and displacement of the isopycnals. MacCready and Rhines (1991) showed that the buoyancy shutdown timescale approached $S^{-1}f^{-1}$ in the nondiffusive limit.

Although the buoyancy generation timescale is equal to the buoyancy shutdown timescale, the buoyancy generation timescale represents the time for buoyancy forces to generate an upslope Ekman flow and the buoyancy shutdown timescale represents the time for buoyancy forces to suppress the initial Ekman flow. For subinertial dynamics, the buoyancy generation and buoyancy shutdown timescales are assumed longer than an inertial period, which means that $S < (2\pi\sigma)^{-1/2} < 1$.

The time-dependent adjustment problem is solved by decomposing the flow into the following buoyancy generation (denoted by $^-$) and buoyancy shutdown (denoted by $\widetilde{\ }$) components:

$$u = \overline{u}(z,t) + \widetilde{u}(y,z,t), \tag{2.13}$$

$$v = \overline{v}(z,t) + \widetilde{v}(y,z,t), \tag{2.14}$$

$$w = \widetilde{w}(y,z,t), \tag{2.15}$$

$$b = \overline{b}(z,t) + \widetilde{b}(y,z,t). \tag{2.16}$$

The linear adjustment of the laterally uniform stratification is considered in section 2.3, the laterally uniform along-isobath flow is examined in section 2.4, and the laterally sheared along-isobath flow is investigated in section 2.5.

2.3 Buoyancy generation of an upslope Ekman flow

The equations for the adjustment of the background stratification are examined on the buoyancy generation timescale. These equations are formed by setting the cross-isobath variations, the velocity component normal to the boundary, and the interior variables to zero. Then, the variables are nondimensionalized in the thermal and Ekman boundary layers by the following set of scalings:

$$\begin{aligned}
\overline{u}_T &= S^{1/2} N \delta_T \; \overline{u}'_T, & \overline{u}_e &= S^{1/2} N \delta_T \; \overline{u}'_e, \\
\overline{v}_T &= S^{1/2} N \delta_T (f\mathcal{T})^{-1} \; \overline{v}'_T, & \overline{v}_e &= S^{1/2} N \delta_T \; \overline{v}'_e, \\
\overline{b}_T &= N^2 \delta_T \; \overline{b}'_T, & \overline{b}_e &= S\sigma N^2 \delta_T \; \overline{b}'_e, \\
\overline{p}_T &= \rho_o N^2 \delta_T^2 \; \overline{p}'_T, & \overline{p}_e &= \rho_o \sigma S N^2 \delta_T \delta_e \; \overline{p}'_e.
\end{aligned}$$

Time is nondimensionalized by the buoyancy generation timescale, where $t' = t/\mathcal{T}$ and $\mathcal{T} = \mathcal{T}_{generation}$. The coordinate normal to the boundary is nondimensionalized in the thermal boundary layer as $\xi' = z/\delta_T$, where $\delta_T = \sqrt{2\kappa\mathcal{T}} = \sigma^{-1} S^{-1} \delta_e$, and in the Ekman boundary layer as $\eta' = z/\delta_e$, where primes denote nondimensional quantities. The leading order equations in the thermal boundary layer, where the primes of the nondimensional variables have been dropped, become

$$\frac{\partial \overline{u}_T}{\partial t} - \overline{v}_T = \frac{\sigma}{2} \frac{\partial^2 \overline{u}_T}{\partial \xi^2}, \tag{2.17}$$

$$\overline{u}_T = -\overline{b}_T, \tag{2.18}$$

$$0 = -\frac{\partial \overline{p}_T}{\partial \xi} + \overline{b}_T, \tag{2.19}$$

$$\frac{\partial \overline{b}_T}{\partial t} = \frac{1}{2} \frac{\partial^2 \overline{b}_T}{\partial \xi^2}. \tag{2.20}$$

For $\sigma = 1$, $\bar{v}_T = 0$ and the along-isobath flow satisfies the buoyancy diffusion equation by (2.18). A cross-isobath flow is induced in the thermal boundary layer for Prandtl numbers not equal to one in order for the along-isobath flow to maintain geostrophic balance. This cross-isobath flow is weaker than the Ekman flow by order σS^2 and, for $\sigma > 1$, is downslope. Then, for Prandtl numbers greater than one, momentum diffuses away from the boundary more slowly than in a nonrotating fluid owing to the

Coriolis acceleration associated with this downslope flow. This process is described as the slow diffusion of momentum by MacCready and Rhines (1991).

The leading order equations in the Ekman layer are

$$-\overline{v}_e = \frac{1}{2}\frac{\partial^2 \overline{u}_e}{\partial \eta^2}, \tag{2.21}$$

$$\overline{u}_e = \frac{1}{2}\frac{\partial^2 \overline{v}_e}{\partial \eta^2}, \tag{2.22}$$

$$0 = -\frac{\partial \overline{p}_e}{\partial \eta} + \overline{b}_e, \tag{2.23}$$

$$-\overline{v}_e = \frac{1}{2}\frac{\partial^2 \overline{b}_e}{\partial \eta^2}. \tag{2.24}$$

In the Ekman layer, cross-isobath Ekman advection of the background stratification balances diffusion of buoyancy. Buoyancy enters into the cross-isobath Ekman momentum equation, (2.22), at order σS and is a higher order correction to the leading order dynamics for order one Prandtl numbers and small slope Burger numbers.

The leading order boundary conditions become

$$\overline{u}_T(\xi = 0) + \overline{u}_e(\eta = 0) = 0, \tag{2.25}$$

$$\overline{v}_e(\eta = 0) = 0, \tag{2.26}$$

$$\frac{\partial \overline{b}_T}{\partial \xi}(\xi = 0) + \frac{\partial \overline{b}_e}{\partial \eta}(\eta = 0) + 1 = 0, \tag{2.27}$$

$$\overline{u}_T, \overline{v}_T, \overline{b}_T \to 0 \quad \text{as} \quad \xi \to \infty, \tag{2.28}$$

$$\overline{u}_e, \overline{v}_e, \overline{b}_e \to 0 \quad \text{as} \quad \eta \to \infty, \tag{2.29}$$

and all variables are initially zero. The general form of the Ekman solution is

$$\overline{u}_e = -\overline{u}_T(\xi = 0)\mathrm{e}^{-\eta}\cos\eta, \tag{2.30}$$

$$\overline{v}_e = \overline{u}_T(\xi = 0)\mathrm{e}^{-\eta}\sin\eta, \tag{2.31}$$

$$\overline{b}_e = -\overline{u}_T(\xi = 0)\mathrm{e}^{-\eta}\cos\eta. \tag{2.32}$$

The Ekman transport is defined as $\overline{M}_e = \int_0^\infty \overline{v}_e(t,\eta)d\eta$ and

$$\overline{M}_e = \frac{1}{2}\overline{u}_T(\xi = 0). \tag{2.33}$$

The dimensional Ekman transport is $(\kappa/\theta)\overline{u}_T(\xi = 0, t)$. The scaling for the Ekman transport, κ/θ, on the buoyancy generation timescale is equal to Thorpe's (1987) steady-state, upslope Ekman transport in the small slope angle approximation. The time and spatial evolution of the along-isobath flow, $\overline{u}_T$, satisfies

$$\frac{\partial \overline{u}_T}{\partial t} = \frac{1}{2}\frac{\partial^2 \overline{u}_T}{\partial \xi^2}, \tag{2.34}$$

and is solved subject to

$$\begin{aligned} \overline{u}_T(t=0) &= 0, & (2.35)\\ \frac{\partial \overline{u}_T}{\partial \xi}(\xi = 0) - \overline{u}_T(\xi = 0) - 1 &= 0, & (2.36)\\ \overline{u}_T \to 0 \quad \text{as} \quad \xi \to \infty. & & (2.37) \end{aligned}$$

A Laplace transform, $\mathcal{L}$, in time is applied. The Laplace transform of the solution, $\overline{U}_T(s,\xi) = \mathcal{L}[\overline{u}_T(t,\xi)] \equiv \int_0^\infty \overline{u}_T(t,\xi)\mathrm{e}^{-st}dt$, becomes

$$\overline{U}_T(s,\xi) = -\frac{\mathrm{e}^{-\xi\sqrt{2s}}}{s(1+\sqrt{2s})}. \tag{2.38}$$

By the inverse Laplace transform (Abramowitz and Stegun 1972), the solution to the along-isobath flow is

$$\overline{u}_T(t,\xi > 0) = \frac{\mathrm{e}^{t/2}}{\sqrt{2\pi}}\int_0^t (\frac{\xi}{\tau} - 1)\frac{\mathrm{e}^{-\tau/2-\xi^2/(2\tau)}}{\sqrt{\tau}}d\tau - \frac{\xi}{\sqrt{2\pi}}\int_0^t \tau^{-3/2}\mathrm{e}^{-\xi^2/(2\tau)}d\tau \tag{2.39}$$

and

$$\overline{u}_T(t,\xi = 0) = \mathrm{e}^{t/2} - 1 - \sqrt{\frac{2t}{\pi}} - \frac{\mathrm{e}^{t/2}}{\sqrt{2\pi}}\int_0^t \tau^{1/2}\mathrm{e}^{-\tau/2}d\tau. \tag{2.40}$$

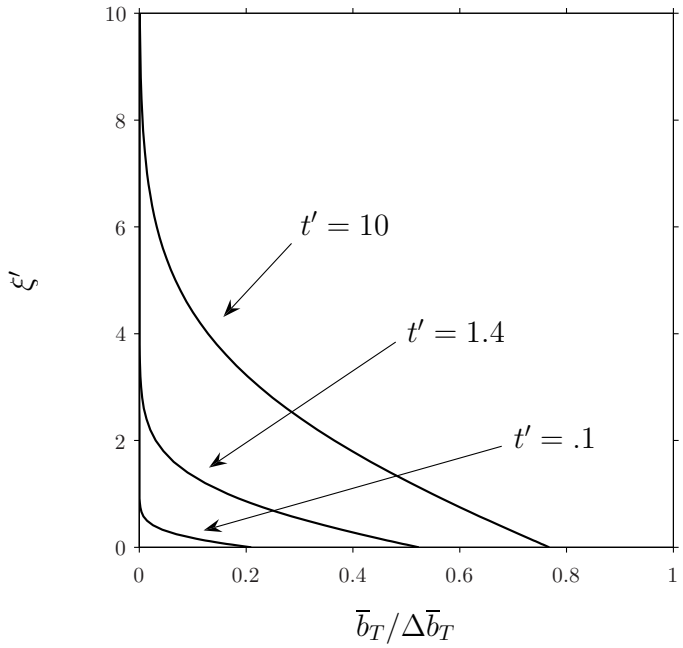

Figure 2-3: The buoyancy field in the thermal boundary layer grows by diffusion in order to satisfy the insulating boundary condition. As the thermal boundary layer thickens, the tilted isopycnals lead to an upslope Ekman transport. Then, the buoyancy field grows more slowly as the Ekman transport advects denser water upslope and reduces the flux of buoyancy into the thermal boundary layer. The scale of the buoyancy anomaly is defined as $\Delta\overline{b}_T = N^2\delta_T$.

Figure 2-3 shows the spatial profile for the buoyancy field, where $\overline{b}_T = -\overline{u}_T$, in time. This solution shows that diffusion of the stratification forms a positive buoyancy anomaly near the bottom, which corresponds to an along-isobath flow in the negative x-direction. By (2.33), the Ekman transport associated with this flow is upslope, *i.e.* in the negative y-direction as shown in figure 2-4, and initially grows as $\sqrt{2t/\pi}$ for $t \ll 1$. This Ekman flow advects denser water upslope and induces an Ekman buoyancy flux that counteracts the buoyancy flux to the thermal boundary layer by diffusion of the background stratification. As a balance is achieved by the buoyancy fluxes, the Ekman transport grows more slowly in time.

The time-dependent solution to the adjustment of the stratification demonstrates the dynamical coupling between the buoyancy field and the Ekman flow. In the

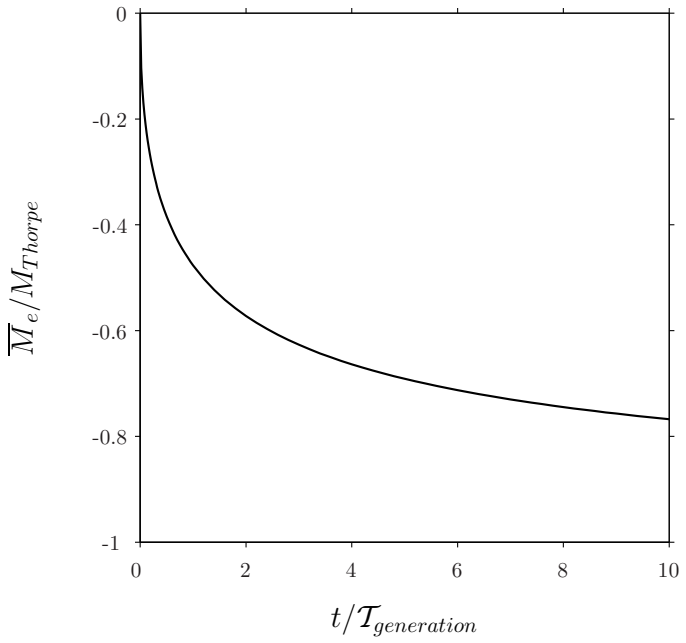

Figure 2-4: The analytical solution for the upslope Ekman transport scales with $M_{Thorpe} = \kappa/\theta$ and evolves in time on the buoyancy generation timescale.

limit $t \to \infty$, $\overline{u}_T(\xi = 0) \to -1$ and the dimensional Ekman transport approaches $-\kappa/\theta$, which is consistent with Thorpe's (1987) steady-state solution. Thus, the question regarding the steady-state solution, in which the magnitude of the Ekman transport, κ/θ, goes to infinity for vanishingly small slope angles, is reconciled by the full time-dependent solution. The timescale to develop a sufficiently large Ekman transport to balance diffusion of the background stratification is proportional to θ^{-4} and $\mathcal{T}_{generation} \to \infty$ as $\theta \to 0$. This result is consistent with the flat bottom solution, where the Ekman transport is identically zero.

2.4 Buoyancy shutdown of a laterally uniform Ekman flow

The buoyancy shutdown problem of MacCready and Rhines (1991) for a laterally uniform along-isobath flow over a sloping bottom is reexamined to solve for the full time-dependence of the Ekman transport. The adjustment of the along-isobath flow

is examined on the buoyancy shutdown timescale. The interior domain is defined as the region above the thermal boundary layer. The interior along-isobath flow, with magnitude U, is geostrophically balanced by a pressure field that varies over a horizontal length scale, L. The variables are nondimensionalized in the interior domain as well as the thermal and Ekman boundary layers by the following set of scalings:

$$\begin{array}{lll}
\widetilde{u}_i = \Lambda U\ \widetilde{u}'_i, & \widetilde{u}_T = \Lambda U\ \widetilde{u}'_T, & \widetilde{u}_e = \Lambda U\ \widetilde{u}'_e, \\
\widetilde{v}_i = 0, & \widetilde{v}_T = \Lambda U(f\mathcal{T})^{-1}\ \widetilde{v}'_T, & \widetilde{v}_e = \Lambda U\ \widetilde{v}'_e, \\
\widetilde{b}_i = 0, & \widetilde{b}_T = \Lambda U N S^{-1/2}\ \widetilde{b}'_T, & \widetilde{b}_e = \Lambda U N S^{1/2}\sigma\ \widetilde{b}'_e, \\
\widetilde{p}_i = \rho_o \Lambda U L f\ \widetilde{p}'_i, & \widetilde{p}_T = \rho_o S^{-1/2}\Lambda U N \delta_T\ \widetilde{p}'_T, & \widetilde{p}_e = \rho_o \sigma S^{1/2}\delta_e \Lambda U N\ \widetilde{p}'_e.
\end{array}$$

The parameter Λ is defined such that the along-isobath flow drives a downslope Ekman flow for $\Lambda = 1$ and an upslope Ekman flow for $\Lambda = -1$. The thermal boundary layer thickness sets the height over which the geostrophic flow is modified because there are no convergences in the Ekman transport to drive an interior secondary circulation over a Prandtl depth. Time is nondimensionalized by the buoyancy shutdown timescale, where $t' = t/\mathcal{T}$ and $\mathcal{T} = \mathcal{T}_{shutdown}$, and primes denote nondimensional quantities. As in section 2.3, the coordinate normal to the boundary is nondimensionalized in the thermal boundary layer as $\xi' = z/\delta_T$, where $\delta_T = \sigma^{-1}S^{-1}\delta_e$, and in the Ekman boundary layer as $\eta' = z/\delta_e$. The leading order equations in the thermal boundary layer, dropping the primes, become

$$\frac{\partial \widetilde{u}_T}{\partial t} - \widetilde{v}_T = \frac{\sigma}{2}\frac{\partial^2 \widetilde{u}_T}{\partial \xi^2}, \tag{2.41}$$

$$\widetilde{u}_T = -\widetilde{b}_T, \tag{2.42}$$

$$0 = -\frac{\partial \widetilde{p}_T}{\partial \xi} + \widetilde{b}_T, \tag{2.43}$$

$$\frac{\partial \widetilde{b}_T}{\partial t} = \frac{1}{2}\frac{\partial^2 \widetilde{b}_T}{\partial \xi^2}. \tag{2.44}$$

For order one Prandtl numbers and small slope Burger numbers, the Ekman layer equations are

$$
\begin{aligned}
-\widetilde{v}_e &= \frac{1}{2}\frac{\partial^2 \widetilde{u}_e}{\partial \eta^2}, && (2.45)\\
\widetilde{u}_e &= \frac{1}{2}\frac{\partial^2 \widetilde{v}_e}{\partial \eta^2}, && (2.46)\\
0 &= -\frac{\partial \widetilde{p}_e}{\partial \eta} + \widetilde{b}_e, && (2.47)\\
-\widetilde{v}_e &= \frac{1}{2}\frac{\partial^2 \widetilde{b}_e}{\partial \eta^2}. && (2.48)
\end{aligned}
$$

At $t = 0$, all variables are zero except for the interior along-isobath flow, which equals one for all time. The leading order boundary conditions become

$$
\begin{aligned}
1 + \widetilde{u}_T(\xi = 0) + \widetilde{u}_e(\eta = 0) &= 0, && (2.49)\\
\widetilde{v}_e(\eta = 0) &= 0, && (2.50)\\
\frac{\partial \widetilde{b}_T}{\partial \xi}(\xi = 0) + \frac{\partial \widetilde{b}_e}{\partial \eta}(\eta = 0) &= 0, && (2.51)\\
\widetilde{u}_T, \widetilde{v}_T, \widetilde{b}_T \to 0 \quad &\text{as} \quad \xi \to \infty, && (2.52)\\
\widetilde{u}_e, \widetilde{v}_e, \widetilde{b}_e \to 0 \quad &\text{as} \quad \eta \to \infty. && (2.53)
\end{aligned}
$$

The general form of the Ekman solution is

$$
\begin{aligned}
\widetilde{u}_e &= -(1 + \widetilde{u}_T(\xi = 0))\mathrm{e}^{-\eta}\cos\eta, && (2.54)\\
\widetilde{v}_e &= (1 + \widetilde{u}_T(\xi = 0))\mathrm{e}^{-\eta}\sin\eta, && (2.55)\\
\widetilde{b}_e &= -(1 + \widetilde{u}_T(\xi = 0))\mathrm{e}^{-\eta}\cos\eta. && (2.56)
\end{aligned}
$$

The Ekman transport is defined as $\widetilde{M_e} = \int_0^\infty \widetilde{v}_e(t, \eta)d\eta$ and

$$
\widetilde{M_e} = \frac{1}{2}(1 + \widetilde{u}_T(\xi = 0)). \qquad (2.57)
$$

The same method from section 2.3 is applied to solve for the thermal boundary layer flow and the Ekman transport. The along-isobath flow evolves as the slow diffusion equation

$$\frac{\partial \widetilde{u}_T}{\partial t} = \frac{1}{2}\frac{\partial^2 \widetilde{u}_T}{\partial \xi^2}, \tag{2.58}$$

subject to

$$\widetilde{u}_T(t=0) = 0, \tag{2.59}$$

$$\frac{\partial \widetilde{u}_T}{\partial \xi}(\xi=0) - \widetilde{u}_T(\xi=0) - 1 = 0, \tag{2.60}$$

$$\widetilde{u}_T \to 0 \quad \text{as} \quad \xi \to \infty. \tag{2.61}$$

The equations governing $\widetilde{u}_T$ and $\overline{u}_T$, (2.58)-(2.61) and (2.34)-(2.37), respectively, are identical and therefore $\widetilde{u}_T = \overline{u}_T$. Thus, the modification of the buoyancy field in the thermal boundary layer by a downwelling Ekman flow arising from a laterally uniform along-isobath flow is mathematically equivalent to the modification of the buoyancy field by the adjustment of the background stratification.

The total dimensional Ekman transport that results from the adjustment of the laterally uniform along-isobath flow and the background stratification is examined. The total Ekman transport is composed of contributions from $M_{initial} = \delta_e U/2$, which is the magnitude of the Ekman transport induced by the initial along-isobath flow, and $M_{Thorpe} = \kappa/\theta$, which is the magnitude of the steady-state upslope Ekman transport. Then, the total dimensional Ekman transport for all time is

$$M_e = M_{Thorpe}\overline{u}'_T(\xi=0,t') + \Lambda M_{initial}(1 + \widetilde{u}'_T(\xi=0,t')). \tag{2.62}$$

For long times, the Ekman transport behaves as

$$M_e(t' \gg 1) = -M_{Thorpe} + (M_{Thorpe} + \Lambda M_{initial})\sqrt{\frac{2}{\pi}}(t/\mathcal{T}_{shutdown})^{-1/2}. \tag{2.63}$$

MacCready and Rhines (1991) found that the long-time behavior of the Ekman transport is given by $M_e = -M_{Thorpe} + (M_{Thorpe} + \Lambda M_{initial})\ \mathcal{C}(t/\mathcal{T}_{shutdown,MR})^{-1/2}$. The constant $\mathcal{C}$ was empirically determined to equal 0.81 using numerical simulations (MacCready and Rhines 1991). A comparison of this result with (2.63) shows that the two solutions are quantitatively consistent since $\sqrt{2/\pi} \approx 0.80$.

2.5 Buoyancy shutdown of Ekman pumping and suction

2.5.1 Analytical results

Next, the dynamics of buoyancy shutdown in the suppression of stratified spindown over a sloping bottom is examined. The adjustment of a laterally sheared along-isobath flow is examined with respect to the spindown timescale, $\mathcal{T}_{spindown} = E^{-1/2} f^{-1}$. The key parameter in this problem is

$$\beta \equiv \frac{\mathcal{T}_{spindown}}{\mathcal{T}_{shutdown}} = \sigma S^2 E^{-1/2}, \tag{2.64}$$

which measures the influence of buoyancy shutdown on stratified spindown. The adjustment problem is examined for $\beta \leq 1$, where $\beta = 0$ corresponds to stratified spindown on a flat bottom.

The parameter space is further constrained to the case where the initial Ekman transport, $M_{initial} = \delta_e U/2$, induced by the along-isobath flow is larger than the steady-state Ekman transport, $M_{Thorpe} = \kappa/\theta$, from the adjustment of the stratification. Thus, the dominant contribution to the evolution of the buoyancy field in the thermal boundary layer is due to cross-isobath Ekman advection of buoyancy rather than diffusion of the background stratification. For linear dynamics in the thermal boundary layer and the Ekman buoyancy equation, Rossby numbers are examined subject to $\epsilon < \sigma^{-1/2} E^{1/4}$, a condition that is further discussed in the following chap-

ter. From these two conditions, the flow subject to $\sigma S > E^{1/2}$ is examined. Although the validity of the analytical solution is then further constrained to $\beta > S$, the solution asymptotes to the stratified spindown solution in the limit $\beta \to 0$.

The initial along-isobath flow is barotropic with magnitude U and sinusoidal cross-isobath variations over a lateral length scale L. The flow is characterized by the Rossby number, ϵ, and the aspect ratio, Γ, which are assumed sufficiently small for linear, hydrostatic flows. The flow is nondimensionalized by the following set of scalings:

$$
\begin{array}{lll}
\widetilde{u}_i = U\ \widetilde{u}'_i, & \widetilde{u}_T = \beta^{1/2} U\ \widetilde{u}'_T, & \widetilde{u}_e = U\ \widetilde{u}'_e, \\
\widetilde{v}_i = E^{1/2} U\ \widetilde{v}'_i, & \widetilde{v}_T = \beta^{1/2} E^{1/2} U\ \widetilde{v}'_T, & \widetilde{v}_e = U\ \widetilde{v}'_e, \\
\widetilde{w}_i = E^{1/2} \Gamma U\ \widetilde{w}'_i, & \widetilde{w}_T = \beta^{1/2} \sigma^{-1/2} E^{3/4} \Gamma U\ \widetilde{w}'_T, & \widetilde{w}_e = E^{1/2} \Gamma U\ \widetilde{w}'_e, \\
\widetilde{b}_i = \epsilon N^2 H_P\ \widetilde{b}'_i, & \widetilde{b}_T = \beta^{1/2} S^{-1/2} \epsilon N^2 H_P\ \widetilde{b}'_T, & \widetilde{b}_e = \sigma S^{1/2} \epsilon N^2 H_P\ \widetilde{b}'_e, \\
\widetilde{p}_i = \rho_o \epsilon N^2 H_P^2\ \widetilde{p}'_i, & \widetilde{p}_T = \rho_o S^{1/2} \epsilon N^2 H_P^2\ \widetilde{p}'_T, & \widetilde{p}_e = \rho_o \sigma S^{1/2} E^{1/2} \epsilon N^2 H_P^2\ \widetilde{p}'_e.
\end{array}
$$

In the rotated, nondimensional system, the leading order initial flow is

$$\widetilde{u}(t = 0, y) = \cos(y). \tag{2.65}$$

Time is nondimensionalized by the spindown timescale, where $t' = t/\mathcal{T}$ and $\mathcal{T} = \mathcal{T}_{spindown}$. The coordinate normal to the boundary is nondimensionalized in the interior as $z' = z/H_P$, in the thermal boundary layer as $\xi' = z/\delta_T$, where $\delta_T = \sqrt{2\kappa\mathcal{T}} = \sigma^{-1/2} E^{1/4} H_P$, and in the Ekman layer as $\eta' = z/\delta_e$, where $\delta_e = E^{1/2} H_P$, and primes denote nondimensional quantities. The leading order equations in the interior domain,

where the primes are dropped, become

$$\begin{aligned}
\frac{\partial \widetilde{u}_i}{\partial t} - \widetilde{v}_i &= 0, && (2.66)\\
\widetilde{u}_i &= -\frac{\partial \widetilde{p}_i}{\partial y}, && (2.67)\\
0 &= -\frac{\partial \widetilde{p}_i}{\partial z} + \widetilde{b}_i, && (2.68)\\
\frac{\partial \widetilde{b}_i}{\partial t} + \widetilde{w}_i &= 0, && (2.69)\\
\frac{\partial \widetilde{v}_i}{\partial y} + \frac{\partial \widetilde{w}_i}{\partial z} &= 0. && (2.70)
\end{aligned}$$

The interior secondary circulation, $\widetilde{\psi}_i$, is defined such that $\widetilde{v}_i = -\frac{\partial \widetilde{\psi}_i}{\partial z}$ and $\widetilde{w}_i = \frac{\partial \widetilde{\psi}_i}{\partial y}$ from the continuity equation. Then, the interior secondary circulation satisfies

$$\frac{\partial^2 \widetilde{\psi}_i}{\partial y^2} + \frac{\partial^2 \widetilde{\psi}_i}{\partial z^2} = 0, \tag{2.71}$$

which is forced by Ekman pumping and suction at the boundary. Next, the leading order equations in the thermal boundary layer are

$$\begin{aligned}
\frac{\partial \widetilde{u}_T}{\partial t} - \widetilde{v}_T &= \frac{\sigma}{2}\frac{\partial^2 \widetilde{u}_T}{\partial \xi^2}, && (2.72)\\
\widetilde{u}_T &= -\widetilde{b}_T, && (2.73)\\
0 &= -\frac{\partial \widetilde{p}_T}{\partial \xi} + \widetilde{b}_T, && (2.74)\\
\frac{\partial \widetilde{b}_T}{\partial t} &= \frac{1}{2}\frac{\partial^2 \widetilde{b}_T}{\partial \xi^2}, && (2.75)\\
\frac{\partial \widetilde{v}_T}{\partial y} + \frac{\partial \widetilde{w}_T}{\partial \xi} &= 0. && (2.76)
\end{aligned}$$

In the thermal boundary layer, buoyancy and the along-isobath flow evolve by diffusion. For $\sigma \neq 1$, a weak secondary circulation exists with a cross-isobath flow that is smaller than the cross-isobath Ekman flow by order $\sqrt{\beta E}$. By continuity, lateral variations in this cross-isobath flow drive a flow in the thermal boundary layer that

is normal to the boundary, but this normal flow is smaller than the normal flow in the interior and the Ekman layer by order $\sqrt{\beta/\sigma}E^{1/4}$. Finally, the leading order equations in the Ekman layer are

$$-\widetilde{v}_e = \frac{1}{2}\frac{\partial^2 \widetilde{u}_e}{\partial \eta^2}, \tag{2.77}$$

$$\widetilde{u}_e = \frac{1}{2}\frac{\partial^2 \widetilde{v}_e}{\partial \eta^2}, \tag{2.78}$$

$$0 = -\frac{\partial \widetilde{p}_e}{\partial \eta} + \widetilde{b}_e, \tag{2.79}$$

$$-\widetilde{v}_e = \frac{1}{2}\frac{\partial^2 \widetilde{b}_e}{\partial \eta^2}, \tag{2.80}$$

$$\frac{\partial \widetilde{v}_e}{\partial y} + \frac{\partial \widetilde{w}_e}{\partial \eta} = 0. \tag{2.81}$$

These equations are solved subject to the boundary conditions

$$\widetilde{u}_i(z=0) + \beta^{1/2}\widetilde{u}_T(\xi=0) + \widetilde{u}_e(\eta=0) = 0, \tag{2.82}$$

$$\widetilde{v}_e(\eta=0) = 0, \tag{2.83}$$

$$\widetilde{w}_i(z=0) + \widetilde{w}_e(\eta=0) = 0, \tag{2.84}$$

$$\frac{\partial \widetilde{b}_T}{\partial \xi}(\xi=0) + \frac{\partial \widetilde{b}_e}{\partial \eta}(\eta=0) = 0, \tag{2.85}$$

$$\widetilde{u}_i \to \widetilde{u}_i(t=0,y) \quad \text{as} \quad z \to \infty, \tag{2.86}$$

$$\widetilde{v}_i, \widetilde{w}_i, \widetilde{b}_i \to 0 \quad \text{as} \quad z \to \infty, \tag{2.87}$$

$$\widetilde{u}_T, \widetilde{v}_T, \widetilde{w}_T, \widetilde{b}_T \to 0 \quad \text{as} \quad \xi \to \infty, \tag{2.88}$$

$$\widetilde{u}_e, \widetilde{v}_e, \widetilde{w}_e, \widetilde{b}_e \to 0 \quad \text{as} \quad \eta \to \infty. \tag{2.89}$$

At the initial time, the along-isobath flow is specified in the interior and the interior buoyancy anomaly is zero. The variables in the thermal boundary layer are initially zero. The Ekman flow that induces Ekman pumping and suction is established within an inertial period and is treated as an initial condition for the subinertial timescales

considered here. The general solution for the Ekman flow is

$$\widetilde{u}_e = -(\widetilde{u}_i(z=0) + \beta^{1/2}\widetilde{u}_T(\xi=0))\mathrm{e}^{-\eta}\cos\eta, \tag{2.90}$$

$$\widetilde{v}_e = (\widetilde{u}_i(z=0) + \beta^{1/2}\widetilde{u}_T(\xi=0))\mathrm{e}^{-\eta}\sin\eta, \tag{2.91}$$

$$\widetilde{w}_e = \frac{1}{2}\frac{\partial}{\partial y}(\widetilde{u}_i(z=0) + \beta^{1/2}\widetilde{u}_T(\xi=0))\mathrm{e}^{-\eta}(\sin\eta + \cos\eta), \tag{2.92}$$

$$\widetilde{b}_e = -(\widetilde{u}_i(z=0) + \beta^{1/2}\widetilde{u}_T(\xi=0))\mathrm{e}^{-\eta}\cos\eta. \tag{2.93}$$

The Ekman transport is defined as $\widetilde{M_e} = \int_0^\infty \widetilde{v}_e(t,y,\eta)d\eta$ and

$$\widetilde{M_e} = \frac{1}{2}(\widetilde{u}_i(z=0) + \beta^{1/2}\widetilde{u}_T(\xi=0)). \tag{2.94}$$

By the no normal flow boundary condition, Ekman pumping is given by

$$\widetilde{w}_i(z=0) = -\frac{1}{2}\frac{\partial}{\partial y}(\widetilde{u}_i(z=0) + \beta^{1/2}\widetilde{u}_T(\xi=0)). \tag{2.95}$$

This expression shows that buoyancy forces modify the Ekman pumping at leading order when $\beta = 1$. The Ekman pumping solution is transformed into a boundary condition on the interior secondary circulation

$$\frac{\partial\widetilde{\psi}_i}{\partial t}(z=0) = \frac{1}{2}(\frac{\partial\widetilde{\psi}_i}{\partial z}(z=0) - \beta^{1/2}\frac{\partial\widetilde{u}_T}{\partial t}(\xi=0)). \tag{2.96}$$

Next, the Ekman buoyancy solution as well as the geostrophic relationship in the thermal boundary layer is used to transform the no normal buoyancy flux boundary condition into a boundary condition on $\widetilde{u}_T$,

$$\frac{\partial\widetilde{u}_T}{\partial\xi}(\xi=0) = \widetilde{u}_i(z=0) + \beta^{1/2}\widetilde{u}_T(\xi=0). \tag{2.97}$$

The lateral structure of the initial along-isobath flow determines the lateral structure of the variables. Separation of variables is applied, where

$$(\widetilde{\psi}_i, \widetilde{u}_i, \widetilde{u}_T) = (\Psi_i(t,z), U_i(t,z), U_T(t,\xi))\cos(y). \tag{2.98}$$

The spatial structure of $\widetilde{\psi}_i$ is determined by (2.71) and

$$\Psi_i(z,t) = \varphi(t)\mathrm{e}^{-z}, \tag{2.99}$$

where φ is the measure of the Ekman transport strength. The dimensional Ekman transport evolves as $-\delta_e U\varphi(t')\cos(y')$ and is equal to $(\delta_e/2)U\cos(y')$ at $t=0$. Then, φ also sets the strength of the Ekman pumping and suction and determines the extent of spindown in the interior along-isobath flow. A closed set of partial differential equations that couple the dynamics of both spindown and buoyancy shutdown are formed, where

$$\frac{\partial U_i}{\partial t} - \varphi(t)\mathrm{e}^{-z} = 0, \tag{2.100}$$

$$\frac{\partial U_T}{\partial t} - \frac{1}{2}\frac{\partial^2 U_T}{\partial \xi^2} = 0, \tag{2.101}$$

subject to the boundary conditions

$$\frac{d\varphi}{dt} + \frac{1}{2}(\varphi + \beta^{1/2}\frac{\partial U_T}{\partial t}(\xi=0)) = 0, \tag{2.102}$$

$$\frac{\partial U_T}{\partial \xi}(\xi=0) - U_i(z=0) - \beta^{1/2}U_T(\xi=0) = 0, \tag{2.103}$$

$$U_i \to 1 \quad \text{as} \quad z \to \infty, \tag{2.104}$$

$$U_T \to 0 \quad \text{as} \quad \xi \to \infty \tag{2.105}$$

and the initial conditions

$$\varphi(t=0) = -\frac{1}{2}, \tag{2.106}$$

$$U_i(t=0) = 1, \tag{2.107}$$

$$U_T(t=0) = 0. \tag{2.108}$$

This system of equations is solved using Laplace transforms in time, such that $(\widetilde{\varphi}(s), \widetilde{U}_i(s,z), \widetilde{U}_T(s,\xi)) = \mathcal{L}[\varphi(t), U_i(t,z), U_T(t,\xi)] \equiv \int_0^\infty (\varphi(t), U_i(t,z) U_T(t,\xi)) \mathrm{e}^{-st} dt$ and

$$\widetilde{\varphi} = -\frac{1}{1+2s+\sqrt{2\beta s}}, \tag{2.109}$$

$$\widetilde{U}_i = \frac{1}{s}\left(1 - \frac{\mathrm{e}^{-z}}{1+2s+\sqrt{2\beta s}}\right), \tag{2.110}$$

$$\widetilde{U}_T = \frac{-2\mathrm{e}^{-\xi\sqrt{2s}}}{2\sqrt{\beta}s + (1+2s)\sqrt{2s}}. \tag{2.111}$$

The solutions are determined by operating on (2.109)-(2.111) by the inverse Laplace transform (Abramowitz and Stegun 1972). The temporal structure of the interior secondary circulation is

$$\begin{aligned}\varphi(t) = & -\frac{1}{2}\mathrm{e}^{at}\cos(bt) + \sqrt{\frac{\beta t}{2\pi}} - \frac{1}{4b}(1+2a)\mathrm{e}^{at}\sin(bt) \\ & + \sqrt{\frac{\beta}{2\pi}}\mathrm{e}^{at}\Bigg\{ \cos(bt)\int_0^t \tau^{1/2}\mathrm{e}^{-a\tau}\left(2a\cos(b\tau) + \left[b^2 - \frac{a^2}{b}\right]\sin(b\tau)\right)d\tau \\ & + \sin(bt)\int_0^t \tau^{1/2}\mathrm{e}^{-a\tau}\left(\left[-b + \frac{a^2}{b}\right]\cos(b\tau) + 2a\sin(b\tau)\right)d\tau\Bigg\},\end{aligned} \tag{2.112}$$

where the coefficients are $a = -(2-\beta)/4$, which is negative for $\beta \leq 1$, and $b = \pm\sqrt{\beta(1-\beta/4)}/2$. In the limit $\beta \to 0$, the coefficients approach $a = -1/2$ and $b = 0$ and, from the first term in (2.112), the Ekman pumping approaches the spindown solution on a flat bottom, where $\varphi_{spindown}(t) = -(1/2)\mathrm{e}^{-t/2}$. The second term represents the opposition to spindown by buoyancy forces that initially grows as $\sqrt{\beta t/(2\pi)}$. The third and fourth terms in (2.112) modulate the long-time behavior of the Ekman

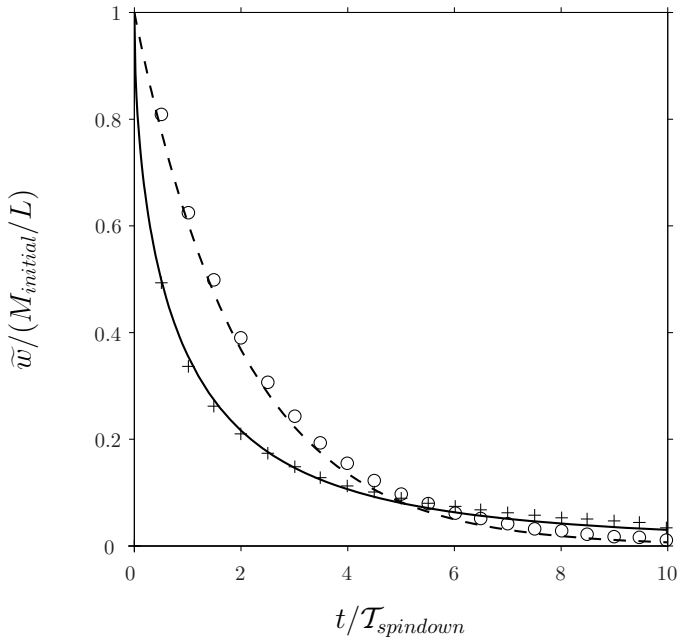

Figure 2-5: The decay of the Ekman pumping for the laterally sheared flow is compared between the stratified spindown solution over a flat bottom (dashed line), $\beta = 0$, and over a sloping bottom (solid line), $\beta = 1$, from the analytical model. The numerical model solution is shown for $\beta = 0$ (o) and $\beta = 1$ (+) every 0.5 spindown times where $\epsilon = 0.1$. Ekman pumping is measured by the vertical velocity evaluated at $z/H_P = 0.08$ in the numerical model and is equal to $\widetilde{w}_i(z' = 0)$ in the analytical model.

pumping. Figure 2-5 shows that Ekman pumping, which is evaluated at $y = \pi/2$, decays faster due to buoyancy shutdown on a sloping bottom, $\beta = 1$, than on a flat bottom, $\beta = 0$. Buoyancy forces cause Ekman pumping to initially decay as $\varphi(t \ll 1) = -(1/2)\mathrm{e}^{(\beta/4-1/2)t} + \sqrt{\beta t/(2\pi)}$. However, Ekman pumping for $\beta = 1$ does not remain weaker than Ekman pumping for $\beta = 0$. Instead, after $t = 5$, Ekman pumping for $\beta = 1$ is *greater* than Ekman pumping for $\beta = 0$. This reversal in magnitudes of the two solutions is explained by the temporal and spatial evolution of the buoyancy field in the thermal boundary layer.

In the thermal boundary layer, the buoyancy anomaly is associated with a

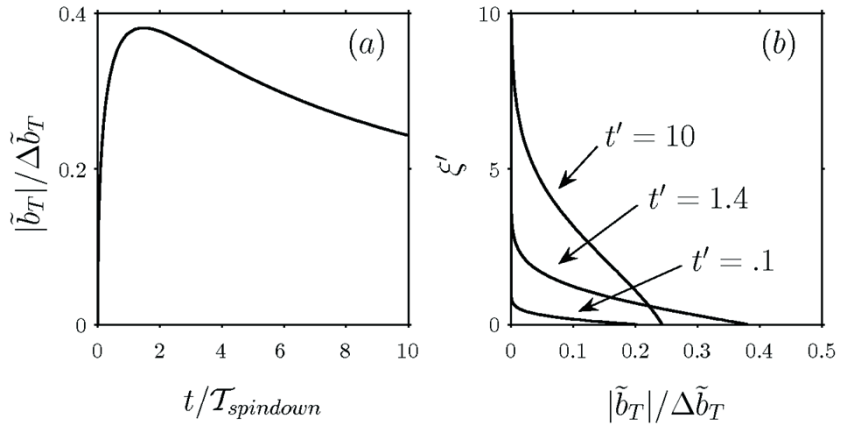

Figure 2-6: (a) The analytical solution for the time evolution of the thermal boundary layer buoyancy anomaly evaluated at the boundary for $\beta = 1$. (b) The vertical structure of the buoyancy anomaly for $\beta = 1$ is presented at $t/\mathcal{T}_{spindown} = 0.1, 1.4, 10$. The scale of the buoyancy anomaly is defined as $\Delta\widetilde{b}_T = \beta^{1/2} S^{-1/2} \epsilon N^2 H_P$.

geostrophically balanced along-isobath flow,

$$U_T(t, \xi > 0) = \frac{\mathrm{e}^{at}}{\sqrt{2\pi}} \Bigg\{ \sin(bt) \int_0^t \frac{\mathrm{e}^{-a\tau - \xi^2/(2\tau)}}{\sqrt{\tau}} \Bigg(\left[\frac{\xi\sqrt{\beta}}{2b\tau} - \frac{\beta}{4b} \right] \cos(b\tau) - \sin(b\tau) \Bigg) d\tau \quad (2.113)$$
$$+ \cos(bt) \int_0^t \frac{\mathrm{e}^{-a\tau - \xi^2/(2\tau)}}{\sqrt{\tau}} \Bigg(\left[-\frac{\xi\sqrt{\beta}}{2b\tau} + \frac{\beta}{4b} \right] \sin(b\tau) - \cos(b\tau) \Bigg) d\tau \Bigg\}$$

and

$$U_T(t, \xi = 0) = \frac{\sqrt{\beta}}{2b} \mathrm{e}^{at} \sin(bt) - \sqrt{\frac{2t}{\pi}} \quad (2.114)$$
$$+ \frac{\mathrm{e}^{at}}{\sqrt{2\pi}} \Bigg\{ \sin(bt) \int_0^t \tau^{1/2} \mathrm{e}^{-a\tau} \Bigg(\left[-\frac{a\beta}{2b} + 2b \right] \cos(b\tau) - \left[\frac{\beta}{2} + 2a \right] \sin(b\tau) \Bigg) d\tau$$
$$+ \cos(bt) \int_0^t \tau^{1/2} \mathrm{e}^{-a\tau} \Bigg(\left[\frac{a\beta}{2b} - 2b \right] \sin(b\tau) - \left[\frac{\beta}{2} + 2a \right] \cos(b\tau) \Bigg) d\tau \Bigg\}.$$

An initial along-isobath flow in the positive x-direction induces a downwelling Ekman flow that gives rise to a positive buoyancy anomaly in the thermal boundary layer. This buoyancy anomaly corresponds to an along-isobath flow that opposes the interior flow and initially grows as $\sqrt{2t/\pi}$. In the limit $\beta \to 0$, the dimensional solution for the thermal boundary layer flow vanishes because buoyancy shutdown

requires the intersection of isopycnals with the bottom boundary.

The time evolution of the buoyancy anomaly in the thermal boundary layer for $\beta = 1$ is shown in figure 2-6a. The buoyancy anomaly grows to its maximum value when $t = 1.4$ for $\beta = 1$. The buoyancy anomaly decays in magnitude beyond this time as buoyancy shutdown reduces the Ekman transport and the Ekman buoyancy flux into the thermal boundary layer. For constant viscosity and diffusivity, the magnitude of the buoyancy anomaly at the boundary weakens because the thermal boundary layer continues to thicken diffusively in time. This initial growth in the buoyancy anomaly near the bottom and its subsequent diffusion is presented in figure 2-6b for $\beta = 1$. The reversal in the magnitude of the Ekman pumping for the $\beta = 0$ and $\beta = 1$ solutions is explained by this diffusion of the buoyancy anomaly that impedes the Ekman transport.

By suppressing Ekman pumping and suction, buoyancy shutdown inhibits the spindown of the interior along-isobath flow. By inverse Laplace transform of (2.110), the interior along-isobath flow is

$$\begin{aligned} U_i(t,z) &= \left\{1 - \mathrm{e}^{-z}(1 - \cos(bt)\mathrm{e}^{at})\right\} - \frac{\beta}{4b}\mathrm{e}^{-z+at}\sin(bt) \\ &\quad + \frac{1}{b}\sqrt{\frac{\beta}{2\pi}}\mathrm{e}^{-z+at}\Bigg\{\sin(bt)\int_0^t \tau^{1/2}\mathrm{e}^{-a\tau}\Big(a\cos(b\tau) + b\sin(b\tau)\Big)d\tau \\ &\quad + \cos(bt)\int_0^t \tau^{1/2}\mathrm{e}^{-a\tau}\Big(-a\sin(b\tau) + b\cos(b\tau)\Big)d\tau\Bigg\}. \end{aligned} \tag{2.115}$$

The first term, which is enclosed by brackets, approaches the spindown solution in the limit $\beta \to 0$, where $U_{i,\ spindown} = 1 - \mathrm{e}^{-z}(1 - \mathrm{e}^{-t/2})$. The extent to which the interior spins down is reflected in the time decay of the interior along-isobath flow evaluated at the boundary. Spindown of the interior flow is compared in figure 2-7 for $\beta = 0$ and $\beta = 1$. For $\beta = 1$, buoyancy shutdown reduces the rate at which the interior along-isobath flow decays, but the flow continues to decay in time because Ekman pumping remains nonzero.

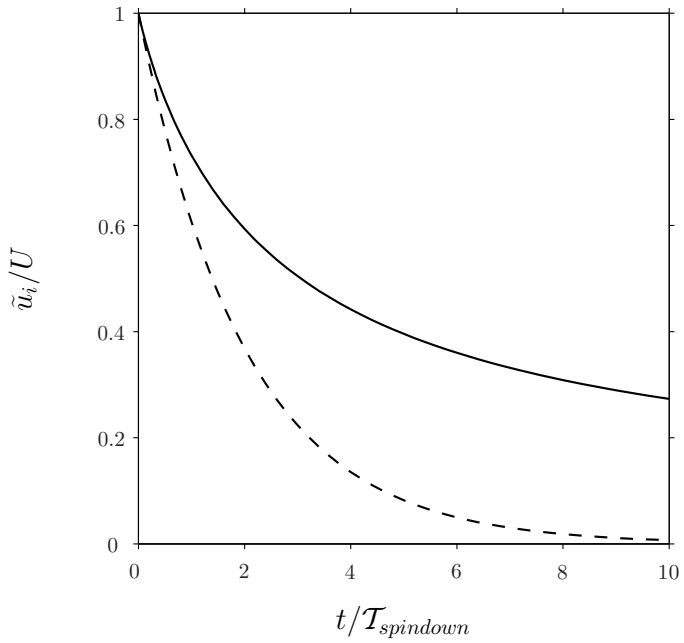

Figure 2-7: The analytical solution for the time evolution of the interior along-isobath flow at $y = 0, z = 0$ is shown for the stratified spindown solution over a flat bottom (dashed line), $\beta = 0$, and over a sloping bottom (solid line), $\beta = 1$.

2.5.2 Numerical model results

The validity of the linear analytical theory is investigated in a series of numerical experiments with application to flows over continental slopes. The experiments are performed using the Regional Ocean Modeling System (ROMS) (Shchepetkin and McWilliams 2005), which is a free-surface, hydrostatic, primitive equation model with stretched, terrain-following coordinates. This model is configured with no along-isobath variations and a bottom boundary that is inclined to the horizontal at an angle θ. The domain is 300 km wide with a uniform horizontal grid spacing of 1 km and is bounded by sidewalls. The total depth is 4.5 km, with a variable vertical grid of 201 points and vertical grid resolution that ranges from $\Delta z = 1$ m to $\Delta z = 55$ m. At the bottom, temperature satisfies the no heat flux boundary condition and an approximate no-slip boundary condition is imposed. Mixing coefficients are uniform and equal to $\nu, \kappa = 2.3$ x 10^{-3} m^2 s^{-1}. Uniform rotation is specified with $f = 10^{-4}$ s^{-1}.

The initial parameters are chosen within the range of possible physical charac-

teristics for flows over the continental slope. The initial along-isobath flow is given by $u(t = 0, y) = U\cos(y/L)$, where $U = 0.1$ m s^{-1}, $L = 10.6$ km for a narrow slope current, and $N^2 = 1.6 \times 10^{-5}$ s^{-2}. From these parameters, the depth of the secondary circulation is $H_P = 266$ m, the Ekman layer thickness is $\delta_e = 6.7$ m, $M_{initial} = 0.34$ m^2 s^{-1}, and $M_{Thorpe} = 0.23$ m^2 s^{-1} for $\beta = 1$. The nondimensional parameters are $\epsilon = 0.09$, $E = 6.4 \times 10^{-4}$, and $\Gamma = 0.03$. The numerical results are shown for flows over a flat bottom, where $\theta = 0$ with $\beta = 0$, and flows over a continental slope, where $\theta = 0.01$ with $\beta = 1$ and $S = 0.16$. When the bottom is flat, the timescale for stratified spindown is $\mathcal{T}_{spindown} = 6.3$ inertial periods. When $\theta = 0.01$, $\mathcal{T}_{spindown} = \mathcal{T}_{shutdown} = 6.3$ inertial periods.

In order to isolate the effect of buoyancy shutdown from buoyancy generation, the model output was decomposed into components corresponding to the adjustment of the stratification and the cross-isobath varying flow. This decomposition was performed by running the model with no initial flow and subtracting the solution from the total model output. The sections for the resulting along-isobath flow, the buoyancy anomaly, and the secondary circulation are compared with the full analytical solutions. The solution for stratified spindown over a flat bottom, $\beta = 0$, is shown in figure 2-8 and over a sloping bottom, $\beta = 1$, in figure 2-9. For $\beta = 1$, the variables are mapped onto the rotated coordinate frame to compare with the flat bottom case. The flow is plotted at $t/\mathcal{T}_{spindown} = 1.4$. At this time, the analytical solution to Ekman pumping for $\beta = 0$ is half of its initial value and the buoyancy anomaly in the thermal boundary layer for $\beta = 1$ is its maximum value.

For stratified spindown on a flat bottom, $\beta = 0$, the sections show agreement in the spatial structure between the analytical and numerical solutions. The interior secondary circulation reduces the along-isobath flow over a height H_P. This circulation also vertically advects the stratification and gives rise to negative (positive) buoyancy anomalies in regions of Ekman pumping (suction). In the numerical model, the buoyancy anomaly is weaker near the bottom than in the analytical model. This weakening occurs because the secondary circulation vertically advects the total

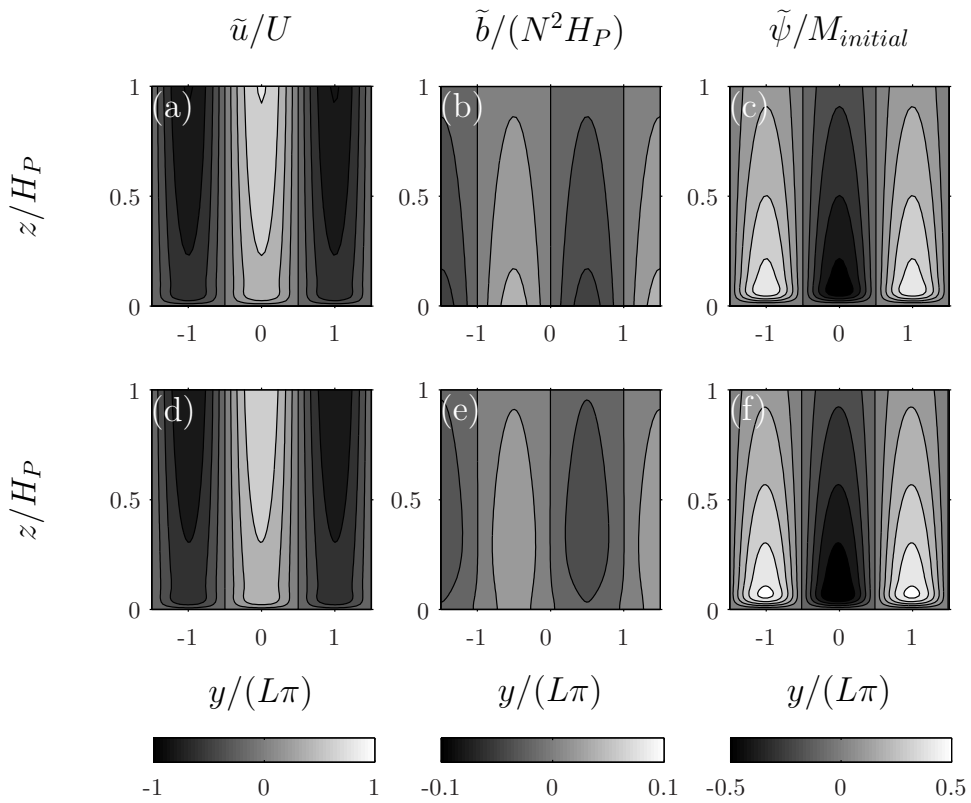

Figure 2-8: The $\beta = 0$ analytical solution (a, b, c) is compared with the $\beta = 0$ numerical solution (d, e, f). The sections are shown at $t/\mathcal{T}_{spindown} = 1.4$. The along-isobath flow, $\widetilde{u}/U$ (a, d), is contoured every 0.2 units, the buoyancy anomaly, $\widetilde{b}/N^2 H_P$ (b, e), is contoured every 0.02 units, and the secondary circulation, $\widetilde{\psi}/M_{initial}$ (c, f), is contoured every 0.1 units.

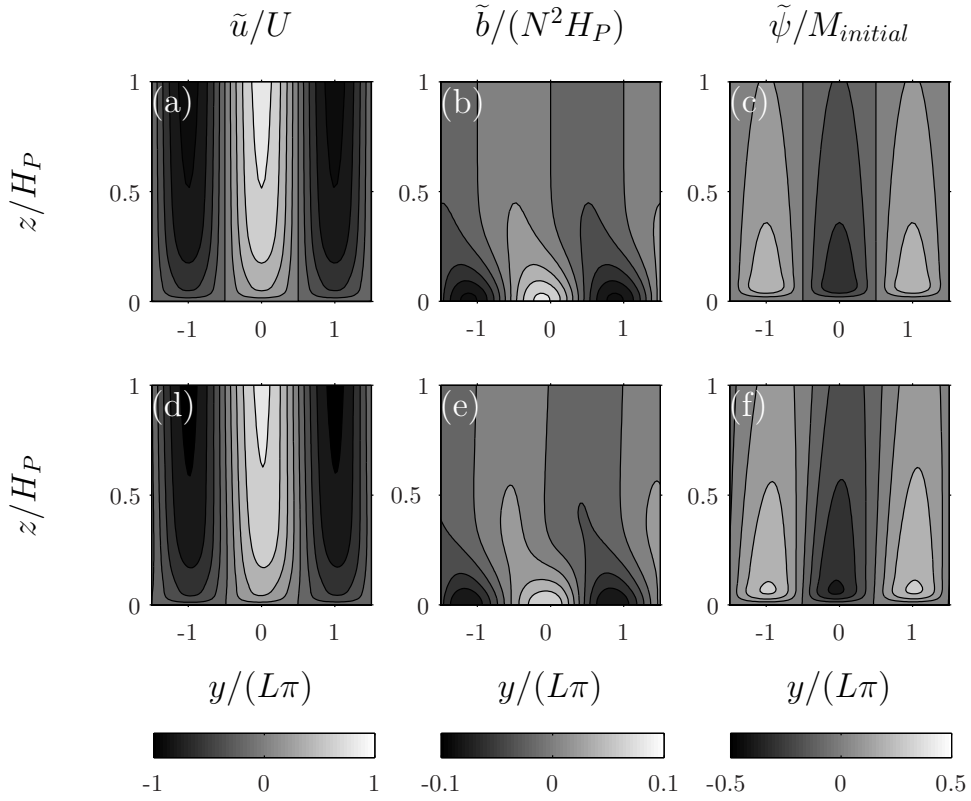

Figure 2-9: The $\beta = 1$ analytical solution (a, b, c) is compared with the $\beta = 1$ numerical solution (d, e, f) for the cross-isobath varying flow in the rotated coordinate frame. The sections are shown at $t/\mathcal{T}_{spindown} = 1.4$. The along-isobath flow, $\widetilde{u}/U$ (a, d), is contoured every 0.2 units, the buoyancy anomaly, $\widetilde{b}/N^2 H_P$ (b, e), is contoured every 0.02 units, and the secondary circulation, $\widetilde{\psi}/M_{initial}$ (c, f), is contoured every 0.1 units.

stratification, which is reduced near the bottom due to diffusion of the stratification. Consequently, vertical advection leads to a stronger secondary circulation, which is consistent with a stronger secondary circulation in the numerical solution than in the analytical solution. This component of the buoyancy anomaly and the secondary circulation is not included in the analytical solution presented here but is further examined in the following chapter.

For stratified spindown on a slope, $\beta = 1$, positive and negative buoyancy anomalies form away from regions of Ekman pumping and suction. These buoyancy anomalies are due to cross-isobath Ekman advection of buoyancy and are the components of the buoyancy field that lead to buoyancy shutdown of the Ekman transport. Buoy-

ancy shutdown for $\beta = 1$ is evident in the secondary circulation, which is weaker than the $\beta = 0$ secondary circulation, as well as in the along-isobath flow, which is not as reduced away from the boundary as in the flat bottom case. For $\beta = 1$, features are apparent in the numerical solution that are not included in the linear analytical solution. First, the secondary circulation in figure 2-9f is tilted, which reflects its tendency to align parallel to the isopycnals intersecting the slope. This order $S^{1/2}$ effect is not included in the equation for the interior secondary circulation. Second, the interior buoyancy anomalies in figure 2-9e are asymmetric in magnitude for cyclonic and anticyclonic vorticity. This asymmetry is due to nonlinear advection of buoyancy and neglected in the linear theory.

The numerical model is used to test the analytical prediction for the decay in the Ekman pumping and suction by buoyancy shutdown. The Ekman pumping at $y = \pi/2$ is calculated from the model output, filtered with a cut-off frequency of $0.12f$, and compared to the analytical solutions for $\beta = 0$ and $\beta = 1$ in figure 2-5. The numerical model confirms the reversal in the strength of the $\beta = 0$ and $\beta = 1$ Ekman pumping solutions at $t/\mathcal{T}_{spindown} = 5$. The overall agreement between the analytical and numerical model supports the physical mechanism for linear buoyancy shutdown formulated in section 2.2. For order one Prandtl numbers and small slope Burger numbers, cross-isobath Ekman advection of buoyancy drives a diffusively growing thermal boundary layer, which reduces the along-isobath flow adjacent to the bottom and hence the Ekman pumping.

2.6 Potential vorticity dynamics

On a stratified sloping boundary, the interplay between buoyancy and frictional dynamics produces potential vorticity (PV) fluxes adjacent to the bottom that can impact the PV distribution and the dynamics of flows away from the boundary. The processes that govern the strength and temporal nature of PV input and extraction are of importance to our understanding of the ocean circulation. This section pro-

vides one of the first attempts to analytically demonstrate the physical mechanisms of PV input or extraction over a stratified sloping boundary and to identify a scaling for the corresponding PV flux. The analytical solutions are applied to estimate the amount of potential vorticity that is transferred into and out of the system over a sloping boundary and to compare the analytically calculated fluxes with the numerical model. The time evolution of potential vorticity is determined by convergences and divergences in the PV flux, where

$$\frac{\partial q}{\partial t} = -\nabla \cdot \mathbf{J}, \tag{2.116}$$

$q = \omega_a \cdot \nabla B$ is the Ertel potential vorticity, $\nabla B = \nabla b + N^2 \hat{k}$ is the total buoyancy gradient, and $\omega_a = f\hat{k} + \nabla \times \mathbf{u}$ is the absolute vorticity, where $\hat{k}$ is the vertical unit vector. The PV flux is given by (Marshall and Nurser 1992, Thomas 2005)

$$\mathbf{J} = q\mathbf{u} + \nabla B \times \mathbf{F} - \mathcal{D}\omega_a, \tag{2.117}$$

and is composed of advective PV fluxes, $\mathbf{J}_a = q\mathbf{u}$, frictional PV fluxes, $\mathbf{J}_F = \nabla B \times \mathbf{F}$, and diabatic PV fluxes, $\mathbf{J}_D = -\mathcal{D}\omega_a$, where

$$\mathbf{F} = \nu \nabla^2 \mathbf{u}, \tag{2.118}$$

$$\mathcal{D} = \kappa \nabla^2 b, \tag{2.119}$$

for the mixing scheme applied in this model. Equation (2.116) is integrated over a control area that is defined by isopycnals intersecting the boundary. No along-isobath variations and weak PV fluxes away from the boundary are assumed. Then, by the impermeability theorem (Haynes and McIntyre 1987), in which there is no PV flux through the isopycnals of the control area, the area-integrated PV is determined only by the PV fluxes at the boundary. The equation for the area-integrated PV, $\mathcal{Q}$, is

$$\frac{d\mathcal{Q}}{dt} = -\int_{y_1}^{y_2} (\mathbf{J}_F + \mathbf{J}_\mathcal{D}) \cdot \hat{n} \; dy, \tag{2.120}$$

where $\mathcal{Q} = \iint_{\mathcal{A}} q \; dA$, $\mathcal{A}$ defines the control area, dA is an infinitesimal unit of area, $\hat{n}$ is the outward normal unit vector at the boundary, and y_1 and y_2 define the cross-isobath positions of the isopycnals at the boundary that enclose $\mathcal{A}$. An outward positive PV flux leads to a reduction in the area-integrated PV, whereas an inward positive PV flux leads to an enhancement. By integrating (2.120) in time, the net change in the area-integrated PV, $\Delta\mathcal{Q} = \mathcal{Q}(t) - \mathcal{Q}(t=0)$, is

$$\Delta\mathcal{Q} = -\int_0^t d\tau \int_{y_1}^{y_2} (J_F^n(\tau, y) + J_D^n(\tau, y)) dy, \tag{2.121}$$

where $J_F^n = \mathbf{J}_F \cdot \hat{n}$ and $J_{\mathcal{D}}^n = \mathbf{J}_{\mathcal{D}} \cdot \hat{n}$ are the outward normal PV fluxes.

Frictional and diabatic processes couple with the components of the total PV flux, in which diabatic and frictional processes induce both frictional and diabatic PV fluxes. In the adjustment of the stratification, diffusion reduces the stratification near the boundary, which leads to an outward positive diabatic PV flux out of the system. On the sloping bottom, the upslope Ekman transport tends to weaken this outward diabatic PV flux by upslope advection of buoyancy. In the adjustment of the along-isobath flow, the initial Ekman transport is either upslope, which tends to stratify and drives an inward PV flux, or downslope, which tends to destratify and drives an outward PV flux. Even though frictional processes induce both diabatic and frictional PV fluxes, the following analysis shows that the diabatic PV fluxes scale larger than the frictional PV fluxes for order one Prandtl numbers and small slope Burger numbers. Thus, the diabatic PV fluxes generate the largest contribution to the total change in PV on the sloping bottom.

In the rotated coordinate system, where the small angle approximation is applied, the PV fluxes normal to the boundary at $z = 0$ are

$$J_F^n = \nu\bigg(- N^2\theta + \frac{\partial b}{\partial y}\bigg)\bigg(\frac{\partial^2 u}{\partial y^2} + \frac{\partial^2 u}{\partial z^2}\bigg), \tag{2.122}$$

$$J_{\mathcal{D}}^n = \kappa\bigg(f - \frac{\partial u}{\partial y}\bigg)\bigg(\frac{\partial^2 b}{\partial y^2} + \frac{\partial^2 b}{\partial z^2}\bigg). \tag{2.123}$$

The variables are decomposed into components corresponding to the interior domain as well as the thermal and Ekman boundary layers. Next, the change in the PV field during the adjustment of the stratification and laterally uniform flow is analytically examined.

2.6.1 PV dynamics for a laterally uniform flow

The analytical solutions for the adjustment of the stratification, from section 2.3, and laterally uniform flow, from section 2.4, are applied to determine the amount of PV transferred into and out of the system. The PV fluxes are nondimensionalized with respect to the scalings for the thermal boundary layer component of the diabatic PV flux. Then, $(J^n_{\mathcal{D}}, J^n_F) = (S\delta_e/2)(fN)^2(J^{n\prime}_{\mathcal{D}}, J^{n\prime}_F)$, where primes denote nondimensional quantities. The nondimensional frictional and diabatic PV fluxes, dropping the primes, become

$$\begin{aligned} J^n_F &= -\sigma S\frac{\partial^2\overline{u}_T}{\partial\xi^2}(\xi=0) - \Lambda\sigma S(M_{initial}/M_{Thorpe})\frac{\partial^2\widetilde{u}_T}{\partial\xi^2}(\xi=0) \\ &- (\sigma S)^{-1}\frac{\partial^2\overline{u}_e}{\partial\eta^2}(\eta=0) - \Lambda(\sigma S)^{-1}(M_{initial}/M_{Thorpe})\frac{\partial^2\widetilde{u}_e}{\partial\eta^2}(\eta=0), \end{aligned} \tag{2.124}$$

$$\begin{aligned} J^n_{\mathcal{D}} &= \frac{\partial^2\overline{b}_T}{\partial\xi^2}(\xi=0) + \Lambda(M_{initial}/M_{Thorpe})\frac{\partial^2\widetilde{b}_T}{\partial\xi^2}(\xi=0) \\ &+ (\sigma S)^{-1}\frac{\partial^2\overline{b}_e}{\partial\eta^2}(\eta=0) + \Lambda(\sigma S)^{-1}(M_{initial}/M_{Thorpe})\frac{\partial^2\widetilde{b}_e}{\partial\eta^2}(\eta=0). \end{aligned} \tag{2.125}$$

For order one Prandtl numbers and small slope Burger numbers, the Ekman components appear to have a larger contribution to the PV flux than the thermal boundary layer components. However, by the no-slip boundary condition from equations (2.21), (2.24), (2.45), and (2.48), the Ekman contributions are zero. Furthermore, the linear Ekman contributions exactly cancel by equations (2.21), (2.24), (2.45), and (2.48) in the sum $J^n_F + J^n_{\mathcal{D}}$. By applying the no-slip condition and the geostrophic relations

(2.18) and (2.42), the PV fluxes become

$$J_F^n = \sigma S \frac{\partial^2 \overline{b}_T}{\partial \xi^2}(\xi = 0) + \Lambda \sigma S (M_{initial}/M_{Thorpe}) \frac{\partial^2 \widetilde{b}_T}{\partial \xi^2}(\xi = 0), \tag{2.126}$$

$$J_{\mathcal{D}}^n = \frac{\partial^2 \overline{b}_T}{\partial \xi^2}(\xi = 0) + \Lambda (M_{initial}/M_{Thorpe}) \frac{\partial^2 \widetilde{b}_T}{\partial \xi^2}(\xi = 0). \tag{2.127}$$

Thus, diffusion of the stratification alone drives a diabatic PV flux out of the system as well as a frictional PV flux out of the system that is smaller by order σS. The modification to the PV flux by the upslope Ekman transport is not explicitly represented in these PV fluxes but is part of the solution. Generation of the upslope Ekman transport reduces the diffusion of the background stratification in the thermal boundary layer and hence the PV flux out of the system. The laterally uniform along-isobath flow drives a frictional PV flux that is smaller than the diabatic PV flux by order σS and is out of the system for downslope Ekman flows, $\Lambda = 1$, and into the system for upslope Ekman flows, $\Lambda = -1$. The relative contributions to the total PV flux is determined by the ratio $M_{initial}/M_{Thorpe}$. The solution to the total PV flux, $J^n = J_F^n + J_{\mathcal{D}}^n$, is

$$J^n = (1 + \sigma S)(1 + \Lambda (M_{initial}/M_{Thorpe}))\left(\sqrt{\frac{2}{\pi t}} - \mathrm{e}^{t/2}\mathrm{erfc}\left(\sqrt{\frac{t}{2}}\right)\right), \tag{2.128}$$

which is positive for all time if $\Lambda M_{initial}/M_{Thorpe} > -1$, zero if $\Lambda M_{initial}/M_{Thorpe} = -1$, and negative for all time if $\Lambda M_{initial}/M_{Thorpe} < -1$.

The change in the area-integrated PV is calculated from (2.121), where l, the distance of separation between the two bounding isopycnals, remains constant in time. Then, the change in the area-integrated PV is nondimensionalized such that $\Delta \mathcal{Q} = \mathcal{Q}_0 \Delta \mathcal{Q}'$, where $\mathcal{Q}_0 = (\sigma S)^{-1}(1 + \sigma S)(1 + \Lambda (M_{initial}/M_{Thorpe}))fN^2\delta_e l$. The scaling for the area-integrated PV is inversely proportional to the slope Burger number due to the slope Burger number dependence of the buoyancy shutdown timescale. From integation of (2.121) and application of $\overline{b}_T = \widetilde{b}_T$ and (2.44), the change in the

area-integrated PV, dropping the primes, is

$$\Delta\mathcal{Q} = -\widetilde{b}_T(\xi = 0). \tag{2.129}$$

This analytical analysis shows that frictional and diabatic processes couple in their modification of the PV field and the change in the area-integrated PV explicitly depends on the buoyancy anomaly in the thermal boundary layer.

2.6.2 PV dynamics for a laterally sheared flow: analytical solution

Next, the change in the PV field during the adjustment of the laterally sheared along-isobath flow is examined. The frictional and diabatic PV fluxes are nondimensionalized as $(J^n_{\mathcal{D}}, J^n_F) = (\sigma^{-1/2}E^{3/4}H_P/2)(fN)^2(J^{n\prime}_{\mathcal{D}}, J^{n\prime}_F)$. The frictional and diabatic PV fluxes become, dropping the primes,

$$\begin{aligned} J^n_F &= -(M_{initial}/M_{Thorpe})(\sigma^{-1/2}E^{-1/4})\frac{\partial^2\widetilde{u}_e}{\partial\eta^2}(\eta=0) - SE^{-1/2}\frac{\partial^2\overline{u}_e}{\partial\eta^2}(\eta=0) \\ &\quad - \sigma S(M_{initial}/M_{Thorpe})\frac{\partial^2\widetilde{u}_T}{\partial\xi^2}(\xi=0) - \sigma S\frac{\partial^2\overline{u}_T}{\partial\xi^2}(\xi=0). \end{aligned} \tag{2.130}$$

$$\begin{aligned} J^n_{\mathcal{D}} &= (M_{initial}/M_{Thorpe})(\sigma^{-1/2}E^{-1/4})\frac{\partial^2\widetilde{b}_e}{\partial\eta^2}(\eta=0) + SE^{-1/2}\frac{\partial^2\overline{b}_e}{\partial\eta^2}(\eta=0) \\ &\quad + (M_{initial}/M_{Thorpe})\frac{\partial^2\widetilde{b}_T}{\partial\xi^2}(\xi=0) + \frac{\partial^2\overline{b}_T}{\partial\xi^2}(\xi=0). \end{aligned} \tag{2.131}$$

The terms are shown in decreasing order of magnitude, where the assumptions of linearity, $\sigma S > E^{1/2}$, $\sigma = O(1)$, and $M_{initial}/M_{Thorpe} > 1$ are applied. By the no-slip condition, the Ekman components are zero, although these terms have the largest scalings. In general, by equations (2.21), (2.24), (3.39), and (3.41), the Ekman components exactly cancel in the sum of the diabatic and frictional PV fluxes. Then,

the total PV flux, J^n, is

$$J^n = (1+\sigma S)\frac{\partial^2 \overline{b}_T}{\partial \xi^2}(\xi=0) + (1+\sigma S)(M_{initial}/M_{Thorpe})\frac{\partial^2 \widetilde{b}_T}{\partial \xi^2}(\xi=0), \quad (2.132)$$

where the frictional PV flux contributes to a smaller PV flux than the diabatic PV flux by order σS. The ratio $M_{initial}/M_{Thorpe}$ determines the relative contributions from the adjustment of the background stratification and the laterally sheared flow. From the laterally sheared flow, frictional processes drive a diabatic PV flux that is spatially variable and outward (inward) where the flow is downwelling (upwelling).

Next, the net change in the area-integrated PV, (2.121), is calculated with a control area $\mathcal{A}$ bound by isopycnals. The cross-isobath positions of these isopycnals depend on changes to the buoyancy field by the adjustment of the stratification and the cross-isobath varying flow. The area-integrated PV is nondimensionalized by $\Delta\mathcal{Q} = \mathcal{Q}_0\Delta\mathcal{Q}'$, where $\mathcal{Q}_0 = \sigma^{-1/2}(1+\sigma S)E^{1/4}L^2Nf^2$. The amount of PV input or extracted increases for increasing slope Burger number, from the slope angle or stratification, and for increasing Ekman number, from the viscosity.

The cross-isobath varying buoyancy anomaly in the thermal boundary layer is partitioned as $\widetilde{b}_T = B_T(t,\xi)\cos(y)$, where $B_T(t,\xi) = -U_T(t,\xi)$. From (2.121), the change in the area-integrated PV, dropping the primes, becomes

$$\begin{aligned}
\Delta\mathcal{Q} \;=\; & -(y_2(t)-y_1(t))\overline{b}_T(t,\xi=0) \\
& - (M_{initial}/M_{Thorpe})(\sin(y_2(t))-\sin(y_1(t)))B_T(t,\xi=0) \\
& + \int_0^t \Bigg((\frac{dy_2}{d\tau}-\frac{dy_1}{d\tau})\overline{b}_T(\tau,\xi=0) \\
& + (M_{initial}/M_{Thorpe})(\cos(y_2(\tau))\frac{dy_2}{d\tau}-\cos(y_1(\tau))\frac{dy_1}{d\tau})B_T(\tau,\xi=0)\Bigg) d\tau.
\end{aligned} \quad (2.133)$$

This expression explicitly shows that the time change in the area-integrated PV can be expressed in terms of the time evolution of the buoyancy anomaly in the thermal boundary layer as well as the position of the isopycnal surfaces. For a laterally uniform flow, the ratio $M_{initial}/M_{Thorpe}$ determines whether there is net PV input or

extraction. For a laterally sheared flow, the net PV input or extraction is not only dependent on $M_{initial}/M_{Thorpe}$ but β as well.

The parameter β controls the magnitude and temporal evolution of the cross-isobath varying buoyancy anomalies that extract or input PV. As β increases, buoyancy shutdown occurs more rapidly to produce larger buoyancy anomalies before the interior flow spins down. In time, the magnitude of the cross-isobath varying buoyancy anomaly at the boundary decays after the initial buoyancy shutdown because the buoyancy anomalies diffuse into the interior. Then, the change in the area-integrated PV owing to the cross-isobath varying flow decays for long times. In contrast, the buoyancy anomaly owing to the adjustment of the stratification grows monotonically to its steady-state value and corresponds to an extraction of PV. Thus, an asymmetry exists for the total amount of PV input or extracted from the flow during spindown, and, for long times, PV extraction dominates.

The change in the area-integrated PV is examined for regions of initially downwelling and upwelling Ekman flows with the parameters used in the numerical simulation, where $\beta = 1$ and $M_{initial}/M_{Thorpe} = 1.5$. For the downwelling Ekman flow, the control area $\mathcal{A}_d$ is defined between $y_1(t = 0) = -\pi/4$ and $y_2(t = 0) = \pi/4$, and for the upwelling Ekman flow, the control area $\mathcal{A}_u$ is defined between $y_1(t = 0) = 3\pi/4$ and $y_2(t = 0) = 5\pi/4$. At initial time, the distance between the isopycnals for the downwelling case, l_d, and the upwelling case, l_u, is $\pi/2$. The displacement of the isopycnals is calculated as the total buoyancy field evolves in time.

The change in the area-integrated PV is shown in figure 2-10a for the downwelling Ekman flow and figure 2-10b for the upwelling Ekman flow. The main contributions to $\Delta\mathcal{Q}$ in figure 2-10 are from the first two terms of (2.133), and the time-integrated contribution from the third term is small in both cases. For $\mathcal{A}_d$, the adjustment of the stratification and Ekman downwelling lead to a net extraction of PV from the system with a negative change in the area-integrated PV. For $\mathcal{A}_u$, Ekman upwelling leads to an initial net input of PV into the system. As spindown progresses, the cross-isobath varying buoyancy anomaly and the input of PV weakens. In time, the

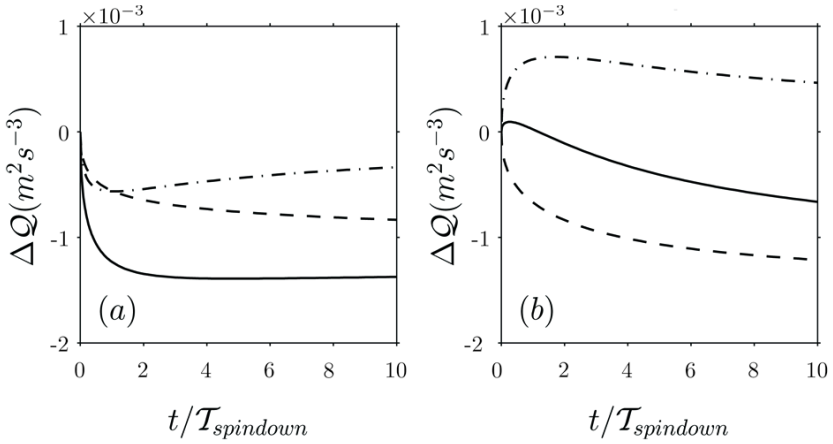

Figure 2-10: The analytical solution for the change in the area-integrated PV is shown for $\beta = 1$ in regions where the flow is downwelling (a) and upwelling (b). The change in $\mathcal{Q}$ associated with diffusion of the background stratification (dashed line, first term in (2.133)) and the laterally sheared flow (dash-dotted line, second term in (2.133)) have the largest contributions to the total change in the area-integrated PV (solid line).

adjustment of the background stratification leads to a net extraction of PV from the system. A comparison between the change in the area-integrated PV shows that the adjustment of the stratification has a larger contribution in the upwelling case than in the downwelling case. This difference occurs because the distance between the bounding isopycnals widens in the upwelling case, where $l_u(t = 10) = \pi/2 + 0.3$, and the distance contracts in the downwelling case, where $l_d(t = 10) = \pi/2 - 0.3$. Then, the adjustment of the stratification extracts additional PV out of the system for the upwelling case than for the downwelling case. This effect contributes to the eventual extraction of PV for an initially upwelling Ekman flow. The analytical estimate for the PV fluxes and change in the area-integrated PV is further examined in the numerical model.

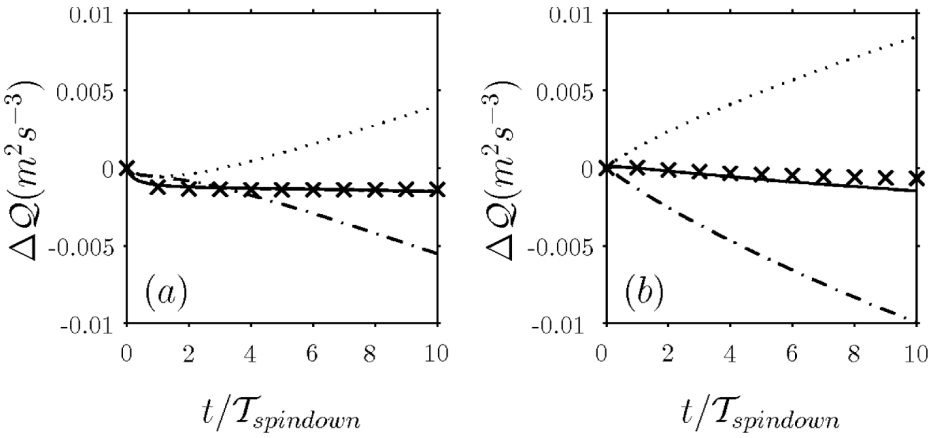

Figure 2-11: The time evolution of the change in the area-integrated PV from the $\beta = 1$ numerical solution is examined for regions of downwelling (a) and upwelling (b). The change in the total area-integrated PV (solid line) has contributions from the diabatic PV flux (dash-dotted line) and the frictional PV flux (dotted line). The analytical estimate (x) for the total change in the area-integrated PV is included for comparison.

2.6.3 PV dynamics for a laterally sheared flow: numerical simulation

The change in the area-integrated PV from the $\beta = 1$ simulation is compared with the analytical theory. The control areas defined in the numerical calculations are the same as in the analytical calculations. The analytical estimate captures the magnitude and temporal structure of the change in the total area-integrated PV. From the upwelling case in the numerical model, the maximum input in the area-integrated PV is $\Delta\mathcal{Q} = 8.5 \times 10^{-5}$ m^2 s^{-3} at $t = 0.3$, and the analytical estimate is $\Delta\mathcal{Q} = 9.4 \times 10^{-5}$ m^2 s^{-3} at $t = 0.3$. The change in the area-integrated PV reverses sign at $t = 1.0$ in the numerical calculation and at $t = 1.2$ in the analytical calculation.

The change in the area-integrated PV from the components of the diabatic and frictional PV fluxes is shown in figure 2-11 for each case. Diabatic and frictional components are of opposite sign but similar magnitude and largely cancel in their contributions to the total change in the area-integrated PV. This calculation differs

from the analytical solution which predicts that the frictional PV flux is smaller than the diabatic PV flux by order σS. The reason for this apparent discrepancy between the analytical and numerical solutions is described as follows.

In the numerical model, the PV flux is calculated at a grid space above the boundary where the no-slip boundary condition is applied. Then, the Ekman components will not only be nonzero but the scalings show that these terms will dominate the diabatic and frictional PV fluxes shown in equations (2.130) and (2.131). However, the linear Ekman components exactly cancel in the sum of the diabatic and frictional PV fluxes. The total change in the area-integrated PV from the $\beta = 1$ numerical calculation is also compared with the analytical solution. The significant cancellation between the frictional and diabatic PV fluxes in their contributions to the total area-integrated PV is consistent with the analytical prediction for the behavior of the PV fluxes with nonzero Ekman components. Therefore, the magnitude of the frictional and diabatic PV fluxes alone provide an overestimate of the total PV flux. The sum of the frictional and diabatic PV fluxes is necessary to estimate changes in the PV field.

2.7 Discussion

Mixing processes control the coupling between the Ekman flow and the buoyancy field on the sloping bottom. The theoretical results demonstrate that different aspects of mixing enter into the dynamics. The timescale for buoyancy generation and shutdown of the Ekman flow depends on the Prandtl number rather than the value of the mixing coefficient itself, as explained in section 2.2. For fixed viscosity, an increase in the diffusivity leads to a faster thickening of thermal boundary layer depth. Then, a longer buoyancy generation time is necessary for the upslope Ekman buoyancy flux to balance the buoyancy flux by diffusion of the stratification. Also, a longer buoyancy shutdown time is necessary for the buoyancy anomaly within this layer to grow to a sufficiently large magnitude to reduce the bottom stress.

In contrast, mixing of momentum, rather than buoyancy, determines the spindown timescale because the viscosity sets the strength of the Ekman pumping. Thus, a reduction in the mixing coefficients for fixed Prandtl number increases the spindown time while keeping the buoyancy shutdown time fixed. Then, buoyancy shutdown can reduce the Ekman transport before Ekman pumping spins down the interior along-isobath flow. This relative roles of mixing of buoyancy and momentum is reflected in the parameter β, the ratio of the spindown timescale to the buoyancy shutdown timescale.

The ratio of timescales, β, is not only dependent on the Prandtl number but also the slope Burger number, with a sensitivity to the slope angle that scales as θ^4. For the weak stratification that is used in the numerical simulations, a slope angle of $\theta = 0.01$ corresponds to $\beta = 1$. However, if the slope angle is reduced by half to $\theta = 0.005$, which is still a significant slope angle in the oceanic regime, β is reduced to $\beta = 0.06$ and spindown dominates over buoyancy shutdown. Physical parameters are applied to examine the range in β values over the continental shelf and slope, under the assumption that $\sigma = 1$ and $f = 10^{-4}$ s^{-1}. The Ekman number is assumed to equal $E = 0.01$, which corresponds to an Ekman depth of $\delta_e = 10$ m over a depth of 100 m. Then, for a range of slope angles $\theta = 0.0001 - 0.001$ over the continental shelf and $\theta = 0.005 - 0.01$ for the upper continental slope near the Middle Atlantic Bight shelfbreak front, with a range of stratifications $N^2 = 10^{-5} - 10^{-4}$ s^{-2} (Linder and Gawarkiewicz 1998), the range of slope Burger numbers is $S = 10^{-5} - 10^{-2}$ over the continental shelf and $S = 0.03 - 1$ over the continental slope. This parameter space corresponds to $\beta = 10^{-9} - 10^{-3}$ over the continental shelf and $\beta = 0.01 - 10$ over the continental slope. This range of values suggests that buoyancy shutdown of Ekman pumping and suction may occur to a greater extent over the continental slope than over the continental shelf.

Although β measures the importance of buoyancy shutdown to the initial adjustment of the along-isobath flow, the long-term behavior of the flow is dependent on the spatial structure of mixing. For constant mixing coefficients, the buoyancy anomaly

that leads to shutdown of the Ekman transport diffuses away from the boundary and enables spindown to progress. If the interior mixing is weak, the buoyancy anomaly remains confined adjacent to the boundary and further limits the spindown of the along-isobath flow. This behavior is consistent with Chapman's analytical model (2002a), in which a geostrophic along-isobath flow over a stratified slope approaches a nonzero steady-state. In his model, the buoyancy anomaly is confined to a bottom mixed layer, which is analogous to our thermal boundary layer except that the thickness of the bottom mixed layer is evaluated by a bulk mixed layer model forced by the cross-isobath Ekman flow rather than a diffusion equation forced by a diffusive Ekman buoyancy flux.

The use of constant mixing coefficients also does not capture the observed asymmetry in the thickness of the buoyancy boundary layers for upwelling and downwelling Ekman flows that has been examined in 1d models (Weatherly and Martin 1978, Trowbridge and Lentz 1991, MacCready and Rhines 1993). Although this asymmetry is shown to arise with state-dependent mixing schemes for 1d upwelling and downwelling flows, the important question to address in future studies is how the cross-isobath structure of the Ekman flow is modified by mixing during the buoyancy shutdown process. If the state-dependent mixing schemes modify convergences and divergences in the Ekman transport, then the frictionally driven vertical circulations can modify the dynamics away from the bottom boundary layer. This subject requires further investigation.

2.8 Conclusions

The time-dependent adjustment of a stratified along-isobath flow with and without lateral shear is examined on an insulated sloping boundary in a model with constant viscosity and diffusivity. This adjustment process has two components. First, the adjustment of the stratification tilts the isopycnals and induces an upslope Ekman transport that arises on a buoyancy generation timescale. The buoyancy field dif-

fusively grows away from the boundary in time and the upslope Ekman transport approaches the steady-state solution of Thorpe (1987).

Second, buoyancy shutdown of the Ekman transport is shown to oppose the spindown of a laterally sheared along-isobath flow. For order one Prandtl numbers, buoyancy shutdown occurs due to cross-isobath Ekman advection of buoyancy that drives an Ekman buoyancy flux into a thicker thermal boundary layer. In this thermal boundary layer, the tilting of isopycnals reduces the geostrophic flow and hence the Ekman transport. The ratio of the spindown to buoyancy shutdown timescales, β, is the key parameter that measures the importance of buoyancy shutdown to the decaying Ekman pumping and suction. In contrast to previous works, an explicit solution to Ekman pumping for $\beta \leq 1$ is constructed and its suppression by buoyancy shutdown is shown.

Finally, the modification of potential vorticity by mixing processes at the stratified sloping boundary is examined. The adjustment of the stratification by diffusion yields an outward PV flux that reduces the area-integrated PV. The adjustment of the along-isobath flow induces an outward (inward) PV flux for downwelling (upwelling) Ekman flows that reduces (increases) the area-integrated PV. The relative contributions of these processes to the total change in the area-integrated PV depends on the ratio of the Ekman transport scalings, $M_{initial}/M_{Thorpe}$. For laterally sheared flows, β also determines the magnitude and temporal evolution in the change of the area-integrated PV, in which PV extraction dominates over PV input for long times. For the total change in the area-integrated PV, the linear Ekman components cancel and the main contribution to the change in PV is due to the diabatic PV flux, which is larger than the frictional PV flux by order σS. The time evolution of the area-integrated PV is explicitly dependent on the magnitude of the buoyancy anomaly in the thermal boundary layer as well as the position of the isopycnals at the boundary. An increase in the slope angle, stratification or viscosity for fixed Prandtl number leads to a larger input or extraction of PV from the system. Thus, mixing over stratified sloping boundaries provides a mechansim by which the PV structure

of the large scale ocean circulation may be modified aside from wind and buoyancy forcing at the surface. For example, flows over the upper continental slope (such as western boundary currents), along the Mid-Atlantic Ridge and over other topographic features are potentially subject to the input and extraction of PV through coupling between the Ekman flow and the buoyancy field. The method in which the boundary modified PV is redistributed, for example, by eddies, and the relative roles of atmospheric and topographic forcing in setting the distribution of PV in the ocean remains to be explored.

Chapter 3

Nonlinear spindown

Abstract

The nonlinear stratified spindown of an along-isobath flow over an insulated sloping boundary gives rise to asymmetry in Ekman pumping and suction. During spindown, Ekman pumping is suppressed to a greater extent than Ekman suction primarily due to nonlinear advection of buoyancy. This asymmetry contrasts with previous studies of nonlinear homogeneous spindown over a flat bottom, in which Ekman pumping is weaker than Ekman suction due to advection of momentum. The asymmetry in Ekman pumping and suction is compared among homogeneous spindown over a flat bottom, stratified spindown over a flat bottom, and stratified spindown over a sloping bottom for increasing Rossby number. Time-dependent feedback between the secondary circulation driven by nonlinear Ekman pumping and suction and the geostrophic flow leads to asymmetry in cyclonic and anticyclonic vorticity. For homogeneous spindown over a flat bottom, a closed-form solution for the vertical velocity and the vertical vorticity field is presented to order Rossby number. This correction shows that the asymmetry in Ekman pumping and suction is due to advection of momentum in the Ekman layer and in the interior. Cyclonic vorticity decays faster than anticyclonic vorticity due to lateral advection of momentum in the interior. For stratified spindown over a slope, an analytical scaling for the nonlinear correction to Ekman pumping and suction is determined for order one Prandtl numbers and small slope Burger numbers. When this nonlinear correction is larger than order Rossby number, anticyclonic vorticity decays faster than cyclonic vorticity in the interior. Numerical simulations are used to examine the asymmetry in Ekman pumping and suction as well as cyclonic and anticyclonic vorticity for flows applicable to the continental slope.

3.1 Introduction

The adjustment of a geostrophically balanced flow over a boundary produces frictionally driven circulations, in which convergences in the Ekman transport eject fluid out of the boundary layer (Ekman pumping) and divergences in the Ekman transport inject fluid into the boundary layer (Ekman suction). The magnitude and lateral structure of Ekman pumping and suction determines the strength and structure of interior secondary circulations that spindown the geostrophic flow. In the linear Ekman balance, the vertical velocity at the top of the frictional boundary layer is dependent on the vertical component of the geostrophic relative vorticity, ζ (Charney and Eliassen 1949). Then, Ekman pumping is symmetric to Ekman suction for a change in the sign of the vertical relative vorticity. The purpose of this chapter is to examine how nonlinearity breaks this symmetry between Ekman pumping and suction and modifies the geostrophic vertical vorticity field during spindown.

Previous studies have shown that Ekman advection of momentum in a homogeneous fluid over a flat bottom weakens Ekman pumping for cyclonic flows, $\zeta > 0$, and strengthens Ekman suction for anticyclonic flows, $\zeta < 0$, at order Rossby number, $\epsilon = U/fL$, where U is the characteristic flow speed, f is the planetary vorticity, and L is the characteristic lateral length scale. For flows with lateral shear that is temporally and spatially constant, Benton *et al.* (1964) identified that the vertical velocity was stronger for anticyclonic flows than cyclonic flows at order Rossby number. For steady flows, Hart (2000) analytically solved for higher order corrections to nonlinear Ekman pumping for general shear lines and circular vortices. The order Rossby number reduction in Ekman pumping and enhancement in Ekman suction is due to horizontal Ekman advection of momentum (Hart 2000). Further examination of the steady Ekman boundary layer structure reveals that the Ekman layer thickness is modified from its linear value, $\delta_e = \sqrt{2\nu/f}$, by momentum advection (Brink 1997, Pedlosky 2008), where ν is the viscosity. For general shear lines, a formal perturbation expansion reveals that vertical advection of momentum causes the Ekman layer

to thicken in cyclonic regions and to thin in anticyclonic regions (Pedlosky 2008). With the nonlinear Ekman layer thickness, the nonlinear correction to Ekman pumping remains unchanged from Hart's formula (2000). These studies detail the relative roles of horizontal and vertical advection of momentum in the nonlinear modification of the Ekman layer thickness and Ekman pumping. However, the feedback between nonlinear Ekman pumping and the interior vertical vorticity field is a fundamental aspect of the time-dependent spindown problem.

The nonlinear spindown of a homogeneous, geostrophic flow is subject to nonlinear Ekman pumping as well as horizontal advection of momentum in the interior. For spatially uniform vertical vorticity, squashing and stretching of vertical relative vorticity by the leading order Ekman pumping and suction dominates over squashing and stretching of planetary vorticity by the order Rossby number Ekman pumping and suction (Hart 1995). Hence, spatially uniform cyclones spin down faster than anticyclones, even though Ekman pumping is weaker than Ekman suction (Hart 1995). Zavala Sansón and van Heijst (2000) compared the homogeneous spindown of cyclonic vortices in a laboratory experiment with a model, in which momentum advection in the interior was included but the nonlinear correction to Ekman pumping was neglected. They justified neglecting the nonlinear correction to Ekman pumping due to good agreement between the laboratory and numerical model for the temporal decay of vertical vorticity. Numerical simulations for the spindown of axisymmetric vortices subject to linear Ekman pumping and suction showed a faster decay in cyclonic vortices than anticyclonic vortices. This behavior is consistent with the hypothesis that horizontal advection of momentum in the interior dominates over the effects of nonlinear Ekman pumping and suction (Zavala Sansón 2001). In order to synthesize these results with analyses of the steady nonlinear Ekman balance, the relative roles of nonlinear Ekman pumping and horizontal advection of momentum in the interior is investigated during the spindown of a general, uni-directional flow that is horizontally bounded or periodic. Horizontal advection of momentum in the interior is shown to control the asymmetric spindown of cyclonic and anticyclonic vorticity and, in doing

so, enhances the asymmetry in Ekman pumping and suction from the magnitude predicted by Hart's formula.

The second focus of this paper is to show how nonlinear advection of buoyancy can modify the asymmetry in Ekman pumping and suction as well as anticyclonic and cyclonic vorticity during stratified spindown over a sloping bottom. In a stratified fluid, the geostrophic flow spins down by a secondary circulation over a Prandtl depth, $H_P = fL/N$, in a spindown time, $T_{spindown} = E^{-1/2} f^{-1}$. The Ekman number, $E = (\delta_e/H_P)^2$, is assumed small. On a stratified sloping bottom, Ekman pumping couples with the buoyancy field. The geostrophic along-isobath flow induces a cross-isobath Ekman flow that advects the buoyancy field. For an insulated boundary, this cross-isobath Ekman advection of buoyancy balances a vertical buoyancy flux into a thicker, diffusively growing boundary layer. This buoyancy flux tilts the isopycnals within the layer, thereby reducing the geostrophic flow near the bottom as well as the Ekman transport. This process, known as buoyancy shutdown of the Ekman transport (MacCready and Rhines 1991), occurs in a time $T_{shutdown} = \sigma^{-1} S^{-2} f^{-1}$, where the Prandtl number, $\sigma = \nu/\kappa$, is assumed order one, the slope Burger number, $S = (N \tan\theta/f)^2$, is assumed small, κ is the diffusivity, N is the buoyancy frequency, and θ is the slope angle.

As shown in Chapter 2, buoyancy shutdown equally reduces Ekman pumping and suction during the linear adjustment of a laterally sheared along-isobath flow over a stratified sloping bottom, where viscosity and diffusity are assumed constant. The extent to which buoyancy shutdown reduces Ekman pumping during spindown is given by the parameter $\beta \equiv T_{spindown}/T_{shutdown}$. The analysis in Chapter 2 is used to determine the correction to Ekman pumping and suction by buoyancy shutdown. This chapter shows that Ekman pumping becomes further suppressed over Ekman suction for increasing nonlinearity. However, the asymmetry in Ekman pumping and suction is predominantly due to nonlinear advection of buoyancy rather than momentum advection. The scaling for the nonlinear correction to Ekman pumping is shown to be greater than order Rossby number when β is order one. This scaling has consequences

for the time evolution of the vertical vorticity field. In this case, interior advection of momentum is shown to not necessarily have primary importance to the asymmetric decay of cyclonic and anticyclonic vorticity. Instead, nonlinear advection of buoyancy can cause anticyclones to spindown faster than cyclones outside the boundary layers. Numerical experiments are performed to examine the extent to which the analytical solutions are valid for idealized flows applicable to continental slopes.

The spindown problem is formulated in section 3.2. In section 3.3, homogeneous spindown on a flat bottom to order Rossby number is examined. In section 3.4, the effect of stratification on nonlinear spindown on a flat bottom is discussed to order Rossby number. In section 3.5, the leading order nonlinear correction to stratified spindown on a sloping bottom is solved for a flow with sinusoidal lateral shear. In section 3.6, the analytical solutions for Ekman pumping and suction as well as cyclonic and anticyclonic vorticity are compared with the flow fields in the numerical simulations. The results are discussed and summarized in section 3.7.

3.2 Basic equations

The equations for an incompressible, Boussinesq fluid rotating about the vertical axis at an angular velocity $f/2$ are

$$\frac{\partial \boldsymbol{u}}{\partial t} + \boldsymbol{u}\cdot\nabla\boldsymbol{u} + f\hat{k}\times\boldsymbol{u} = -\frac{1}{\rho_o}\nabla P - \frac{g\rho}{\rho_o} + \nu\nabla^2\boldsymbol{u}, \tag{3.1}$$

$$\nabla\cdot\boldsymbol{u} = 0, \tag{3.2}$$

$$\frac{\partial \rho}{\partial t} + \boldsymbol{u}\cdot\nabla\rho = \kappa\nabla^2\rho, \tag{3.3}$$

where $\boldsymbol{u}$ is the velocity field, P is the pressure field, ρ is the density field, g is the acceleration of gravity, and $\hat{k}$ is the vertical unit vector. The density field is defined as $\rho = \rho_o + \rho_b(z) - \frac{\rho_o}{g}b$, where ρ_o is a constant reference value of density, $N^2 = -\frac{\rho_o}{g}\frac{d\rho_b}{dz}$, and b is the buoyancy anomaly. In the homogeneous spindown problem, ρ_b and b are zero. The pressure field is assumed hydrostatically balanced and is defined as

$P = P_b + p$, where P_b satisfies $\frac{dP_b}{dz} = -g(\rho_o + \rho_b)$, and p is the dynamical component of the total pressure. The viscosity, ν, and the diffusivity, κ, are assumed constant. The flow is assumed to have no spatial variations in the x-direction. The fluid is unbounded in the y-direction. This set of equations is solved for the leading order nonlinear correction during homogenous spindown over a flat bottom, in section 3.3 and stratified spindown over a sloping boundary in section 3.5.

3.3 Nonlinear homogeneous spindown on a flat bottom

The spindown of a barotropic, laterally sheared geostrophic flow is examined to order Rossby number in a homogeneous fluid of constant depth, H. In order to filter inertial oscillations, the assumption $\epsilon > E^{1/2}$, where $E = (\delta_e/H)^2 \ll 1$, is made. The aspect ratio, $\Gamma = H/L$, is assumed sufficiently small so that the flow is hydrostatic. Within the Ekman layer, vertical variations in the pressure field are negligible. The upper boundary is assumed rigid, where the Froude number, $F = U/\sqrt{gH}$, satisfies $F < \epsilon E^{1/4}$. The flow is subject to the following no-slip and no normal flow boundary conditions:

$$u = v = 0 \quad \text{at} \quad z = 0, \tag{3.4}$$

$$w = 0 \quad \text{at} \quad z = 0 \text{ and } H, \tag{3.5}$$

The initial geostrophic flow is assumed either horizontally bounded such that $|\boldsymbol{u}| \to 0$ as $y \to \pm\infty$ or periodic with zero spatial average.

The flow, $\boldsymbol{u}$, is decomposed into a frictionless interior region and an Ekman layer, with subscripts i and e denoting the respective domains. Time is nondimensionalized by the homogeneous spindown timescale as $t' = t/\mathcal{T}_{spindown}$ and $\mathcal{T}_{spindown} = E^{-1/2}f^{-1}$. Then, with primes denoting nondimensional quantities, the variables are nondimensionalized in the interior and Ekman boundary layers by the following set of scalings:

$$
\begin{aligned}
u_i &= U\ u_i', & u_e &= U\ u_e',\\
v_i &= UE^{1/2}\ v_i', & v_e &= Uv_e',\\
w_i &= UE^{1/2}\Gamma w_i', & w_e &= UE^{1/2}\Gamma w_e',\\
p_i &= \rho_o f U L p_i'.
\end{aligned}
$$

The vertical coordinate is nondimensionalized in the Ekman boundary layer as $\eta' = z/\delta_e$. The interior equations to order Rossby number, primes dropped, become

$$
\begin{aligned}
\frac{\partial u_i}{\partial t} + \epsilon v_i \frac{\partial u_i}{\partial y} - v_i &= 0, && (3.6)\\
u_i &= -\frac{\partial p_i}{\partial y}, && (3.7)\\
\frac{\partial v_i}{\partial y} + \frac{\partial w_i}{\partial z} &= 0. && (3.8)
\end{aligned}
$$

The Ekman layer equations to order Rossby number, where slow variations in the Ekman layer thickness are not explicitly expressed, become

$$
\begin{aligned}
\epsilon v_e\left(\frac{\partial u_e}{\partial y} + \frac{\partial u_i}{\partial y}\right) + \epsilon(w_e + w_i(z=0))\frac{\partial u_e}{\partial \eta} - v_e &= \frac{1}{2}\frac{\partial^2 u_e}{\partial \eta^2} && (3.9)\\
\epsilon v_e \frac{\partial v_e}{\partial y} + \epsilon(w_e + w_i(z=0))\frac{\partial v_e}{\partial \eta} + u_e &= \frac{1}{2}\frac{\partial^2 v_e}{\partial \eta^2}, && (3.10)\\
\frac{\partial v_e}{\partial y} + \frac{\partial w_e}{\partial \eta} &= 0. && (3.11)
\end{aligned}
$$

The interior vertical velocity is evaluated at $z = 0$ because vertical variations of the interior flow within the Ekman layer are $O(E^{1/2})$. The nondimensional boundary conditions to order Rossby number become

$$
\begin{aligned}
u_i + u_e(\eta = 0) &= 0, && (3.12)\\
v_e(\eta = 0) &= 0, && (3.13)\\
w_i(z=0) + w_e(\eta = 0) &= 0, && (3.14)\\
w_i(z=1) &= 0, && (3.15)\\
u_e, v_e, w_e \to 0 \quad &\text{as} \quad \eta \to \infty. && (3.16)
\end{aligned}
$$

The flow variables are expanded in terms of the Rossby number as $\boldsymbol{u} = \boldsymbol{u}^{(0)} + \epsilon\ \boldsymbol{u}^{(1)}$. The Ekman pumping solution to $O(\epsilon)$ for time-independent flows (Hart 2000, Pedlosky 2008) is modified to include time-dependent feedback with the $O(\epsilon)$ geostrophic flow, where

$$w_i(z=0) = -\frac{1}{2}\frac{\partial u_i^{(0)}}{\partial y} - \frac{7}{40}\epsilon\left(u_i^{(0)}\frac{\partial^2 u_i^{(0)}}{\partial y^2} + (\frac{\partial u_i^{(0)}}{\partial y})^2\right) - \frac{1}{2}\epsilon\frac{\partial u_i^{(1)}}{\partial y}. \tag{3.17}$$

This expression for Ekman pumping includes the first term, which is symmetric for a change in sign of the vertical relative vorticity, the second term, which is Hart's nonlinear correction (2000) to Ekman pumping due to Ekman advection of momentum, and the third term, which represents feedback with the time-dependent $O(\epsilon)$ interior vorticity field.

At leading order, the geostrophic flow spins down by the $O(1)$ secondary circulation, where

$$\frac{\partial u_i^{(0)}}{\partial t} - v_i^{(0)} = 0. \tag{3.18}$$

The solution to the flow is determined by vertically integrating the interior continuity equation and applying the Ekman pumping condition. The resulting expression

$$-\frac{\partial v_i^{(0)}}{\partial y} = -\frac{1}{2}\frac{\partial u_i^{(0)}}{\partial y} \tag{3.19}$$

is integrated horizontally from y_0 to y, under the constraint that $u(y_0) = v(y_0) = 0$. This constraint is applicable for flows that are horizontally bounded, in which $|\boldsymbol{u}| \to 0$ as $y \to \pm\infty$, or periodic with zero horizontal average. Then, the secondary circulation is given by

$$v_i^{(0)} = -\frac{1}{2}u_i^{(0)}, \tag{3.20}$$

$$w_i^{(0)} = -\frac{1}{2}\frac{\partial u_i^{(0)}}{\partial y}(1-z), \tag{3.21}$$

which is nonzero at initial time due to its spinup on the inertial timescale. By integrating (3.18) in time, the leading order geostrophic flow decays as

$$u_i^{(0)} = u_i^{(0)}(t=0,y)\mathrm{e}^{-t/2}. \tag{3.22}$$

Next, the $O(\epsilon)$ interior flow is solved to show that lateral advection of momentum in the interior causes cyclones to spindown faster than anticyclones and enhances the asymmetry in Ekman pumping and suction from Hart's nonlinear correction (2000). The $O(\epsilon)$ equations for the interior flow field are

$$\begin{aligned} \frac{\partial u_i^{(1)}}{\partial t} + v_i^{(0)}\frac{\partial u_i^{(0)}}{\partial y} - v_i^{(1)} &= 0, & (3.23)\\ \frac{\partial v_i^{(1)}}{\partial y} + \frac{\partial w_i^{(1)}}{\partial z} &= 0. & (3.24) \end{aligned}$$

The continuity equation, (3.24), is integrated vertically, subject to the Ekman pumping condition, (3.17), and then integrated horizontally from y_0 to y under the assumption $u_i^{(0)}(y_0) = v_i^{(0)}(y_0) = 0$. The resulting secondary circulation is given by

$$\begin{aligned} v_i^{(1)} &= -\frac{7}{40}u_i^{(0)}\frac{\partial u_i^{(0)}}{\partial y} - \frac{1}{2}u_i^{(1)}, & (3.25)\\ w_i^{(1)} &= \left\{ -\frac{7}{40}\left(u_i^{(0)}\frac{\partial^2 u_i^{(0)}}{\partial y^2} + (\frac{\partial u_i^{(0)}}{\partial y})^2 \right) - \frac{1}{2}\frac{\partial u_i^{(1)}}{\partial y} \right\}(1-z). & (3.26) \end{aligned}$$

The equation for the $O(\epsilon)$ geostrophic flow becomes

$$\frac{\partial u_i^{(1)}}{\partial t} + \frac{1}{2}u_i^{(1)} = -\frac{7}{40}u_i^{(0)}\frac{\partial u_i^{(0)}}{\partial y} + \frac{1}{2}u_i^{(0)}\frac{\partial u_i^{(0)}}{\partial y}. \tag{3.27}$$

The interior geostrophic flow is forced by two opposing components from the $O(1)$ flow. The first term on the right side of (3.27) is from Hart's nonlinear Ekman pumping formula (2000), and the second term is from lateral advection of the interior geostrophic flow. Lateral advection of momentum in the interior not only dominates the forcing of the $O(\epsilon)$ interior geostrophic flow but is opposite in sign to the contribu-

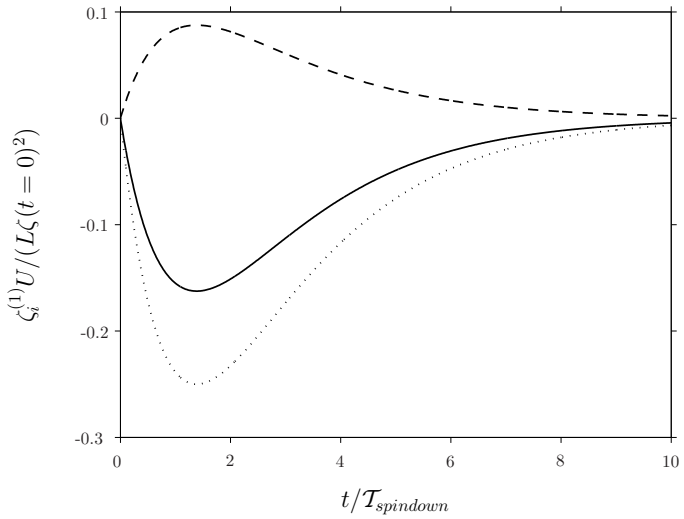

Figure 3-1: The $O(\epsilon)$ vertical relative vorticity, which is scaled with the square of the initial relative vertical vorticity, is shown on the cyclonic and anticyclonic axis. The total correction (solid line) has contributions from lateral advection of momentum in the interior (dotted line), which leads to stretching and squashing of vertical relative vorticity, as well as feedback with the $O(\epsilon)$ Ekman pumping, which includes modification by Ekman advection of momentum (dashed line).

tion from Hart's (2000) nonlinear Ekman pumping formula. Thus, Hart's nonlinear Ekman pumping (2000) alone predicts a change to the $O(\epsilon)$ geostrophic flow that is of the opposite sign than if lateral advection of the geostrophic flow is taken into account. Furthermore, forcing by only the lateral advection of the geostrophic flow overestimates the change to the $O(\epsilon)$ flow. As the $O(1)$ forcing decays in time, the feedback term, which is the second term on the left side of (3.27), dominates and spins down the $O(\epsilon)$ geostrophic flow.

The nonlinear modification of the geostrophic flow field can also be represented in terms of vertical relative vorticity, $\zeta_i = -\frac{\partial u_i}{\partial y}$. From (3.23), the $O(\epsilon)$ vertical relative vorticity evolves as

$$\frac{\partial \zeta_i^{(1)}}{\partial t} + v_i^{(0)} \frac{\partial \zeta_i^{(0)}}{\partial y} = \frac{\partial w_i^{(1)}}{\partial z} + \zeta_i^{(0)} \frac{\partial w_i^{(0)}}{\partial z}. \tag{3.28}$$

Lateral advection of momentum contributes to both lateral advection as well as stretching and squashing of vertical relative vorticity. The $O(\epsilon)$ Ekman pumping and

suction modifies stretching and squashing of planetary vorticity. Figure 3-1 compares the contributions to $\zeta_i^{(1)}$ from right side of (3.28) on the cyclonic and anticyclonic axis, where $\frac{\partial \zeta_i}{\partial y} = 0$. In terms of vorticity, stretching and squashing of vertical relative vorticity dominates over stretching and squashing of planetary vorticity, which is of opposite sign. Thus, stretching and squashing of vertical relative vorticity, *i.e.* lateral advection of momentum in the interior, causes cyclones to spindown faster than anticyclones. Nonlinear Ekman pumping at $O(\epsilon)$ tends to reduce this effect.

The solution to the $O(\epsilon)$ geostrophic flow and the vertical relative vorticity is

$$u_i^{(1)} = \frac{13}{80}\mathrm{e}^{-t/2}\frac{\partial}{\partial y}\int_0^t \mathrm{e}^{\tau/2}(u_i^{(0)})^2 d\tau, \tag{3.29}$$

$$\zeta_i^{(1)} = \frac{13}{40}\mathrm{e}^{-t/2}\int_0^t \mathrm{e}^{\tau/2}\left(u_i^{(0)}\frac{\partial \zeta_i^{(0)}}{\partial y} - (\zeta_i^{(0)})^2\right) d\tau. \tag{3.30}$$

The nonlinear correction to the vertical relative vorticity shows that the total vertical relative vorticity is weakened on the cyclonic axis, where $\zeta_i^{(0)} > 0$ and $\frac{\partial \zeta_i^{(0)}}{\partial y} = 0$, and strengthened on the anticyclonic axis, where $\zeta_i^{(0)} < 0$ and $\frac{\partial \zeta_i^{(0)}}{\partial y} = 0$, due to lateral advection of the interior geostrophic flow.

During spindown, the asymmetry in cyclonic vorticity, ζ_c, and anticyclonic vorticity, ζ_a, is measured by the ratio ζ_c/ζ_a. Consider the spindown of a cyclone and an anticyclone, where $\zeta_c(t=0) = -\zeta_a(t=0)$, of initial magnitude $|\zeta(t=0)|$. On the cyclonic and anticyclonic axis of the flow, the ratio of cyclonic to anticyclonic vorticity evolves as

$$\left|\frac{\zeta_c}{\zeta_a}\right| = \frac{1-\epsilon F_1(t)}{1+\epsilon F_1(t)}, \text{ where} \tag{3.31}$$

$$F_1(t) = \frac{13}{20}|\zeta(t=0)|(1-\mathrm{e}^{-t/2}).$$

At initial time, $F_1(t=0) = 0$, but in the limit $t \to \infty$, $F_1 \to (13/20)|\zeta(t=0)|$. Thus, the asymmetry in cyclonic and anticyclonic vorticity increases with time and increasing Rossby number.

Next, the complete solution to the time-dependent $O(\epsilon)$ correction to the Ekman

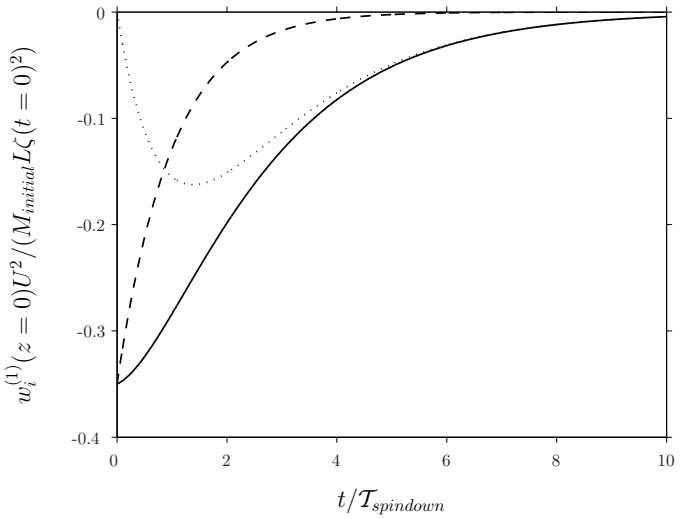

Figure 3-2: The $O(\epsilon)$ Ekman pumping, which is scaled with the square of the initial relative vertical vorticity, is shown on the cyclonic or anticyclonic axis. The total correction (solid line) has contributions from Hart's (2000) formula (dashed line) as well as feedback with the interior geostrophic flow, which is predominantly modified by lateral advection of the momentum (dotted line).

pumping solution is

$$\begin{aligned} w_i^{(1)}(z=0) &= \frac{7}{40}\left(u_i^{(0)}\frac{\partial \zeta_i^{(0)}}{\partial y} - (\zeta_i^{(0)})^2\right) \\ &+ \frac{13}{80}\mathrm{e}^{-t/2}\int_0^t \mathrm{e}^{\tau/2}\left(u_i^{(0)}\frac{\partial \zeta_i^{(0)}}{\partial y} - (\zeta_i^{(0)})^2\right)d\tau. \end{aligned} \tag{3.32}$$

On the cyclonic and anticyclonic axis, where $\frac{\partial \zeta_i^{(0)}}{\partial y} = 0$, Ekman pumping becomes

$$w_i^{(1)}(z=0) = -\frac{7}{40}(\zeta_i^{(0)})^2 - \frac{13}{40}\mathrm{e}^{-t/2}\int_0^t \mathrm{e}^{\tau/2}(\zeta_i^{(0)})^2 d\tau, \tag{3.33}$$

which is negative for all time. Thus, Ekman suction on the anticyclonic axis strengthens and Ekman pumping on the cyclonic axis weakens at $O(\epsilon)$. The first term in the nonlinear correction, (3.33), is Hart's (2000) nonlinear Ekman pumping, which is nonzero at initial time. As shown in figure 3-2, the second term in (3.33) provides a significant contribution to the asymmetry in Ekman pumping and suction due to feedback with the interior vorticity field. This time-dependent contribution is neces-

sary for an accurate calculation of the $O(\epsilon)$ Ekman pumping and suction.

The asymmetry in Ekman pumping, w_p, and Ekman suction, w_s, is measured by the ratio w_p/w_s. Consider the time evolution of Ekman pumping and suction for cyclonic and anticyclonic vorticity, where $\zeta_c(t=0) = -\zeta_a(t=0)$ and $w_p(t=0) = -w_s(t=0)$, for vertical relative vorticity of initial magnitude $|\zeta(t=0)|$. On the cyclonic and anticyclonic axis of the flow, the ratio of Ekman pumping to Ekman suction evolves as

$$\begin{aligned} \left|\frac{w_p}{w_s}\right| &= \frac{1-\epsilon F_2(t)}{1+\epsilon F_2(t)}, \text{ where} \\ F_2(t) &= \frac{13}{20}|\zeta(t=0)|\big(1-\frac{6}{13}\mathrm{e}^{-t/2}\big). \end{aligned} \tag{3.34}$$

At initial time, $F_2(t=0) = (7/20)|\zeta(t=0)|$, but in the limit $t \to \infty$, $F_2 \to (13/20)|\zeta(t=0)|$. Within an inertial period, lateral Ekman advection of momentum leads to asymmetry in Ekman pumping and suction. With time, this asymmetry increases by advection of momentum in the Ekman layer and the interior.

Figure 3-3 summarizes the roles of advection of momentum in the Ekman layer and the interior domain in setting the asymmetry in Ekman pumping and suction and the asymmetric decay of cyclonic and anticyclonic vorticity. The temporal and spatial structure of Ekman pumping is further examined in section 3.5, in which the nonlinear correction to homogeneous spindown over a flat bottom is contrasted with the nonlinear correction to stratified spindown over a sloping bottom.

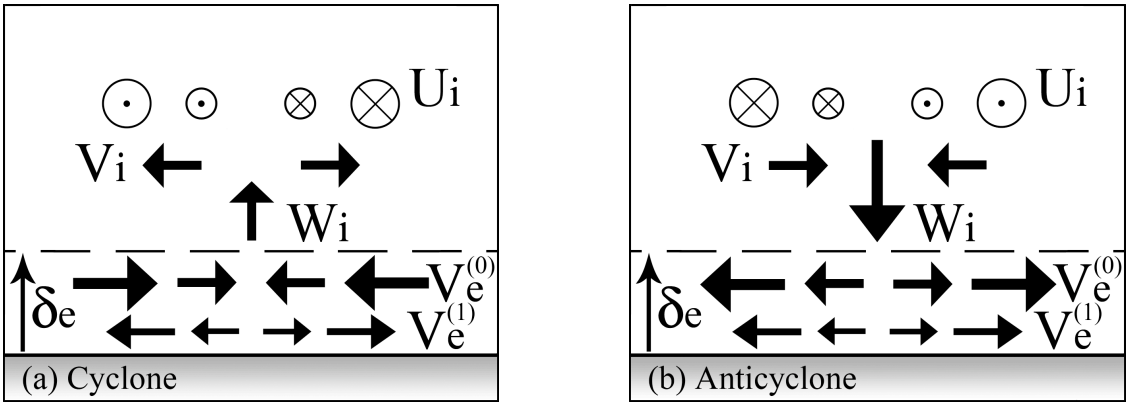

Figure 3-3: (a) Cyclone. A geostrophic flow, U_i, induces an Ekman flow, $V_e^{(0)}$, that is directed laterally toward the cyclonic axis. Ekman advection of momentum contributes to an Ekman flow, $V_e^{(1)}$, that is directed laterally outward. This nonlinear correction weakens Ekman pumping, W_i, from its zeroth-order approximation. Ekman pumping drives an interior lateral circulation, V_i, that spins down the geostrophic flow. This secondary circulation also advects lower momentum fluid outward, which causes the cyclone to spindown faster.

(b) Anticyclone. A geostrophic flow, U_i, induces an Ekman flow, $V_e^{(0)}$, that is directed laterally outwards from the anticyclonic axis. Ekman advection of momentum contributes to an Ekman flow, $V_e^{(1)}$, that is also directed laterally outward. This nonlinear correction strengthens Ekman suction, W_i, from its zeroth-order approximation. Ekman suction drives an interior lateral circulation, V_i, that spins down the geostrophic flow. This secondary circulation also advects higher momentum fluid inward, which causes the anticyclone to spindown slower.

3.4 Nonlinear stratified spindown on a flat bottom

As discussed in Chapter 2, stratification modifies linear spindown over a flat, insulated bottom in two ways. First, a thermal boundary layer grows adjacent to the bottom, weakening the stratification in time. The laterally uniform buoyancy anomaly in this layer does not modify Ekman pumping and suction. Second, the secondary circulation driven by Ekman pumping and suction vertically advects the density field and tilts the isopycnals in the interior. By thermal wind balance, the geostrophic flow develops vertical shear during spindown. For increasing Ekman number or Rossby number, coupling between the frictionally driven secondary circulation and the buoyancy field modifies Ekman pumping and suction. Appendix A.1 summarizes the corrections to $O(\epsilon)$ for an initially barotropic, geostrophic flow with sinusoidal variations. With stratification, the main differences from nonlinear homogeneous spindown are described as follows.

For increasing Ekman number, vertical advection of the laterally uniform buoyancy anomaly in the thermal boundary layer causes Ekman pumping and suction to strengthen at $O(\sigma^{-1/2}E^{1/4})$. Ekman pumping acting on this buoyancy anomaly further weakens the stratification, whereas Ekman suction tends to increase it. The induced horizontal pressure gradient causes slower decay of the geostrophic flow overlying the Ekman layer. This horizontal pressure gradient leads to additional Ekman transport towards the cyclonic axis and away from the anticyclonic axis. Thus, both Ekman pumping and suction strengthen from the leading order approximation. Consequently, the stronger interior secondary circulation spins down both interior cyclonic and anticyclonic vorticity faster. However, the total geostrophic flow overlying the Ekman layer spins down slower than in the leading order approximation. When $\epsilon < \sigma^{-1/2}E^{1/4}$ is assumed, as in Chapter 2, this correction to Ekman pumping and suction is larger than $O(\epsilon)$.

For increasing Rossby number, buoyancy effects modify asymmetry in Ekman pumping and suction as well as spindown of cyclonic and anticyclonic vorticity. As

in homogeneous spindown, Ekman advection of momentum at $O(\epsilon)$ weakens Ekman pumping and strengthens Ekman suction. However, for a geostrophic flow with sinusoidal shear, Appendix A.1 shows that this asymmetry is modified by three other nonlinear corrections. Lateral Ekman advection of the interior buoyancy anomaly balances diffusion and leads to a buoyancy flux into the thicker thermal boundary layer. This process modifies the lateral pressure gradient and enhances the asymmetry in Ekman pumping and suction. In contrast, lateral Ekman advection and vertical advection of the buoyancy anomaly associated with the $O(\sigma^{-1/2}E^{1/4})$ correction to Ekman pumping reduce the asymmetry in Ekman pumping and suction. Numerical simulations are later presented to examine whether the net effect of these buoyancy effects is to enhance or reduce the asymmetry in Ekman pumping and suction.

In the interior, cyclonic vorticity decays faster than anticyclonic vorticity for increasing Rossby number. As in homogeneous spindown, lateral advection of momentum in the interior contributes to this asymmetry. However, since the geostrophic flow is vertically sheared during stratified spindown, vertical advection of momentum in the interior also contributes to this asymmetry. In regions of cyclonic vorticity, vertical advection brings lower momentum fluid upward and tends to enhance spindown of the cyclone. In contrast, in regions of anticyclonic vorticity, vertical advection brings higher momentum fluid downward and tends to slow spindown of the anticyclone. The interior vertical relative vorticity equation, nondimensionalized by the scalings for the interior flow in Chapter 2, is

$$\frac{\partial \zeta_i}{\partial t} + \epsilon \boldsymbol{u}_i \cdot \nabla \zeta_i = \frac{\partial w_i}{\partial z}(1 + \epsilon \zeta_i) + \epsilon \frac{\partial w_i}{\partial y}\frac{\partial u_i}{\partial z}. \tag{3.35}$$

Lateral advection of momentum contributes to the lateral advection and stretching of vertical relative vorticity. Vertical advection of momentum contributes to the vertical advection of vertical relative vorticity and tilting of horizontal relative vorticity in the x-direction. On the cyclonic or anticyclonic axis, the interior vertical vorticity

equation to $O(\epsilon)$ becomes

$$\frac{\partial \zeta_i}{\partial t} = \frac{\partial w_i}{\partial z}(1 + \epsilon\zeta_i) - \epsilon w_i \frac{\partial \zeta_i}{\partial z}. \tag{3.36}$$

Thus, during stratified spindown on a flat bottom, cyclones decay faster than anticyclones due to stretching and squashing of vertical relative vorticity as well as vertical advection of vertical relative vorticity. This asymmetry in spindown is further examined with numerical simulations in section 3.6.

3.5 Nonlinear stratified spindown on a sloping bottom

On a stratified sloping bottom, the Ekman flow couples with the buoyancy field. Chapter 2 examines how this coupling suppresses Ekman pumping and suction as well as the spindown of the geostrophic flow in the linear regime. In this section, the linear analysis is extended into the nonlinear regime. During both homogeneous and stratified spindown over a flat bottom, *advection of momentum* plays a dominant role in the asymmetry in Ekman pumping and suction and the asymmetrical spindown of cyclonic and anticyclonic vorticity. In contrast, over a stratified sloping bottom, *nonlinear advection of buoyancy* can dominate over advection of momentum in modifying the vertical velocity and vorticity fields. First, a scaling for the nonlinear correction to the flow field due to nonlinear advection of buoyancy is presented. Then, for an initially barotropic flow with sinusoidal shear, the time-dependent evolution of this nonlinear correction is solved from a closed set of equations.

The analytical model is formulated following section 2.5.1. The Boussinesq equations are rotated at an angle θ with respect to the horizontal and the small angle approximation is applied. The vertical domain is assumed semi-infinite, where the Prandtl depth, H_P, is assumed less than the domain height, H. As in Chapter 2, the flow is decomposed into an interior domain over a height H_P, a thermal bound-

ary layer of depth δ_T, and an Ekman layer of depth δ_e, where the subscripts i, T, and e, denote the respective domains. At the boundary, the no-slip, no normal flow, and no normal buoyancy flux conditions are applied. Contributions to the nonlinear dynamics from the adjustment of the background stratification are neglected under the assumption $M_{initial} > M_{Thorpe}$. The Prandtl number is assumed order one, the slope Burger number is assumed small, where $S < (2\pi\sigma)^{-1/2}$, and the flow is assumed hydrostatic given a small aspect ratio, $\Gamma = H_P/L$. The flow is examined subject to $\beta \equiv \mathcal{T}_{spindown}/\mathcal{T}_{shutdown} = \sigma S^2 E^{-1/2} \leq 1$, where β is later assumed $O(1)$, in which case Ekman advection of buoyancy modifies the leading order Ekman flow.

The scaling for the nonlinear correction to the flow by advection of buoyancy is derived following section 2.2. By the insulating boundary condition, a thermal boundary layer develops, in which isopycnal tilting modifies the cross-isobath pressure gradient and the Ekman flow. In the linear theory, cross-isobath Ekman advection of the background stratification balances vertical diffusion of buoyancy. At zeroth-order, an Ekman buoyancy flux, which scales as $\kappa\Delta b_e^{(0)}/\delta_e \sim N^2\theta U\delta_e$, into the thermal boundary layer results in a buoyancy anomaly of magnitude $\Delta b_T^{(0)} \sim \Delta b_e^{(0)}\delta_T/\delta_e$. This buoyancy anomaly balances a geostrophic along-isobath flow that scales as $\Delta u_T^{(0)} \sim \Delta b_T^{(0)}\theta/f$, which equals $\beta^{1/2}U$ on the spindown timescale. This flow opposes the interior along-isobath flow, reducing the geostrophic flow near the bottom. Hence, buoyancy shutdown suppresses the Ekman transport at order $\beta^{1/2}$, and Ekman pumping and suction are symmetrically weakened.

As illustrated in figure 3-4, this symmetry in Ekman pumping and suction is broken by two forms of nonlinear advection of buoyancy. First, cross-isobath Ekman advection of the zeroth-order thermal boundary layer buoyancy anomaly produces an additional Ekman buoyancy flux. This higher-order Ekman buoyancy flux yields an additional buoyancy anomaly in the thermal boundary layer. The Ekman flow advects buoyancy toward (away from) the cyclonic (anticyclonic) axis of the interior flow. Thus, the additional buoyancy anomaly causes greater (less) weakening of the geostrophic flow in cyclonic (anticyclonic) regions than in the linear case. Second, ver-

tical advection of the zeroth-order buoyancy anomaly in the thermal boundary layer enhances the effect of nonlinear Ekman advection of buoyancy at the same order. In cyclonic regions, Ekman pumping strengthens the total buoyancy anomaly, and in anticyclonic regions, Ekman suction weakens the total buoyancy anomaly. Therefore, nonlinear advection of buoyancy weakens Ekman pumping to a greater extent than Ekman suction, and this process is defined as *nonlinear buoyancy shutdown*.

From the above scaling argument, the correction to the flow by nonlinear buoyancy shutdown occurs at order $\sigma^2 S(\delta_T/\delta_e)^2\epsilon$. On the spindown timescale, the scaling for the nonlinear correction to the flow by nonlinear buoyancy shutdown is equal to

$$\sigma^{1/2}\beta^{1/2}E^{-1/4}\epsilon, \tag{3.37}$$

where $\delta_T/\delta_e = \sigma^{-1/2}E^{-1/4}$. When buoyancy shutdown enters into the leading order dynamics, *i.e.* $\beta = O(1)$, and the Prandtl number is order one, this scaling shows that nonlinear advection of buoyancy can dominate over $O(\epsilon)$ momentum advection. This nonlinear correction enters into the leading order dynamics when $\epsilon = \sigma^{-1/2}\beta^{-1/2}E^{1/4}$.

Nonlinear buoyancy shutdown can lead to asymmetry in the spindown of cyclonic and anticyclonic vorticity in the interior domain. During homogeneous spindown over a flat bottom, $O(\epsilon)$ stretching and squashing of vertical relative vorticity through lateral advection of momentum causes cyclonic vorticity to decay faster than anticyclonic vorticity. With stratification, $O(\epsilon)$ vertical advection of vertical relative vorticity contributes to this asymmetry. When $\sigma\beta > E^{1/2}$, nonlinear buoyancy shutdown can lead to an asymmetry in Ekman pumping and suction that is greater than an asymmetry by $O(\epsilon)$ advection of momentum. Then, an asymmetry in cyclonic and anticyclonic vorticity can arise by stretching and squashing of planetary vorticity at $O(\sigma^{1/2}\beta^{1/2}E^{-1/4}\epsilon)$. Since Ekman suction is stronger than Ekman pumping, anticyclonic vorticity can decay faster than cyclonic vorticity. This asymmetric decay in vertical relative vorticity contrasts with homogeneous and stratified spindown over a flat bottom, in which cyclonic vorticity decays faster than anticyclonic vorticity

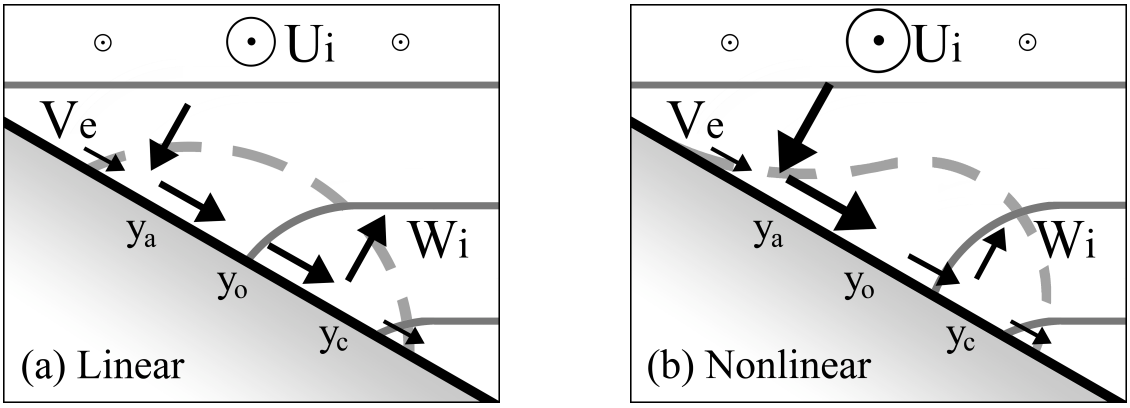

Figure 3-4: (a) Linear buoyancy shutdown. Consider the linear adjustment of an initially barotropic jet, U_i, that is laterally symmetric about y_o. Convergence in the cross-isobath Ekman flow, V_e, induces Ekman pumping, W_i, and suction. Since the jet is laterally symmetric, Ekman pumping on the cyclonic axis, y_c, is equal to Ekman suction on the anticyclonic axis, y_a. Ekman advection of the stratification leads to a positive buoyancy anomaly, enclosed within the grey dashed line, within the thermal boundary layer. This positive buoyancy anomaly tilts the isopycnals, indicated by the grey solid line, and weakens the Ekman flow. Thus, the jet spins down with a symmetric decay in cyclonic and anticyclonic vorticity.

(b) Nonlinear buoyancy shutdown. Consider the nonlinear adjustment of the jet, U_i, in (a) but at higher Rossby number due to stronger initial flow. Two forms of nonlinear advection of buoyancy strengthen the positive buoyancy anomaly, enclosed within the grey dashed line, around the cyclonic axis, y_c, and weaken the anomaly around the anticyclonic axis, y_a. First, cross-isobath Ekman flow, V_e, advects the buoyancy anomaly from (a) downslope. Second, in the thermal boundary layer, Ekman pumping advects the buoyancy anomaly upward and Ekman suction advects the anomaly downward. The isopycnals, indicated by the grey solid line, tilt more steeply around the cyclonic axis. The resulting buoyancy anomalies enhance the weakening of the Ekman flow around the cyclonic axis but reduce the weakening around the anticyclonic axis. Thus, by nonlinear buoyancy shutdown, Ekman pumping is suppressed to a greater extent than Ekman suction. Asymmetry in the interior relative vorticity field arises from vertical advection of vertical relative vorticity or stretching and squashing of absolute vertical vorticity. At $O(\epsilon)$, vertical advection of vertical relative vorticity and stretching and squashing of vertical relative vorticity causes cyclonic vorticity, at y_c, to decay faster than anticyclonic vorticity, at y_a. If the nonlinear modification to Ekman pumping and suction at $O(\sigma^{1/2}\beta^{1/2}E^{-1/4}\epsilon)$ is greater than $O(\epsilon)$, the stretching and squashing of planetary vorticity induced by the modified interior secondary circulation dominates and anticyclonic vorticity, at y_a, spins down faster than cyclonic vorticity, y_c.

in the interior. Figure 3-4 illustrates the coupling between the Ekman flow and the stratification during linear and nonlinear buoyancy shutdown.

In order to perform a perturbation expansion, the scaling (3.37) for the nonlinear correction is assumed less than $O(1)$. Therefore, the Rossby number is constrained to $\epsilon < \sigma^{-1/2}E^{1/4}$ and, from these assumptions, $\sigma S > E^{1/2}$. Appendix A.2 summarizes the hierarchy of nonlinear corrections that occur due to coupling between the Ekman flow and the buoyancy field and are greater than $O(\epsilon)$. From these assumptions, the dominant nonlinear correction to spindown over a stratified sloping bottom occurs by nonlinear buoyancy shutdown rather than advection of momentum. Next, equations are formulated to examine the impact of nonlinear buoyancy shutdown on Ekman pumping and its subsequent feedback into the interior along-isobath flow.

The equations of motion are nondimensionalized by the set of scalings presented in section 2.5.1, where the tilde ($\tilde{}$) notation is removed below. The equations are examined to $O(\epsilon E^{-1/4}\sigma^{1/2})$, where the factor of $\beta^{1/2}$ is already accounted for in the scaling of the thermal boundary layer variables. Time is nondimensionalized by the spindown timescale, where $t' = t/\mathcal{T}_{spindown}$. The vertical coordinate is nondimensionalized in the interior as $z' = z/H_P$, in the thermal boundary layer as $\xi' = z/\delta_T$, and in the Ekman layer as $\eta' = z/\delta_e$, where $\delta_T = \sigma^{-1/2}E^{1/4}H_P$, $\delta_e = E^{1/2}H_P$, and primes denote nondimensional quantities. With the primes dropped, the leading order initial condition in the rotated coordinate system becomes

$$u_i(t = 0, y) = \cos y. \tag{3.38}$$

The Ekman flow is set-up within an inertial period and is treated as an initial condition on the spindown timescale. The interior buoyancy anomaly and all variables in the thermal boundary layer are initially zero. The Ekman layer equations to

$O(\epsilon E^{-1/4}\sigma^{1/2})$ are

$$-v_e = \frac{1}{2}\frac{\partial^2 u_e}{\partial \eta^2}, \tag{3.39}$$

$$u_e = \frac{1}{2}\frac{\partial^2 v_e}{\partial \eta^2}, \tag{3.40}$$

$$-v_e + \epsilon E^{-1/4}\sigma^{1/2} v_e \frac{\partial b_T}{\partial y}(\xi = 0) = \frac{1}{2}\frac{\partial^2 b_e}{\partial \eta^2}, \tag{3.41}$$

$$\frac{\partial v_e}{\partial y} + \frac{\partial w_e}{\partial \eta} = 0. \tag{3.42}$$

In the Ekman layer, advection of momentum is smaller than nonlinear advection of buoyancy by $O(\sigma^{-1/2}E^{1/4})$. Also, vertical variations in the thermal boundary layer quantities are assumed small because the Ekman layer is thinner than the thermal boundary layer by $O(\sigma^{1/2}E^{1/4})$.

Next, the thermal boundary layer equations to $O(\epsilon E^{-1/4}\sigma^{1/2})$ are

$$\frac{\partial u_T}{\partial t} - v_T + \epsilon E^{-1/4}\sigma^{1/2} w_i(z=0)\frac{\partial u_T}{\partial \xi} = \frac{\sigma}{2}\frac{\partial^2 u_T}{\partial \xi^2}, \tag{3.43}$$

$$u_T = -b_T, \tag{3.44}$$

$$\frac{\partial b_T}{\partial t} + \epsilon E^{-1/4}\sigma^{1/2} w_i(z=0)\frac{\partial b_T}{\partial \xi} = \frac{1}{2}\frac{\partial^2 b_T}{\partial \xi^2}, \tag{3.45}$$

$$\frac{\partial v_T}{\partial y} + \frac{\partial w_T}{\partial \xi} = 0. \tag{3.46}$$

In the thermal boundary layer, the interior vertical velocity is approximated by its value at the bottom due to small vertical variations over the thermal boundary layer thickness. By geostrophy, (3.44), the along-isobath flow satisfies the buoyancy equation, (3.45). For $\sigma \neq 1$, a secondary circulation exists to maintain geostrophic balance. The cross-isobath flow is weaker than the cross-isobath Ekman flow by order $\sqrt{\beta E}$ and the thermal boundary layer flow normal to the slope is weaker than the normal flow in the interior and the Ekman layer by order $\sqrt{\beta/\sigma}E^{1/4}$.

The equations in the interior domain to $O(\epsilon E^{-1/4}\sigma^{1/2})$ are

$$\begin{aligned}
\frac{\partial u_i}{\partial t} - v_i &= 0, && (3.47)\\
u_i &= -\frac{\partial p_i}{\partial y}, && (3.48)\\
0 &= -\frac{\partial p_i}{\partial z} + b_i, && (3.49)\\
\frac{\partial b_i}{\partial t} + w_i &= 0, && (3.50)\\
\frac{\partial v_i}{\partial y} + \frac{\partial w_i}{\partial z} &= 0. && (3.51)
\end{aligned}$$

The interior secondary circulation, ψ_i, is defined as $v_i = -\frac{\partial \psi_i}{\partial z}$ and $w_i = \frac{\partial \psi_i}{\partial y}$, where

$$\frac{\partial^2 \psi_i}{\partial y^2} + \frac{\partial^2 \psi_i}{\partial z^2} = 0 \qquad (3.52)$$

is forced by Ekman pumping and suction at the boundary.

The equations are solved subject to the following boundary conditions, which are valid to $O(\epsilon E^{-1/4}\sigma^{1/2})$:

$$\begin{aligned}
u_i(z=0) + \beta^{1/2} u_T(\xi=0) + u_e(\eta=0) &= 0, && (3.53)\\
v_e(\eta=0) &= 0, && (3.54)\\
w_i(z=0) + w_e(\eta=0) &= 0, && (3.55)\\
\frac{\partial b_T}{\partial \xi}(\xi=0) + \frac{\partial b_e}{\partial \eta}(\eta=0) &= 0, && (3.56)\\
u_i \to u_i(t=0,y) \quad &\text{as} \quad z \to \infty, && (3.57)\\
v_i, w_i, b_i \to 0 \quad &\text{as} \quad z \to \infty, && (3.58)\\
u_T, v_T, w_T, b_T \to 0 \quad &\text{as} \quad \xi \to \infty, && (3.59)\\
u_e, v_e, w_e, b_e \to 0 \quad &\text{as} \quad \eta \to \infty. && (3.60)
\end{aligned}$$

Next, the nonlinear correction to the flow is solved by expanding the variables as

$$(\boldsymbol{u}, b, p) = (\boldsymbol{u}^{(0)}, b^{(0)}, p^{(0)}) + \epsilon E^{-1/4}\sigma^{1/2}(\boldsymbol{u}^{(1)}, b^{(1)}, p^{(1)}). \qquad (3.61)$$

The zeroth-order solution is decomposed as

$$(\psi_i^{(0)}, u_i^{(0)}, u_T^{(0)}) = (\varphi^{(0)}(t)\mathrm{e}^{-z}, U_i^{(0)}(t,z), U_T^{(0)}(t,\xi))\cos(y), \tag{3.62}$$

where $\varphi^{(0)}$ measures the strength of the interior secondary circulation, which exponentially decays over the Prandtl depth. The zeroth-order solution subject to buoyancy shutdown is referred to in Chapter 2 and the $O(\epsilon E^{-1/4}\sigma^{1/2})$ solution is presented here. The general Ekman layer solution to $O(\epsilon E^{-1/4}\sigma^{1/2})$ is

$$u_e^{(n)} = -(u_i^{(n)}(z=0) + \beta^{1/2}u_T^{(n)}(\xi=0))\mathrm{e}^{-\eta}\cos\eta, \tag{3.63}$$

$$v_e^{(n)} = (u_i^{(n)}(z=0) + \beta^{1/2}u_T^{(n)}(\xi=0))\mathrm{e}^{-\eta}\sin\eta, \tag{3.64}$$

$$w_e^{(n)} = \frac{1}{2}\frac{\partial}{\partial y}(u_i^{(n)}(z=0) + \beta^{1/2}u_T^{(n)}(\xi=0))\mathrm{e}^{-\eta}(\sin\eta + \cos\eta), \tag{3.65}$$

$$b_e^{(0)} = -(u_i^{(0)}(z=0) + \beta^{1/2}u_T^{(0)}(\xi=0))\mathrm{e}^{-\eta}\cos\eta, \tag{3.66}$$

$$b_e^{(1)} = -(u_i^{(1)}(z=0) + \beta^{1/2}u_T^{(1)}(\xi=0) + \varphi^{(0)}U_T^{(0)}(\xi=0)\sin(2y))\mathrm{e}^{-\eta}\cos\eta, \tag{3.67}$$

for $n = 0, 1$. The Ekman transport is defined as $M_e = \int_0^\infty v_e(t,y,\eta)d\eta = \sum_{n=0}^{n=1} M_e^{(n)}$ and

$$M_e^{(n)} = \frac{1}{2}(u_i^{(n)}(z=0) + \beta^{1/2}u_T^{(n)}(\xi=0)). \tag{3.68}$$

By the no normal flow boundary condition, Ekman pumping to $O(\epsilon E^{-1/4}\sigma^{1/2})$ is given by $w_i(z=0) = \sum_{n=0}^{n=1} w_i^{(n)}(z=0)$ and

$$w_i^{(n)}(z=0) = -\frac{1}{2}\frac{\partial}{\partial y}(u_i^{(n)}(z=0) + \beta^{1/2}u_T^{(n)}(\xi=0)). \tag{3.69}$$

The Ekman pumping solution is transformed into a boundary condition on ψ_i,

$$\frac{\partial\psi_i^{(n)}}{\partial t}(z=0) = \frac{1}{2}(\frac{\partial\psi_i^{(n)}}{\partial z}(z=0) - \beta^{1/2}\frac{\partial u_T^{(n)}}{\partial t}(\xi=0)). \tag{3.70}$$

Next, the Ekman buoyancy solutions, (3.66, 3.67), as well as the geostrophic relationship, (3.44), are used to transform the no normal buoyancy flux boundary condition, (3.56), into a boundary condition on u_T,

$$\frac{\partial u_T^{(n)}}{\partial \xi}(\xi = 0) = u_i^{(n)}(z = 0) + \beta^{1/2} u_T^{(n)}(\xi = 0). \tag{3.71}$$

The $n = 1$ solution structure is decomposed as

$$(\psi_i^{(1)}, u_i^{(1)}, u_T^{(1)}) \;=\; (\varphi^{(1)}(t)\mathrm{e}^{-2z}\sin(2y), U_i^{(1)}(t)\mathrm{e}^{-2z}\sin(2y), U_T^{(1)}(t,\xi)\sin(2y)). \tag{3.72}$$

The lateral length scale of the second harmonic is half of the lowest-order mode. Subsequently, by (3.52), the interior secondary circulation is confined closer to the boundary over half of the Prandtl depth. The time evolution of the nonlinear correction is determined by the following closed set of partial differential equations:

$$\frac{dU_i^{(1)}}{dt} - 2\varphi^{(1)} \;=\; 0, \tag{3.73}$$

$$\frac{\partial U_T^{(1)}}{\partial t} - \frac{1}{2}\frac{\partial^2 U_T^{(1)}}{\partial \xi^2} \;=\; \frac{1}{2}\varphi^{(0)}\frac{\partial U^{(0)}}{\partial \xi}, \tag{3.74}$$

subject to the boundary conditions

$$\frac{\partial \varphi^{(1)}}{\partial t} + (\varphi^{(1)} + \frac{1}{2}\beta^{1/2}\frac{\partial U_T^{(1)}}{\partial t}(\xi = 0)) \;=\; 0, \tag{3.75}$$

$$\frac{\partial U_T^{(1)}}{\partial \xi}(\xi = 0) - U_i^{(1)} - \beta^{1/2} U_T^{(1)}(\xi = 0) \;=\; \varphi^{(0)} U_T^{(0)}(\xi = 0), \tag{3.76}$$

$$U_T^{(1)} \to 0 \quad \text{as} \quad \xi \to \infty, \tag{3.77}$$

and the variables are initially zero. This set of equations is solved numerically for $\beta = 1$ and $\sigma = 1$ by the Crank-Nicolson scheme. The details of the numerical calculation are provided in Appendix B.2 and B.3. The resulting correction to the flow from nonlinear buoyancy shutdown is presented and compared with the nonlinear correction from momentum advection during homogeneous spindown on a flat bottom.

In both homogeneous spindown on a flat bottom and stratified spindown over a sloping bottom, the nonlinear correction to the flow leads to asymmetry in Ekman pumping, on the cyclonic axis, and Ekman suction, on the anticyclonic axis. Figure 3-5 compares the nonlinear corrections, which are calculated from $w_i^{(1)}(z=0) = 2\varphi^{(1)}\cos(2y)$ for nonlinear buoyancy shutdown and (3.33) for nonlinear homogeneous spindown of the sinusoidally sheared flow. For each case, the nonlinear correction to Ekman pumping and suction has the same sign and magnitude on the anticyclonic axis, $y_a = -\pi/2 + 2m\pi$, and the cyclonic axis, $y_c = \pi/2 + 2m\pi$, where m is an integer. During homogeneous spindown over a flat bottom, the nonlinear correction is negative and includes contributions from Ekman and interior momentum advection. Initially, this correction is nonzero because the Ekman flow is set-up within an inertial period. Since the correction is negative, Ekman pumping is weakened at y_c and Ekman suction is strengthened at y_a. During stratified spindown over a sloping bottom, the nonlinear correction becomes negative by nonlinear buoyancy shutdown and Ekman pumping is weaker than Ekman suction. In contrast to the homogeneous case, this correction is initially zero and grows to its maximum negative value at $t = 0.5$. Then, the correction decays while reversing sign at $t = 4.7$, reaches its maximum positive value at $t = 8.3$, and then decays to zero. The temporal evolution of this correction is explained by the forcing from the leading order flow and diffusion as this forcing decays.

Forcing by the leading order Ekman flow weakens in time due to linear buoyancy shutdown and spindown. Then, the nonlinear Ekman buoyancy flux to the thermal boundary layer and the vertical advection of the buoyancy anomalies weaken as well. For example, the forcing term on the right side of (3.76) reaches its maximum value at $t = 0.3$. As the forcing terms decay, the higher-order buoyancy anomaly in the thermal boundary layer diffuses away from the boundary and reaches its maximum value at $t = 2.9$. The corresponding along-isobath flow, $U_T^{(1)}$, is negative, enhancing (weakening) the vertical shear in the geostrophic flow about the cyclonic (anticyclonic) axis. The higher-order interior along-isobath flow, $U_i^{(1)}$, is positive, opposing

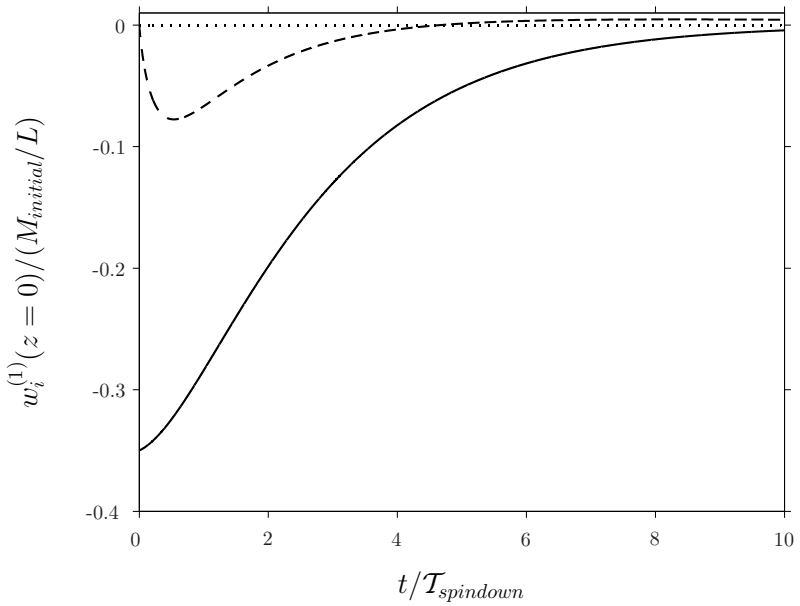

Figure 3-5: For homogeneous spindown on a flat bottom and stratified spindown over a sloping bottom, the analytical nonlinear correction to Ekman pumping and suction on the cyclonic and anticyclonic axis, respectively, is examined in time for an initially barotropic flow with sinusoidal lateral shear. The nonlinear correction is compared between homogeneous spindown (solid line) and stratified spindown over a sloping boundary (dashed line), where $\beta = 1$ and $\sigma = 1$. The axis $w_i^{(1)}(z = 0) = 0$ is also indicated (dotted line). Note that the full contribution of these nonlinear corrections is multiplied by ϵ for homogeneous spindown and $\epsilon E^{-1/4}\sigma^{1/2}$ for stratified spindown on a sloping bottom.

the geostrophic flow in the thermal boundary layer. The higher-order Ekman flow, proportional to $\varphi^{(1)}$, is dependent on the sum of these components to the geostrophic flow, $U_i^{(1)} + \beta^{1/2} U_T^{(1)}(\xi = 0)$. So, the higher-order Ekman flow decays as diffusion weakens the negative $U_T^{(1)}$ as the positive $U_i^{(1)}$ grows by the interior secondary circulation. When the higher-order correction to Ekman pumping and suction reverses sign at $t = 4.7$, the correction to the interior along-isobath flow reaches it maximum value. The reversal in the interior secondary circulation causes $U_i^{(1)}$ to decay in time. For long times, the nonlinear corrections decay to zero, leading to the spindown of the along-isobath flow. The nonlinear correction to Ekman pumping is now used to examine the nonlinear correction to the vertical relative vorticity field.

The vertical relative vorticity field develops asymmetry by both momentum advection and nonlinear advection of buoyancy. However, the asymmetry in cyclonic and anticyclonic vorticity evolves differently for each of these mechanisms. The nonlinear correction to the interior vertical relative vorticity on the cyclonic and anticyclonic axis is shown in figure 3-6. During nonlinear homogeneous spindown over a flat bottom, the nonlinear correction $\zeta_i^{(1)}$ at y_c and y_a from (3.30) is negative by $O(\epsilon)$ momentum advection. Stretching and squashing of vertical relative vorticity causes cyclonic vorticity to spindown faster than anticyclonic vorticity. Similarly, $O(\sigma^{1/2}\beta^{1/2}E^{-1/4}\epsilon)$ buoyancy advection can lead to asymmetry in vertical relative vorticity during stratified spindown over a sloping bottom.

Nonlinear buoyancy shutdown modifies the vertical relative vorticity field in the interior and thermal boundary layer. The geostrophic components to the vertical relative vorticity field are $\zeta_i^{(1)} = -2U_i^{(1)}(t)\mathrm{e}^{-2z}\cos(2y)$ and $\zeta_T^{(1)} = -2U_T^{(1)}(t,\xi)\cos(2y)$. The total nonlinear correction to vertical relative vorticity in the thermal boundary layer is measured by $\zeta_i^{(1)}(t, z = 0) + \beta^{1/2}\zeta_T^{(1)}(t, \xi = 0)$ evaluated on the cyclonic or anticyclonic axis. Figure 3-6 shows the analytical nonlinear corrections to the vertical relative vorticity field in the interior and the thermal boundary layer, where $\beta = 1$, $\sigma = 1$ and the nonlinear correction is greater than $O(\epsilon)$ by $E^{-1/4}$. In the thermal boundary layer, nonlinear buoyancy shutdown weakens the geostrophic flow

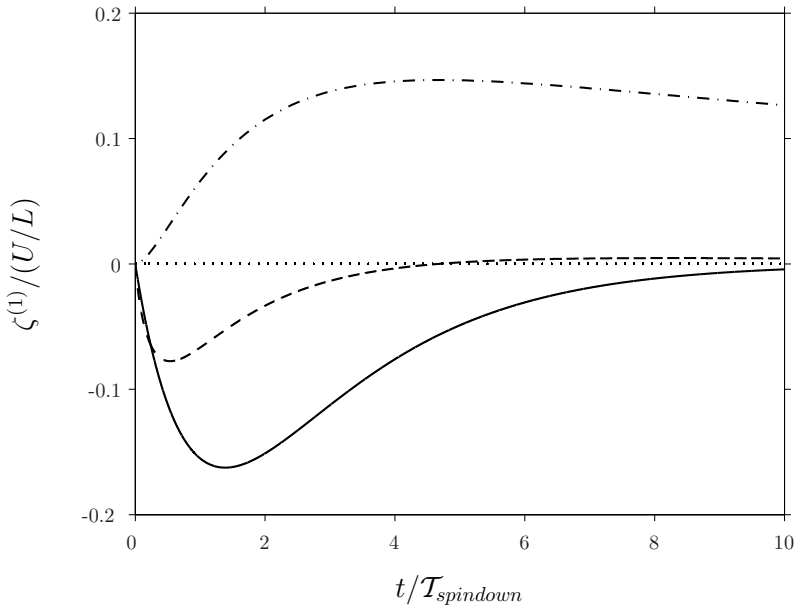

Figure 3-6: The analytical nonlinear correction to vertical relative vorticity on the cyclonic and anticyclonic axis is examined in time for an initially barotropic flow with sinusoidal lateral shear. During homogeneous spindown on a flat bottom, the nonlinear correction to the interior vertical relative vorticity (solid line), $\zeta_i^{(1)}$, is negative. During stratified spindown on a sloping bottom, where $\beta = 1$ and $\sigma = 1$, the nonlinear correction to the interior vertical relative vorticity evaluated at the boundary (dot-dashed line), $\zeta_i^{(1)}(z = 0)$, is positive. The vertical relative vorticity in the thermal boundary layer (dashed line) is measured by $\beta^{1/2}\zeta_T^{(1)}(\xi = 0) + \zeta_i^{(1)}(z = 0)$. Note that the full contribution of these nonlinear corrections is multiplied by ϵ for homogeneous spindown and $\epsilon E^{-1/4}$ for stratified spindown on a sloping bottom. The axis $\zeta^{(1)} = 0$ is also indicated (dotted line).

to a greater extent around the cyclonic axis than the anticyclonic axis. This weakening causes the cyclonic vorticity to decay faster than the anticyclonic vorticity in the thermal boundary layer, which is demonstrated by a negative nonlinear correction. This correction is proportional to Ekman pumping and suction.

In the interior, if the correction to Ekman pumping and suction by nonlinear buoyancy shutdown at $O(\sigma^{1/2}\beta^{1/2}E^{-1/4}\epsilon)$ scales larger than $O(\epsilon)$, then stretching and squashing of planetary vorticity controls the evolution of the vertical relative vorticity field. Over a stratified flat bottom, stretching and squashing of vertical relative vorticity as well as vertical advection of vertical relative vorticity causes cyclonic vorticity to decay faster than anticyclonic vorticity at $O(\epsilon)$. When $\beta = 1$ and $\sigma = 1$,

the nonlinear correction by nonlinear buoyancy shutdown scales greater than $O(\epsilon)$. Then, since Ekman pumping is suppressed to an even greater extent than Ekman suction, cyclonic vorticity decays slower than anticyclonic vorticity in the interior. The interior vertical vorticity is measured by $\zeta_i^{(1)}(z = 0)$ evaluated on the cyclonic or anticyclonic axis. This correction is positive and reaches a maximum at $t = 4.7$, at which point the interior secondary circulation reverses directions and spins down the nonlinear correction to the interior geostrophic flow.

In the next section, numerical simulations are run to address two questions. First, to what extent does the theory of nonlinear buoyancy shutdown explain the asymmetry in Ekman pumping and suction? Second, does the asymmetry in cyclonic and anticyclonic vorticity evolve as predicted by nonlinear buoyancy shutdown when momentum advection is also present? During stratified spindown over a sloping bottom, nonlinear buoyancy shutdown effects are shown as necessary to interpret the asymmetry in Ekman pumping and suction as well as the evolution of the vertical relative vorticity field.

3.6 Numerical experiments

Numerical simulations are run to compare homogeneous spindown over a flat bottom, stratified spindown over a flat bottom, and stratified spindown over a sloping bottom. These simulations are also used to test the analytical solutions for the first and last of these cases. The numerical simulations are run for increasing Rossby number within and outside the parameter range for which the analytical theory is valid. For stratified spindown over a slope, the numerical simulations are used to show that the asymmetry in Ekman pumping and suction cannot be explained by Ekman advection of momentum alone. The extent to which nonlinear buoyancy shutdown explains the asymmetry in Ekman pumping and suction and asymmetry in cyclonic and anticyclonic vorticity is investigated.

The Regional Ocean Modeling System (ROMS) is the numerical model used for

the simulations. The model configuration for the stratified cases is detailed in section 2.5.2. For homogeneous spindown, $N^2 = 0$, over a flat bottom, $\theta = 0$, the domain height is $H = 266$ m, so that the spindown time is the same as in the stratified simulations. For this case, the vertical domain has 60 grid points, with a grid resolution varying from $\Delta z = 1$ m to $\Delta z = 6$ m. In order to compare with the analytical theory, the mixing coefficients are set to $\nu, \kappa = 2.27$ x 10^{-3} m^2 s^{-1}, and uniform rotation is specified with $f = 10^{-4}$ s^{-1}, such that the Ekman layer thickness is $\delta_e = 6.7$ m.

The initial parameters are applied following section 2.5.2, where the flow field is an idealized representation of flows over the continental shelf or slope. The initial along-isobath flow is given by $u(t = 0, y) = U \cos(y/L)$, where $L = 10.6$ km is fixed and U increases for increasing Rossby number. For the stratified cases, the initial stratification is constant with $N^2 = 1.6 \times 10^{-5}$ s^{-2} and the Prandtl depth is $H_P = 266$ m. The nondimensional parameters are $E = 6.4 \times 10^{-4}$, $\Gamma = 0.03$, and $\sigma = 1$. Over a sloping bottom, the slope angle is set to $\theta = 0.01$ where $\beta = 1$. As described in section 2.5.2, in order to remove the effects of the laterally uniform flow that arises from the adjustment of the stratification, the model output from simulations with no initial flow is subtracted from the model output with an initial flow. This decomposition assumes that the coupling between the laterally uniform and laterally sheared flow is a higher order effect given that $M_{initial}/M_{Thorpe} > 1$. In order to focus on the subinertial response of the system, the model output is further processed by filtering the secondary circulation by a Butterworth low-pass filter with a cut-off frequency of $0.12f$.

In this section, the time-dependent evolution of stratified spindown over a flat and sloping bottom for $\epsilon = 0.4$ is presented to demonstrate the different roles of momentum advection and buoyancy advection in the dynamics. Then, the asymmetry in Ekman pumping and suction is examined for increasing Rossby number and compared with the analytical solutions. Finally, the asymmetry in cyclonic and anticyclonic vorticity is also compared for increasing Rossby number.

A comparison between nonlinear stratified spindown over a flat bottom and slop-

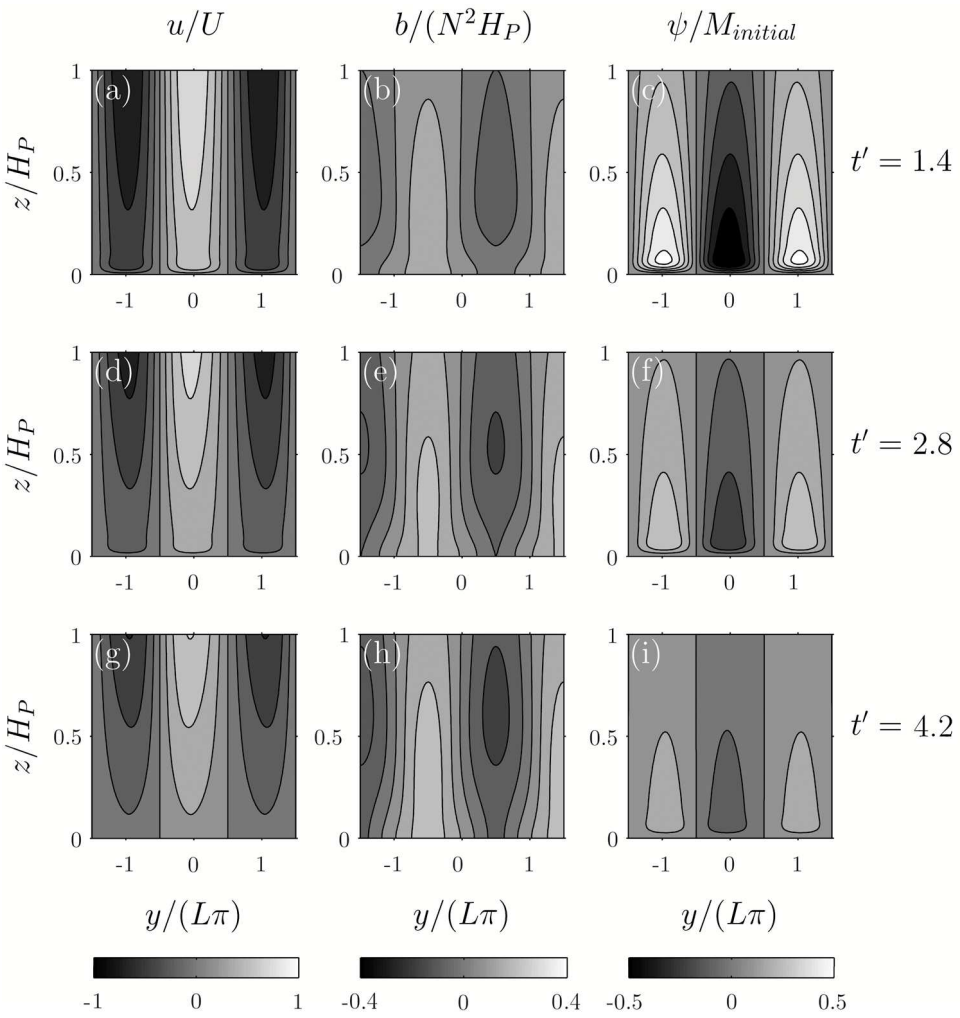

Figure 3-7: $\beta = 0$, $\theta = 0$. The sections from the $\epsilon = 0.4$ numerical stratified spindown simulation are shown for $t/\mathcal{T}_{spindown} = 1.4$ (a, b, c), 2.8 (d, e, f), and 4.2 (g, h, i). The flow, $u/U, (a, d, g)$ is contoured every 0.2 units, the buoyancy anomaly, $b/(N^2H_P), (b, e, h)$ is contoured every 0.08 units, and the secondary circulation, $\psi/M_{initial}, (c, f, i)$ is contoured every 0.1 units.

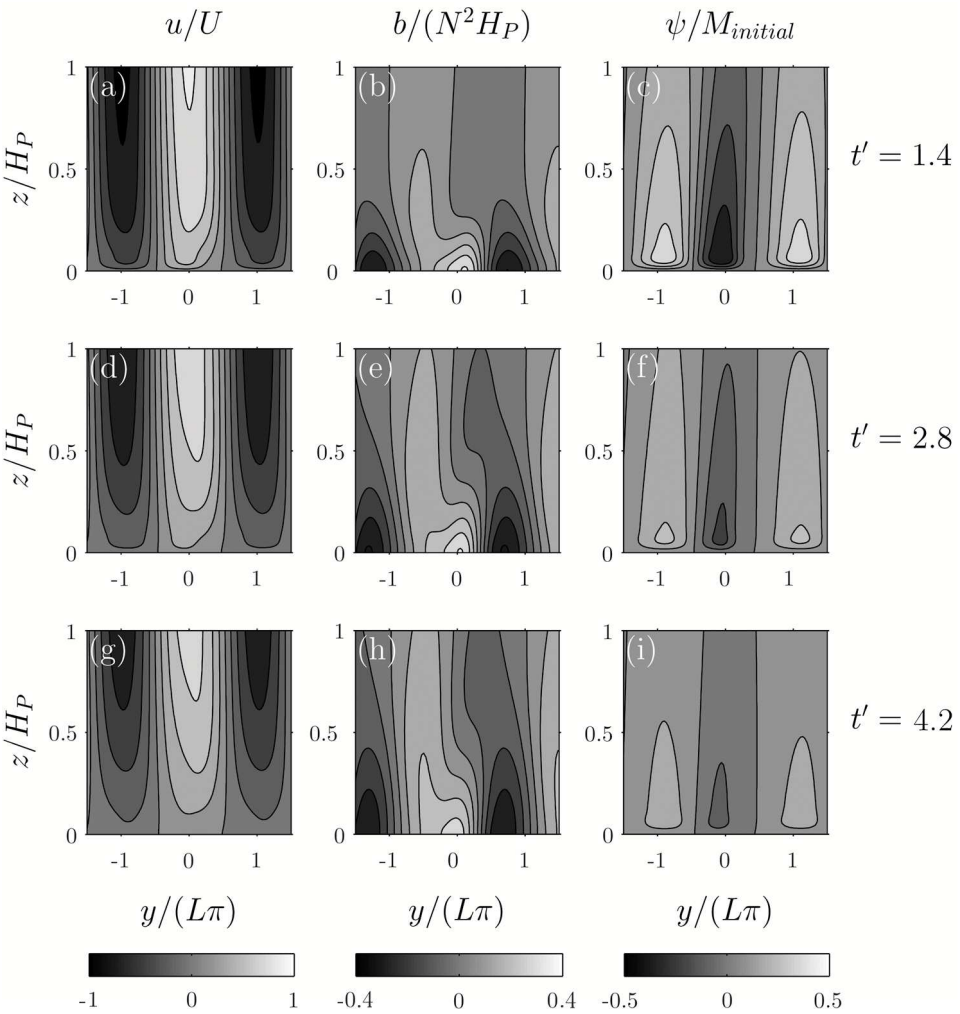

Figure 3-8: $\beta = 1$, $\theta = 0.01$. The sections from the $\epsilon = 0.4$ numerical stratified spindown simulation are shown in the rotated coordinate frame for $t/\mathcal{T}_{spindown} = 1.4$ (a, b, c), 2.8 (d, e, f), and 4.2 (g, h, i). The along-isobath flow, $u/U, (a, d, g)$ is contoured every 0.2 units, the buoyancy anomaly, $b/(N^2H_P), (b, e, h)$ is contoured every 0.08 units, and the secondary circulation, $\psi/M_{initial}, (c, f, i)$ is contoured every 0.1 units.

ing bottom for $U = 0.4$ m s$^{-1}, \epsilon = 0.4$, shows that nonlinear buoyancy shutdown plays a significant role in modifying the flow and buoyancy field. Over a flat bottom, figure 3-7, momentum advection modifies stratified spindown in several ways. First, interior momentum advection causes cyclonic vorticity to decay faster than anticyclonic vorticity. Second, momentum advection causes Ekman pumping to decay faster than Ekman suction, as demonstrated by the secondary circulation streamlines, which spread apart on the cyclonic axis and squeeze together on the anticyclonic axis near the bottom. The buoyancy anomaly is modified by two forms of buoyancy advection. Despite weaker Ekman pumping than Ekman suction, the interior buoyancy anomalies are stronger on the cyclonic axis than the anticyclonic axis due to nonlinear advection of buoyancy at $O(\epsilon)$. Near the bottom, vertical advection of the laterally uniform buoyancy field in the thermal boundary layer leads to an $O(\sigma^{-1/2}E^{1/4})$ correction to the buoyancy field, positive on the cyclonic axis and negative on the anticyclonic axis. This correction explains why the interior buoyancy anomaly does not attain its maximum negative value on the cyclonic axis near the bottom. New features emerge during nonlinear stratified spindown over a sloping bottom.

Over a sloping bottom, nonlinear advection of buoyancy modifies the spindown dynamics. Figure 3-8 shows the time-evolution of the flow for $\theta = 0.01$, $\beta = 1$ and $U = 0.4$ m s^{-1}, $\epsilon = 0.4$. In contrast to the flat bottom case, the buoyancy field shows significant variations within the thermal boundary layer, which grows in thickness from $\delta_T/H_P = 0.2$ at $t = 1.4$ to $\delta_T/H_P = 0.3$ at $t = 4.2$ in the sections shown. For small Rossby numbers, these buoyancy anomalies are maximum where the interior geostrophic flow is maximum due to linear Ekman advection of buoyancy. For large Rossby numbers, e.g. $\epsilon = 0.4$ in this case, nonlinear advection of buoyancy causes these buoyancy anomalies to converge on the cyclonic axis. The isopycnals (not shown) indicate the formation of a density front, a maximum in the cross-isobath density gradient, on the cyclonic axis. Consequently, nonlinear buoyancy shutdown influences the along-isobath flow within the thermal boundary layer. The convergence in thermal boundary layer buoyancy anomalies is correlated

with a reduction in the geostrophic flow, and the cyclonic vorticity, on the cyclonic axis. Then, Ekman pumping is weaker than Ekman suction because cyclonic vorticity is weaker than anticyclonic vorticity. The secondary circulation sections show that the streamlines are more closely spaced on the anticyclonic axis than the cyclonic axis, which is consistent with both nonlinear buoyancy shutdown and Ekman advection of momentum. The correction from nonlinear buoyancy shutdown scales as $O(\sigma^{1/2}\beta^{1/2}E^{-1/4}\epsilon) \sim 6.3\ \epsilon$ and is expected to modify the secondary circulation to a greater extent than momentum advection. In the interior, cyclonic vorticity spins down slower than anticyclonic vorticity, which is consistent with weaker Ekman pumping than Ekman suction. This behavior shows that nonlinear buoyancy shutdown causes Ekman pumping to weaken to a greater extent than Ekman suction and dominates over $O(\epsilon)$ momentum advection in controlling the asymmetry in cyclonic and anticyclonic vorticity. Next, the role of momentum advection is compared to buoyancy advection in setting the asymmetry in Ekman pumping and suction.

The asymmetry in Ekman pumping and suction is examined for increasing Rossby number during homogeneous and stratified spindown. The numerical model is compared with the analytical theory to evaluate the relative contributions of momentum advection and nonlinear advection of buoyancy to Ekman pumping and suction. The temporal decay in Ekman pumping at y_c and Ekman suction at y_a from the analytical theory and the numerical simulations is shown in figure 3-9 for homogeneous spindown over a flat bottom and figure 3-10 for stratified spindown over a sloping bottom. In the analytical model, Ekman pumping is measured as $w_i(z = 0)$. In the numerical model, Ekman pumping and suction are measured by the vertical velocity evaluated at $z = 0.08$, outside the base of the Ekman layer at $z = 0.03$. This height is chosen from the average height of the maximum absolute vertical velocity on the cyclonic and anticyclonic axes. During stratified spindown over a sloping bottom, Ekman pumping and suction is influenced by both nonlinear buoyancy shutdown and momentum advection. Despite the order Rossby number correction by momentum advection, the modification to Ekman pumping and suction by nonlinear buoyancy shutdown shows

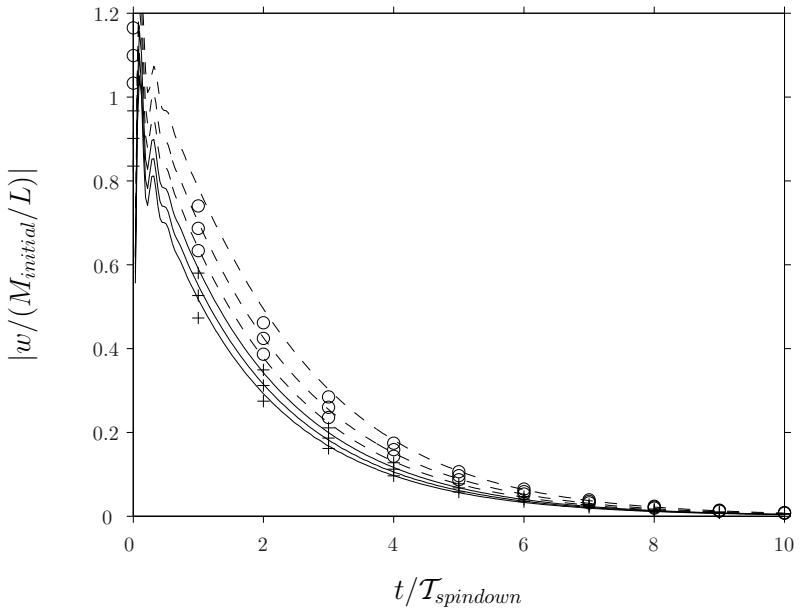

Figure 3-9: For homogeneous spindown over a flat bottom, Ekman pumping (solid line) on the cyclonic axis and Ekman suction (dashed line) on the anticyclonic axis from the numerical simulations are compared with the analytical solutions for Ekman pumping (+) and Ekman suction ($\circ$). The solutions are shown for $\epsilon = 0.1, 0.3, 0.5$ with increasing asymmetry in Ekman pumping and suction for increasing Rossby number.

good initial agreement with the numerical simuluations. Although the analytical theory for nonlinear buoyancy shutdown is strictly valid for $\epsilon < \sigma^{-1/2}\beta^{-1/2}E^{1/4} = 0.16$ given the model parameters, the correction is included to $\epsilon = 0.5$.

The numerical simulations show a different decay rate than the analytical solutions. For homogeneous spindown over a flat bottom, this difference may arise due to an imperfect implementation of the no-slip boundary condition in the numerical simulation. The difference is also explained by the $O(\epsilon^2)$ correction providing a non-negligible contribution at higher Rossby number. From Hart's formula (2000), the $O(\epsilon^2)$ correction, without feedback with the $O(\epsilon^2)$ interior flow, is $15\epsilon/56$ as large as the $O(\epsilon)$ correction, ranging from 0.02 for $\epsilon = 0.1$ to 0.13 for $\epsilon = 0.5$. This $O(\epsilon^2)$ correction tends to enhance both Ekman pumping and suction, which is consistent with the discrepency between the numerical model and the analytical solution.

For stratified spindown over a sloping bottom, the different decay rates may be

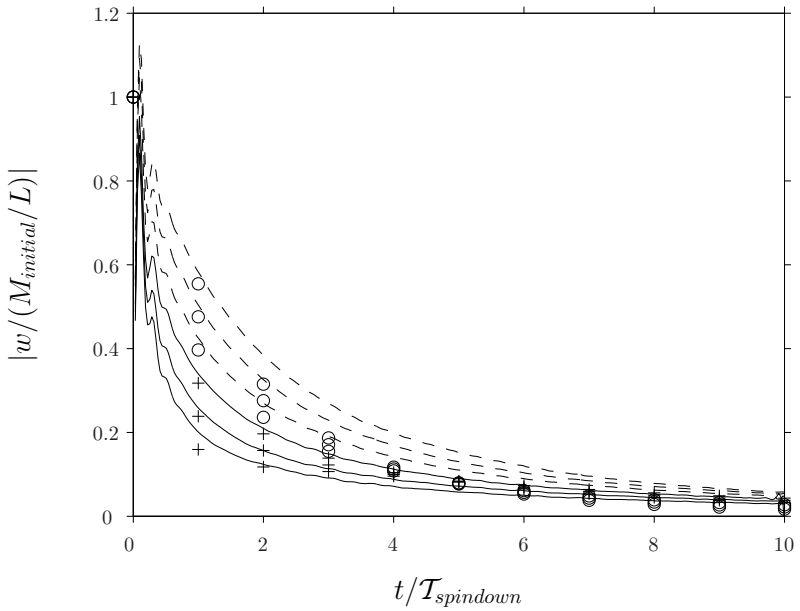

Figure 3-10: For stratified spindown over a sloping bottom, where $\beta = 1$, Ekman pumping (solid line) on the cyclonic axis and Ekman suction (dashed line) on the anticyclonic axis from the numerical simulations are compared with the analytical solution for Ekman pumping (+) and Ekman suction ($\circ$). The solutions are shown for $\epsilon = 0.1, 0.3, 0.5$ with increasing asymmetry in Ekman pumping and suction for increasing Rossby number.

explained by a number of different reasons, including an imperfect no-slip boundary condition in the numerical simulation. At early time, $t < 1$, the correction from nonlinear buoyancy shutdown captures the time evolution of Ekman pumping and suction, although these quantities are systematically larger than the analytical calculation. This systematic error may be explained by the $O(\sigma^{-1/2}E^{1/4})$ correction from vertical advection of the laterally uniform buoyancy anomaly in the thermal boundary layer (see correction 1.a in Appendix A.1). This correction causes Ekman pumping and suction to increase from the $O(1)$ solution during stratified spindown on a flat bottom. At later times, $t > 1$, the correction due to nonlinear buoyancy shutdown underestimates the difference between Ekman pumping and suction. The breakdown in the theory is in part due to the neglect of momentum advection. In the analytical theory, vertical diffusion of the buoyancy anomalies weakens the nonlinear correction to Ekman pumping and leads to its reversal in sign. In the numerical model, as the

correction by nonlinear buoyancy shutdown decays, Ekman advection of momentum appears to become important in sustaining the asymmetry in Ekman pumping and suction throughout spindown. Despite the discrepency between the analytical solution and numerical model, the asymmetry in Ekman pumping and suction at early times is consistent with the prediction by nonlinear buoyancy shutdown and indicates that nonlinear advection of momentum plays a secondary role then.

In order to further illustrate the asymmetry in Ekman pumping and suction in each case, the ratio of Ekman pumping, w_p, on the cyclonic axis, $y_c = \pi/2$, to Ekman suction, w_s, on the anticyclonic axis, $y_a = -\pi/2$, is shown in figure 3-11 at $t = 1.4$ for increasing Rossby number. From the ratio of Ekman pumping to Ekman suction for homogeneous spindown on a flat bottom, (3.34), $F_2(t = 1.4) = 0.50$, and a MacLaurin series expansion in Rossby number yields the ratio $|w_p/w_s| = 1 - \epsilon$ for $\epsilon \ll 1$. For stratified spindown over a sloping bottom, where $\beta = \sigma = 1$, $w_p^{(1)}/w_p^{(0)} = -0.18$ at $t = 1.4$, and a MacLaurin series expansion in Rossby number yields the ratio $|w_p/w_s| = 1 - 0.36\ \sigma^{1/2}E^{-1/4}\epsilon$ or $1 - 2.3\ \epsilon$ for $\epsilon \ll 1$. These measures show that the asymmetry in Ekman pumping and suction becomes more pronounced by nonlinear buoyancy shutdown than advection of momentum for increasing Rossby number. Although the analytical calculations for the temporal evolution of Ekman pumping and suction show deviations from the numerical simulation, the ratio $|w_p/w_s|$ shows agreement. The ratio of Ekman pumping to Ekman suction from stratified spindown on a flat bottom is weaker than the ratio from homogeneous spindown. This result occurs because the $O(\sigma^{-1/2}E^{1/4})$ correction (see correction 1.a in Appendix A.1) increases both Ekman pumping and suction, thereby reducing the ratio. The significant point shown here is that the asymmetry in Ekman pumping and suction shown for stratified spindown over a sloping bottom cannot be accounted for by advection of momentum alone.

The difference in Ekman pumping on the cyclonic axis and Ekman suction on the anticyclonic axis modifies the lateral structure of Ekman pumping. Figure 3-12 shows the spatial and time evolution of Ekman pumping for increasing Rossby num-

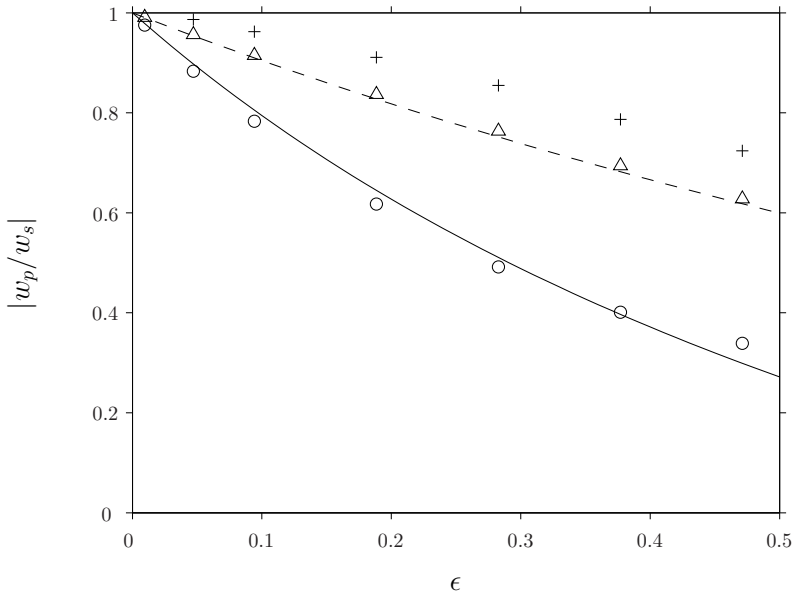

Figure 3-11: The ratio of Ekman pumping, w_p, on the cyclonic axis to Ekman suction, w_s, on the anticyclonic axis is examined at $t/\mathcal{T}_{spindown} = 1.4$ for increasing Rossby number. The symbols denote the numerical model solutions for homogeneous spindown on a flat bottom ($\triangle$), stratified spindown on a flat bottom ($+$), and stratified spindown on a sloping bottom ($\circ$). The analytical solutions, calculated from (3.34) for homogeneous spindown on a flat bottom (dashed line) and section 3.5 for stratified spindown on a sloping bottom (solid line), are also shown for comparison.

ber for homogeneous spindown (HSD) on a flat bottom, stratified spindown (SSD) on a flat bottom and on a sloping bottom. In each case considered, weaker Ekman pumping at y_c than Ekman suction at y_a is balanced by Ekman pumping where the initial geostrophic flow is an absolute maximum or minimum, *i.e.* at $y/\pi = m$ and $m = -1, 0, 1$. As the asymmetry in Ekman pumping and suction increases for increasing Rossby number, Ekman pumping off of the cyclonic axis increases. For SSD on a flat bottom, the contours indicate that, for $\epsilon = 0.1$, Ekman pumping and suction is stronger than in HSD, which is consistent with the $O(\sigma^{-1/2}E^{1/4})$ correction. In contrast to HSD, the asymmetry in Ekman pumping and suction becomes more pronounced along with stronger Ekman pumping off of the cyclonic axis for increasing Rossby number and time. These features may be explained by the nonlinear corrections documented in Appendix A.1. For SSD on a flat bottom, Ekman advection of the interior buoyancy anomlies, correction 5.a, along with Ekman advection of momentum, correction 4.a, tend to increase the asymmetry in Ekman pumping and suction in time. These effects contribute to an increasing difference in Ekman pumping on the cyclonic axis and Ekman suction on the anticyclonic axis, leading to increasing Ekman pumping off of the cyclonic axis.

For SSD on a sloping bottom, the sections for Ekman pumping show notable differences with the flat bottom case. For $\epsilon = 0.1$, Ekman pumping and suction are weaker than in SSD on a flat bottom, due to linear buoyancy shutdown, and also show evidence of asymmetry from nonlinear buoyancy shutdown. With increasing Rossby number, the asymmetry becomes more pronounced. As in the flat bottom case, Ekman pumping becomes larger off of the cyclonic axis than on the cyclonic axis. Furthermore, the Ekman pumping adjacent to $y = 0$, on the downwelling side, becomes larger than Ekman pumping near $y/\pi = -1, 1$, on the upwelling side. This feature could be due to nonlinear corrections 3.b and 4.b in Appendix A.2 because they tend to increase Ekman pumping at $y = 0$ and decrease Ekman pumping at $y/\pi = -1, 1$. Interestingly, for $\epsilon = 0.5$, an intense spike of Ekman pumping, with a maximum value of 0.91, occurs at $t = 1.71$ and $y/\pi = 0.13$. The only other time when

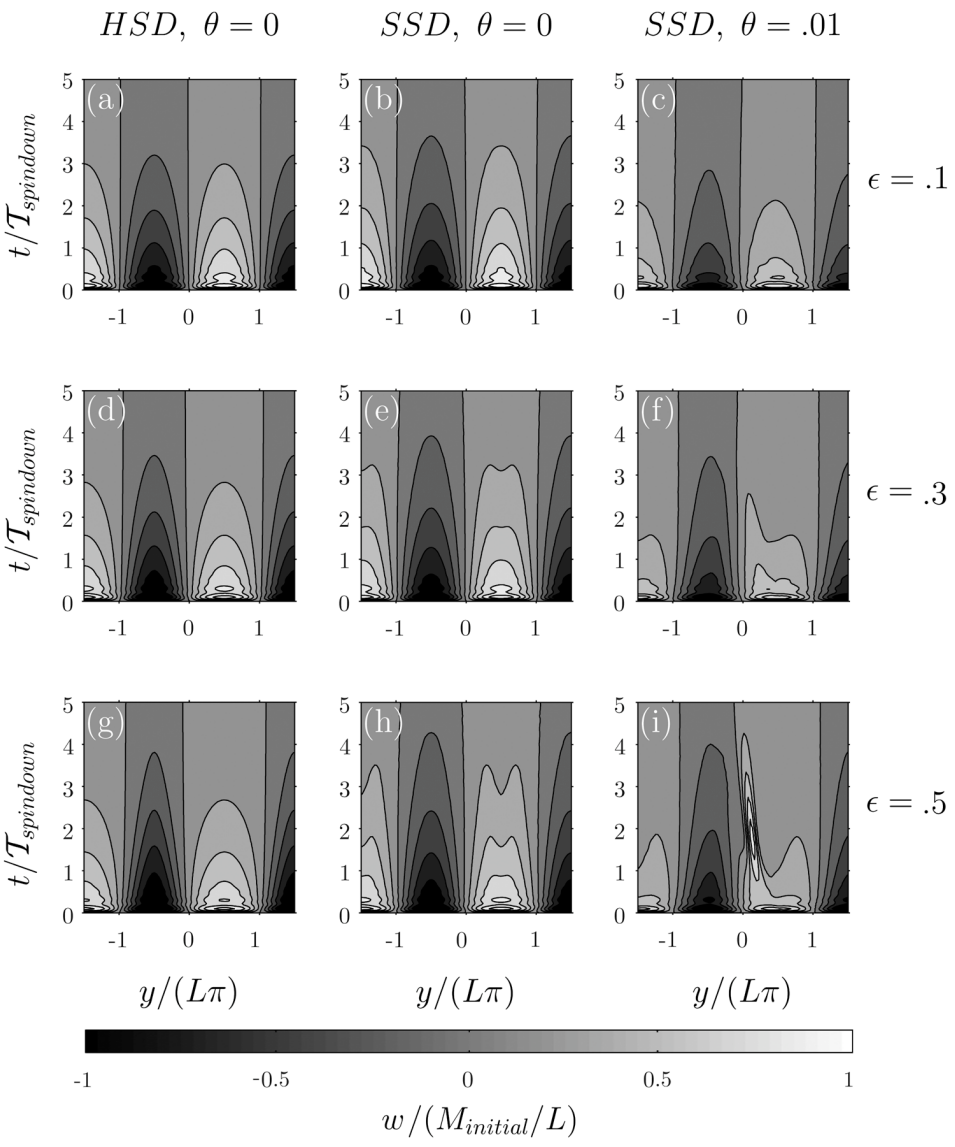

Figure 3-12: Ekman pumping is shown for $\epsilon = 0.1$ $(a, b, c), 0.3$ $(d, e, f), 0.5$ (g, h, i), during its spatial and temporal evolution, and contoured every 0.2 units. The sections are from the numerical simulations of homogeneous spindown on a flat bottom (HSD) (a, d, g), stratified spindown (SSD) on a flat bottom (b, e, h) as well as on a sloping bottom (c, f, i).

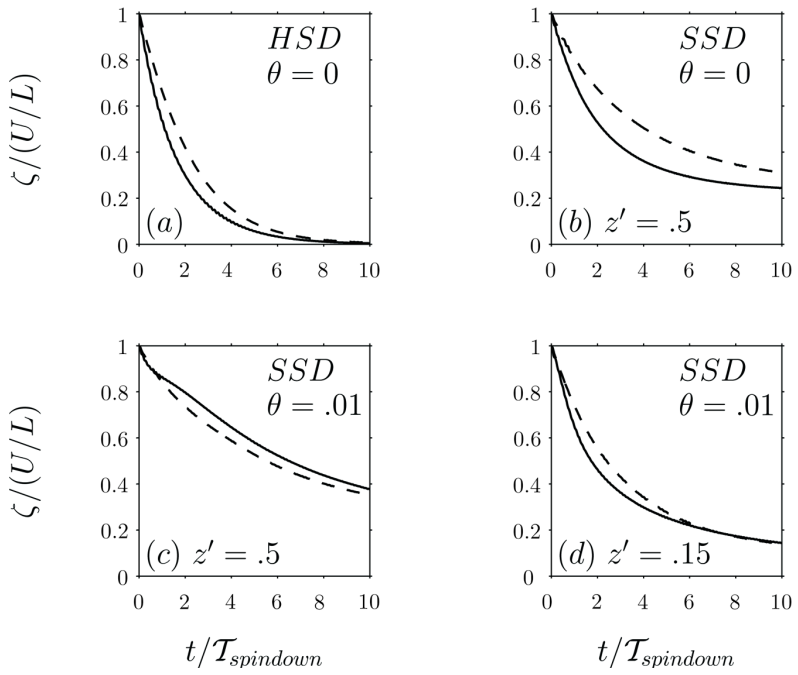

Figure 3-13: Cyclonic vorticity (solid line), at $y_c = \pi/2$, and anticyclonic vorticity (dashed line), at $y_a = -\pi/2$, decay asymmetrically for $\epsilon = 0.4$. The profiles are from the numerical simulations of homogeneous spindown (HSD) on a flat bottom in the interior domain (a), stratified spindown (SSD) on a flat bottom in the interior at $z = 0.5$ (b), and stratified spindown on a sloping bottom in the interior at $z = 0.5$ (c), and in the thermal boundary layer at $z = 0.15$ (d).

the Ekman pumping reaches this value is at $t = 0.09$, during the initial formation of the Ekman layer. In Chapter 2, buoyancy shutdown is shown to modify Ekman pumping on the cyclonic axis and Ekman suction on the anticyclonic axis. Here, nonlinear advection of buoyancy is shown to play a significant role in altering Ekman pumping away from the cyclonic axis and to produce intense vertical flows out of the boundary layer where the interior geostrophic flow is an initial maximum.

Next, the results from the asymmetry in Ekman pumping and suction are used to interpret the evolution of the vertical relative vorticity field. The spindown of the vertical relative vorticity on the cyclonic axis, $y_c = \pi/2$, and on the anticyclonic axis, $y_a = \pi/2$, is compared in figure 3-13 for each of the $\epsilon = 0.4$ numerical simulations. The vertical relative vorticity during stratified spindown on a flat bottom, figure 3-13b, does not decay as fast as during homogeneous spindown on a flat bottom, figure 3-13a, due to vertical shear in the geostrophic flow. In both cases, cyclonic vorticity, ζ_c, decays faster than anticyclonic vorticity, ζ_a. The ratio $|\zeta_c/\zeta_a|$ decreases from 0.76 at $t = 1.4$ to 0.69 at $t = 2.8$ in figure 3-13a and from 0.83 at $t = 1.4$ to 0.74 at $t = 2.8$ in figure 3-13b.

Similarly, on a stratified sloping bottom, the interior cyclonic vorticity initially decays faster than anticyclonic vorticity, as shown in figure 3-13c at z = 0.5. This behavior is explained by interior advection of momentum initially causing cyclonic vorticity to weaken faster than anticyclonic vorticity. However, in contrast to the flat bottom cases, cyclonic vorticity becomes larger than anticyclonic vorticity at $t = 0.7$ and remains larger. At $z = 0.5$, the ratio $|\zeta_c/\zeta_a|$ grows from 1.05 at $t = 1.4$ to 1.10 at $t = 2.8$. In contrast to the interior, cyclonic vorticity decays faster than anticyclonic vorticity in the thermal boundary layer, as shown in figure 3-13d at $z = 0.15$. The greater weakening of cyclonic vorticity over anticyclonic vorticity is correlated with the convergence of the buoyancy anomalies on the cyclonic axis, which is consistent with nonlinear advection of buoyancy. Thus, the temporal evolution of vertical relative vorticity in the interior is interpreted as follows. In time, nonlinear buoyancy shutdown suppresses Ekman pumping over Ekman suction to the extent that

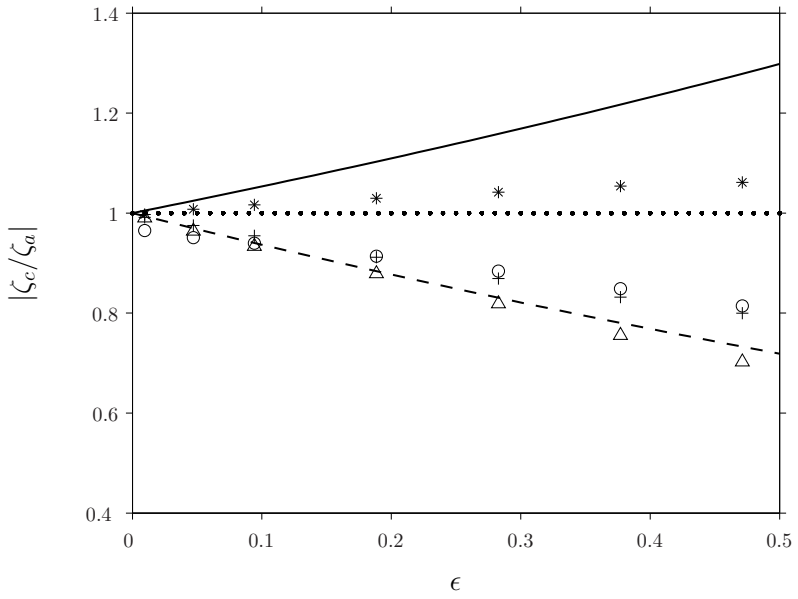

Figure 3-14: The ratio of cyclonic vorticity, ζ_c, on the cyclonic axis to anticyclonic vorticity, ζ_a, on the anticyclonic axis is examined at $t/\mathcal{T}_{spindown} = 1.4$ for increasing Rossby number. The symbols denote the numerical model solutions for homogeneous spindown on a flat bottom ($\triangle$) at $z/H = 0.5$, stratified spindown on a flat bottom at $z/H_P = 0.5$ ($+$), and stratified spindown on a sloping bottom at $z/H_P = 0.15$ ($\circ$) and at $z/H_P = 0.5$ ($*$). The analytical solutions, calculated from (3.31) for homogeneous spindown on a flat bottom at $z/H = 0.5$ (dashed line) and section 3.5 for stratified spindown on a sloping bottom at $z/H_P = 0.5$ (solid line), are also shown for comparison. The axis $|\zeta_c/\zeta_a| = 0$ is also indicated (dotted line).

stretching and squashing of planetary vorticity by the $O(\sigma^{1/2}\beta^{1/2}E^{-1/4}\epsilon)$ correction to the interior secondary circulation dominates over stretching and squashing of vertical relative vorticity and vertical advection of vertical relative vorticity. Therefore, nonlinear buoyancy shutdown plays an important role in controlling the asymmetric decay of cyclonic and anticyclonic vorticity.

The ratio of cyclonic vorticity at $y_c = \pi/2$ to anticyclonic vorticity at $y_a = -\pi/2$ is shown in figure 3-14 for increasing Rossby number to measure the asymmetry between cyclonic and anticyclonic vorticity. At $t = 1.4$, the numerical model's vorticity ratios from homogeneous spindown on a flat bottom and stratified spindown on a flat bottom at $z = 0.5$ as well as stratified spindown on a sloping bottom at $z = 0.15$ show that cyclonic vorticity is increasingly weaker than anticyclonic vorticity for increas-

ing Rossby number. The ratio from the analytical solution, (3.31), for homogeneous spindown agrees with the numerical model.

For stratified spindown on a sloping bottom, the vorticity ratio at $z = 0.5$ from the numerical model shows that the ratio of cyclonic to anticyclonic vorticity increases for increasing Rossby number. The analytical solution from section 3.5 overestimates the ratio. Thus, at this time, nonlinear buoyancy shutdown alone overestimates the asymmetry between cyclonic and anticyclonic vorticity. This overestimate occurs because momentum advection is neglected in the analytical nonlinear buoyancy shutdown solution. The interior secondary circulation is set-up within an inertial period, laterally advecting momentum and initially causing cyclonic vorticity to spindown faster than anticyclonic vorticity over a Prandtl depth. This effect is shown in figure 3-13c, where momentum advection controls the ratio for $t < 0.7$. In contrast to momentum advection, nonlinear buoyancy shutdown's modification of the interior secondary circulation is initially zero because the buoyancy anomalies are initially zero. As the buoyancy anomalies grow in the thermal boundary layer, nonlinear buoyancy shutdown suppresses Ekman pumping to a greater extent than Ekman suction. When nonlinear buoyancy shutdown modifies the interior secondary circulation to a greater extent than $O(\epsilon)$, stretching and squashing of planetary vorticity by the $O(\sigma^{1/2}\beta^{1/2}E^{-1/4}\epsilon)$ correction to the secondary circulation causes the interior anticyclonic vorticity to decay faster than cyclonic vorticity over a vertical scale that is half a Prandtl depth. Thus, momentum advection reduces the ratio of cyclonic to anticyclonic vorticity from the ratio predicted by nonlinear buoyancy shutdown alone. However, nonlinear buoyancy shutdown is still necessary to explain the asymmetry in cyclonic and anticyclonic vorticity in the numerical model for stratified spindown on a sloping bottom.

3.7 Conclusions

During the nonlinear spindown of a geostrophic flow, two primary mechanisms lead to an asymmetry in the strength of Ekman pumping and suction and an asymmetry in the decay of cyclonic and anticyclonic vorticity for increasing Rossby number. For homogeneous spindown over a flat bottom, a complete analysis of the order Rossby number correction shows that momentum advection in both the Ekman layer and the interior reduces Ekman pumping and enhances Ekman suction. The full time-dependent solution to order Rossby number shows that horizontal advection of momentum in the interior causes cyclonic vorticity to decay faster than anticyclonic vorticity despite weaker Ekman pumping than Ekman suction. Thus, stretching and squashing of vertical relative vorticity dominates over stretching and squashing of planetary vorticity. This result is consistent with Zavala Sansón's (2001) findings in numerical experiments, in which the cyclonic vortices decay faster than anticyclonic vortices. Although the numerical simulations in that work neglect the nonlinear contribution to Ekman pumping, the simulations in this work show the same behavior, a faster decay of cyclonic vorticity than anticyclonic vorticity. However, without the nonlinear contribution to Ekman pumping, the measure of the vertical circulation within the vortices will overestimate Ekman pumping and underestimate Ekman suction.

For stratified spindown over a sloping bottom, new criteria have been identified for when nonlinear advection of buoyancy is important to the asymmetries in vertical velocity and vorticity. Nonlinear advection of buoyancy strengthens (weakens) buoyancy anomalies within the thermal boundary layer about the cyclonic (anticyclonic) axis through an Ekman buoyancy flux and by vertical advection from the interior secondary circulation. Then, by geostrophy, the cyclonic vorticity is weakened to a greater extent than anticyclonic vorticity in the thermal boundary layer. This process, defined here as nonlinear buoyancy shutdown, weakens Ekman pumping over Ekman suction at $O(\sigma^{1/2}\beta^{1/2}E^{-1/4}\epsilon)$. When $\sigma\beta > E^{1/2}$, this nonlinear correction is greater

than the $O(\epsilon)$ correction due to momentum advection, and when $\epsilon > \sigma^{-1/2}\beta^{-1/2}E^{1/4}$, this nonlinear correction can enter into the leading order dynamics.

If $\sigma\beta > E^{1/2}$, the suppression of Ekman pumping over Ekman suction by nonlinear buoyancy shutdown can modify the nonlinear evolution of the interior vertical vorticity field. Then, stretching and squashing of planetary vorticity dominates over both $O(\epsilon)$ stretching and squashing of vertical relative vorticity and $O(\epsilon)$ vertical advection of vertical relative vorticity. Consequently, the interior anticyclonic vorticity decays faster than cyclonic vorticity, in contrast to nonlinear stratified spindown on a flat bottom. Numerical simulations support the predictions of the asymmetry in the Ekman pumping and suction by nonlinear buoyancy shutdown and show that this mechanism can cause the interior anticyclonic vorticity to decay faster than cyclonic vorticity.

Nonlinear buoyancy shutdown may play an important role in the evolution of high Rossby number flows over topography with large slope Burger number. For a laterally symmetric along-isobath current with a downwelling Ekman flow, as shown in figure 3-4, a thicker boundary layer in buoyancy and weaker Ekman transport on the downslope side may signify evidence of nonlinear buoyancy shutdown. In Chapter 2, estimates of β indicate that linear buoyancy shutdown could modify the dynamics over the upper continental slope. On the lower continental slope, measurements of the North Atlantic Deep Western Boundary Current at the Blake Outer Ridge reveal a frictional bottom boundary layer embedded within a thicker bottom mixed layer (Stahr and Sanford 1999). The bottom mixed layer is thicker and the Ekman transport is weaker on the downslope side of the current (see figure 1-7). This configuration would also hold if nonlinear buoyancy shutdown was important to the flow. However, the cross-isobath density gradients within the bottom mixed layer are small with little vertical shear in the along-slope flow, indicating that other processes govern the dynamics other than linear and nonlinear buoyancy shutdown.

In summary, this work has provided insight into the nonlinear coupling between frictionally driven flows and the buoyancy field. Future challenges include identifying

features of nonlinear buoyancy shutdown in observations and understanding how this mechanism can modify the evolution of three-dimensional structures, such as slope vortices, and their vertical circulation.

Chapter 4

Stratified spindown over a shelfbreak

Abstract

The adjustment of an initially uniform along-isobath flow is examined in a stratified fluid over a shelfbreak, where a flat shelf intersects a steep slope. On the shelf, the along-isobath flow drives an offshore Ekman transport. On the slope, the offshore Ekman transport advects buoyancy downslope, which causes the bottom mixed layer to thicken and the Ekman transport to weaken by buoyancy shutdown. Near the shelfbreak, convergence in the offshore Ekman transport induces Ekman pumping. Over the slope, Ekman pumping drives a secondary circulation that accelerates the along-isobath flow. Scalings are identified for the strength of Ekman pumping near the shelfbreak, the length scale over which it occurs, and the time scale for the along-isobath flow acceleration over the slope. A simple model of the secondary circulation over the slope reveals the formation of a jet near the shelfbreak. The scalings are tested in a series of numerical simulations with application to flows near the Middle Atlantic Bight shelfbreak.

4.1 Introduction

In the previous two chapters, linear and nonlinear stratified spindown over a constant slope demonstrate how coupling between the frictionally driven flow and the buoyancy field can impact the vertical circulation and the temporal evolution of the vertical vorticity field. In this chapter, stratified spindown over an idealized shelfbreak shows how this coupling can generate both upwelling and the formation of a jet near the shelfbreak.

This theoretical study is motivated by observations of flows near the Middle Atlantic Bight shelfbreak and previous modelling studies of buoyant shelf flows that attempt to explain the observed front located at the shelfbreak. The shelfbreak is the location in which the gently sloping continental shelf transitions to the more steeply sloping continental slope. Near the Middle Atlantic Bight shelfbreak, observations support the existence of a partially density-compensating thermohaline front and jet (e.g. Linder and Gawarkiewicz 1998, Fratantoni and Pickart 2007) as well as upwelling from the bottom boundary layer (e.g. Pickart 2000, Linder et al. 2004). Fratantoni and Pickart (2007) recently showed how the Middle Atlantic Bight shelfbreak front and jet is one component of a continuous flow along the western North Atlantic shelfbreak. Estimates of the Middle Atlantic Bight shelfbreak jet speed ranges from 0.2-0.3 m s^{-1} from climatology (Linder and Gawarkiewicz 1998) although synoptic sections can reveal faster flow speeds of 0.6 m s^{-1} (Rasmussen et al. 2005). The climatological jet width ranges from 10-15 km (Linder and Gawarkiewicz 1998), leading to Rossby numbers on the order of -0.1 on the onshore (anticyclonic) side of the jet and 0.4 on the offshore (cyclonic) side of the jet (Linder and Gawarkiewicz 1998). North of Cape Hatteras, Rossby numbers as large as 2 have been estimated for the shelfbreak jet (Gawarkiewicz et al. 2008).

Previous observational studies have identified upwelling near the shelfbreak from the bottom boundary layer into the interior along the density front. This upwelling leads to a detached bottom boundary layer, in which tracer gradients are weakened

along the isopycnal where upwelling occurs (Pickart 2000, Linder et al. 2004). Upwelling brings nutrients up from depth, supporting biological productivity, and hence its rate is important to quantify. Upwelling rates range from vertical velocities of 9 $\pm$ 2 m day^{-1} (Barth et al. 1998) and 23 m day^{-1} (Pickart 2000) from ADCP measurements, 4-7 m day^{-1} (Houghton and Visbeck 1998) and 6-10 m day^{-1} (Houghton et al. 2006) from dye tracer experiments, and an along-isopycnal vertical velocity of 17.5 m day^{-1} from a subsurface isopycnal float (Barth et al. 2004). The physical mechanisms that set the strength and structure of the front, jet, and upwelling remain an open question.

Past modelling studies have indicated that an offshore Ekman buoyancy flux acts as a control on the bottom boundary layer and the flow dynamics near the Middle Atlantic Bight shelfbreak. Modelling of the shelfbreak front includes three-dimensional approaches to examine the role of bottom friction in the adjustment of buoyant shelf flows. Chapman and Lentz (1994) examined the along-shelf evolution of a front formed by a buoyant discharge over a constant sloping shelf. Bottom Ekman transport advects lighter fluid under denser fluid and pushes the front offshore. When the front reaches the depth where the along-shelf vertical shear leads to a reversal in the cross-shelf Ekman flow, the coastal density front becomes trapped. Their model reveals vertical velocities of 4 m day^{-1} with the strongest upwelling occurring onshore of the density front. Yankovsky and Chapman (1997) derived an approximation for the trapping isobath given a specified buoyant inflow transport and density anomaly, and Chapman (2000) revised the estimate to include ambient stratification. Through numerical simulations, Chapman (2000) found that the estimate for the frontal trapping depth held well even with the inclusion of a shelfbreak into the model, in which the front was either located onshore or offshore of the shelfbreak. Chapman (2000) asked the question: "Is the shelf break dynamically important in determining the location of the shelfbreak front? If so, what are the dynamics. If not, are shelfbreak fronts located near the shelf break by coincidence?"

Other modelling studies examined the dynamical significance of the shelfbreak to

the formation of the front, jet, and upwelling. Gawarkiewicz and Chapman (1992) examined the along-shelf evolution of flows near the shelfbreak, in which vertical mixing induced by downslope Ekman advection of buoyancy created a density front that was formed at the shelfbreak. They considered cases with either initial or no lateral shear at the shelfbreak and noted in both cases the formation of a density front as well as upwelling. In their model with a uniform inflow, vertical upwelling at the shelfbreak is on the order of 4 m day^{-1}.

Previous studies have also applied one-dimensional bottom boundary layer models to explain how the bottom boundary layer structure changes about the shelfbreak. For a one-dimensional (vertical) along-isobath flow over a stratified sloping bottom, downslope Ekman advection of buoyancy leads to a thickening bottom mixed layer. Within this bottom mixed layer, isopycnals tilt downward toward the slope. Then, by thermal wind balance, vertical shear in the geostrophic flow leads to a weaker geostrophic flow near the bottom, weaker bottom stress, and weaker Ekman transport (e.g. MacCready and Rhines 1991, Trowbridge and Lentz 1991, Brink and Lentz 2009). This process can lead to a steady-state when the buoyancy anomaly shuts down the Ekman transport and occurs faster and leads to thinner bottom mixed layers for steeper slope angles or stronger stratification (e.g. Brink and Lentz 2009).

Chapman and Lentz (1997) examined the adjustment of a stratified along-isobath current over a slope and showed thicker (thinner) bottom mixed layers in regions of smaller (larger) slope angle for a linear background stratification. However, this model did not take into account the time-dependent adjustment to reach this state, which may result in Ekman pumping from convergences in the Ekman transport. The model also neglected the feedback of Ekman pumping on the along-isobath flow due to the assumption of flat isopycnals outside of the bottom mixed layer.

In a numerical model, Romanou and Weatherly (2001) examined the Ekman pumping arising from a spatially uniform along-isobath flow on a constant slope with increasing stratification downslope, an analogous configuration to a linearly stratified fluid with a steeper slope angle offshore of a shelfbreak. They showed that this

configuration generated Ekman pumping where the stratification changed, although they did not examine the feedback of this vertical flow on the geostrophic flow. They also indicated that this process could be applied at shelfbreaks with the generation of Ekman pumping, but, for this scenario, they did not give any estimates of the vertical velocity arising by buoyancy shutdown. Thus, further work is necessary to clarify the dynamical relevance of the shelfbreak and the coupling between Ekman flows and the buoyancy field in setting the location of the density front, the strength of the upwelling, the horizontal length scale over which it occurs, the structure of the interior ageostrophic secondary circulation, and its feedback into the geostrophic flow.

In this work, the adjustment of a laterally uniform along-isobath flow over a stratified shelfbreak is examined in order to address the following questions: (i) In the vicinity of the shelfbreak, what determines the height and temporal evolution of the bottom mixed layer arising from cross-isobath Ekman advection of buoyancy? (ii) What sets the strength of the Ekman pumping near the shelfbreak, where does this upwelling occur with respect to the shelfbreak, and over what lateral length scale? (iii) How does the secondary circulation driven by Ekman pumping impact the along-isobath flow, *i.e.* how does the secondary circulation accelerate the flow on the continental slope or decelerate the flow on the shelf? Can this secondary circulation form a jet near the shelfbreak?

These questions are first considered in section 4.2, in which scalings are derived to quantify the strength of the upwelling, the horizontal length scale over which the upwelling occurs, and the timescale for the interior along-isobath flow to accelerate over the slope due to the vertical circulation. The feedback of the along-isobath flow acceleration over the slope on the bottom boundary layer dynamics and upwelling is also considered. In section 4.3, a simple model of upwelling at the shelfbreak is presented to demonstrate the preferential formation of a jet near the shelfbreak. In section 4.4, process-oriented numerical simulations are run with application to the Middle Atlantic Bight shelfbreak in order to test these scalings and the hypothe-

sized structure for the secondary circulation and shelfbreak jet. In section 4.5, the role of mixing processes at the shelfbreak is discussed. Results from Gawarkiewicz and Chapman (1992) are compared with this model, and results from Romanou and Weatherly (2001) are interpreted in light of this model's scalings. Finally, in section 4.6, the main results of this study are summarized.

4.2 Theoretical formulation and scaling arguments

The adjustment of an along-isobath flow over a stratified shelfbreak is considered in a horizontally unbounded domain. The flow is assumed incompressible, Boussinesq, and hydrostatic with no along-isobath variations. At initial time, the density field is linearly stratified in temperature, with a constant buoyancy frequency N, and the background salinity field is constant. The initial along-isobath flow, U, is spatially uniform, geostrophically balanced by a tilted free surface, and downwelling favorable. For clarity, the along-isobath flow is denoted as U_{shelf} over the shelf and U_{slope} over the slope. The continental shelf is modelled as flat under the assumption that the local buoyancy shutdown timescale, discussed below, is long compared to the timescale for the dynamics of interest near the shelfbreak. The continental slope is modelled with a constant slope angle, θ, over a horizontal width L_{slope} that intersects the continental shelf at the shelfbreak, where there is a discontinuity in the slope angle. Farther offshore, the continental slope intersects a flat, deep region. The initial flow configuration is shown in figure 4-1a.

Next, the speed, length, and time scales that characterize the adjustment of the bottom boundary layer flow over the slope are considered. In the early stage of the along-isobath flow's temporal adjustment, an offshore Ekman flow develops within an inertial period, $\mathcal{T}_{inertial} = 2\pi/f$, where f is the planetary vorticity. Within this time period, the density field also goes through an initial adjustment, in which a bottom boundary layer forms over a height on the order of $u_*(fN)^{-1/2}$ (Pollard et al. 1973), where u_* is the friction velocity. This height scale characterizes the bottom boundary

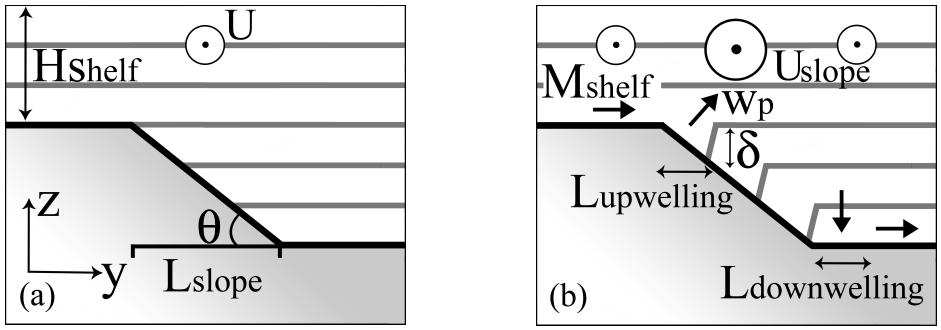

Figure 4-1: Stratified spindown over a shelfbreak. (a) At initial time, the along-isobath flow, U, is uniform. The density field is linearly stratified and isopycnals are indicated by the grey contours. The shelf is flat with a depth H_{shelf}. The slope is inclined at a constant slope angle, θ, over a width L_{slope} and intersects a deep, flat region.

(b) On the flat shelf, an offshore Ekman transport, M_{shelf}, passes over the shelfbreak and onto the slope, where it advects buoyancy downslope. When the bottom mixed layer has thickened to a depth δ, the Ekman transport on the slope is arrested. Thus, the Ekman transport converges over a horizontal length scale $L_{upwelling}$, which leads to Ekman pumping, $w_p \equiv w_{upwelling}$. Ekman pumping drives an interior secondary circulation on the slope, which accelerates the along-isobath flow, U_{slope}, over the slope. In this configuration, the secondary circulation closes offshore on the deep, flat region over a length scale $L_{downwelling}$, where there is a divergence in the Ekman transport.

layer height over the shelf for all time.

On the slope, the offshore Ekman flow advects buoyancy downslope, forming a bottom mixed layer that thickens in time until the Ekman flow is arrested by buoyancy shutdown. In the arrested state, the height of the bottom mixed layer is

$$\begin{aligned} \delta &= \frac{\Gamma U_{slope} f}{N^2 \theta}, \\ \Gamma &= \frac{1}{2}(1 + (1 + 4Ri^D S)^{1/2}), \end{aligned} \tag{4.1}$$

where $\Gamma \geq 1$ and accounts for nonzero stratification in the bottom mixed layer (Brink and Lentz 2009). In the above expression, the nondimensional parameters include the gradient Richardson number, $Ri^D = (\partial b/\partial z)/(\partial u/\partial z)^2$, which is constant in the arrested state. Note that $\partial b/\partial z$ is the vertical gradient in buoyancy and $\partial u/\partial z$ is the vertical shear in the along-shelf flow. The slope Burger number is given by $S = (N\theta/f)^2$, where the small slope angle approximation is applied. In the limit of a well-mixed bottom mixed layer, $\Gamma = 1$, the height scale reduces to the previously derived height scale

$$\delta_{TL} = \frac{U_{slope} f}{N^2 \theta} \tag{4.2}$$

that is presented in Trowbridge and Lentz (1991). The buoyancy shutdown timescale for downslope Ekman flow (Brink and Lentz 2009) is

$$\mathcal{T}_{shutdown} = \frac{\Gamma(1+S)U_{slope}}{2b_* r N S^{3/2}}, \tag{4.3}$$

where a linear bottom drag law is applied. In this expression, r is the linear drag coefficient, b_* is the ratio between the along-isobath flow speed near the bottom to its speed in the interior and $b_*^2 = 0.4$ is assumed. For small slope Burger numbers, this shutdown timescale is the same order of the buoyancy shutdown timescale estimated in Garrett et al. (1993).

The scale for the steady-state bottom mixed layer height is used to determine

scalings for the vertical upwelling near the shelfbreak, the horizontal length scale over which it occurs, and the timescale for the acceleration of the interior along-isobath flow over the slope. Over the upper part of the slope, a transition region develops between the Ekman transport on the shelf, M_{shelf}, that flows offshore of the shelfbreak unimpeded by buoyancy shutdown and the Ekman transport on the slope that is arrested due to thermal wind shear in a bottom mixed layer height given by (4.1). The isopycnal initially intersecting the shelfbreak is pushed offshore until this bottom mixed layer height is reached. The horizontal length scale between the shelfbreak and the offshore location of this isopycnal defines the horizontal boundary layer over which the Ekman transport converges. This convergence in the Ekman transport induces upwelling, $w_{upwelling}$, over a length $L_{upwelling}$. As illustrated in figure 4-1b, a geometric argument can be applied to determine the length scale over which the upwelling occurs, subject to the small slope angle approximation,

$$L_{upwelling} = \frac{\delta}{\theta} = \frac{\Gamma U_{slope}}{Sf}. \tag{4.4}$$

Given this length scale, the scaling for the strength of the upwelling,

$$w_{upwelling} = \frac{M_{shelf}}{L_{upwelling}} = \frac{SM_{shelf}f}{\Gamma U_{slope}}, \tag{4.5}$$

explicitly shows a slope Burger number dependence. The upwelling drives a secondary circulation that closes in the deeper part of the domain, where the slope intersects the flat bottom. The offshore Ekman transport advects water from the slope region onto the deep, flat region. In this flat region, offshore Ekman advection of buoyancy tilts the isopycnals within the bottom mixed layer and weakens the bottom stress. In contrast to the horizontal boundary layer over which upwelling occurs, the horizontal length scale over which downwelling occurs, $L_{downwelling}$, continually broadens in time as isopycnals are advected offshore. The focus of this study is on the upwelling at the shelfbreak since the location where the secondary circulation closes offshore may result from other processes over the slope other than a change in topography, e.g.

weakening stratification.

Over the slope, the interior secondary circulation accelerates the interior along-isobath flow and generates anticyclonic (cyclonic) vorticity in regions of vortex squashing (stretching) by Ekman pumping (suction). The timescale over which vertical relative vorticity is generated is determined from the linear along-isobath momentum equation and the continuity equation. In terms of vertical relative vorticity, $\zeta = -\partial u/\partial y$, where

$$\frac{\partial \zeta}{\partial t} = f\frac{\partial w}{\partial z}, \tag{4.6}$$

Ekman pumping near the shelfbreak drives the growth of anticyclonic vorticity in a flow with no initial lateral shear. This anticyclonic vorticity is characterized by a local Rossby number, $\epsilon = \zeta/f$, that is negative. The timescale for the generation of anticyclonic vorticity is determined from dimensional analysis. Near the shelfbreak, the vertical velocity is set by Ekman pumping near the bottom and reduces to zero at the surface by the rigid lid condition. Then, the timescale for anticyclonic vorticity to develop (denoted by the jet, ζ-subscript) is

$$\mathcal{T}_{jet,\zeta} = \frac{\epsilon H_{shelf}}{w_{upwelling}}. \tag{4.7}$$

If stratification is sufficiently strong, as noted in the next section, and the height of the secondary circulation is reduced to a Prandtl depth, H_P, then modifications to this expression are necessary. From the upwelling strength, (4.5), a larger slope Burger number leads to faster acceleration of the along-isobath flow over the slope. Note that the ratio of the timescale to generate anticyclonic vorticity of order ϵf to the buoyancy shutdown timescale is

$$\frac{\mathcal{T}_{jet,\zeta}}{\mathcal{T}_{shutdown}} = \frac{2b_* r \epsilon S^{1/2} N H_{shelf}}{(1+S) f M_{shelf}}. \tag{4.8}$$

This expression shows that the time scale separation between $\mathcal{T}_{jet,\zeta}$ and $\mathcal{T}_{shutdown}$ increases with increasing N and S (for small slope Burger numbers) and decreases with increasing S (for large slope Burger numbers greater than one) and increasing M_{shelf}. In the time-dependent model, these estimates for the strength of the upwelling and the length scale over which it occurs is subject to time-dependent feedback with the formation of the interior jet, which may influence the direct applicability of these scalings.

The temporal feedback between the bottom boundary layer and the interior flow can be examined by considering the above scalings subject to the linear drag parameterization. Then, the Ekman transport and Ekman pumping, (4.5), scales as

$$M_{shelf} = \frac{rb_* U_{shelf}}{f}, \tag{4.9}$$

$$w_{upwelling} = \left(\frac{Srb_*}{\Gamma}\right)\left(\frac{U_{shelf}}{U_{slope}}\right). \tag{4.10}$$

The horizontal length scale, L_{jet}, over which the horizontal flow varies and leads to jet acceleration is not known a priori. The secondary circulation's spatial structure that sets this length scale is examined in the next section. Here, suppose that time scales for changes in L_{jet} and U_{shelf} are long compared to $\mathcal{T}_{jet,\zeta}$ and that U_{slope} depends only on time. Then, from the linear along-isobath momentum equation and the continuity equation, the along-isobath flow near the shelfbreak over the slope evolves as

$$\frac{dU_{slope}}{dt} = \left(\frac{Sf^2 L_{jet}}{\Gamma H_{shelf}}\right)\left(\frac{M_{shelf}}{U_{slope}}\right). \tag{4.11}$$

The solution to this equation gives expressions for the temporal evolution of the interior along-isobath flow over the slope,

$$U_{slope}(t) = U(1 + 2t/\mathcal{T}_{jet,U})^{1/2}, \tag{4.12}$$

the Ekman pumping,

$$w_{upwelling}(t) = \frac{rb_* S U_{shelf}}{\Gamma U (1 + 2t/\mathcal{T}_{jet,U})^{1/2}}, \tag{4.13}$$

and the length scale over which it occurs,

$$L_{upwelling}(t) = \frac{\Gamma U (1 + 2t/\mathcal{T}_{jet,U})^{1/2}}{Sf}, \tag{4.14}$$

where

$$\mathcal{T}_{jet,U} = \frac{\Gamma H_{shelf} U^2}{Sf^2 L_{jet} M_{shelf}} \tag{4.15}$$

is the timescale for the along-isobath flow to accelerate (denoted by the jet, U-subscript) and $U_{slope}(t = 0) = U_{shelf} = U$. These expressions show the magnitude of the interior along-isobath flow over the slope grows as $t^{1/2}$, which strengthens the downslope Ekman buoyancy flux, thickening the bottom mixed layer and causing the upwelling region to widen in time as $t^{1/2}$. Then, this widening of the upwelling region weakens Ekman pumping, which decays as $t^{-1/2}$. This feedback, with increasing U_{slope}, also lengthens the buoyancy shutdown timescale, $\mathcal{T}_{shutdown}$. The timescale $\mathcal{T}_{jet,U}$ suggests that U_{slope}/U increases faster with weaker U and all other parameters fixed. These scalings and temporal relationships are tested in numerical simulations in section 4.4. In the next section, an examination of the interior secondary circulation's spatial structure over the slope shows that Ekman pumping leads to jet formation near the shelfbreak.

4.3 A simple model of jet formation at a shelfbreak

In this section, the spatial structure of a modelled secondary circulation over a slope reveals the formation of a shelfbreak jet by buoyancy shutdown of the Ekman transport on the slope. The secondary circulation structure is considered under the ap-

proximation that the topographic change in fluid height over the slope as small with respect to the fluid height over the shelf. This approximation enables an analytical examination of how topography modifies the secondary circulation, although this approximation may not hold for realistic shelfbreak configurations. This problem is formulated by considering the initial flow configuration in the previous section. In this section, the focus is on the interior flow, subject to the following equations for the subinertial, linear dynamics:

$$\begin{aligned}
\frac{\partial u}{\partial t} - fv &= 0, && (4.16)\\
fu &= -\frac{1}{\rho_o}\frac{\partial p}{\partial y}, && (4.17)\\
0 &= -\frac{1}{\rho_o}\frac{\partial p}{\partial z} + b, && (4.18)\\
\frac{\partial b}{\partial t} + N^2 w &= 0, && (4.19)\\
\frac{\partial v}{\partial y} + \frac{\partial w}{\partial z} &= 0, && (4.20)
\end{aligned}$$

where u is the along-isobath flow in the x-direction, v is directed positive offshore in the y-direction, and w is the vertical flow in the z-direction. Density is assumed only dependent on temperature, where $\rho = \rho_o + \hat{\rho}(z) - \rho_o b/g$ and $N^2 = -\frac{g}{\rho_o}\frac{d\hat{\rho}}{dz}$ is constant. The variable b is the buoyancy anomaly with respect to the background density field, $\rho_o + \hat{\rho}(z)$. The total pressure field is composed of contributions from the background density field and the dynamic pressure field, p.

From the continuity equation, the interior secondary circulation, ψ, is defined as

$$v = -\frac{\partial \psi}{\partial z},\ w = \frac{\partial \psi}{\partial y}. \qquad (4.21)$$

The component of the secondary circulation from the bottom boundary layer circulation is neglected. From the above equations, the interior secondary circulation

satisfies the Eliassen-Sawyer equation,

$$N^2 \frac{\partial^2 \psi}{\partial y^2} + f^2 \frac{\partial^2 \psi}{\partial z^2} = 0, \tag{4.22}$$

within $0 < y < L_{slope}, -H_{shelf} - \theta y < z < 0$.

The set-up of this problem is configured as discussed in section 4.2. The domain is configured with a flat shelf that intersects the continental slope at the shelfbreak at $y = 0$. The continental slope is inclined at a constant slope angle θ with respect to the horizontal and intersects a flat region at $y = L_{slope}$. In order to focus on the secondary circulation over the slope, the domain is considered horizontally unbounded onshore of $y = 0$ and offshore of $y = L_{slope}$. At the shelfbreak, Ekman pumping from the bottom boundary layer is represented as a delta-function in y and constant in time. At $y = L_{slope}$, Ekman suction into the bottom boundary layer is represented with a delta-function of the same magnitude but opposite sign. Along the bottom for $y < 0$ and $y > L_{slope}$, Ekman pumping and suction is zero to confine the interior secondary circulation to the slope. At the surface, a rigid lid approximation is applied and the vertical velocity is zero.

The interior secondary circulation is determined from these boundary conditions. For a semi-infinite domain as considered in Chapters 2 and 3, the height of the leading order secondary circulation is set by the Prandtl depth, $H_P = fL_{slope}/N$. In contrast to the previous chapters, the secondary circulation is also vertically confined to the height of the fluid column, $h(y)$, over the slope. The fluid height is specified as $h(y) = H_{shelf} + \theta y$, where the small slope angle approximation, $\sin\theta \approx \theta$, is applied.

The boundary conditions on ψ are

$$\psi = 0 \quad \text{at} \quad z = 0, \tag{4.23}$$

$$\psi = 0 \quad \text{at} \quad y \leq 0,\ z = -H_{shelf}, \tag{4.24}$$

$$\psi = 0 \quad \text{at} \quad y \geq L_{slope},\ z = -H_{shelf} - \theta L_{slope}, \tag{4.25}$$

$$\psi = \Psi \quad \text{at} \quad 0 < y < L_{slope},\ z = -H_{shelf} - \theta y, \tag{4.26}$$

where $\Psi > 0$. The variables are nondimensionalized by

$$y' = y/L_{slope},\ z' = z/H_{shelf},\ \psi' = \psi/\Psi, \tag{4.27}$$

where primes denote nondimensional variables. The nondimensional Eliassen-Sawyer equation, primes dropped, becomes

$$\mathcal{H}^2 \frac{\partial^2 \psi}{\partial z^2} + \frac{\partial^2 \psi}{\partial y^2} = 0, \tag{4.28}$$

within $-1 - \chi y < z < 0,\ 0 < y < 1$, where $\mathcal{H} \equiv H_P/H_{shelf}$ and $\chi \equiv \theta L_{slope}/H_{shelf}$. These two parameters control the spatial structure of the secondary circulation. The parameter $\mathcal{H}$ specifies whether the Prandtl depth or the fluid height over the shelf is more significant in controlling the vertical extent of the secondary circulation. The parameter χ describes the ratio of the change in fluid depth over the slope with respect to the fluid depth over the shelf. This examination is restricted to $\chi \ll 1$, since this parameter leads to a breaking of symmetry in the secondary circulation.

The nondimensional boundary conditions, primes dropped, become

$$\psi = 0 \quad \text{at} \quad z = 0, \tag{4.29}$$

$$\psi = 0 \quad \text{at} \quad y \leq 0,\ z = -1, \tag{4.30}$$

$$\psi = 0 \quad \text{at} \quad y \geq 1,\ z = -1 - \chi, \tag{4.31}$$

$$\psi = 1 \quad \text{at} \quad 0 < y < 1,\ z = -1 - \chi y. \tag{4.32}$$

In order to solve (4.28) subject to the above boundary conditions, the boundary condition (4.32) is expanded in a Taylor series about $z = -1$,

$$\psi(y, z = -1 - \chi y) = \psi(y, z = -1) + \frac{\partial \psi}{\partial z}(y, z = -1)(-\chi y) + \cdots = 1. \tag{4.33}$$

Furthermore, ψ is expanded in a power series of χ, where

$$\psi = \psi^{(0)} + \chi\psi^{(1)} + \ldots \tag{4.34}$$

The solution to ψ is determined to $O(\chi)$. At $O(1)$, the secondary circulation satisfies

$$\mathcal{H}^2 \frac{\partial^2 \psi^{(0)}}{\partial z^2} + \frac{\partial^2 \psi^{(0)}}{\partial y^2} = 0, \tag{4.35}$$

within $-1 < z < 0,\ 0 < y < 1$. This equation is solved subject to the boundary conditions

$$\psi^{(0)} = 0 \quad \text{at} \quad z = 0, \tag{4.36}$$

$$\psi^{(0)} = 0 \quad \text{at} \quad y \leq 0,\ z = -1, \tag{4.37}$$

$$\psi^{(0)} = 0 \quad \text{at} \quad y \geq 1,\ z = -1, \tag{4.38}$$

$$\psi^{(0)} = 1 \quad \text{at} \quad 0 < y < 1,\ z = -1. \tag{4.39}$$

The $O(1)$ solution is solved by separation of variables and is given by

$$\psi^{(0)} = \sum_{n=1}^{\infty} A_n^{(0)} \sinh\left(\frac{n\pi z}{\mathcal{H}}\right) \sin(n\pi y), \tag{4.40}$$

where

$$A_n^{(0)} = \frac{2}{n\pi}(-1 + (-1)^n)\mathrm{csch}\left(\frac{n\pi}{\mathcal{H}}\right). \tag{4.41}$$

At $O(\chi)$, the secondary circulation satisfies

$$\mathcal{H}^2 \frac{\partial^2 \psi^{(1)}}{\partial z^2} + \frac{\partial^2 \psi^{(1)}}{\partial y^2} = 0, \tag{4.42}$$

within $-1 < z < 0,\ 0 < y < 1$. This equation is solve subject to

$$\psi^{(1)} = 0 \quad \text{at} \quad z = 0, \tag{4.43}$$

$$\psi^{(1)} = 0 \quad \text{at} \quad y \leq 0,\ z = -1, \tag{4.44}$$

$$\psi^{(1)} = 0 \quad \text{at} \quad y \geq 1,\ z = -1, \tag{4.45}$$

$$\psi^{(1)} = \frac{\partial \psi^{(0)}}{\partial z}(y, z = -1)y \quad \text{at} \quad 0 < y < 1,\ z = -1. \tag{4.46}$$

By separation of variables, the solution to $\psi^{(1)}$ is

$$\psi^{(1)} = \sum_{m=1}^{\infty} A_m^{(1)} \sinh\left(\frac{m\pi z}{\mathcal{H}}\right) \sin(m\pi y), \tag{4.47}$$

where

$$\begin{aligned} A_m^{(1)} &= \left(\frac{2}{\mathcal{H}\pi^2}\right) \text{csch}\left(\frac{m\pi}{\mathcal{H}}\right) \sum_{n=1}^{\infty} (1 - (-1)^n) \coth\left(\frac{n\pi}{\mathcal{H}}\right) \\ &\times \left(\frac{(\cos(\pi(n-m)) - 1)}{(n-m)^2} - \frac{(\cos(\pi(n+m)) - 1)}{(n+m)^2} + \frac{\pi \sin(\pi(n-m))}{(n-m)}\right). \end{aligned} \tag{4.48}$$

Note that in the limit $n \to m, (\cos(\pi(n-m)) - 1)(n-m)^{-2} \to -\pi^2/2$ and $\sin(\pi(n-m))(n-m)^{-1} \to \pi$.

Figure 4-2 shows the secondary circulation to $O(\chi)$, where the values for $\mathcal{H}$ are chosen from the numerical model parameters in section 4.4 and χ is either 0 or 0.1 in order to demonstrate the changes to the structure of ψ. In the numerical model, the depth of the shelf is fixed to 100 m and the Prandtl depth is varied yielding $\mathcal{H} = 6.32, 4.0, 2.83$ for increasing stratification. At leading order, the structure of the secondary circulation is symmetric about $y = 0.5$. For increasing $\mathcal{H}$ (weakening stratification) the ψ-contours become increasingly flattened within the vertical domain.

In the next section, numerical experiments are run to test the scalings and hypotheses regarding the growth of the bottom mixed layer over the slope, the corresponding weakening in Ekman transport, the upwelling near the shelfbreak, the secondary circulation over the slope, and jet formation near the shelfbreak.

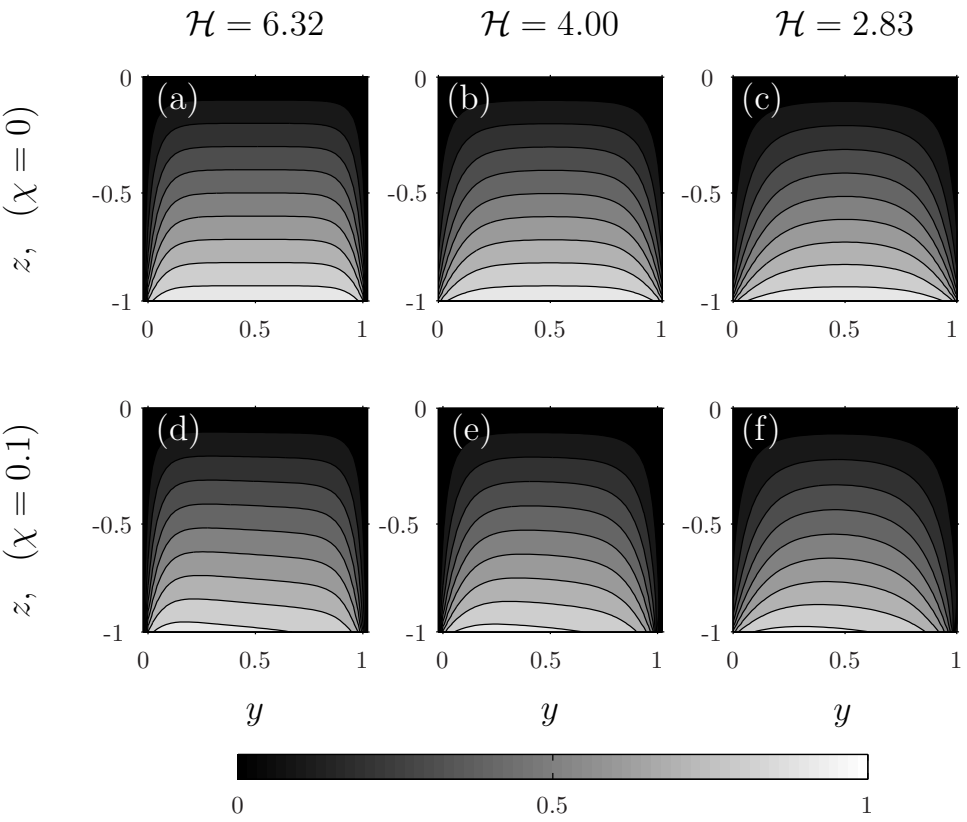

Figure 4-2: The structure of the secondary circulation, ψ, is shown for $\mathcal{H} = 6.32\ (a,d), 4.0\ (b,e), 2.83\ (c,f)$ and $\chi = 0\ (a,b,c), 0.1\ (d,e,f)$. Increasing χ leads to an asymmetrical structure in ψ, with stronger vortex squashing near the shelf-break than vortex stretching on the deeper side of the domain. ψ is contoured every 0.1 units.

At $O(\chi)$, the symmetry of the structure to ψ is broken by the tilting bottom slope, in which the secondary circulation closes offshore deeper down in the domain (not shown). Along a horizontal level, an increase in χ weakens the vertical gradient in ψ near the $z = -1$ geopotential on the offshore side of the domain. From (4.16), the along-isobath flow (in dimensional form) is

$$\frac{\partial u}{\partial t} = -f\frac{\partial \psi}{\partial z}. \tag{4.49}$$

Thus, increasing χ leads to preferential acceleration of the along-isobath near the shelfbreak rather than in the deeper domain offshore. In terms of vertical relative vorticity, (4.6), the formation of a jet near the shelfbreak is explained by an asymmetry in vortex squashing, near $y = 0$, and vortex stretching, near $y = 1$. On the offshore side of the domain, vortex stretching weakens for increasing χ because the vertical variation in the vertical velocity, which has its magnitude set by Ekman suction at the bottom, is weaker owing to a greater fluid depth. Therefore, stronger vortex squashing near the shelfbreak leads to jet formation near the shelfbreak rather than farther offshore.

4.4 Numerical experiments

In order to test the scalings for the flows and the structure of the shelfbreak jet, a series of numerical experiments were run using the Regional Ocean Modeling System (ROMS), which solves the hydrostatic, primitive equations in a terrain-following coordinate system. The model is configured with no along-isobath variations and density variations depend only on temperature variations. The horizontal domain is 80 km wide with a uniform horizontal grid spacing of 250 m. The domain has a 20 km flat shelf, a 20 km slope that is inclined to the horizontal at an angle θ, and a 60 km deep, flat region. Two slope angles are considered, $\theta = 0.01,\ 0.02$. In the vertical domain, the height of the water column over the shelf is fixed to 100 m and the height of the domain is 300 m for $\theta = 0.01$ and 500 m for $\theta = 0.02$. The vertical grid has 50 levels

and the vertical grid resolution ranges from $\Delta z = 1$ m at the bottom to $\Delta z = 8$ m in the interior for $\theta = 0.01$ or $\Delta z = 13$ m for $\theta = 0.02$.

At the surface, no heat flux and no momentum flux boundary conditions are applied. At the boundaries of the horizontal domain, open boundary conditions are applied, with no heat flux, no momentum flux, and the free surface height satisfying the Chapman condition. At the bottom, the no heat flux boundary condition is applied to the temperature field and bottom shear stress is specified with a linear drag law, $\tau_b/\rho_o = r\ \mathbf{u}_b$, where the linear drag coefficient is $r = 5.0 \times 10^{-4}$ m s^{-1} and $\mathbf{u}_b$ is the horizontal velocity at the first grid point above the bottom. The vertical mixing coefficients are determined from Mellor-Yamada Level 2.5 mixing scheme, which is Richardson number dependent. Background vertical mixing coefficients are set to 10^{-5} m^2 s^{-1}. The time step is 30 s. Biharmonic horizontal viscosity and diffusivity are applied with coefficients equal to 10^5 m^4 s^{-1}. The coefficient of thermal expansion is set to 2.2×10^{-4} °C^{-1} in the linear equation of state.

The model parameters are motivated by flow characteristics near the Middle Atlantic Bight shelfbreak. Uniform rotation is specified with $f = 10^{-4}$ s^{-1}. The initial along-isobath flow speeds are given by $U = 5,\ 10,\ 15,\ 20$ cm s^{-1} in a linearly stratified fluid, where $N^2 = (1.0,\ 2.5,\ 5.0) \times 10^{-5}$ s^{-2}. Table 4.1 summarizes the parameters used for each of these different runs and the corresponding scalings for δ, $L_{upwelling}$, $w_{upwelling}$, and $\mathcal{T}_{jet,\zeta}$. All simulations were run for 15.0 inertial periods.

Figure 4-3 illustrates the temporal evolution of the along-isobath flow, the temperature field, and the secondary circulation from Run 10. The secondary circulation has been low-pass filtered with a cut-off frequency of 0.12 f. In time, the along-isobath flow over the slope accelerates, in which $U_{slope}/U = 2$ by $t/\mathcal{T}_{shutdown} = 4.0$. The temperature field shows a thickening bottom mixed layer over the slope. The position of the isotherm that initially intersected the shelfbreak moves farther offshore along the bottom in time. At $t/\mathcal{T}_{shutdown} = 1.0$, the isotherm is located at 1.6 km, which is on the order of the upwelling length scale, $L_{upwelling} = 2.2$ km, estimated from initial flow parameters. In time, this isotherm is displaced farther offshore, surpassing

Table 4.1: Numerical model parameters. Note that for clarity the variables are labelled as $L_u \equiv L_{upwelling}$, $w_{up} \equiv w_{upwelling}$, $\mathcal{T}_{sh} \equiv \mathcal{T}_{shutdown}$, $\mathcal{T}_i \equiv \mathcal{T}_{inertial}$, and N^2 is shown in units of $\times 10^{-5} s^{-2}$. The scalings are determined from the initial flow parameters and the timescale for $\mathcal{T}_{jet,\zeta}$ corresponds to $\epsilon = 0.1$ and Ri^D is assumed equal to 0.25.

Run	N^2	θ	S	U (cm/s)	δ (m)	L_u (km)	w_{up} (m/day)	$\mathcal{T}_{sh}/\mathcal{T}_i$	$\mathcal{T}_{jet,\zeta}/\mathcal{T}_i$
1	1.0	0.01	0.10	5	51	5.1	2.7	14.2	5.2
2	1.0	0.01	0.10	10	102	10.2	2.7	28.4	5.2
3	1.0	0.01	0.10	15	154	15.4	2.7	42.5	5.2
4	1.0	0.01	0.10	20	205	20.5	2.7	56.7	5.2
5	2.5	0.01	0.25	5	21	2.1	6.4	2.7	2.1
6	2.5	0.01	0.25	10	42	4.2	6.4	5.3	2.1
7	2.5	0.01	0.25	15	64	6.4	6.4	8.0	2.1
8	2.5	0.01	0.25	20	85	8.5	6.4	10.7	2.1
9	5.0	0.01	0.50	5	11	1.1	12.3	0.8	1.1
10	5.0	0.01	0.50	10	22	2.2	12.3	1.7	1.1
11	5.0	0.01	0.50	15	33	3.3	12.3	2.5	1.1
12	5.0	0.01	0.50	20	45	4.5	12.3	3.4	1.1
13	1.0	0.02	0.40	10	55	2.8	10.0	4.8	1.4
14	2.5	0.02	1.00	10	24	1.2	22.6	1.2	6.1
15	5.0	0.02	2.00	10	14	0.7	40.0	0.5	3.4

the initial estimate of the length scale by $t/\mathcal{T}_{shutdown} = 2.0$. In between the location of this isotherm and the shelfbreak, the isotherms deflect upward, which suggests vertical advection of buoyancy by Ekman pumping and a thickening of the bottom mixed layer. The secondary circulation shows Ekman pumping near the shelfbreak with a ψ-contour deflecting upward from the shelfbreak into the interior before closing offshore. Note that small scale structures arise in the secondary circulation by $t/\mathcal{T}_{shutdown} = 4.0$. These small scale features are indicative of symmetric instability within the bottom mixed layer (see Allen and Newberger (1998) for a thorough discussion). Next, the measures corresponding to the length scale over which upwelling occurs, the Ekman pumping from the bottom boundary layer, and the acceleration of the along-isobath flow over the slope are examined in time.

First, the length scale over which upwelling occurs is considered. In section 4.2, the analytical scalings over the slope assume that the bottom mixed layer height

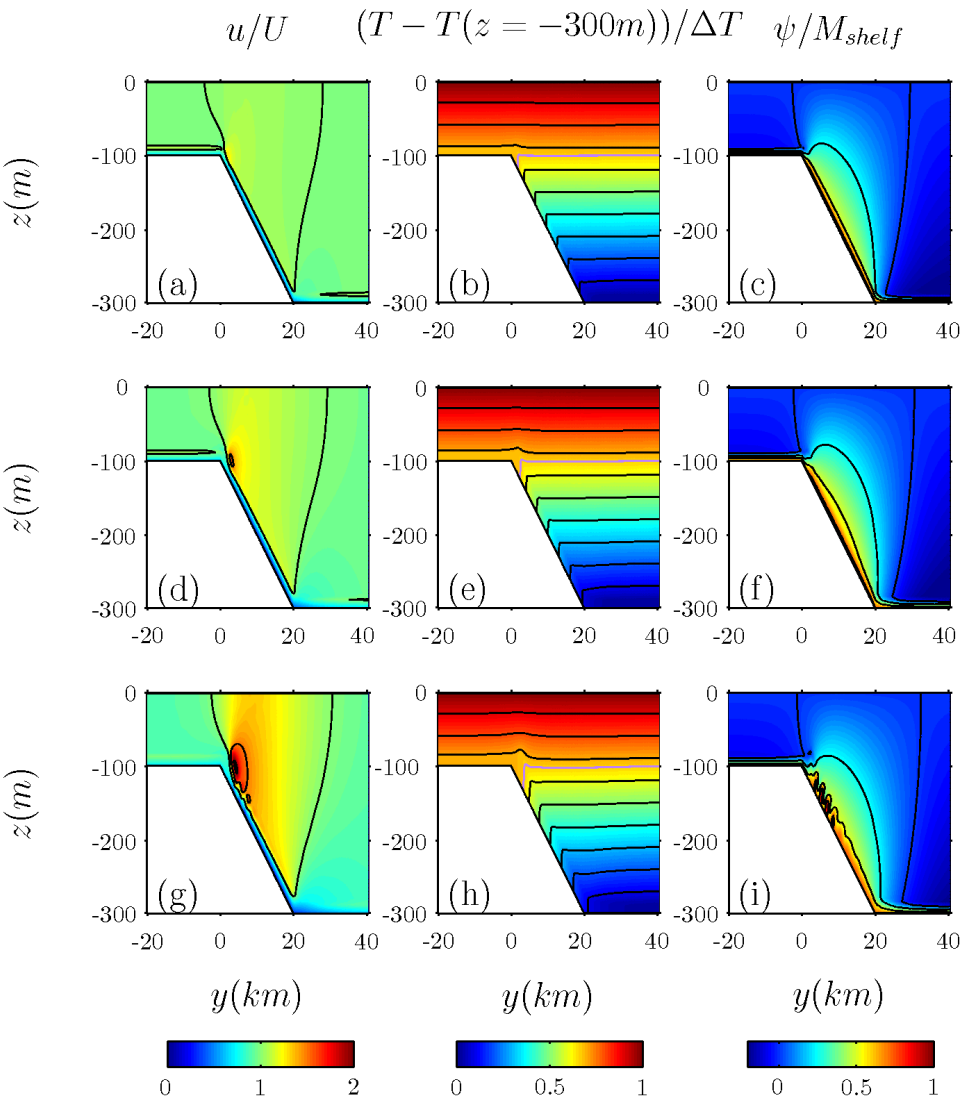

Figure 4-3: Run 10: temporal evolution. The adjustment of the along-isobath flow, where $U = 10$ cm s^{-1}, is shown at $t/\mathcal{T}_{shutdown} = 1.0$ (a,b,c), 2.0 (d,e,f), 4.0 (g,h,i). The along-isobath flow, u/U, is shown in (a,d,g) and is contoured at 1.0, 1.5, 2.0 units. The maximum along-isobath flow is $u/U = 1.3$ (a), 1.6 (d), and 2.1 (g). The temperature field, $T - T(z = -300m)/\Delta T$, is shown in (b,e,h), where ΔT is the change in temperature over 300 m. The temperature field is contoured every 0.1 units. The purple contour indicates the isotherm that initially intersected the shelfbreak. The horizontal distance of the isotherm at the bottom to the shelfbreak is $y = 1.8$ km (b), 2.5 km (e), and 3.3 km (h). The secondary circulation is shown in (c,f,i), where ψ is normalized by $M_{shelf} = 0.32$ m^2 s^{-1} and contoured every 0.25 units from zero. The maximum Ekman pumping is 4.1 m day^{-1} (c), 3.1 m day^{-1} (f), and 2.7 m day^{-1} (i). From the initial flow parameters, $L_{upwelling} = 2.2$ km and $w_{upwelling} = 12.3$ m day^{-1}.

reaches a thickness, δ on a buoyancy shutdown timescale. The bottom mixed layer corresponding to the isopycnal $\rho_{shelfbreak}$ that initially intersects the shelfbreak is also assumed to grow on this time scale. Then, the offshore position of this isopycnal sets a horizontal length scale over which the Ekman transport converges and drives Ekman pumping. From the simulations, Ekman pumping is calculated normal to the boundary and low-pass filtered. In figure 4-4, the time series for this isopycnal's offshore displacement evolves on the buoyancy shutdown timescale and correlates well with the offshore position of the maximum Ekman pumping. This correlation supports the assumption in section 4.2 that the offshore position of the isopycnal that is initially located at the shelfbreak sets the horizontal length scale of upwelling. In section 4.2, temporal feedback between the jet formation near the shelfbreak and the bottom boundary layer suggests that the buoyancy shutdown timescale increases with time, the bottom mixed layer continues to thicken, and the horizontal length scale over which upwelling occurs continues to widen past its initial estimate. Simulations run longer than a buoyancy shutdown time indicate that this feedback occurs as the positions for $\rho_{shelfbreak}$ and the maximum Ekman pumping extend beyond the $L_{upwelling}$ estimate from the initial flow parameters.

Next, the calculated maximum Ekman pumping, w_p, is examined with respect to the scaling for Ekman pumping, $w_{upwelling}$, from initial flow parameters. Figure 4-5 shows the temporal evolution of the nondimensional Ekman pumping in time, which reaches a local maximum within an inertial period. The calculated Ekman pumping is on the order of magnitude of the estimated Ekman pumping. However, the calculated Ekman pumping tends to be weaker than the estimated value for increasing stratification and decreasing initial along-isobath flow speed. From section 4.2, the temporal feedback between the acceleration of the along-isobath flow over the slope is hypothesized to widen the upwelling region and weaken Ekman pumping in time. Since the acceleration of the flow is hypothesized to occur faster for stronger Ekman pumping (larger S), the scaling for Ekman pumping from initial flow parameters may overestimate the strength of the upwelling for increasing S. Also, for the cases run

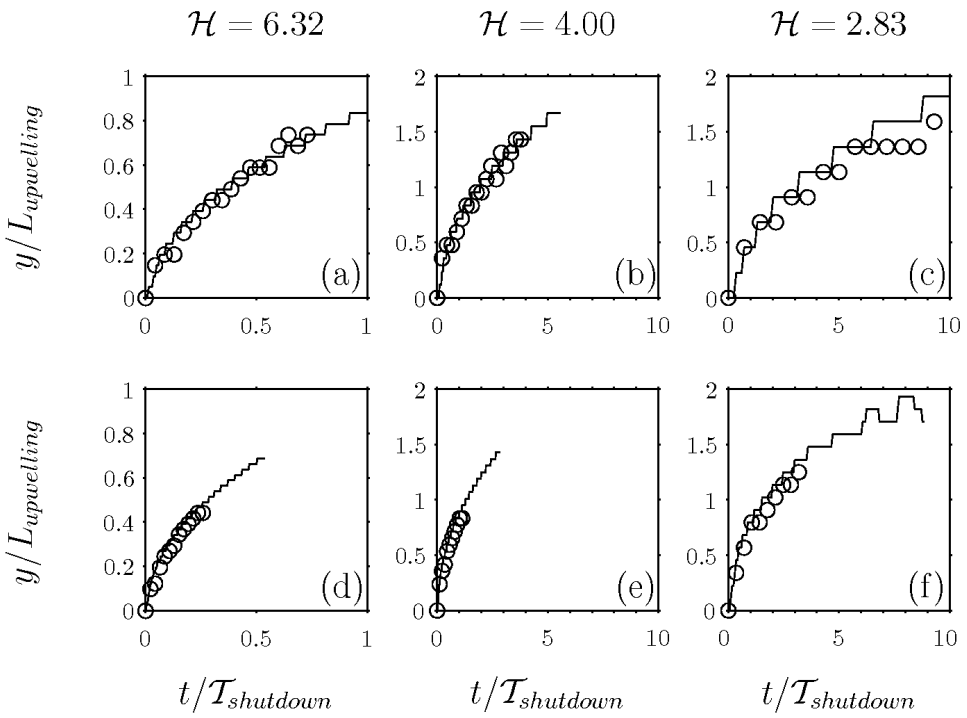

Figure 4-4: Upwelling length scale. With respect to the shelfbreak, the offshore position of the maximum Ekman pumping ($\circ$) is correlated with the position of the isopycnal $\rho_{shelfbreak}$ (solid line) that initially intersected the shelfbreak. The position of maximum Ekman pumping is shown every 0.6 inertial periods and its time series is truncated at the onset of symmetric instability. The profiles are shown for $\theta = 0.01$ and $U = 5$ cm s^{-1} (a,b,c) and $U = 10$ cm s^{-1} (d,e,f). The profiles correspond to $N^2 = 1.0 \times 10^{-5}$ s$^{-2}, \mathcal{H} = 6.32$ (a,d), $N^2 = 2.5 \times 10^{-5}$ s$^{-2}, \mathcal{H} = 4.00$ (b,e), and $N^2 = 5.0 \times 10^{-5}$ s$^{-2}, \mathcal{H} = 2.83$ (c,f). The variables are nondimensionalized with respect to the scalings derived from initial flow parameters for each of the runs, as presented in Table 4.1. In (f), the position of $\rho_{shelfbreak}$ oscillates at later times, deviating from the monotonic offshore displacement in the other profiles, which suggests that symmetric instability impacts the buoyancy field by upslope or downslope buoyancy advection.

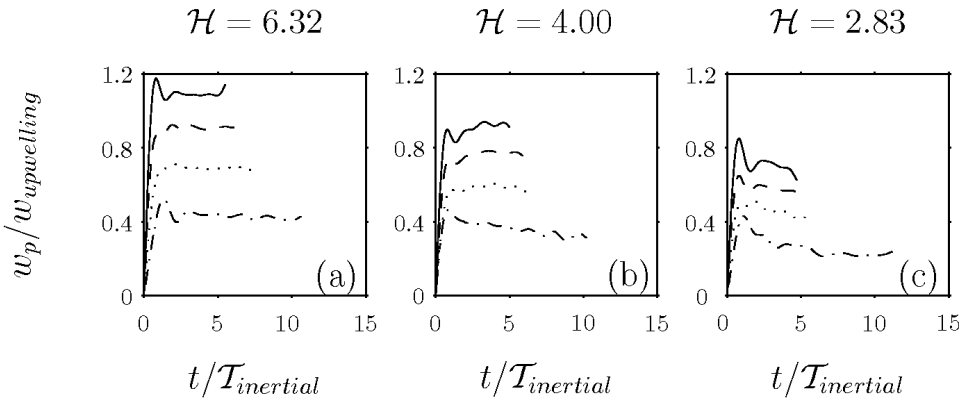

Figure 4-5: Maximum Ekman pumping. The ratio of the measured Ekman pumping, w_p, to the scaling, $w_{upwelling}$, determined from the initial flow parameters is shown in time. The runs corresponding to $\theta = 0.01$ are shown in (a) Runs 1-4: $N^2 = 1.0 \times 10^{-5}$ s^{-2}, $\mathcal{H} = 6.32$, $w_{upwelling} = 2.7$ m day^{-1}, (b) Runs 5-8: $N^2 = 2.5 \times 10^{-5}$ s^{-2}, $\mathcal{H} = 4.00$, $w_{upwelling} = 6.4$ m day^{-1}, and (c) Runs 9-12: $N^2 = 5.0 \times 10^{-5}$ s^{-2}, $\mathcal{H} = 2.83$, $w_{upwelling} = 12.3$ m day^{-1}. The curves correspond to initial along-isobath flow speeds of $U = 5$ cm s^{-1} (dot-dashed line), $U = 10$ cm s^{-1} (dotted line), $U = 15$ cm s^{-1} (dashed line), and $U = 20$ cm s^{-1} (solid line). The curves are truncated at the time that symmetric instability dominates the vertical velocity field near the bottom.

longer than a buoyancy shutdown time, notably figure 4-5c, the maximum Ekman pumping tends to weaken in time. The temporal feedback in (4.12) suggests that the ratio of the along-isobath flow over the slope to its initial speed accelerates faster for smaller initial flow speeds, thus leading to greater disparity between the calculated Ekman pumping and its initial estimate for smaller initial flow speeds.

The average Ekman pumping between 1.0 to 4.0 inertial periods is compared with the scaling for the upwelling strength for increasing slope Burger number in figure 4-6. For small slope Burger number, the scaling for the upwelling strength is on the order of the calculated Ekman pumping in the model. The deviation of the estimated upwelling strength from the initial flow parameters increases for increasing slope Burger number and decreasing initial flow speeds. The figure includes a line indicating weaker upwelling strength given $U_{slope}/U_{shelf} = 2$. This line accounts for temporal feedback with the along-isobath flow acceleration over the slope and a weakening of Ekman pumping in time. Ekman pumping from most of the runs fall between these two upwelling estimates. In comparison with previous work, Gawarkiewicz and

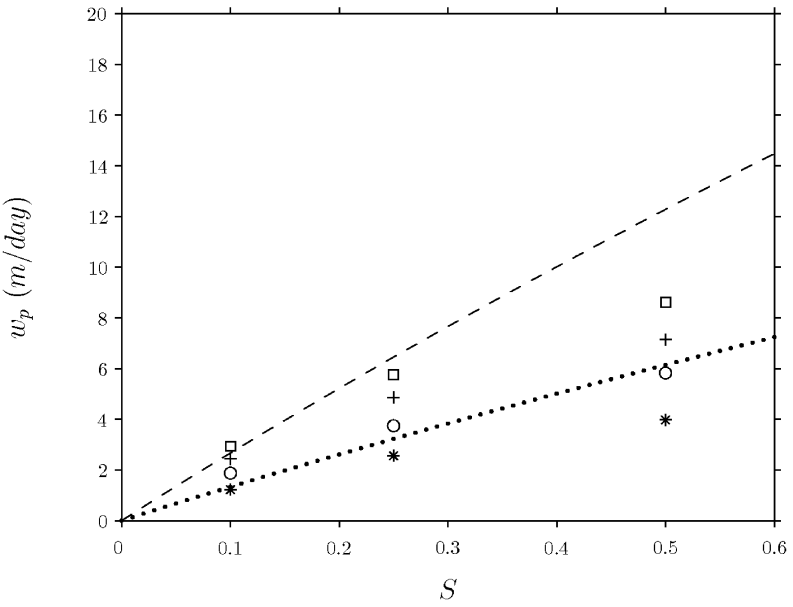

Figure 4-6: The average Ekman pumping, w_p, calculated from $t/\mathcal{T}_{inertial} = 1.0 - 4.0$, is shown with respect to S from the $\theta = 0.01$ runs. The symbols correspond to $U = 5$ cm s^{-1} ($*$), $U = 10$ cm s^{-1} ($\circ$), $U = 15$ cm s^{-1} ($+$), $U = 20$ cm s^{-1} ($\square$). The dashed line indicates the estimated $w_{upwelling}$ as a function of S from the initial flow parameters, where $U_{slope} = U_{shelf} = U$, and the dotted line corresponds to $w_{upwelling}$, where $U_{slope}/U_{shelf} = 2$.

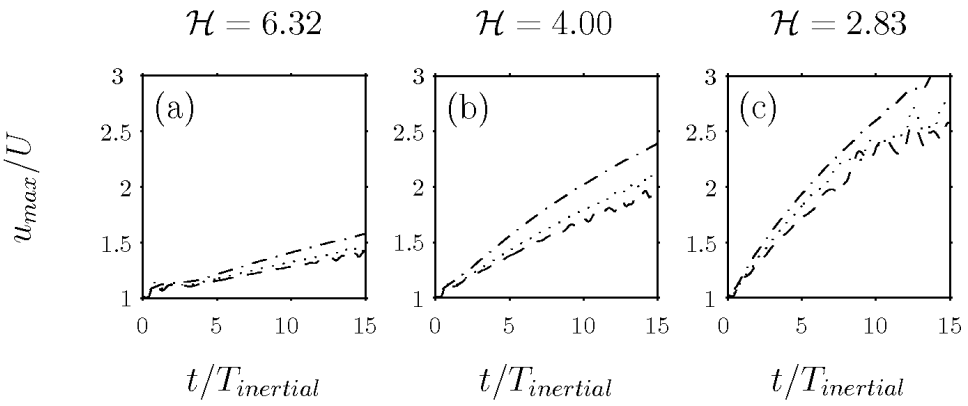

Figure 4-7: Normalized maximum along-isobath flow speed. The ratio of maximum along-isobath flow speed, u_{max}, over the slope to the initial along-isobath flow speed, U, is shown in time. The runs corresponding to $\theta = 0.01$ are shown in (a) Runs 1-3: $N^2 = 1.0 \times 10^{-5}$ s^{-2}, $\mathcal{H} = 6.32$, (b) Runs 5-7: $N^2 = 2.5 \times 10^{-5}$ s^{-2}, $\mathcal{H} = 4.00$, and (c) Runs 9-11: $N^2 = 5.0 \times 10^{-5}$ s^{-2}, $\mathcal{H} = 2.83$. The curves correspond to initial along-isobath flow speeds of $U = 5$ cm s^{-1} (dot-dashed line), $U = 10$ cm s^{-1} (dotted line), $U = 15$ cm s^{-1} (dashed line). For clarity, the curves corresponding to $U = 20$ cm s^{-1} (Runs 4, 8, 12) are not shown since they closely follow the $U = 15$ cm s^{-1} curves.

Chapman's (1992) model shows a vertical velocity of 4 m day^{-1} for a uniform inflow of 10 cm s^{-1} over a shelfbreak with $S = 0.36$ on the slope. Their model result falls within the estimated bounds on the upwelling strength.

The maximum along-isobath flow speed, u_{max}, over the slope is examined for each of the $\theta = 0.01$ simulations. The profiles in figure 4-7 show greater acceleration of the along-isobath flow with respect to its initial flow speed for increasing slope Burger number. This greater acceleration is due to increasing Ekman pumping for increasing slope Burger number. From the timescale $\mathcal{T}_{jet,U}$, the maximum along-isobath flow speed with respect to its initial speed, u_{max}/U, increases faster for increasing slope Burger number and weaker initial flow speeds with the other parameters kept fixed. The profiles for u_{max}/U qualitatively follow this pattern at early times, $t < 5$ inertial periods. The ratio u_{max}/U is larger for weaker initial along-isobath flow speeds, which is consistent with the predicted temporal evolution from (4.12). At later times, oscillations in the maximum along-isobath flow indicate the influence of symmetric instability on the geostrophic flow structure.

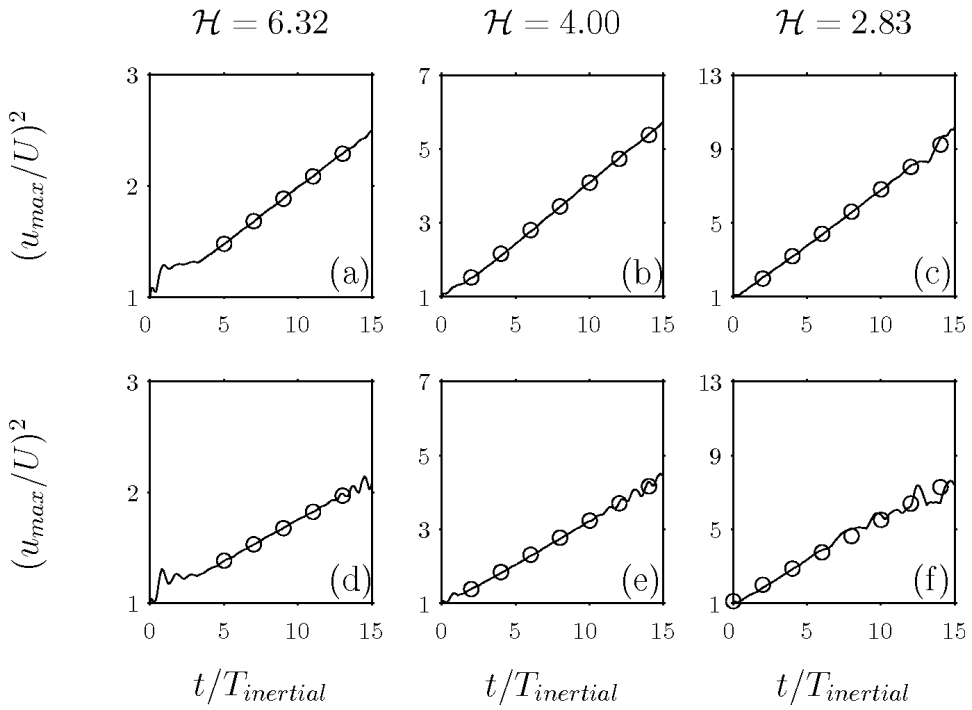

Figure 4-8: Normalized along-isobath flow speed squared. The square of the ratio of maximum along-isobath flow speed, u_{max}, over the slope to the initial along-isobath flow speed, U, is shown in time. The runs for $\theta = 0.01$ and $U = 5$ cm s^{-1} (a,b,c) and $U = 10$ cm s^{-1} (d,e,f) are shown. The curves ($\circ$) are fit to the numerical model solution (solid line) from $t/\mathcal{T}_{inertial} = 5.0-15.0$ for $U = 5$ cm s^{-1} and from $t/\mathcal{T}_{inertial} = 0-15.0$ for $U = 10$ cm s^{-1}. The profiles correspond to $N^2 = 1.0 \times 10^{-5}$ s^{-2}, $\mathcal{H} = 6.32$ (a,d), $N^2 = 2.5 \times 10^{-5}$ s^{-2}, $\mathcal{H} = 4.00$ (b,e), and $N^2 = 5.0 \times 10^{-5}$ s^{-2}, $\mathcal{H} = 2.83$ (c,f).

The predicted temporal structure of the interior along-isobath flow's evolution, (4.12), is tested by fitting linear curves to $(u_{max}/U)^2$. For $\theta = 0.01$, the curves are fit to the numerical model solution from $t/\mathcal{T}_{inertial} = 5.0 - 15.0$ for $U = 5$ cm s^{-1} and $t/\mathcal{T}_{inertial} = 0 - 15.0$ for $U = 10$, 15, 20 cm s^{-1}. Figure 4-8 shows a comparison of the data and the fitted curves for $U = 5$ cm s^{-1} and $U = 10$ cm s^{-1}. The agreement between the predicted temporal structure and the flow evolution in the model supports the temporal coupling between the interior along-isobath flow acceleration and the bottom boundary layer dynamics, with a widening region of upwelling and a weakening Ekman pumping. Given the predicted temporal structure, (4.12), the slope of the fitted curves is used to estimate the timescale $\mathcal{T}_{jet,U}$ and the length scale L_{jet} in the model. The results of these estimated values for all $\theta = 0.01$ cases are

Table 4.2: Linear curves are fit to the square of the ratio of the maximum along-isobath flow speed to its initial flow speed. From the initial flow parameters and the assumption that $Ri^D = 0.25$, the slope of the curve is used to determine $\mathcal{T}_{jet,U}$ and L_{jet}. The coefficient of determination, R^2, gives the fraction of variation in the data that is explained by the fitted curve and ranges in values from 0.96-0.99.

Run	N^2	θ	S	U (cm/s)	$\mathcal{T}_{jet,U}/\mathcal{T}_{inertial}$	L_{jet} (km)
1	1.0	0.01	0.10	5	19.7	1.3
2	1.0	0.01	0.10	10	27.4	1.9
3	1.0	0.01	0.10	15	31.3	2.5
4	1.0	0.01	0.10	20	34.6	3.0
5	2.5	0.01	0.25	5	6.2	1.7
6	2.5	0.01	0.25	10	8.6	2.5
7	2.5	0.01	0.25	15	10.3	3.1
8	2.5	0.01	0.25	20	11.1	3.9
9	5.0	0.01	0.50	5	3.3	1.7
10	5.0	0.01	0.50	10	4.5	2.5
11	5.0	0.01	0.50	15	5.1	3.3
12	5.0	0.01	0.50	20	5.3	4.2

shown in Table 4.2. The quantity L_{jet} ranges from approximately 1 to 4 km and shows a dependence on the initial flow speed as well as the slope Burger number.

Next, sections of the along-isobath flow are presented at long times for $\theta = 0.01$ and $\theta = 0.02$ in figure 4-9. These sections serve as measures of the time-integrated secondary circulation over the slope. As demonstrated in figure 4-7, increasing stratification for fixed slope angle leads to faster acceleration of the along-isobath flow over the slope. For increasing slope angle, the sections show that the magnitude of the along-isobath flow is stronger as well as more intensified near the shelfbreak. These sections are compared with the predicted secondary circulation structure in figure 4-2, although χ is no longer a small parameter. The simple model of jet formation near the shelfbreak suggests that the structure of the secondary circulation becomes increasingly asymmetrical over the slope for increasing χ, in which the deeper region leads to a greater vertical length scale for the secondary circulation. Thus, the jet forms near the shelfbreak due to stronger vortex squashing near the shelfbreak than vortex stretching over the deeper region offshore. In the numerical model, χ is dou-

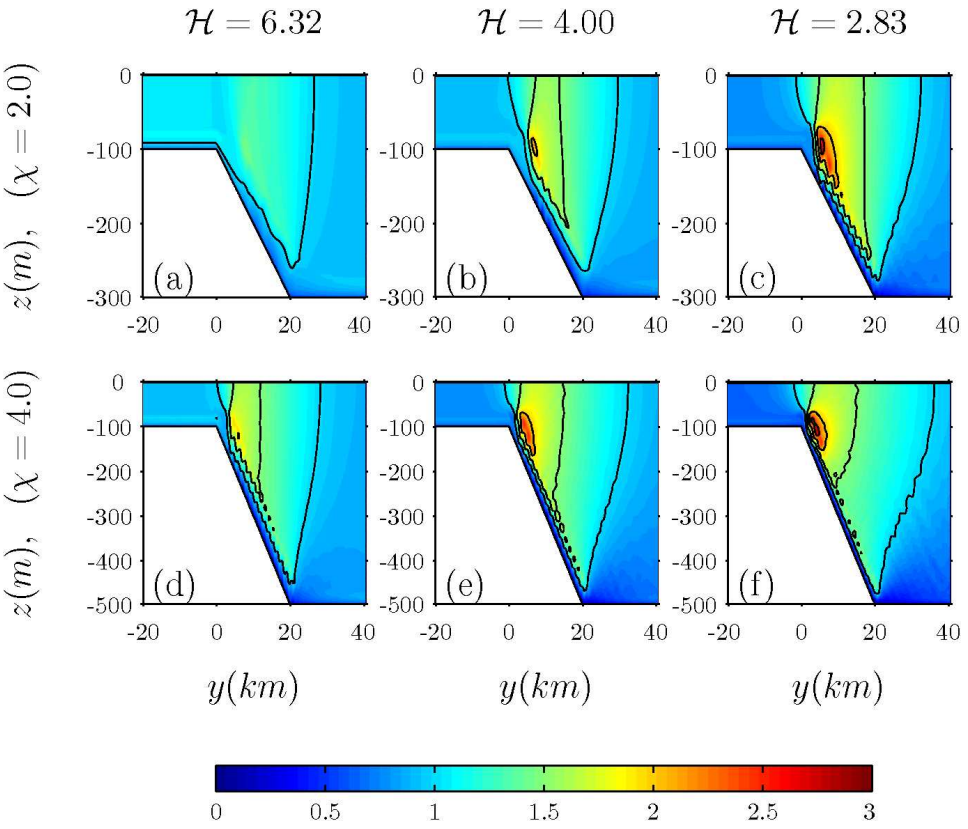

Figure 4-9: The along-isobath flow, u/U, is shown at $t/\mathcal{T}_{inertial} = 15.0$ for $U = 10$ cm s^{-1}. The flow is contoured every 0.5 units for $u/U \geq 1.0$. The sections are shown for the following cases (as well as the maximum flow speed at this time) :
(a) Run 2: $\theta = 0.01, N^2 = 1.0 \times 10^{-5} s^{-2}, (u_{max}/U = 1.4)$,
(b) Run 6: $\theta = 0.01, N^2 = 2.5 \times 10^{-5} s^{-2}, (u_{max}/U = 2.1)$,
(c) Run 10: $\theta = 0.01, N^2 = 5.0 \times 10^{-5} s^{-2}, (u_{max}/U = 2.7)$,
(d) Run 13: $\theta = 0.02, N^2 = 1.0 \times 10^{-5} s^{-2}, (u_{max}/U = 2.0)$,
(e) Run 14: $\theta = 0.02, N^2 = 2.5 \times 10^{-5} s^{-2}, (u_{max}/U = 2.5)$, and
(f) Run 15: $\theta = 0.02, N^2 = 5.0 \times 10^{-5} s^{-2}, (u_{max}/U = 2.8)$.

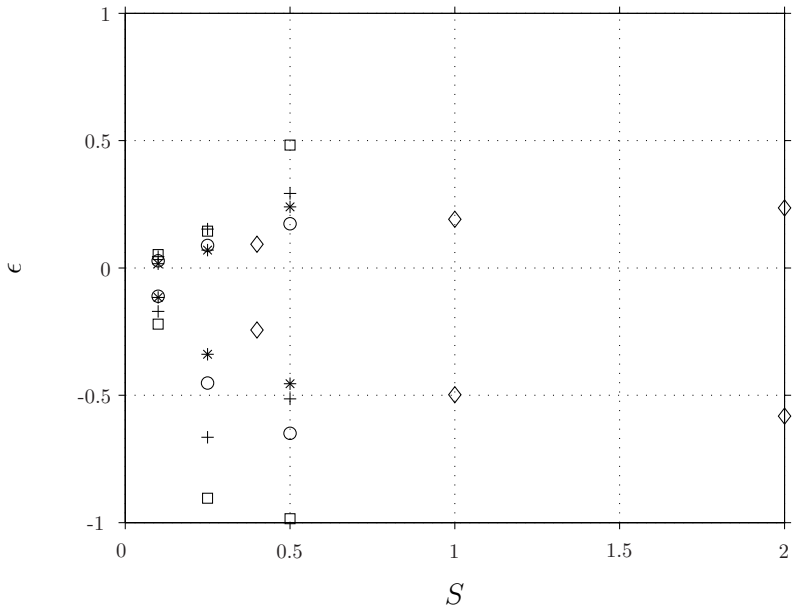

Figure 4-10: Jet Rossby number versus slope Burger number. The Rossby number onshore of u_{max} ($\epsilon < 0$) and offshore of u_{max} ($\epsilon > 0$) is estimated from all runs at $t = 15.0$ inertial periods. The symbols correspond to $U = 5$ cm s^{-1} ($*$), $U = 10$ cm s^{-1} ($\circ$), $U = 15$ cm s^{-1} ($+$), $U = 20$ cm s^{-1} ($\Box$) for $\theta = 0.01$. The ($\diamond$) symbol corresponds to $U = 10$ cm s^{-1} for $\theta = 0.02$.

bled with an increase in $\theta = 0.01$ to $\theta = 0.02$ with H_{shelf} and L_{slope} kept constant. These sections support the analytical scalings for the strength of the along-isobath flow, which increases for increasing slope Burger number. These sections also agree with the structure predicted by the simple model, in which the jet becomes more confined to the shelfbreak for increasing χ.

Finally, Rossby numbers are estimated with respect to either the anticyclonic (onshore) or the cyclonic (offshore) side of the jet. The Rossby number is calculated by first identifying the location of u_{max} over the slope. Then, the horizontal positions corresponding to $u_{max} + (u_{max} - U)/2$ are identified along the geopotential corresponding to the position of u_{max}. The distances between these horizontal positions and the location of u_{max} give length scales to measure the Rossby numbers on either side of the jet. The Rossby number is calculated from $(u_{max} - U)/2$ divided by the length scale and the planetary vorticity.

In figure 4-10, the calculated Rossby numbers are shown with respect to slope

Burger numbers from along-isobath profiles at $t = 15.0$ inertial periods. Two features are apparent. First, for $\theta = 0.01$, the Rossby number corresponding to anticyclonic vorticity tends to increase with increasing initial flow speed and slope Burger number. The maximum along-isobath flow increases with increasing initial flow speed and slope Burger number, while the horizontal length scale on the anticyclonic side of the jet remains nearly constant. For $S = 0.5,\ U = 15$ cm s^{-1}, this relationship appears not to hold because symmetric instability modifies the structure of the maximum geostrophic flow, which is located near the bottom boundary. On the cyclonic side of the jet, the relationship between the Rossby number and the slope Burger number is less clear.

Second, these estimates reveal an asymmetry in the Rossby number on either side of the jet. For $\theta = 0.01$, Rossby number magnitudes corresponding to anticyclonic vorticity are significantly larger than magnitudes corresponding to cyclonic vorticity. This relationship occurs because vortex squashing on the shallower side of the domain is stronger than vortex stretching on the deeper side. For $\theta = 0.02$ (an increase in χ), this asymmetry in Rossby number is less pronounced as the jet core is increasingly confined to the shelfbreak. The offshore length scale decreases and becomes comparable to the onshore length scale. Note that the Rossby numbers for $\theta = 0.02$ tend to increase in magnitude for increasing slope Burger number.

4.5 Discussion

In this section, mixing processes in the shelfbreak model and comparisons with previous numerical studies are discussed. Mixing processes enter into the flow evolution in two ways. First, the downslope Ekman buoyancy flux weakens the stratification, which enhances vertical mixing and thickens the bottom mixed layer on a buoyancy shutdown timescale. The redistribution of buoyancy modifies the cross-isobath pressure gradient and induces Ekman pumping offshore of the shelfbreak. Another mechanism, which has not been thoroughly explored in the present work, could also

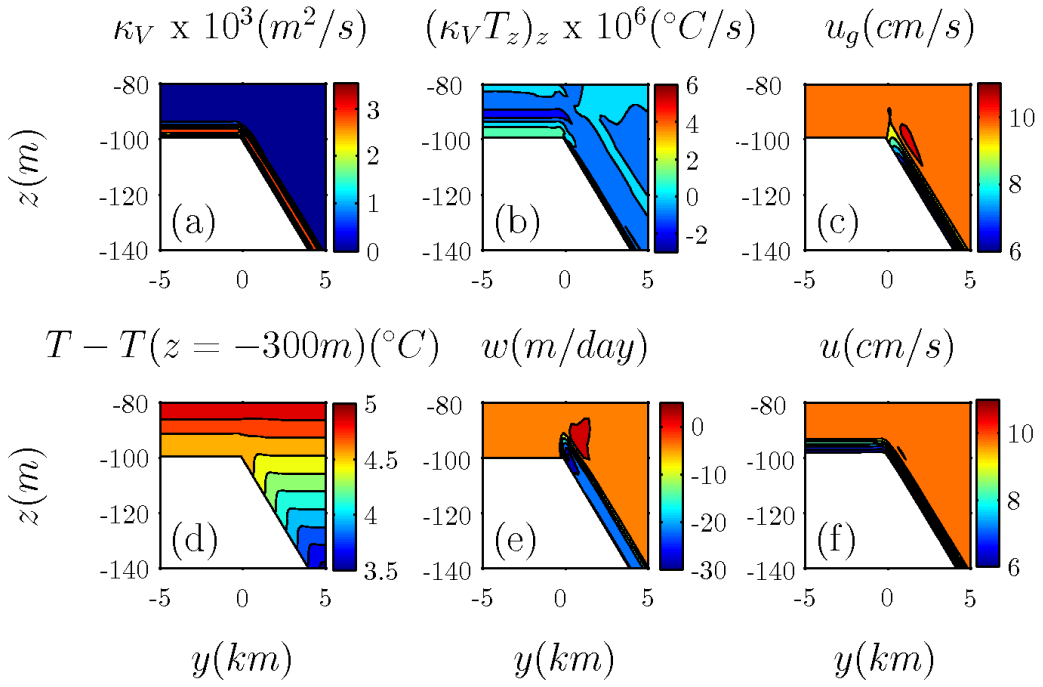

Figure 4-11: At t = 0.5 inertial periods, sections are shown from the $\theta = 0.01$, $N^2 = 5.0 \times 10^{-5}$ s^{-2}, $U = 10.0$ cm s^{-1} simulation for (a) the vertical diffusivity, (b) the vertical diffusion term in the temperature equation, (c) the geostrophic along-isobath flow, (d) the temperature field, (e) the vertical velocity, and (f) the along-isobath flow. Shear-driven mixing over the slope tilts the isopycnals and modifies the horizontal pressure gradient and the geostrophic flow in (c). The nonzero vertical velocity offshore of the shelfbreak may arise from convergences in the Ekman transport as a result of this buoyancy redistribution. In (a), the vertical diffusivity ranges from 10^{-5} m^2 s^{-1} in the interior to 3.5 x 10^{-3} m^2 s^{-1} in the bottom boundary layer. In (b), positive vertical diffusion leads to downward isopycnal tilting over the slope and is contoured every 1.0 x 10^{-6} °C s^{-1} from -3.0 x 10^{-6} °C s^{-1} to 7.0 x 10^{-6} °C s^{-1}. In (c), the geostrophic flow is computed from the horizontal pressure gradient force and is contoured every 0.75 cm s^{-1} from 6.0 cm s^{-1} to 10.5 cm s^{-1}. In (d), the isotherms are contoured every 0.15°C from 3.5°C to 5.0°C. In (e), the vertical velocity has a maximum value of 5.0 m day^{-1} and is contoured every 6.0 m day^{-1} from -28.0 m day^{-1} to 2.0 m day^{-1}. The negative vertical velocity reflects the downslope Ekman flow and the positive vertical velocity reflects flow out of the bottom boundary layer. In (f), the along-shelf flow is contoured every 0.75 cm s^{-1} from 6.0 cm s^{-1} to 10.5 cm s^{-1} and reveals the Ekman layer, where near bottom along-shelf flow is reduced, over the shelf.

modify the cross-isobath pressure gradient. Within an inertial period, the impulsively applied along-isobath flow causes shear-driven mixing, which leads to the formation of a bottom mixed layer (e.g. Pollard et al. 1973, Trowbridge and Lentz 1991). This redistribution of buoyancy could also modify the cross-isobath pressure gradient near the shelfbreak and induce Ekman pumping as shown in figure 4-11. In the case where the buoyancy shutdown timescale is significantly longer than an inertial period (e.g. figure 4-5a), the early onset of Ekman pumping in the model suggests that this process may be dominating over Ekman advection of buoyancy in modifying the cross-isobath pressure gradient at early times. However, Ekman advection of buoyancy can explain the longer time behavior in which along-isobath flow acceleration causes a thickening in the bottom mixed layer beyond the estimate from initial flow parameters and a weakening in Ekman pumping.

The two-dimensional shelfbreak configuration used in this model is similar to a cross-shelf section in the three-dimensional configuration used in Gawarkiewicz and Chapman (1992). For an upstream, uniform inflow over a shelfbreak, their model shows vertical homogenization of density over the shelf and a density front near the shelfbreak. In contrast, the model in this study shows a nonzero stratification over the bottom mixed layer on the shelf and does not show a density front along the bottom near the shelfbreak. These differences may be due to differences in the configuration of the shelf and the horizontal boundary conditions in the two models. In Gawarkiewicz and Chapman (1992), the shelf is inclined at an angle and intersects a coastal wall, whereas in this model, the shelf is flat and open boundary conditions are applied along the horizontal boundary. With an inclined bottom, downslope Ekman advection of buoyancy leads to vertical mixing of buoyancy and can vertically homogenize the density field over the shelf. Furthermore, with a coastal boundary, the secondary circulation driven by Ekman pumping at the shelfbreak must close on the shelf, leading to a region near the coastal boundary where an onshore interior flow turns downward and then offshore in the Ekman layer. This secondary circulation can advect isopycnals downward and then offshore, leading to a region of vertically

homogenized fluid near the boundary.

In contrast, this model uses a flat shelf, which precludes the possiblity of downslope Ekman advection of buoyancy driving vertical mixing. Furthermore, the open boundary condition on the shallower side of the domain allows an Ekman inflow into the domain and interior outflow. Thus, the secondary circulation on the shelf does not close in the domain. Then, the isopycnals near the horizontal boundary are not advected downward and then offshore. If the horizontal boundary were a wall, the closed secondary circulation may contribute to spindown of the geostrophic flow on the shelf, weakening the offshore Ekman transport, the Ekman pumping near the shelfbreak, and the acceleration of the along-isobath flow over the slope. These potential outcomes suggest that the choice of model configurations and boundary conditions can play an important role in setting the structure and temporal evolution of the flow and density fields at the shelfbreak.

Both this shelfbreak model and the Romanou and Weatherly (2001) constant slope model indicate that cross-shelf variations in the slope Burger number can lead to cross-shelf Ekman buoyancy flux variations and consequently Ekman pumping or suction. In their model, a downslope Ekman flow from a neutrally stratified region in the upper half of the domain proceeds into a linearly stratified region in the lower half of the domain. In this stratified region, a downslope Ekman buoyancy flux tilts the isopycnals downward, which arrests the Ekman flow and leads to Ekman pumping on the onshore side of the density front. From numerical simulations, they determine that the horizontal length scale over which the Ekman transport converges is on the order of 10 km. They state that this length scale is not known a priori.

However, from this shelfbreak model, the method for determining the upwelling strength and the length scale over which it occurs can be applied to the constant slope case. The bottom mixed layer within the stratified region will grow until reaching a height δ (4.1). The offshore Ekman transport, M_{shelf}, converges over a length scale $L_{upwelling}$ (4.4), and leads to Ekman pumping, $w_{upwelling}$ (4.5), from the bottom boundary layer. Figure 4-12 shows the configuration used in Romanou and Weath-

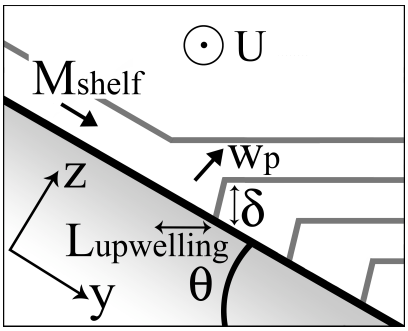

Figure 4-12: Ekman pumping at a density front, a reexamination of the Romanou and Weatherly (2001) model. At initial time, the along-isobath flow, U, is uniform. The density field is neutral in the upper half of the domain and linearly stratified below a certain depth (isopycnals are indicated by the grey contours). The boundary is inclined at a constant slope angle, θ, to the horizontal. The along-isobath flow drives a downslope Ekman transport, M_{shelf}, which advects buoyancy downslope in the stratified region. Within this region, the bottom mixed layer grows to a depth δ, at which time the Ekman transport is arrested by buoyancy shutdown. Thus, the Ekman transport converges over a horizontal length scale, $L_{upwelling}$, which leads to Ekman pumping, $w_p \equiv w_{upwelling}$. Ekman pumping drives an interior secondary circulation, but its horizontal and vertical structure depends on the horizontal and vertical boundary conditions.

erly (2001) and includes references to these scalings. In their model, N = 1.28 x 10^{-2} s^{-1}, θ = 2.4 x 10^{-3}, f = 6.3 x 10^{-5}s^{-1} so that $S = 0.24$. The initial along-isobath flow is U = 15 cm s^{-1}. Assuming that $Ri^D = 0.25$, application of (4.4) yields $L_{upwelling}$ = 10.6 km, which is consistent with their numerical model results. Thus, these scalings show that the horizontal length scale over which Ekman pumping occurs can be estimated a priori. Near the Middle Atlantic Bight shelfbreak, the region in which Ekman pumping will occur depends on the cross-shelf gradient in the slope Burger number. Thus, hydrographic observations can be used to identify regions of convergence and divergence in the Ekman transport around the shelfbreak front, assuming that buoyancy shutdown processes are significant to the dynamics.

4.6 Conclusions

The adjustment of an initially uniform geostrophic current over a shelfbreak leads to Ekman pumping and the formation of a jet near the shelfbreak. An offshore Ekman transport passes over the shelfbreak and onto the slope. On the slope, downslope Ekman advection of buoyancy forms a bottom mixed layer that thickens in time, weakening the bottom stress and the Ekman transport. This process creates a horizontal region in which the Ekman transport converges and leads to Ekman pumping. Ekman pumping drives an interior secondary circulation over the slope that closes offshore in the deep, flat region, where the Ekman transport diverges.

Scalings are derived for the strength of the upwelling, the length scale over which it occurs, and the timescale for jet formation near the shelfbreak. Time-dependent feedback between the jet and the bottom mixed layer is predicted to increase the length scale over which upwelling occurs, thereby weakening the Ekman pumping. This feedback increases the buoyancy shutdown timescale.

A simple model of the secondary circulation over the slope demonstrates two key parameters that control the structure of the secondary circulation. The first parameter, $\mathcal{H} \equiv H_{shelf}/H_P$, sets the vertical structure of the secondary circulation, in which the secondary circulation becomes more confined to the bottom for increasing stratification (decreasing H_P). The second parameter, $\chi = \theta L_{slope}/H_{shelf}$, also plays an important role in the secondary circulation's structure. For increasing χ, the secondary circulation becomes increasingly asymmetric about the middle of the slope due to a larger vertical length scale on the offshore, deeper side of the domain. Increasing asymmetry in the secondary circulation leads to more pronounced acceleration of the along-isobath flow near the shelfbreak and the formation of a shelfbreak jet.

Process-oriented numerical simulations are run to test the scalings and the hypothesized temporal and spatial structures of the flow. The cross-shelf position of the maximum Ekman pumping correlates with the bottom, cross-shelf position of the

isopycnal that initially intersected the shelfbreak. These positions evolve on a buoyancy shutdown timescale and are on the same order of magnitude as the predicted upwelling length scale from initial flow parameters.

Next, Ekman pumping from the model is compared with the scaling for Ekman pumping, which predicts an increase in Ekman pumping for increasing slope Burger number. The scaling for Ekman pumping is of the same order of magnitude as Ekman pumping in the model. The discrepency between the values and the temporal behavior of Ekman pumping in the model is a subject for future investigation. When along-isobath flow acceleration over the slope is taken into account, most values from the model fall within the bounds. A comparison with the Gawarkiewicz and Chapman (1992) model shows that the vertical velocity from their run with an initial laterally uniform along-isobath flow over the shelfbreak falls within the scaling bounds. In the model runs for $\theta = 0.01$, the maximum Ekman pumping is 8.5 m day^{-1}, which is within observed estimates. Thus, this scaling for Ekman pumping may provide a measure to compare with observed upwelling rates near the Middle Atlantic Bight shelfbreak front.

An examination of the along-isobath flow over the slope shows that it accelerates consistently with the predicted temporal evolution. The ratio u_{max}/U tends to grow faster for smaller initial flow speeds and larger slope Burger numbers. In most cases, the ratio $(u_{max}/U)^2$ temporally evolves as predicted, with a linear growth in time before the onset of symmetric instability. A jet forms near the shelfbreak which becomes more pronounced for increasing χ.

Other features arise that can modify the structure of the flow. Cross-isobath Ekman advection of buoyancy is shown to thicken the bottom mixed layer height but vertical advection of buoyancy can also increase the height. Offshore of the shelfbreak, vertical advection of buoyancy can lead to a thickening bottom mixed layer, which is analogous to Pickart's (2000) detached bottom boundary layer. Symmetric instability becomes evident in the temperature field, the secondary circulation, and the geostrophic flow. This feature modifies the structure of the bottom boundary

layer and can impact the dynamics and the scaling arguments presented here. Further work is necessary to quantify the impact of symmetric instability on the Ekman pumping, the interior secondary circulation, and the jet acceleration.

Chapter 5

Conclusions

The purpose of this dissertation is to examine the dynamics of frictionally driven flows over stratified sloping boundaries. The main idea explored in this work is that frictionally driven flows couple with the buoyancy field to redistribute tracers, modify Ekman pumping and suction, and influence the geostrophic vertical vorticity field through feedback with interior secondary circulations. In **Chapter 1**, previous research with a focus on observations is presented to identify unanswered questions on this subject and to motivate further examination of the coupled dynamics with analytical and numerical techniques. Theoretical frameworks are formulated and applied to investigate this coupling and feedback process. The following three scenarios are considered: the linear spindown of a laterally sheared along-isobath flow over a stratified slope inclined to the horizontal at a constant angle, the transition of linear spindown into the nonlinear regime, and the stratified spindown of an initially uniform along-isobath flow over a shelfbreak. This section summarizes the key findings of each chapter, places these findings in the context of previous research, and presents questions for future work.

In **Chapter 2**, the linear adjustment of a laterally sheared along-isobath flow is examined over a stratified sloping boundary inclined at a constant angle to the horizontal. An analytical framework for viscous, diffusive flows in a uniformly rotating fluid is used to examine how buoyancy forces and Ekman dynamics couple on

the insulated slope. The flow's linear adjustment consists of a component from the adjustment of the stratification, which leads to the generation of an upslope Ekman transport, as well as a component from the adjustment of the laterally sheared flow, which leads to the suppression of the laterally sheared initial Ekman transport.

Within this framework, the temporal adjustment of the stratification alone shows that diffusion causes the initially flat isopycnals to tilt in a thermal boundary layer adjacent to the slope. Then, the horizontal pressure gradient induces a geostrophic along-isobath flow and an upslope Ekman transport, which advects denser fluid upslope and tends to reduce the diffusive heating of the thermal boundary layer. In contrast to previous steady-state works (e.g. Thorpe 1987), the timescale is identified for the generation of upslope Ekman transport, under the assumption of small slope Burger numbers and order one Prandtl numbers. Furthermore, the time-dependent solution is shown to asymptote to Thorpe's (1987) steady-state solution.

Next, the temporal adjustment of the laterally sheared flow shows that the initial Ekman transport drives a downslope or upslope buoyancy flux, which buoyancy into or out of a thicker thermal boundary layer. This buoyancy flux causes the isopycnals to tilt within the thermal boundary, weakening the bottom stress and hence the Ekman transport. In the limit of small slope Burger numbers and order one Prandtl numbers, the buoyancy shutdown timescale considered in this case is equal to the buoyancy shutdown timescale in previous studies (e.g. MacCready and Rhines 1991). In contrast with previous works that did not have lateral variations (e.g. MacCready and Rhines 1991) or did not explicitly calculate the Ekman pumping and suction (Chapman 2002a), the time-dependent solution for Ekman pumping and suction is explicitly solved. A comparison of this solution with the classical stratified spindown solution over a flat bottom reveals the linear suppression of Ekman pumping and suction by buoyancy shutdown. The ratio of the spindown timescale to buoyancy shutdown timescale is the key parameter that determines the extent of coupling between the frictionally driven flow and the buoyancy field. When this ratio is order one, buoyancy shutdown weakens both Ekman pumping and suction at leading order.

Finally, the analytical theory is used to examine how the potential vorticity (PV) field is modified by frictional and diabatic processes near the sloping boundary. For small slope Burger numbers and order one Prandtl numbers, diabatic PV fluxes are shown to scale larger than frictional PV fluxes. In contrast to previous density-layered models (e.g. Williams and Roussenov 2003), which did not clarify the coupling between frictional and diabatic forcings, this work shows that frictional processes can drive diabatic PV fluxes and diabatic processes can drive frictional PV fluxes in a continuously stratified model. Furthermore, Ekman components dominate the diabatic and frictional PV fluxes but cancel in the total PV flux, which suggests that an estimate of the total PV flux by the magnitude of either contribution alone can lead to an overestimate of the total PV flux. The ratio of the initial Ekman transport to the steady-state upslope Ekman transport determines the relative contributions to the total PV flux from adjustment of the laterally sheared flow and the adjustment of the stratification. Diffusion of the stratification extracts PV, while upslope (downslope) Ekman flows tend to input (extract) PV. Finally, a scaling for the change in the area-integrated PV shows that the slope Burger number also controls the amount of PV extracted from or input into the system.

In **Chapter 3**, homogeneous or stratified spindown over a flat bottom as well as stratified spindown over a sloping bottom are examined for increasing nonlinearity. This work reveals an asymmetry that arises in Ekman pumping and suction as well as an asymmetry in the spindown of cyclonic and anticyclonic vorticity. The adjustment of a laterally sheared geostrophic flow with sinusoidal lateral shear is used to contrast the relative roles of momentum advection and nonlinear buoyancy advection in these asymmetries.

For nonlinear homogeneous spindown over a flat bottom, previous works indicate an asymmetry in Ekman pumping and suction at order Rossby number (e.g. Hart 2000), where Ekman pumping is weaker than Ekman suction. Other works (e.g. Zavala Sansón and van Heijst 2000) note that cyclonic vorticity decays faster than anticyclonic vorticity for increasing Rossby number. In order to synthesize these two

features in time-dependent spindown, a uni-directional geostrophic flow is expanded to order Rossby number. The general solution shows that time-dependent feedback between lateral advection of momentum in the interior and the interior geostrophic flow is an important contribution which enhances the time-dependent asymmetry in Ekman pumping and suction. Furthermore, the solution shows that lateral advection of momentum in the interior causes cyclonic vorticity to decay faster than anticyclonic vorticity. Thus, stretching and squashing of vertical relative vorticity dominates over stretching and squashing of planetary vorticity by nonlinear Ekman pumping and suction in setting the asymmetry in spindown of vertical relative vorticity.

For nonlinear stratified spindown over a sloping bottom, the linear analysis from the preceding chapter is extended into the nonlinear regime. An analytical expansion shows that nonlinear Ekman advection of buoyancy leads to a correction to the flow that can scale larger than order Rossby number corrections by momentum advection. A theoretical formulation shows that nonlinear Ekman advection of buoyancy leads to *nonlinear buoyancy shutdown*, in which the bottom stress is suppressed to a greater extent in regions of cyclonic flow than regions of anticyclonic flow. Vertical advection of buoyancy in the thermal boundary layer tends to enhance this effect. This distribution of buoyancy enhances suppression of Ekman pumping over Ekman suction. Then, since the correction to Ekman pumping and suction can scale larger than order Rossby number, stretching and squashing of planetary vorticity can dominate over stretching and squashing of vertical relative vorticity in setting the asymmetrical decay of vertical relative vorticity. Numerical experiments support the analytical analysis and show that anticyclonic vorticity can decay faster than cyclonic vorticity when nonlinear advection of buoyancy dominates over momentum advection. For flows over upper continental slopes, where timescale estimates, e.g. on the order of a day, indicate that buoyancy shutdown may be important to the Ekman flow, corrections to Ekman pumping and suction by nonlinear buoyancy shutdown can enter into the leading order dynamics. Then, an asymmetry in Ekman pumping and suction may arise and lead to faster spindown of anticyclonic vorticity than cyclonic vorticity

outside of the bottom boundary layers.

In **Chapter 4**, the adjustment of an initially uniform along-isobath flow over a stratified shelfbreak is examined. This work investigates the dynamical significance of the shelfbreak, a questioned posed in previous research. The adjustment process demonstrates how coupling between the Ekman flow and the buoyancy field leads to the generation of Ekman pumping and jet formation near the shelfbreak. From a flat shelf, an offshore Ekman transport flows past the shelfbreak and onto the slope, where downslope Ekman advection of buoyancy forms a thickening bottom mixed layer which weakens the bottom stress. Then, a horizontal boundary layer forms over which the Ekman transport converges and leads to Ekman pumping. Ekman pumping drives an interior secondary circulation that accelerates the along-isobath flow over the slope. Scalings are derived for the upwelling strength, the length scale over which it occurs, and the timescale for jet formation.

An analytical analysis of the secondary circulation over the slope reveals that the horizontal structure of the secondary circulation becomes increasingly asymmetrical for an increasing change in fluid depth over the slope with respect to the fluid depth over the shelf. This asymmetrical structure leads to the preferential formation of a jet near the shelfbreak.

Temporal feedback between the accelerating flow over the slope and the bottom boundary layer dynamics is also considered. An accelerating along-isobath flow thickens the bottom mixed layer, widens the upwelling region, and weakens Ekman pumping. Thus, this feedback increases the buoyancy shutdown timescale as well as the timescale for along-isobath flow acceleration over the slope.

Process-oriented numerical simulations are used to further explore the coupled dynamics, test the scalings, and the hypothesized temporal evolution and spatial structure of the flow. Agreement between the maximum Ekman pumping, the maximum along-isobath flow over the slope, and the width of the upwelling region in the model with the analytical scalings and predicted evolution suggest that these scalings may be used in understanding flow features near shelfbreaks. Ekman pumping by

buoyancy shutdown is comparable to observed rates of upwelling near the Middle Atlantic Bight shelfbreak front.

Future work

The theoretical work presented in this thesis provides motivation for future numerical and observational studies. In this section, ideas for future research are presented. In Chapter 2, diabatic and frictional processes along the stratified sloping boundary lead to potential vorticity input and extraction from the ocean. However, the modified potential vorticity remains confined within the thermal boundary layer as the non-eddying model is not able to transmit this modified potential vorticity into the quasi-inviscid interior. Future numerical work is necessary in order to understand how this modified potential vorticity is transferred into the interior and the role of these processes in setting the structure of potential vorticity in the deep ocean and, for example, deep western boundary currents. Stratified sloping boundaries serve as sources or sinks of potential vorticity and their net effect on the circulation still remains to be quantified.

In Chapter 3, the relative roles of momentum and buoyancy advection in the dynamics of nonlinear spindown show that nonlinear buoyancy advection can dominate the frictionally driven circulation, modifying both the vertical circulation as well as the spindown of cyclonic and anticyclonic vorticity. The two-dimensional analysis considered here raises the question of how this process could modify not only the structure of narrow boundary currents but the spindown of small scale, geostrophically balanced eddies or vortices over stratified sloping topography. The coupling between the Ekman flow and the buoyancy field may lead to a vertical circulation and an asymmetrical spindown of vorticity with a temporal and spatial structure unlike that predicted for a homogeneous fluid. For increasing Rossby number, the characteristics of three-dimensional instabilities that may arise during the adjustment process remain to be explored.

In Chapter 4, an analytical and numerical examination of coupling between the Ekman flow and the buoyancy field leads to upwelling and jet formation near the shelfbreak. The numerical study chose parameter regimes applicable to the Middle Atlantic Bight shelfbreak front. This work could potentially be extended to other shelfbreak currents, such as in the Beaufort Sea where a halocline exists at depth, or in the Irminger Sea. Application of the scaling for upwelling by buoyancy shutdown requires hydrographic information on the cross-isobath buoyancy gradients at the bottom as well as velocity measurements of the geostrophic along-shelf flow.

Future observational studies are necessary to test the extent to which buoyancy shutdown processes play a crucial role in setting the position of the shelfbreak front, the upwelling along the front, and the strength of the shelfbreak jet. In contrast to the two-dimensional shelfbreak problem examined in this work, flow temporal variability, three-dimensional instability, as well as surface and offshore forcing complicate the dynamics of the observed shelfbreak front. The relative roles of these processes and bottom boundary layer processes to the shelfbreak front is subject to further investigation.

Appendix A

Nonlinear corrections to Ekman pumping in stratified spindown

In this appendix, the nonlinear corrections to Ekman pumping are documented for an along-isobath flow that is initially $u = U\cos(y/L)$ during stratified spindown over a flat or sloping bottom. The purpose of documenting these corrections is to show how frictionally driven secondary circulations can couple with the buoyancy field to modify both the strength and lateral structure of Ekman pumping. In Chapter 3, these nonlinear corrections are used to contrast the roles of momentum advection and buoyancy advection in setting the asymmetry in Ekman pumping and suction. In contrast to homogeneous spindown over a flat bottom, buoyancy advection by the secondary circulation can modify Ekman pumping at a lower order than at order Rossby number. These corrections are listed from lowest to highest order up to order Rossby number under the following assumptions. In Chapter 2, over a sloping bottom, $\sigma = O(1)$, $\epsilon < \sigma^{-1/2}E^{1/4} < 1$, $S < 1$, $\sigma S > E^{1/2}$ and $M_{initial}/M_{Thorpe} > 1$. Over a flat bottom, the corrections are listed in order subject to the first two of these assumptions.

The higher order corrections are denoted by a superscript, $n > 1$. Note that the leading order Ekman pumping scales as $E^{1/2}\Gamma U$ for $n = 0$ and this scaling has been factored out from the corrections. The magnitude, lateral structure, and sign of the

correction to Ekman pumping is presented and the corresponding nondimensional equations used to determine that structure is also presented when necessary. The equations not listed in the below documentation are the linear equations previously given in Chapter 2 subject to a flat or sloping bottom. At the end of Chapter 3, these corrections to Ekman pumping are used to interpret the temporal and spatial structure of Ekman pumping for increasing Rossby number for homogeneous spindown, stratified spindown over a flat bottom, and stratified spindown over a sloping bottom.

A.1 Flat bottom

For stratified spindown over a flat bottom, there are five corrections to Ekman pumping, $w_p \equiv \widetilde{w}_i(z=0)$, to order Rossby number.

1.a. $w_p^{(1)} \propto \sigma^{-1/2} E^{1/4} \sin(y)$.
Vertical advection of the laterally uniform buoyancy anomaly, $\overline{b}_T$, as shown in

$$\frac{\partial \widetilde{b}_T^{(1)}}{\partial t} + \widetilde{w}_i^{(0)}(z=0)\frac{\partial \overline{b}_T}{\partial \xi} = \frac{1}{2}\frac{\partial^2 \widetilde{b}_T^{(1)}}{\partial \xi^2}, \tag{A.1}$$

reduces the total tilt of isopycnals in the thermal boundary layer. This reduction in tilting of isopycnals leads to anomalously lower (higher) pressure in the cyclonic (anticyclonic) region and a horizontal pressure gradient that enhances the Ekman transport in phase with the Ekman transport in the linear approximation. Thus, this correction to Ekman transport enhances the leading order Ekman pumping and suction. In the wind forced problem, Thomas and Rhines (2002) note that vertical advection of the laterally uniform buoyancy anomaly in the surface thermal boundary layer is necessary for an accurate representation of the temperature field and the flow evolution. This nonlinear correction is solved numerically in time in Appendix B.1. Ekman pumping at $y = \pi/2$ is plotted in figure A-1 with and without this nonlinear

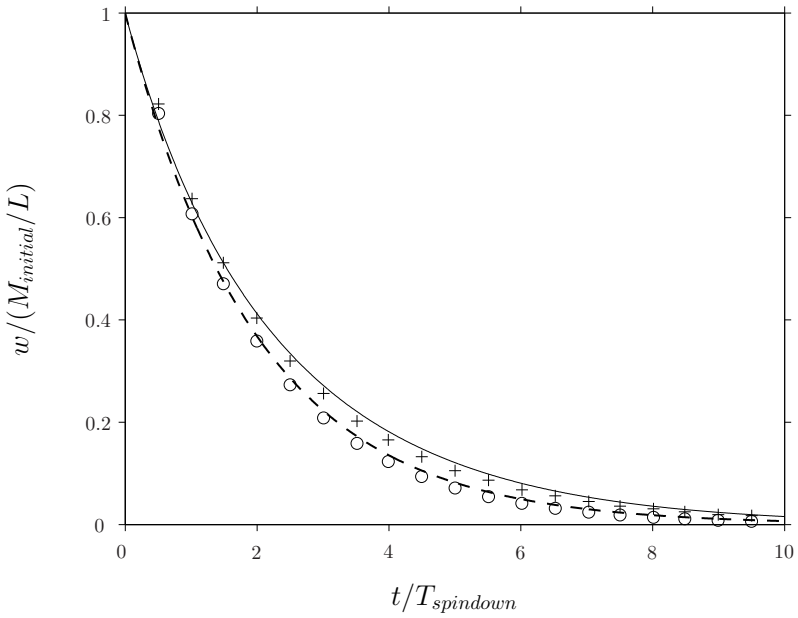

Figure A-1: Ekman pumping at $y = \pi/2$ increases from its linear analytical solution (dashed line) when the $O(E^{1/4})$ correction is included (solid line). Ekman pumping is measured by the vertical velocity evaluated at $z' = 0.08$ in the numerical model and by $w_i(z = 0)$ in the analytical model. Numerical simulations, where $\epsilon = 0.01, \sigma = 1$, and $E^{1/4} = 0.16$, show that this nonlinear correction can account for the greater Ekman pumping in stratified spindown than in homogeneous spindown over a flat bottom. The filtered Ekman pumping solution from homogeneous spindown (o) decays over the timescale $\mathcal{T}_{spindown} = E^{-1/2} f^{-1}$, where $E = (\delta_e/H)^2$. The filtered Ekman pumping solution from stratified spindown over a flat bottom (+) decays over the timescale $\mathcal{T}_{spindown} = E^{-1/2} f^{-1}$, where $E = (\delta_e/H_P)^2$. In both homogeneous and stratified spindown, $M_{initial} = 0.07$ m^2 s^{-1} and $L = 10.6$ km.

correction as well as the filtered Ekman pumping from the homogeneous and stratified spindown simulations for $\epsilon = 0.01, \sigma = 1$ and $E^{1/4} = 0.16$. The greater Ekman pumping in stratified spindown than in homogeneous spindown over a flat bottom is consistent with the addition of this nonlinear correction.

2.a. $w_p^{(2)} \propto -\sigma^{1/2}\epsilon\cos(2y)$.

Vertical advection of the thermal boundary layer buoyancy anomaly, $\widetilde{b}_T^{(1)}$, from cor-

rection 1.a, where

$$\frac{\partial \widetilde{b}_T^{(2)}}{\partial t} + \widetilde{w}_i^{(0)}(z=0)\frac{\partial \widetilde{b}_T^{(1)}}{\partial \xi} = \frac{1}{2}\frac{\partial^2 \widetilde{b}_T^{(2)}}{\partial \xi^2}, \tag{A.2}$$

contributes to a secondary circulation which tends to enhance Ekman pumping at $y = \pi/2$ and reduce Ekman suction at $y = -\pi/2$. This $O(\epsilon)$ correction tends to oppose the effect of momentum advection, which tends to reduce Ekman pumping and enhance Ekman suction. However, since the buoyancy anomalies, $\widetilde{b}_T^{(1)}, \widetilde{b}_T^{(2)}$, need to grow in time in order for this effect to occur, numerical simulations are necessary in order to see whether this correction has a nonnegligible effect on Ekman pumping and suction for increasing Rossby number.

3.a. $w_p^{(2)} \propto -\epsilon \cos(2y)$.

Lateral Ekman advection of the thermal boundary layer buoyancy anomaly, $\widetilde{b}_T^{(1)}$, from correction 1.a, balances diffusion of buoyancy,

$$\widetilde{v}_e^{(0)}\frac{\partial \widetilde{b}_T^{(1)}}{\partial y} = \frac{1}{2}\frac{\partial \widetilde{b}_e^{(2)}}{\partial \eta^2}, \tag{A.3}$$

and, by the no buoyancy flux boundary condition, leads to a higher order thermal boundary layer buoyancy anomaly that grows by diffusion. This correction modifies Ekman pumping at the same order and with the same structure as correction 2.a, but, as previously noted, the buoyancy anomaly needs to grow in time in order to counter the effects of momentum advection at order Rossby number.

4.a. $w_p^{(2)} \propto \epsilon \cos(2y)$.

As in homogeneous spindown over a flat bottom, horizontal Ekman advection of momentum leads to an asymmetry in Ekman pumping and suction, in which Ekman pumping at $y = \pi/2$ is reduced and Ekman suction at $y = -\pi/2$ is enhanced. In contrast to the corrections to Ekman pumping that arise from buoyancy modifying the pressure field, this nonlinear correction is nonzero within an inertial period, whereas

the buoyancy anomalies arise in time.

5.a. $w_p^{(2)} \propto \epsilon \cos(2y)$.

Lateral Ekman advection of the interior buoyancy anomaly balances diffusion of buoyancy,

$$\widetilde{v}_e^{(0)} \frac{\partial \widetilde{b}_i^{(0)}}{\partial y} = \frac{1}{2} \frac{\partial \widetilde{b}_e^{(2)}}{\partial \eta^2}, \tag{A.4}$$

leads to a thermal boundary layer buoyancy anomaly by the no buoyancy flux boundary condition. This buoyancy anomaly modifies the horizontal pressure gradient and the Ekman transport such that it enhances the asymmetry in Ekman pumping and suction from Ekman advection of momentum. Since corrections 2.a and 3.a tend to oppose corrections 4.a and 5.a, the numerical simulations are needed to examine which effects play a more substantial role for increasing Rossby number.

A.2 Sloping bottom

For stratified spindown over a sloping bottom, there are 10 corrections to Ekman pumping that arise from coupling between the frictionally driven circulation and the buoyancy field and are larger than order Rossby number. Correction 1.b modifies the linear dynamics in spindown over a sloping bottom and, in order to keep consistent notation with Chapters 2 and 3, is denoted as $n = 0$. The nonlinear corrections are only documented for the first or second harmonic. Furthermore, in order to simplify this analysis, the examination is restricted to coupling between the Ekman flows due to the laterally sheared along-isobath flow and the buoyancy field, *i.e.* higher order coupling with the flows arising from diffusion of the stratification is neglected.

In this section, the equations are shown in the rotated coordinate frame. In the thermal boundary layer, the geostrophic along-isobath flow is balanced by two components to the pressure field. By using the hydrostratic relationship, this expression

in dimensional form is

$$f\widetilde{u}_T = \frac{\partial}{\partial y}\int_{\xi}^{\infty} \widetilde{b}_T d\xi' - \theta\widetilde{b}_T. \tag{A.5}$$

As applied in Chapters 2 and 3, the second term on the right hand side of the above expression leads to buoyancy shutdown of the Ekman transport and is larger than the first term on the right hand side when $E^{1/2} < \sigma S$ on the spindown timescale. So, from stratified spindown over a flat bottom, all the nonlinear corrections to Ekman pumping from coupling at order Rossby number due to coupling with the buoyancy field can give rise to an additional correction that is larger than order Rossby number on a sloping bottom if $E^{1/2} < \sigma S$.

1.b. $w_p^{(0)} \propto -\beta^{1/2}\sin(y)$.

Lateral Ekman advection of the background stratification balances diffusion of buoyancy, where

$$-\widetilde{v}_e^{(0)} = \frac{1}{2}\frac{\partial \widetilde{b}_e^{(0)}}{\partial \eta^2}, \tag{A.6}$$

and leads to buoyancy shutdown of the Ekman pumping at $O(\beta^{1/2})$ from the second term in (A.5). As detailed in Chapter 2, when $\beta = 1$, this correction reduces the leading order Ekman pumping and suction equally.

2.b. $w_p^{(1)} \propto \beta^{1/2}\sigma^{1/2}E^{-1/4}\epsilon\cos(2y)$.

Lateral Ekman advection of the buoyancy anomaly in correction 1.b balances diffusion

$$\widetilde{v}_e^{(0)}\frac{\partial \widetilde{b}_T^{(0)}}{\partial y} = \frac{1}{2}\frac{\partial \widetilde{b}_e^{(1)}}{\partial \eta^2}, \tag{A.7}$$

and leads to a larger buoyancy anomaly in regions of cyclonic flow than anticyclonic flow. From the second term in (A.5), this buoyancy anomaly leads to nonlinear buoyancy shutdown, in which Ekman pumping is suppressed to a greater extent than

Ekman suction. At the same order, this buoyancy anomaly is enhanced by vertical advection in the thermal boundary layer, where

$$\frac{\partial \widetilde{b}_T^{(1)}}{\partial t} + \widetilde{w}_i^{(0)}(z=0)\frac{\partial \widetilde{b}_T^{(0)}}{\partial \xi} = \frac{1}{2}\frac{\partial^2 \widetilde{b}_T^{(1)}}{\partial \xi^2}, \tag{A.8}$$

which contributes to a larger buoyancy anomaly in regions of cyclonic flow than anti-cyclonic flow. Since this correction occurs at $O(\beta^{1/2}\sigma^{1/2}E^{-1/4}\epsilon)$, nonlinear advection of buoyancy can lead to more pronounced asymmetry in Ekman pumping and suction than by Ekman advection of momentum alone at $O(\epsilon)$.

3.b. $w_p^{(2)} \propto S^{1/2}\cos(y)$.

From lateral Ekman advection of the background stratification in correction 1.b, the buoyancy anomaly that arises in the thermal boundary layer balances an along-isobath flow from the first term in (A.5). In contrast to the component that leads to linear buoyancy shutdown, this correction does not enter into the leading order dynamics.

4.b. $w_p^{(2)} \propto S^{1/2}\cos(y)$.

From vertical advection of the laterally uniform buoyancy anomaly in the thermal boundary layer, the resulting buoyancy anomaly that is noted in 1.a leads to another component of the along-isobath flow from the second term in (A.5). Both nonlinear corrections 3.b and 4.b cause Ekman pumping (suction) where the initial interior along-isobath flow is a (maximum) minimum, rather than modify Ekman pumping and suction on the cyclonic and anticyclonic axes.

5.b. $w_p^{(3)} \propto \sigma^{1/2}E^{-1/4}S^{1/2}\epsilon\sin(2y) = \beta^{1/2}S^{-1/2}\epsilon\sin(2y)$.

In correction 2.a, vertical advection of the cross-isobath varying buoyancy anomaly leads to another buoyancy anomaly in the thermal boundary layer. This buoyancy anomaly balances an along-isobath flow from the second term in (A.5).

6.b. $w_p^{(3)} \propto \sigma^{1/2} E^{-1/4} S^{1/2} \epsilon \sin(2y) = \beta^{1/2} S^{-1/2} \epsilon \sin(2y)$.

In correction 3.a, lateral Ekman advection of the cross-isobath varying buoyancy anomaly balances diffusion. By the no normal buoyancy flux boundary condition, the buoyancy flux from the Ekman layer leads to a higher order buoyancy anomaly in the thermal boundary layer. This buoyancy anomaly balances an along-isobath flow from the second term in (A.5).

7.b. $w_p^{(3)} \propto -\sigma^{1/2} E^{-1/4} S^{1/2} \epsilon \sin(2y) = -\beta^{1/2} S^{-1/2} \epsilon \sin(2y)$.

In correction 5.a, lateral Ekman advection of the interior buoyancy anomaly balances diffusion. By a buoyancy flux from the Ekman layer, the buoyancy anomaly arises in the thermal boundary layer. This buoyancy anomaly balances an along-isobath flow from the second term in (A.5).

8.b. $w_p^{(3)} \propto \sigma^{1/2} E^{-1/4} S^{1/2} \epsilon \sin(2y) = \beta^{1/2} S^{-1/2} \epsilon \sin(2y)$.

In correction 1.b, lateral Ekman advection of the background stratification balances diffusion and gives rise to a buoyancy anomaly in the thermal boundary layer that leads to buoyancy shutdown. From vertical advection of this buoyancy anomaly in the thermal boundary layer, another buoyancy anomaly is formed and balances an along-isobath flow from the first term in (A.5).

9.b. $w_p^{(3)} \propto \sigma^{1/2} E^{-1/4} S^{1/2} \epsilon \sin(2y) = \beta^{1/2} S^{-1/2} \epsilon \sin(2y)$.

In correction 2.b, the buoyancy anomaly that corresponds to nonlinear buoyancy shutdown from the second term in (A.5) also contributes to an additional along-isobath flow that is balanced by the first term in (A.5). Note that this correction does not modify the Ekman pumping and suction on the cyclonic and anticyclonic axes of the interior along-isobath flow.

10.b. $w_p^{(4)} \propto \sigma^{-1/2} E^{1/4} \sin(y)$.

As previously documented in 1.a, vertical advection of the laterally uniform buoyancy anomaly leads to an $O(E^{1/4})$ correction to Ekman pumping and suction. However, in contrast to stratified spindown over a flat bottom, this correction is not the most dominant correction.

The order of the corrections listed above are justified as follows. In Chapter 2, in order to focus on the dynamics of buoyancy shutdown, $E^{1/4}\sigma^{-1/2} < S^{1/2}$, so that the second term in (A.5) dominated over the first term. This assumption means that the $O(S^{1/2})$ corrections dominate over the $O(\sigma^{-1/2}E^{1/4})$ correction. The corrections 5.b-9.b are larger than $O(\sigma^{-1/2}E^{1/4})$ given the assumption that $M_{initial}/M_{Thorpe} \equiv \epsilon E^{-1/2}S^{1/2}\sigma > 1$. Correction 10.b still remains larger than $O(\epsilon)$ under the assumption that $\epsilon < \sigma^{-1/2}E^{1/4}$. This assumption is necessary so that the nonlinear corrections do not modify the leading order dynamics in the analytical analysis. The numerical simulations examine the case in which the Rossby number is not restricted to this constraint.

Appendix B

Discretization of the equations for linear and nonlinear stratified spindown

This appendix presents the numerical method that is used to solve for the leading order correction to stratified spindown (SSD) on a flat bottom, *i.e.* correction 1.a in Appendix A, and the nonlinear correction on a sloping bottom, *i.e.* correction 2.b in Appendix B. The equations are solved using the Crank-Nicolson method (Crank and Nicolson 1947), in which the partial derivatives in time and space are discretized at a fictitious point in between two time steps.

The labels j and k denote the nondimensional time index and the thermal boundary layer vertical coordinate index, respectively. The numerical solution is calculated on a grid from $1 \leq j \leq J$ and $1 \leq k \leq K$, where the initial conditions are applied at $j = 1$ and the maximum number of time steps and spatial steps in the domain are given by J and K, respectively. For stratified spindown on a flat bottom, the forcing term to the nonlinear correction is applied from the analytical linear solution. On a sloping bottom, the forcing terms in the equations for the nonlinear correction are applied from the numerical solution to the linear problem. The linear problem is solved by first discretizing the set of equations, boundary conditions, and initial con-

ditions (2.100)-(2.108) that describe the linear dynamics of spindown and buoyancy shutdown. Then, the numerical solution for the linear dynamics is applied to the set of equations and boundary conditions that describe nonlinear buoyancy shutdown and (3.73)-(3.77).

B.1 Discretization of the equations for the correction to SSD on a flat bottom

The vertical advection of the laterally uniform buoyancy anomaly, $\overline{b}_T$, in the thermal boundary layer by the zeroth-order Ekman pumping, leads to a buoyancy anomaly, where $\widetilde{b}_T^{(1)}(t,y,\xi) = \mathrm{e}^{-t/2}\sin(y)B_T^{(1)}(t,\xi)$. In the thermal boundary, the equations for the buoyancy anomaly and the along-isobath flow become

$$\frac{\partial B_T^{(1)}}{\partial t} - \frac{1}{2}B_T^{(1)} - \frac{1}{2}\frac{\partial^2 B_T^{(1)}}{\partial \xi^2} = -\frac{1}{2}\frac{\partial \overline{b}_T}{\partial \xi}, \tag{B.1}$$

$$U_T^{(1)} = \mathrm{e}^{-t/2}\int_\xi^\infty B_T^{(1)}(t,\xi')d\xi', \tag{B.2}$$

for $t > 0, 0 < \xi < \infty$. In the interior, the along-isobath flow satisfies

$$\frac{\partial U_i^{(1)}}{\partial t} = \varphi^{(1)}, \tag{B.3}$$

where $\varphi^{(1)}(t)$ determines the temporal evolution of the interior secondary circulation. From the analytical solution,

$$\frac{\partial \overline{b}_T}{\partial \xi} = -\mathrm{erfc}(\frac{\xi}{\sqrt{2t}}). \tag{B.4}$$

is applied.

These equations are solved subject to the following Ekman pumping, no normal buoyancy flux at the bottom, and no far-field thermal boundary layer flow boundary conditions:

$$\frac{d\varphi^{(1)}}{dt} + \frac{1}{2}(\varphi^{(1)} + \frac{\partial U_T^{(1)}}{\partial t}(t, \xi = 0)) = 0, \tag{B.5}$$

$$\frac{\partial B_T^{(1)}}{\partial \xi}(t, \xi = 0) = 0, \tag{B.6}$$

$$U_T^{(1)}, B_T^{(1)} \to \infty \quad \text{as} \quad \xi \to 0. \tag{B.7}$$

These equations are discretized, where $\lambda \equiv 1/2$ for the Crank-Nicolson scheme, $r \equiv \Delta t/(2(\Delta\xi)^2)$, Δt is the nondimensional time step, and $\Delta\xi$ is the nondimensional thermal boundary layer grid step. The discretized diffusion equation is

$$\begin{aligned} & -\lambda r B_T^{(1)}|_{j+1}^{k+1} + (1 + 2\lambda r - \frac{\Delta t}{4}) B_T^{(1)}|_{j+1}^{k} - \lambda r B_T^{(1)}|_{j+1}^{k-1} \\ = \; & (1-\lambda) r B_T^{(1)}|_{j}^{k+1} + (1 - 2r(1-\lambda) + \frac{\Delta t}{4}) B_T^{(1)}|_{j}^{k} + (1-\lambda) r B_T^{(1)}|_{j}^{k-1} \\ - \; & \frac{\Delta t}{4}(\frac{\partial \bar{b}_T}{\partial \xi}|_{j+1}^{k} + \frac{\partial \bar{b}_T}{\partial \xi}|_{j}^{k}), \end{aligned} \tag{B.8}$$

for $j > 1, 1 < k < K$. The boundary condition for $B_T^{(1)}$ at $\xi = 0$ is derived such that it is consistent with the diffusion equation. From an expansion of $B_T^{(1)}$ at $k = 1$, where the no buoyancy flux boundary condition is applied,

$$\frac{\partial^2 B_T^{(1)}}{\partial \xi^2}|_{j}^{k=1} = \frac{2}{(\Delta\xi)^2}(B_T^{(1)}|_{j}^{k=2} - B_T^{(1)}|_{j}^{k=1}). \tag{B.9}$$

From substituting (B.9) into equation (B.1), the boundary condition for $B_T^{(1)}$, $j > 1$ at $\xi = 0$, becomes

$$\begin{aligned} & (1 + 2\lambda r - \frac{\Delta t}{4}) B_T^{(1)}|_{j}^{k=1} - 2\lambda r B_T^{(1)}|_{j}^{k=2} \\ = \; & (1 - 2(1-\lambda) r + \frac{\Delta t}{4}) B_T^{(1)}|_{j-1}^{k=1} + 2(1-\lambda) r B_T^{(1)}|_{j-1}^{k=2} + \frac{\Delta t}{2}. \end{aligned} \tag{B.10}$$

For $\xi \to \infty$, the no far-field thermal boundary layer buoyancy anomaly boundary condition becomes

$$B_T^{(1)}|_j^{k=K} = 0. \tag{B.11}$$

The initial condition for $B_T^{(1)}$ becomes

$$B_T^{(1)}|_{j=1}^{k} = 0. \tag{B.12}$$

From equation (B.8), $B_T^{(1)}$ is determined at each time step, $j > 1$, by solving

$$\mathbf{A} B_T^{(1)}|_j^{1\leq k\leq K-1} = \mathbf{b}, \tag{B.13}$$

where $\mathbf{A}$ is a $K-1 \times K-1$ tridiagonal coefficient matrix with elements determined by the left hand side of (B.8), $B_T^{(1)}|_j^{1\leq k\leq K-1}$ is the $K-1 \times 1$ solution column vector, and $\mathbf{b}$ is the $K-1 \times 1$ column vector with elements determined by the right hand side of (B.8), subject to the boundary condition (B.11). This tridiagonal system of equations is solved with the Thomas algorithm. Then, $U_T^{(1)}$ is determined from (B.2) by vertically integrating the solution to $B_T^{(1)}$. Then, $\varphi^{(1)}$ is determined from the discretized Ekman pumping boundary condition

$$\varphi^{(1)}|_j = (\frac{4-\Delta t}{4+\Delta t})\varphi^{(1)}|_{j-1} - (\frac{2}{4+\Delta t})(U_T^{(1)}|_j^{k=1} - U_T^{(1)}|_{j-1}^{k=1}). \tag{B.14}$$

Finally, the time evolution of the interior along-isobath flow is solved the interior momentum balance

$$U_i^{(1)}|_j = U_i^{(1)}|_{j-1} + \frac{\Delta t}{2}(\varphi^{(1)}|_j + \varphi^{(1)}|_{j-1}). \tag{B.15}$$

This system of equations is solved with $\Delta t = 0.01$, $\Delta\xi = 0.02$ on a grid from $t = 0$ to $t = 10$ and $\xi = 0$ to $\xi = 10$. Thus, $J = 1001, K = 501$ and $r = 12.5$.

B.2 Discretization of the linear SSD equations on a sloping bottom

In Chapter 2, the zeroth order linear solution for the interior along-isobath flow is decomposed as $U_i^{(0)}(t,z) = 1 - \Psi^{(0)}(t)\mathrm{e}^{-z}$. The time evolution of the interior along-isobath flow is determined by

$$\frac{d\Psi^{(0)}}{dt} + \varphi^{(0)} = 0, \tag{B.16}$$

after the solution $\varphi^{(0)}$ is solved below. The coupled set of partial differential equations reduces to the diffusion equation

$$\frac{\partial U_T^{(0)}}{\partial t} = \frac{1}{2}\frac{\partial^2 U_T^{(0)}}{\partial \xi^2}, \tag{B.17}$$

for $t > 0$, $0 < \xi < \infty$, subject to the following no-slip, Ekman pumping, no normal buoyancy flux at the bottom, and no far-field thermal boundary layer flow boundary conditions:

$$\varphi^{(0)} + \frac{1}{2}(1 - \Psi^{(0)} + \beta^{1/2} U_T^{(0)}(\xi = 0)) = 0, \tag{B.18}$$

$$\frac{d\varphi^{(0)}}{dt} + \frac{1}{2}(\varphi^{(0)} + \beta^{1/2}\frac{\partial U_T^{(0)}}{\partial t}(\xi = 0)) = 0, \tag{B.19}$$

$$\frac{\partial U_T^{(0)}}{\partial \xi}(\xi = 0) + 2\varphi^{(0)} = 0, \tag{B.20}$$

$$U_T^{(0)} \to 0 \quad \text{as} \quad \xi \to \infty, \tag{B.21}$$

and the following initial conditions:

$$(\Psi^{(0)}(t=0), U_T^{(0)}(t=0), \varphi^{(0)}(t=0)) = (0, 0, -\frac{1}{2}). \tag{B.22}$$

These equations are discretized, where $\lambda \equiv 1/2$ for the Crank-Nicolson scheme, $q \equiv \Delta t/\Delta\xi$, $r \equiv \Delta t/(2(\Delta\xi)^2)$, Δt is the nondimensional time step, and $\Delta\xi$ is the

nondimensional thermal boundary layer grid step. The discretized diffusion equation is

$$\begin{aligned} & -\lambda r U_T^{(0)}|_{j+1}^{k+1} + (1+2\lambda r) U_T^{(0)}|_{j+1}^{k} - \lambda r U_T^{(0)}|_{j+1}^{k-1} \\ = \;& (1-\lambda) r U_T^{(0)}|_{j}^{k+1} + (1-2r(1-\lambda)) U_T^{(0)}|_{j}^{k} + (1-\lambda) r U_T^{(0)}|_{j}^{k-1}, \end{aligned} \tag{B.23}$$

for $j > 1, 1 < k < K$. The boundary condition for $U_T^{(0)}$ at $\xi = 0$ is derived such that it is consistent with the diffusion equation, where

$$\frac{\partial U_T^{(0)}}{\partial t}|_{j+\frac{1}{2}}^{k=1} = (\frac{\lambda}{2}) \frac{\partial^2 U_T^{(0)}}{\partial \xi^2}|_{j+1}^{k=1} + (\frac{1-\lambda}{2}) \frac{\partial^2 U_T^{(0)}}{\partial \xi^2}|_{j}^{k=1}. \tag{B.24}$$

From an expansion of $U_T^{(0)}$ at k,

$$\frac{\partial^2 U_T^{(0)}}{\partial \xi^2}|_j^k = \frac{2}{(\Delta\xi)^2}(U_T^{(0)}|_j^{k+1} - U_T^{(0)}|_j^k) - (\frac{2}{\Delta\xi}) \frac{\partial U_T^{(0)}}{\partial \xi}|_j^k. \tag{B.25}$$

Then, at $k = 1$, with (B.20),

$$\frac{\partial^2 U_T^{(0)}}{\partial \xi^2}|_j^{k=1} = \frac{2}{(\Delta\xi)^2}(U_T^{(0)}|_j^{k=2} - U_T^{(0)}|_j^{k=1}) + (\frac{4}{\Delta\xi})\varphi^{(0)}|_j. \tag{B.26}$$

Equation (B.19) is discretized on the Crank-Nicolson stencil at $j+1/2, k = 1$, so that

$$\varphi^{(0)}|_{j+1} = (\frac{4-\Delta t}{4+\Delta t})\varphi^{(0)}|_j - (\frac{2\beta^{1/2}}{4+\Delta t})(U_T^{(0)}|_{j+1}^{k=1} - U_T^{(0)}|_j^{k=1}). \tag{B.27}$$

Then, from substituting equations (B.26)-(B.27) into equation (B.24), the boundary condition for $U_T^{(0)}$, $j > 1$, becomes

$$\begin{aligned} & (1 + 2\lambda r + \frac{4\beta^{1/2}\lambda q}{4+\Delta t}) U_T^{(0)}|_j^{k=1} - 2\lambda r U_T^{(0)}|_j^{k=2} \\ = \;& (1 + \frac{4\beta^{1/2}\lambda q}{4+\Delta t} - 2(1-\lambda)r) U_T^{(0)}|_{j-1}^{k=1} + 2(1-\lambda) r U_T^{(0)}|_{j-1}^{k=2} \\ + \;& (2\lambda q(\frac{4-\Delta t}{4+\Delta t}) + 2(1-\lambda)q)\varphi^{(0)}|_{j-1}. \end{aligned} \tag{B.28}$$

The boundary condition as $\xi \to \infty$ becomes

$$U_T^{(0)}|_j^{k=K} = 0. \tag{B.29}$$

The initial conditions become

$$(\Psi^{(0)}|_{j=1}, U_T^{(0)}|_{j=1}^{k}, \varphi^{(0)}|_{j=1}) = (0, 0, -\frac{1}{2}). \tag{B.30}$$

From equation (B.23), $U_T^{(0)}$ is determined at each time step, $j > 1$, by solving

$$\mathbf{A}_0 U_T^{(0)}|_j^{1\leq k\leq K-1} = \mathbf{b}_0, \tag{B.31}$$

where $\mathbf{A}_0$ is a $K-1 \times K-1$ tridiagonal coefficient matrix with elements determined by the left hand side of (B.23), $U_T^{(0)}|_j^{1\leq k\leq K-1}$ is the $K-1 \times 1$ solution column vector, and $\mathbf{b}_0$ is the $K-1 \times 1$ column vector with elements determined by the right hand side of (B.23), subject to the boundary conditions (B.28) - (B.29). Then, once the solution for $U_T^{(0)}$ is solved at each time step, $\varphi^{(0)}$ is determined from (B.27). Finally, the time evolution for the interior along-isobath flow is solved from the discretized no-slip boundary condition, (B.18), such that

$$\Psi^{(0)}|_j = 1 + 2\varphi^{(0)}|_j + \beta^{1/2} U_T^{(0)}|_j^{k=1}. \tag{B.32}$$

This set of equations is solved with the Thomas algorithm for $\sigma = 1$ and $\beta = 1$, where $\Delta t = 0.001,\ \Delta\xi = 0.02$ on a grid from $t = 0$ to $t = 20$ and $\xi = 0$ to $\xi = 10$. Thus, $J = 20001$, $K = 501$, $r = 1.25$, and $q = 0.05$. The maximum error between the numerical solution for $\varphi^{(0)}$ as calculated above and the analytical solution, (2.112), is 0.02%.

B.3 Discretization of the nonlinear SSD equations on a sloping bottom

For the nonlinear correction to the linear dynamics by nonlinear buoyancy shutdown, the interior along-isobath flow is already decomposed in time and space, such that $\Psi^{(1)}(t) \equiv U_i^{(1)}(t)$. Now, the time evolution of the interior along-isobath flow is

$$\frac{d\Psi^{(1)}}{dt} - 2\varphi^{(1)} = 0, \tag{B.33}$$

and the forced diffusion equation is

$$\frac{\partial U_T^{(1)}}{\partial t} - \frac{1}{2}\frac{\partial^2 U_T^{(1)}}{\partial \xi^2} = \frac{1}{2}\varphi^{(0)}\frac{\partial U_T^{(0)}}{\partial \xi}, \tag{B.34}$$

for $t > 0$, $0 < \xi < \infty$, subject to the following no-slip, Ekman pumping, no normal buoyancy flux at the bottom, and no far-field thermal boundary layer flow boundary conditions:

$$\varphi^{(1)} + \frac{1}{2}(\Psi^{(1)} + \beta^{1/2} U_T^{(1)}(\xi = 0)) = 0, \tag{B.35}$$

$$\frac{d\varphi^{(1)}}{dt} + \varphi^{(1)} + (\frac{\beta^{1/2}}{2})\frac{\partial U_T^{(1)}}{\partial t}(\xi = 0) = 0, \tag{B.36}$$

$$\frac{\partial U_T^{(1)}}{\partial \xi}(\xi = 0) + 2\varphi^{(1)} = \varphi^{(0)} U_T^{(0)}(\xi = 0), \tag{B.37}$$

$$U_T^{(1)} \to 0 \quad \text{as} \quad \xi \to \infty, \tag{B.38}$$

and the following initial conditions:

$$(\Psi^{(1)}(t = 0), U_T^{(1)}(t = 0), \varphi^{(1)}(t = 0)) = (0, 0, 0). \tag{B.39}$$

The forced diffusion equation is discretized using the Crank-Nicolson scheme, where $\lambda \equiv 1/2$ and

$$\begin{aligned} - \quad & \lambda r U_T^{(1)}|_j^{k+1} + (1+2\lambda r) U_T^{(1)}|_j^k - \lambda r U_T^{(1)}|_j^{k-1} \\ = \quad & (1-\lambda) r U_T^{(1)}|_{j-1}^{k+1} + (1-2r(1-\lambda)) U_T^{(1)}|_{j-1}^k + (1-\lambda) r U_T^{(1)}|_{j-1}^{k-1} \\ + \quad & \frac{q}{16}(\varphi^{(0)}|_j + \varphi^{(0)}|_{j-1})(U_T^{(0)}|_{j-1}^{k+1} - U_T^{(0)}|_{j-1}^{k-1} + U_T^{(0)}|_j^{k+1} - U_T^{(0)}|_j^{k-1}), \end{aligned} \tag{B.40}$$

for $j > 1, 1 < k < K$. The boundary conditions are discretized as in the previous section such that they are consistent with the diffusion equation. Then, at $k = 1$, with (B.37),

$$\begin{aligned} \frac{\partial^2 U_T^{(1)}}{\partial \xi^2}|_j^{k=1} \quad = \quad & \frac{2}{(\Delta\xi)^2}(U_T^{(1)}|_j^{k=2} - U_T^{(1)}|_j^{k=1}) \\ + \quad & (\frac{4}{\Delta\xi})\varphi^{(1)}|_j - (\frac{2}{\Delta\xi})\varphi^{(0)}|_j U_T^{(0)}|_j^{k=1}. \end{aligned} \tag{B.41}$$

Equation (B.36) is discretized on the Crank-Nicolson stencil at $j+1/2, k = 1$, so that

$$\varphi^{(1)}|_{j+1} = (\frac{2-\Delta t}{2+\Delta t})\varphi^{(1)}|_j - \frac{\beta^{1/2}}{2+\Delta t}(U_T^{(1)}|_{j+1}^{k=1} - U_T^{(1)}|_j^{k=1}). \tag{B.42}$$

By substitution of equations (B.41)-(B.42) into diffusion equation on the stencil used in the Crank-Nicolson scheme, the boundary condition for $j > 1$ becomes

$$\begin{aligned} & (1 + 2\lambda r + \frac{2\beta^{1/2}\lambda q}{2+\Delta t}) U_T^{(1)}|_j^{k=1} - 2\lambda r U_T^{(1)}|_j^{k=2} \\ = \quad & (1 + \frac{2\beta^{1/2}\lambda q}{2+\Delta t} - 2(1-\lambda)r) U_T^{(1)}|_{j-1}^{k=1} + 2(1-\lambda) r U_T^{(1)}|_{j-1}^{k=2} \\ + \quad & (2\lambda q(\frac{2-\Delta t}{2+\Delta t}) + 2(1-\lambda)q)\varphi^{(1)}|_{j-1} - \lambda q \varphi^{(0)}|_j U_T^{(0)}|_j^{k=1} \\ - \quad & (1-\lambda) q \varphi^{(0)}|_{j-1} U_T^{(0)}|_{j-1}^{k=1} - (\frac{\Delta t}{4})(\varphi^{(0)}|_{j-1} + \varphi^{(0)}|_j)^2. \end{aligned} \tag{B.43}$$

The boundary condition as $\xi \to \infty$ becomes

$$U_T^{(1)}|_j^{k=K} = 0. \tag{B.44}$$

The initial conditions become

$$(\Psi^{(1)}|_{j=1}, U_T^{(1)}|_{j=1}^{k}, \varphi^{(1)}|_{j=1}) = (0, 0, 0). \tag{B.45}$$

From equation (B.40), $U_T^{(0)}$ is determined at each time step, $j > 1$, by solving

$$\mathbf{A}_1 U_T^{(1)}(j, 1 \leq k \leq K-1) = \mathbf{b}_1, \tag{B.46}$$

where $\mathbf{A}_1$ is a $K-1 \times K-1$ tridiagonal coefficient matrix with elements determined by the left hand side of (B.40), $U_T^{(1)}|_j^{1 \leq k \leq K-1}$ is the $K-1 \times 1$ solution column vector, and $\mathbf{b}_1$ is a $K-1 \times 1$ column vector with elements determined by the right hand side of (B.40), subject to the boundary conditions (B.43) - (B.44). Then, $\varphi^{(1)}$ is determined from (B.42), after the solution for $U_T^{(1)}$ is solved at each time step. Finally, the time evolution for the interior along-isobath flow is solved from the discretized no-slip boundary condition, (B.35), such that

$$\Psi^{(1)}|_j = -2\varphi^{(1)}|_j - \beta^{1/2} U_T^{(1)}|_j^{k=1}. \tag{B.47}$$

The above set of equations is solved with the Thomas algorithm, subject to the previously calculated numerical solution for $U_T^{(0)}$ and $\varphi^{(0)}$ with $\sigma = 1$ and $\beta = 1$. The grid is set-up from $t = 0$ to $t = 10$ and $\xi = 0$ to $\xi = 10$, where $\Delta t = 0.001,\ \Delta\xi = 0.02$, $J = 10001$, $K = 501$, $r = 1.25$, and $q = 0.05$.

Bibliography

Abramowitz, M. and I. A. Stegun, 1972: *Handbook of Mathematical Functions*. Dover.

Allen, J. S. and P. A. Newberger, 1998: On symmetric instabilities in oceanic bottom boundary layers. *Journal of Physical Oceanography*, **28**, 1131–1151.

Amos, A. F., A. L. Gordon, and E. D. Schneider, 1971: Water masses and circulation patterns in the region of the Blake-Bahama Outer Ridge. *Deep-Sea Research*, **18**, 145–165.

Armi, L., 1978: Some evidence for boundary mixing in the deep ocean. *Journal of Geophysical Research*, **83 (C4)**, 1971–1979.

Barth, J. A., D. Bogucki, S. D. Pierce, and P. M. Kosro, 1998: Secondary circulation associated with a shelfbreak front. *Geophysical Research Letters*, **25 (15)**, 2761–2764.

Barth, J. A., D. Hebert, A. C. Dale, and D. S. Ullman, 2004: Direct observations of along-isopycnal upwelling and diapycnal velocity at a shelfbreak front. *Journal of Physical Oceanography*, **34**, 543–565.

Beardsley, R. C. and W. C. Boicourt, 1981: On estuarine and continental-shelf circulation in the Middle Atlantic Bight. *Evolution of Physical Oceanography, Scientic Surveys in Honor of Henry Stommel*, B. A. Warren and C. Wunsch, Eds., MIT Press, Cambridge, 198–233.

Beardsley, R. C. and C. N. Flagg, 1976: The water structure, mean currents, and shelf/slope water front on the New England continental shelf. *Mémoires de la Société Royale des Sciences de Liége*, **6(X)**, 209–225.

Benton, G. S., F. B. Lipps, and S.-Y. Tuann, 1964: The structure of the Ekman layer for geostrophic flows with lateral shear. *Tellus*, **XVI**, 186–199.

Brink, K. H., 1997: Time-dependent motions and the nonlinear bottom Ekman layer. *Journal of Marine Research*, **55**, 613–631.

Brink, K. H. and S. J. Lentz, 2009, accepted: Buoyancy arrest and bottom Ekman transport: Part I, Steady flow. *Journal of Physical Oceanography*.

Chapman, D. C., 1986: A simple model of the formation and maintenance of the shelf/slope front in the Middle Atlantic Bight. *Journal of Physical Oceanography*, **16**, 1273–1279.

Chapman, D. C., 2000a: A numerical study of the adjustment of a narrow stratified current over a sloping bottom. *Journal of Physical Oceanography*, **30**, 2927–2940.

Chapman, D. C., 2000b: Boundary layer control of buoyant coastal currents and the establishment of a shelfbreak front. *Journal of Physical Oceanography*, **30**, 2941–2955.

Chapman, D. C., 2002a: Deceleration of a finite-width, stratified current over a sloping bottom: frictional spindown or buoyancy shutdown? *Journal of Physical Oceanography*, **32**, 336–352.

Chapman, D. C., 2002b: Sensitivity of a model shelfbreak front to the parameterization of vertical mixing. *Journal of Physical Oceanography*, **32**, 3291–3298.

Chapman, D. C., J. A. Barth, R. C. Beardsley, and R. G. Fairbanks, 1986: On the continuity of mean flow between the Scotion shelf and the Middle Atlantic Bight. *Journal of Physical Oceanography*, **16**, 758–772.

Chapman, D. C. and R. C. Beardsley, 1989: On the origin of shelf water in the Middle Atlantic Bight. *Journal of Physical Oceanography*, **19**, 384–391.

Chapman, D. C. and S. J. Lentz, 1994: Trapping of a coastal density front by the bottom boundary layer. *Journal of Physical Oceanography*, **24**, 1464–1479.

Chapman, D. C. and S. J. Lentz, 1997: Adjustment of stratified flow over a sloping bottom. *Journal of Physical Oceanography*, **27**, 340–356.

Charney, J. G. and A. Eliassen, 1949: A numerical method of predicting the perturbations of the middle-latitude westerlies. *Tellus*, **1**, 38–54.

Crank, J. and P. Nicolson, 1947: A practical method for numerical evaluation of solutions of partial differential equations of the heat-conduction type. *Proceedings of the Cambridge Philosophical Society*, **43 (50)**, 50–67.

Csanady, G. T., 1976: Mean circulation in shallow seas. *Journal of Geophysical Research*, **81 (30)**, 5389–5399.

Duck, P. W., M. R. Foster, and R. Hewitt, 1997: On the boundary layer arising in the spin-up of a stratified fluid in a container with sloping walls. *Journal of Fluid Mechanics*, **335**, 233–259.

Eittreim, S., P. E. Biscaye, and A. F. Amos, 1975: Benthic nepheloid layers and the Ekman thermal pump. *Journal of Geophysical Research*, **80 (36)**, 5061–5067.

Fratantoni, P. S. and R. S. Pickart, 2007: The western North Atlantic shelfbreak current system in summer. *Journal of Physical Oceanography*, **37**, 2509–2533.

Fratantoni, P. S., R. S. Pickart, D. J. Torres, and A. Scotti, 2001: Mean structure and dynamics of shelfbreak jet in the Middle Atlantic Bight during fall and winter. *Journal of Physical Oceanography*, **31**, 2135–2156.

Garrett, C., P. MacCready, and P. Rhines, 1993: Boundary mixing and arrested Ekman layers: Rotating stratified flow near a sloping boundary. *Annual Reviews of Fluid Mechanics*, **25**, 291–323.

Gawarkiewicz, G. and D. C. Chapman, 1992: The role of stratification in the formation and maintenance of shelf-break fronts. *Journal of Physical Oceanography*, **22**, 753–772.

Gawarkiewicz, G., J. Churchill, F. Bahr, C. Linder, and C. Marquette, 2008: Shelfbreak frontal structure and processes north of Cape Hatteras in winter. *Journal of Marine Research*, **66**, 775–799.

Hallberg, R. and P. Rhines, 1996: Buoyancy-driven circulation in an ocean basin with isopycnals intersecting the sloping boundary. *Journal of Physical Oceanography*, **26**, 913–940.

Hart, J. E., 1995a: Nonlinear Ekman suction and ageostrophic effects in rapidly rotating flows. *Geophysical and Astrophysical Fluid Dynamics*, **79**, 201–222.

Hart, J. E., 1995b: A note on nonlinear corrections to the Ekman layer pumping velocity. *Physics of Fluids*, **12**, 131–135.

Haynes, P. H. and M. E. McIntyre, 1987: On the evolution of vorticity and potential vorticity in the presence of diabatic heating and frictional or other forces. *Journal of Atmospheric Sciences*, **44**, 828–841.

Holton, J. R., 1965: The influence of viscous boundary layers on transient motions in a stratified rotating fluid: Part i. *Journal of Atmospheric Sciences*, **22**, 402–411.

Houghton, R. W., 1995: The bottom boundary layer structure in the vicinity of the Middle Atlantic Bight shelfbreak front. *Continental Shelf Research*, **15 (10)**, 1173–1194.

Houghton, R. W., 1997: Lagrangian flow at the foot of a shelfbreak front using a dye tracer injected into the bottom boundary layer. *Geophysical Research Letters*, **24 (16)**, 2035–2038.

Houghton, R. W., D. Hebert, and M. Prater, 2006: Circulation and mixing at the New England shelfbreak front: Results of purposeful tracer experiments. *Progress in Oceanography*, **70**, 289–312.

Houghton, R. W. and M. Visbeck, 1998: Upwelling and convergence in the Middle Atlantic Bight shelfbreak front. *Geophysical Research Letters*, **25 (15)**, 2765–2768.

J. P. Ryan, P. C. C., J. A. Yoder, 1999: Enhanced chlorophyll at the shelfbreak of the Mid-Atlantic Bight and Georges Bank during the spring transition. *Limnology and Oceanography*, **44 (1)**, 1–11.

Kundu, P. K., 1976: Ekman veering observed near the ocean bottom. *Journal of Physical Oceanography*, **6**, 238–242.

Lentz, S. and J. Trowbridge, 2001: A dynamical description of fall and winter mean current profiles over the Northern California shelf. *Journal of Physical Oceanography*, **31**, 914–931.

Lentz, S. J., 2008: Observations and a model of the mean circulation over the Middle Atlantic Bight continental shelf. *Journal of Physical Oceanography*, **38**, 1203–1221.

Lentz, S. J. and J. H. Trowbridge, 1991: The bottom boundary layer over the Northern California shelf. *Journal of Physical Oceanography*, **21**, 1186–1201.

Linder, C. A. and G. Gawarkiewicz, 1998: A climatology of the shelfbreak front in the Middle Atlantic Bight. *Journal of Geophysical Research*, **103(C9)**, 18 405–18 423.

Linder, C. A., G. Gawarkiewicz, and R. S. Pickart, 2004: Seasonal characteristics of bottom boundary layer detachment at the shelfbreak front in the Middle Atlantic Bight. *Journal of Geophysical Research*, **109**, C03 049, doi:10.1029/2003JC002 032.

Loder, J. W., B. Petrie, and G. Gawarkiewicz, 1998: The coastal ocean off Northeastern North America: A large-scale view. *The Sea*, A. R. Robinson and K. H. Brink, Eds., John Wiley and Sons, Inc., New York, 105–133.

MacCready, P. and P. B. Rhines, 1991: Buoyant inhibition of Ekman transport on a slope and its effect on stratified spin-up. *Journal of Fluid Mechanics*, **223**, 631–661.

MacCready, P. and P. B. Rhines, 1993: Slippery bottom boundary layers on a slope. *Journal of Physical Oceanography*, **23**, 5–22.

Madron, X. D. D. and G. Weatherly, 1994: Circulation, transport, and bottom boundary layers of the deep currents in the Brazil Basin. *Journal of Marine Research*, **52**, 583–638.

Malone, T. C., T. S. Hopkins, P. G. Falkowski, and T. E. Whitledge, 1983: Production and transport of phytoplankton biomass over the continental shelf of the New York Bight. *Continental Shelf Research*, **1 (4)**, 305–337.

Marra, J., R. W. Houghton, and C. Garside, 1990: Phytoplankton growth at the shelf-break front in the Middle Atlantic Bight. *Journal of Marine Research*, **48**, 851–868.

Marshall, J. C. and A. J. G. Nurser, 1992: Fluid dynamics of oceanic thermocline ventilation. *Journal of Physical Oceanography*, **22**, 583–595.

McPhee-Shaw, E. E. and E. Kunze, 2002: Boundary layer intrusions from a sloping bottom: A mechanism for generating intermediate nepheloid layers. *Journal of Geophysical Research*, **107 (C6)**, doi:10.1029/2001JC000 801.

Mercado, A. and J. V. Leer, 1976: Near bottom velocity and temperature profiles observed by cyclesonde. *Geophysical Research Letters*, **3 (10)**, 633–636.

Middleton, J. F. and D. Ramsden, 1996: The evolution of the bottom boundary layer on the sloping continental shelf: A numerical study. *Journal of Geophysical Research*, **101 (C8)**, 18 061–18 077.

Moum, J. N., A. Perlin, J. M. Klymak, M. D. Levine, T. Boyd, and P. M. Kosro, 2004: Convectively driven mixing in the bottom boundary layer. *Journal of Physical Oceanography*, **34**, 2189–2202.

O'Dwyer, J. and R. G. Williams, 1997: The climatological distribution of potential vorticity over the abyssal ocean. *Journal of Physical Oceanography*, **27**, 2488–2506.

Pak, H. and J. R. V. Zaneveld, 1977: Bottom nepheloid layers and bottom mixed layers observed on the continental shelf off Oregon. *Journal of Geophysical Research*, **82 (27)**, 3921–3931.

Pedlosky, J., 2008: On the weakly nonlinear Ekman layer: Thickness and flux. *Journal of Physical Oceanography*, **38**, 1334–1339.

Perlin, A., J. N. Moum, and J. M. Klymak, 2005: Response of the bottom boundary layer over a sloping shelf to variations in alongshore wind. *Journal of Geophysical Research*, **110**, C10S09, doi:10.1029/2004JC002 500.

Phillips, O. M., 1970: On flows induced by diffusion in a stably stratified fluid. *Deep-Sea Research*, **17**, 435–443.

Pickart, R. S., 2000: Bottom boundary layer structure and detachment in the shelf-break jet of the Middle Atlantic Bight. *Journal of Physical Oceanography*, **30**, 2668–2686.

Pollard, R. T., P. B. Rhines, and R. O. R. Y. Thompson, 1973: The deepening of the wind-mixed layer. *Geophysical Fluid Dynamics*, **3**, 381–404.

Ramsden, D., 1995: Response of an oceanic bottom boundary layer on a slope to interior flow. Part I: Time-independent interior flow. *Journal of Physical Oceanography*, **25**, 1672–1687.

Rasmussen, L. L., G. Gawarkiewicz, W. B. Owens, and M. S. Lozier, 2005: Slope water, Gulf Stream, and seasonal influences on southern Mid-Atlantic Bight circulation during fall-winter transition. *Journal of Geophysical Research*, **110**, C02 009, doi:10.1029/2004JC002 311.

Rhines, P. B., 1998: Circulation, convection and mixing in rotating, stratified basins with sloping topography. *Physical Processes in Lakes and Oceans*, J. Imberger, Ed., 209–226, AGU Coastal and Estuarine Series 54.

Romanou, A. and G. L. Weatherly, 2001: Numerical simulations of buoyant Ekman layers in the presence of stratification. Part I: Constant interior forcing. *Journal of Physical Oceanography*, **31**, 3096–3120.

Shchepetkin, A. F. and J. C. McWilliams, 2005: The regional oceanic modeling system (ROMS): a split-explicit, free-surface, topography-following-coordinate oceanic model. *Ocean Modelling*, **9**, 347–404.

Siegmann, W. L., 1971: The spin-down of rotating stratified fluids. *Journal of Fluid Mechanics*, **47**, 689–711.

Stahr, F. R. and T. B. Sanford, 1999: Transport and bottom boundary layer observations of the North Atlantic Deep Western Boundary Current at the Blake Outer Ridge. *Deep-Sea Research Part II*, **46**, 205–243.

Stommel, H. and A. Leetmaa, 1972: Circulation on the continental shelf. *Proceedings of the National Academy of Sciences of the United States of America*, **69 (11)**, 3380–3384.

Thomas, L. N., 2005: Destruction of potential vorticity by winds. *Journal of Physical Oceanography*, **35**, 2457–2466.

Thomas, L. N. and P. B. Rhines, 2002: Nonlinear stratified spin-up. *Journal of Fluid Mechanics*, **473**, 211–244.

Thorpe, S. A., 1987: Current and temperature variability on the continental slope. *Philosophical Transactions of the Royal Society A*, **323**, 471–517.

Trowbridge, J. H. and S. J. Lentz, 1991: Asymmetric behavior of an oceanic boundary layer above a sloping bottom. *Journal of Physical Oceanography*, **21**, 1171–1185.

Trowbridge, J. H. and S. J. Lentz, 1998: Dynamics of the bottom boundary layer on the Northern California shelf. *Journal of Physical Oceanography*, **28**, 2075–2093.

Weatherly, G. L., 1972: A study of the bottom boundary layer of the Florida Current. *Journal of Physical Oceanography*, **2**, 54–72.

Weatherly, G. L. and J. C. V. Leer, 1977: On the importance of stable stratification to the structure of the bottom boundary layer on the Western Florida shelf. *Bottom Turbulence*, J. C. J. Nihoul, Ed., 103–122, Elsevier Oceanography Series.

Weatherly, G. L. and P. J. Martin, 1978: On the structure and dynamics of the oceanic bottom boundary layer. *Journal of Physical Oceanography*, **8**, 557–570.

Weatherly, G. L. and P. P. Niiler, 1974: Bottom homogeneous layers in the Florida current. *Geophysical Research Letters*, **1 (7)**, 316–319.

Williams, R. G. and V. Roussenov, 2003: The role of sloping sidewalls in forming potential vorticity contrasts in the ocean interior. *Journal of Physical Oceanography*, **33**, 633–648.

Wimbush, M. and W. Munk, 1970: The benthic boundary layer. *The Sea: Ideas and Observations on Progress in the Study of the Seas, Volume 4: New Concepts of Sea Floor Evolution, Part I: Regional Observations*, A. E. Maxwell, Ed., Wiley-Interscience, New York, 731–758.

Wright, D. G., 1989: On the alongshelf evolution of an idealized density front. *Journal of Physical Oceanography*, **19**, 532–541.

Wright, W. R., 1976: The limits of shelf water south of Cape Cod. *Journal of Marine Research*, **34**, 1–14.

Wunsch, C., 1970: On oceanic boundary mixing. *Deep-Sea Research*, **17**, 293–301.

Yankovsky, A. E. and D. C. Chapman, 1997: A simple theory for the fate of buoyant coastal discharges. *Journal of Physical Oceanography*, **27**, 1386–1401.

Zavala Sansón, L., 2001: The asymmetric Ekman decay of cyclonic and anticyclonic vortices. *European Journal of Mechanics-B/Fluids*, **20**, 541–556.

Zavala Sansón, L. and G. J. F. van Heijst, 2000: Nonlinear Ekman effects in rotating barotropic flows. *Journal of Fluid Mechanics*, **412**, 75–91.